Habilitationsschrift

zur
Erlangung der Venia legendi
für das Fach Physik
der
Ruprecht-Karls-Universität
Heidelberg

vorgelegt von
Dr. rer. nat. Christoph S. Garbe
aus Bochum

2006

Measuring and Modeling Fluid Dynamic Processes using Digital Image Sequence Analysis

Abstract

In this thesis novel motion models have been developed and incorporated into an extended parameter estimation framework that allows to accurately estimate the parameters and regularize them if needed. The performance of this framework has been increased to real time and implemented on inexpensive graphics hardware. Confidence and situation measures have been designed to discard inaccurate estimates. A phase field approach was developed to estimate piecewise smooth motion while detecting object boundaries at the same time. These algorithmic improvements have been successfully applied to three areas of fluid dynamics: air-sea interaction, microfluidics and plant physiology. At the ocean surface, the fluxes of heat and momentum have been measured with thermographic techniques, both spatially and temporally highly resolved. These measurement techniques present milestones for research in air-sea interaction, where point measurements and particle based laboratory measurements represent the state-of-the art. Calculations were done with two models, both making complement assumptions. Still, results derived from both models agree remarkably well. Measurements were conducted in laboratory settings as well as in the field. Microfluidic flow was measured with a new approach to molecular tagging velocimetry that explicitly models Taylor dispersion. This has lead to an increase in accuracy and applicability. Inaccuracies and problems of previous approaches due to Taylor dispersion were successfully evaded. Ground truth test measurements have been conducted, proving the accuracy of this novel technique. For the first time, flow velocities were measured in the xylem of plant leaves with active thermography. This represents a technique for measuring these flows on extended leaf areas on free standing plants, minimizing the impact caused by the measurement. Ground truth measurements on perfused leafs were performed. Measurements were also conducted on free standing plants in a climatic chamber, to measure xylem flows and relate flow velocities to environmental parameter. With a cuvette, environmental factors were varied locally. These measurements underlined the sensitivity of the new approach. A linear relationship in between flow rates and xylem diameter was found.

Contents

Chapter 1

Introduction

1.1 Motivation

The transport of energy, mass and momentum is one ubiquitous phenomenon in our world, spanning all branches of science. It is one condition for the continued existence of complex dynamic systems. As such, only through this transport living organisms can coordinate and keep upright their metabolism and other processes of life. Plants, for example, have developed complex vascular systems (the xylem) to transport nutrients and water from the roots to the rest of the plant. At the same time, all living tissue is continuously supplied with energy from the leaves, in form of the organic products of photosynthesis.

In plant physiology, it is a longstanding question how water and nutrients are transported in the xylem of the plant's leaf and which external factors influence it. While bulk dependencies are known, a detailed analysis has eluded research due to inadequate measurement techniques. The transport processes in leaves are especially important since it is known that they can be regulated by plants according to environmental forcing. Also, due to these regulatory mechanisms, the plant can cope with cuts in the leaf and still supply areas affected by these cuts with xylem sap by other pathways. Still, very little is known about these mechanisms.

On much smaller scales, a current trend in chemical and biochemical analytics as well as in medical diagnostics is the move to microfluidic mixers and "lab-on-a-chip" applications. Huge surface to volume ratios are achievable by micro channels with highly controlled boundary conditions, leading to more efficient reaction kinetics with less by-products. Even on these minute structures, the transport of energy, mass and momentum as well as the measurements thereof is vital for a better understanding of the processes involved. In these flow regimes, molecular tagging velocimetry (MTV) is an alternative approach to the standard technique of micro particle imaging velocimetry (μPIV) for measuring fluid flows. In MTV, a pattern is written to the fluid with an UV laser to uncage dyes and thus making them fluorescent. Although this approach has been used since the late eighties of the last century, measuring fluid flow with this technique has had one significant drawback: Due to the flow profile, the uncaged dyes would appear to diffuse in a process termed Taylor dispersion. This leads to significant uncertainties in the measurements, as it is difficult to correct for this dispersion.

Due to Taylor dispersion, the use of MTV is very limited. Nevertheless, it represents the only technique available for situations in which particles cannot be used for visualizing the flow, such as packed columns.

In environmental sciences, it is the transport of the same quantities, energy, momentum and mass, that is the driving force in most weather conditions on short scales and in climatic variability on longer time periods. It plays the dominant role on aquatic processes in the oceans such as ocean currents and the thermohaline circulation, the meridional overturning circulation (MOC). The two compartments of atmosphere and ocean are in contact at the ocean surface where energy, mass and momentum is exchanged between them. In atmosphere-ocean interactions, there exists a long standing problem of parameterizing the transfer of energy and mass to easily measurable quantities such as the wind velocity at a given reference height. Current parameterizations are semi-empirical relations that are based on a number of sea going experiments. There exists considerable scatter in the data for such parameterizations. This scatter introduces uncertainties in the parameterization and subsequent uses of them, for instance for global models and predictions of our future climate. There are a number of reasons for these high uncertainties. Among these are open questions as to other sources of near surface turbulence besides those induced by wind shear, intermittency of the transport process due to singular events such as microscale wave breaking and the suppression of turbulence and waves due to natural and anthropogenic surfactants at low to medium wind speeds. Only by finding answers to these open questions a physically based parametrization can ultimately be found that will reduce scatter in the data and hence deliver a better predictability. The dominant resistance to the transport between ocean and atmosphere is the laminar boundary layer in which turbulent transport is greatly suppressed. Therefore, the transport processes across the boundary layer play the dominant role in exchange between the two compartments. A better physical understanding of the processes involved, backed by accurate measurements is required in order to make advances in this field. The thickness of this boundary layer is roughly 0.2-2mm for energy (heat), 20-200µm for CO_2 (at 20°C) and 100-200 µm for momentum. This leads directly to one fundamental question for measuring these processes with standard techniques: How can one resolve these minute boundary layers which are undulated by surface waves bigger by a few order or magnitudes? The same problem arises on temporal scales. Here the processes take place on timescales less than a second. Microscale wave breaking is one example of such a fast process of turbulence generation. Standard techniques, which are point measurements with integration times of a few minutes, cannot resolve these intermittent events. Hence, they are not the best choice for detailed process studies.

All these problems necessitate novel measurement techniques. Only by measuring the transported quantities directly, both spatially and temporally highly resolved, a deeper understanding of the underlying processes can be gained. This holds true for the transport processes at the air-sea interface as it does for transport processes in plants or in microfluidic mixers. Due to these requirements on the measurement technique, imaging sensors are an ideal solution. Non-invasive, fast and accurate measurements are feasible with these sensors. While the accuracy and resolution of imaging devices improves, prices are steadily decreasing with advances of technology. This makes them an ideal tool for the visualization of fluid dynamic

transport phenomena with an increasing range of applications. Novel imaging devices are not limited to acquiring data in the visible spectrum. Infrared cameras can visualize temperature distributions with noise levels well below 20 mK. Also, devices on satellites or for medical applications can deliver temporally and spatially highly resolved multispectral image data.

Linked to new visualization techniques is the need for novel algorithms to extract physical parameters out of the imaging data. One key parameter is the displacement of physical structures from one frame to the next or over a sequence of frames. Since the early eighties of the last century, long standing effort has been put into the estimation of motion by the computer science community. Here the main focus was to retrieve motion for the compression of video sequences or in applications such as object tracking in robotics. However, estimating motion from image sequences is a classical inverse problem in the sense of Hadamard. As such, it is closely related to the formulation of an adequate model. This modeling has largely been ignored in computer sciences, where the focus is usually a different one due to the applications under consideration. For the quantitative analysis of fluid dynamic problems, constructing a model that closely approximates the phenomena of interest can be as important as actually solving the parameters of that model. Based on the specific model, it is then important to construct a suitable parameter estimator framework to reduce biases in the computed parameters.

1.2 Contribution

The main focus of this thesis is put on modeling and measuring transport phenomena in fluids. Image driven techniques were developed and used, relying on the development and adaptation of digital image processing techniques for describing and estimating the processes involved. The contribution of this work is threefold:

1. Modeling of intensity changes due to fluid flow and motion processes
2. Estimation of motion
3. Application to transport processes in environmental and life sciences

Regarding point 1, the emphasis is put on local models. The locality of models is defined by the spatio-temporal extend of their support. The rational is that local phenomena can usually be described by much simpler models than global phenomena. This leads to higher accuracy of the models without the danger of imposing wrong assumptions on the data and subsequent estimation steps. Models for physically motivated brightness changes in the data were conceived, such as those given rise by heat fluxes and diffusion processes in geophysical heat transport processes visualized with thermal imagers. Also, velocity profiles and effects due to integrating across them by the visualization process were adequately modeled.

The novel models were embedded into a local gradient based motion estimator. This estimator is based on an extension to the well known structure tensor approach. The structure tensor can be seen as a special formulation of the general problem of parameter estimation.

In this framework, accuracy of the estimator was amended and the computational efficiency improved to real time performance. An implementation on standard graphics hardware was conducted, further improving estimation speed and applicability. By implementing the algorithms on inexpensive graphics hardware, a speedup of 5% was achieved, making real time estimation possible. This resulted in a tool for the estimation and visualization of optical flow. It has been applied to industrial and medical applications. The presented estimators are optimal with respect to the underlying noise model of the imaged data. Novel confidence measures were developed and tested against well known ones for detecting problematic areas in the data set and discarding wrong estimated. Drawbacks of local approaches, such as susceptibility to the aperture problem and generally no dense flow fields were circumvented by incorporating the local estimator into a global framework. Here, parameter fields were regularized, leading to dense fields and stabilized estimates. All available information about local gray value structures was incorporated into the variational approach. This gives fine control of the diffusion of information from different areas of the image sequences. Also, a global framework was developed for jointly estimating motion, detecting edges and denoiseing the input data.

The motion models and algorithmic improvements to motion estimation were in part motivated by applications, the third major area of contribution of this thesis. These applications range from small scales such as microfluidic flows to flows at the free water surface to xylem flows of complex botanical systems such as plant leaves. Only through the use of the novel techniques developed within this thesis, accurate imaging measurements were feasible, in a number of applications for the first time. Especially in the field of air-sea interactions, the main topic amongst applications presented here, major advances were achieved.

In microfluidics, the technique of molecular tagging velocimetry (MTV) was addressed. As of yet, Taylor dispersion and the resulting apparent diffusion of tracer concentration caused inaccuracies in the proposed measuring techniques. In this thesis, this transport process and apparent intensity changes in the visualization technique were explicitly modeled. This has lead to the applicability of novel techniques for motion estimation to the field of MTV for the first time. This has lead to an improvement in accuracy, evading adverse effects found in prior techniques. Also, due to this model the velocity estimates stem from a well defined layer in between the channel boundaries, making a full 3D reconstruction of the velocity profile feasible. Verifications of this technique were conducted on simulated data as well as in a micromixer with well defined flow properties. For the micromixer, ground truth of the flow velocities was given. The accuracy of this novel approach was verified by comparing results to this ground truth. The scatter in the estimated velocities in comparison to the ground truth was found to be less than 4%. The new technique was also tested on a different flow geometry, thus representing a valuable tool for accurate measurements of microfluidic flows with MTV.

In the complex system of a plant leaf, it is still an unresolved question how xylem sap is transported in detail and which external factors influence it. With the advent of magnetic resonance imaging (MRI) for measurements on plants, unprecedented measurements of xylem flow in the stalk of plants have been conducted. However, this technique is not well equipped for measuring on extended areas such as plant leaves inside climatic chambers. Therefore, a

novel technique was developed that made it possible to estimate fluid flow inside the xylem, similarly to the technique of MTV used in microfluidics. Here, water parcels are not marked with caged dyes but by applying heat with a CO_2 laser. The transport of heat inside the xylem is visualized with an infrared camera, similar to the measurements conducted at the air-sea interface. The transport processes inside the xylem are modeled and the parameters of this model are estimated from the infrared image sequences in the motion estimation framework developed in this thesis. This has lead to a novel technique for measuring xylem flows accurately without strongly limiting constraints. Test measurements were conducted on technical capillaries as well as on perfused central veins of *Ricinus communis* leaves. Ground truth was attained from these test measurements and compared to the estimation of the novel thermographic technique. Based on a good agreement of test measurements to ground truth, measurements were also conducted to free standing plants in a climatic chamber. Environmental conditions were varied globally and locally and the effects on the flow velocities measured. The novel thermographic technique presents an excellent tool for conducting research in the transport processes in plant leaves. With the technique presented in this thesis, xylem flows in plant leaves of free standing plants could be measured for the first time. A host of new measurements under varying environmental forcing are conceivable. This will undoubtedly shed some light on open questions of plant physiology in the nearest future.

In the field of air-sea interactions, a number of important advances were also made in this thesis. Besides employing a well known transport model for measuring important parameter of heat transfer from infrared thermography, a new one was developed and compared to the former. This is particularly interesting since both models are based on complementary assumptions in terms of spatial homogeneity or temporal stationarity of the transport processes. Parameters measured from these models include the temperature difference ΔT across the thermal boundary layer at the air-water interface as well as the net heat flux. The output of the techniques developed for the two models were verified in laboratory measurements. Subsequently they were employed on an international sea going experiment in the equatorial pacific and compared on actual field data. Results of these measurements were surprisingly close, with almost identical estimates for ΔT and a difference of only 6% for the net heat flux. Also, the transfer velocity of heat was estimated from these two models, both in the laboratory and in the field. This transfer velocity of heat can be scaled to the one for mass. This lead to estimates of transfer velocities of gases such as CO_2, which were then compared to current parameterizations. From these techniques it was possible for the first time to measure the transport of energy directly at the sea surface, both temporally and spatially resolved. Using a CO_2 laser, a novel technique was developed that allows to measure accurate surface flows as well as the viscous shear stress directly at the interface. This is a direct measure for the flux of momentum impulse due to viscous shear. Measurements were conducted in a laboratory setting. This is the first time that this quantity can be measured reliably in the laboratory and possibly in the field directly on the ocean. With these techniques it is for the first time possible to measure the transport of energy and momentum directly at the sea surface in the same footprint and with the same sensors. This effectively eliminates cross calibration issues and overlap of footprints. Additionally, the transport of mass can be deduced from the scaling

relation of transfer velocity. It should be noted that this scaling represents an indirect measure that is still subject of current research. These novel techniques have only been possible through achievements in model formulation as well as to parameter estimation from image sequences. These measurements are not limited to laboratory measurements, but are well suited for field work. Due to the high resolution of parameters, the ultimate goal of a better understanding of transport processes and formulating a physically based parameterization has been drawn significantly closer. This research is fueled by the author's active membership in the international Working Group on Surface Fluxes (WGSF), a subsidiary of the World Climate Research Program (WCRP). Also, a first step in deriving a physically based parameterization was taken in bringing together modelers and experimenters, as well as the leading experts on parameterizations in an international workshop on transport at the air-sea interface. Selected publications of this workshop will appear in a monograph [Garbe et al., 2007b].

On first sight, it might appear as if the three applications, environmental physics, microfluidics and botany are disjunct. However, in all three applications basically the same transport processes are of interest. Also, from the measurement aspect, in all three cases fluid parcels are marked with a continuous tracer. This can either be an uncaging dye in microfluidics or heat applied with a CO_2 laser that is visualized with an IR camera in botany and environmental physics. The visualized intensity changes of these markers are modeled explicitly by the physical transport processes. This makes it possible to accurately estimate flow velocities in botany and microfluidics, and additionally measure the momentum flux at the atmosphere-ocean interface. The algorithms used for estimating model parameters from image processing are effectively the same. This makes it possible to apply an extensive framework to all of these applications, drawing upon synergetic effects between them.

One such effect should not be concealed: during the author's PhD thesis, first measurements in air-sea interactions were conducted and motion estimated from thermographic image sequences. Knowledge gained in this field was then applied to MTV in microfluidics. Here models were developed for Taylor dispersion due to the parabolic flow profile between two plates. Knowledge gained in this field was then taken back to oceanographic research, where the techniques could be adapted to the flow profiles found in the viscous boundary layer. Ultimately, this has lead to the development of a technique for estimating viscous shear stress at the sea surface!

This thesis is written in a self-consistent way. Due to its interdisciplinary nature, it is written to be understandable for people coming from different backgrounds. It was therefore necessary to explain some elementary topics in more detail.

1.3 Thesis Outline

This thesis is structured into two main parts. The first part focuses on the concept of motion models and the estimation of model parameter, encompassing Chapters 2 to 6. Applications of this novel modeling and estimation framework will be the topic of the second part, ranging from Chapter 7 to 9.

Chapter 2 recapitulates some commonly made models and assumptions in general, which are used in the estimation of optical flow. These models are then extended to link physically motivated brightness changes to motion. These models will include brightness changes due to projections trough velocity profiles of fluid flow. Here Couette flow and Poiseuille flow are examples of such fluid flows.

Techniques for estimating the parameters of the previously introduced motion models will be presented in Chapter 3. Here the standard approach of estimating motion with the structure tensor will be embedded into a parameter estimation framework which allows to adapt the estimator to the noise model depending on the motion model used. A technique will also be introduced for regularizing these model parameters, yielding dense and highly accurate parameter fields.

In Chapter 4 very efficient implementations of two estimators of motion are presented. With this approach is it possible to estimate motion as well as linear brightness changes or range flow in real time. The efficiency of the algorithm is further improved by implementing it on standard graphics hardware. Industrial as well as medical applications are presented. At the same time, it is possible to perform a real time estimation of net heat fluxes at the air-sea interface, as will be presented in Chapter 7.

The computation of confidence measures is closely related to the estimation of model parameters from image sequences. Based on this measure, estimates can be discarded from subsequent analysis. Also, in the regularization steps, the smoothing can be steered by this confidence, thus increasing the overall accuracy of the estimation. In Chapter 5 a comparison of a number of confidence and situation measures known from literature will be presented. Also, a number of improvements to these measures will be presented as well as new measures. The measures will be scrutinized on ground truth synthetic and real world sequences.

In Chapter 6 a phase field method for joint denoising, edge detection and motion estimation will be presented. This novel technique makes it possible to compute piecewise smooth motion field, while at the same time segmenting objects and denoising the image data. This type of approach has a number of applications in computer vision as well as in scientific applications. For example, thermal image sequences are commonly corrupted by reflections. These reflections can be segmented by this approach and the motion field is regularized without incorporating artifacts due to the reflections. At the same time missing information due to the reflections can be inpainted and the images denoised.

The second part of this thesis commences with applications of the developed models and estimators to fluid dynamical problems. Chapter 7 presents themographic applications for measuring parameters of energy and momentum transfer between atmosphere and ocean. Two different models describing the exchange between water and air will be developed and parameters estimated from them will be compared. These parameters are the temperature difference across the thermal water sided boundary layer, the net heat flux and the transfer velocity of heat. Measurements of these parameters are conducted in the laboratory as well as in the field. From active thermography, a technique is presented for estimating the wind induced shear stress at the sea surface. This technique is verified in laboratory experiments. To sum up, in this chapter techniques are presented that allow measuring all parameters of

heat transfer as well as the momentum flux in the same footprint with the same sensor.

Chapter 8 deals with a microfluidic application. A technique is developed for measuring fluid flows in microfluidic mixers using molecular tagging velocimetry (MTV). Here, Taylor dispersion is explicitly modeled in the motion model. Problems and inaccuracies of previous approaches could therefore be avoided. The novel technique is also tested on ground truth measurements.

Measurements of fluid flows in the xylem of plant leaves are presented in Chapter 9. Here a technique based on active thermography is developed that allows to visualize and estimate xylem sap flows in vivo. Test measurements were conducted on technical capillaries and on perfused *Ricinus communis* leaves. Also, measurements were conducted on cut leaves of *Zea mays*. It was clearly visible that the flow velocity increases next to the cut. On free standing *Ricinus communis* leaves, flow measurements were also conducted inside a climatic chamber. This allowed to globally vary environmental conditions. The sensitivity of the technique was also tested by clamping only part of the leaf inside a cuevette and varying the parameters inside a very localized area.

Chapter 10 concludes this thesis with a summary and a possible outlook of future research.

1.4 Collaborations

Measuring and modeling of fluid dynamic flows is a long standing problem in environmental, biological and technical flows. In this thesis, some of these problems could be solved through combining modeling, novel image processing techniques as well as advanced measurements.

The goals set in this thesis were only achievable through interdisciplinary research. Novel algorithms in image processing were developed and tested through the author's involvement in the Priority Program "Mathematical methods for time series analysis and digital image processing (DFG-SPP1114)" by the German Science Foundation (DFG) through two funded projects (GA 1271/1-1 and GA 1271/2-3). Through close collaboration with Prof. Til Aach (Institute of Imaging & Computer Vision, RWTH-Aachen, Germany), PD Dr. Erhardt Barth (Institute for Neuro- and Bioinformatics, University of Lübeck, Germany), Dr. Ingo Stuke (Institute for Signal Processing, University of Lübeck, Germany), and Dr. Cicero Mota (Instituto de Ciências Exatas, Universidade do Amazonas, Manaus, Brazil) the accuracy of motion models were tested and the algorithms applied to scientific data analysis.

Filters were optimized for a number of applications and the accuracy of the subsequent analyses improved. This was achieved in a collaboration with Prof. Rudolf Mester and Kai Kraijsek (Visual Sensorics & Information Processing, Univeristy of Frankfurt, Germany) and Dr. Hanno Scharr (Institute of Chemistry and Dynamics of the Geosphere ICG-III: Phytosphere, Research Center Jülich, Germany).

Together with Prof. Martin Rumpf (Institute for Numerical Simulation, University of Bonn, Germany), Dr. Tobias Preusser (CeVis, Universität Bremen, Germany), Prof. Alexandru C. Telea, (Department of Mathematics and Computing Science, Eindhoven University of Technology, The Netherlands) and Dr. Marc Droske (Mathematical Sciences Department,

University of California Los Angeles, USA) a new variational approach to joint denoising of image data, motion estimation and edge detection was developed and tested. Advances have been made to detect and correct corrupted image data, such as those caused by reflections.

Together with Dr. Robert Strzodka (Computer Science, Stanford University, USA) fast Algorithms for the estimation of motion in the presence of intensity change have been developed and implemented on standard graphics hardware. The same algorithms were also applied to range data, an expanding field in the presence of novel detector technologies.

Only one part of this thesis is concerned with image processing and algorithmic development. The main goal of this thesis is the measurement and modeling of fluid dynamic processes. As it turns out, modern image driven technique make it feasible to interconnect measurement and modeling, thus making the actual model an integrated part of the measurement. Only through this connection of the model, an accurate estimation of important transport parameters is feasible. Moreover, the accuracy of measurements is significantly increased.

The novel image processing techniques were applied to measurements of the air-sea interface conducted with thermographic techniques under the NOAA grant "Parameterization of CO_2 Transfer Velocity using Surface Roughness" in a close collaboration with Dr. Nelson Frew (Marine Chemistry & Geochemistry, Woods Hole Oceanographic Institution, USA), Prof. Tetsu Hara (Graduate School of Oceanography, University of Rhode Island, USA) and Dr. Uwe Schimpf (Institute of Environmental Physics, University of Heidelberg, Germany). These measurements were conducted during the international "Equatorial Pacific Air-Sea CO2 Exchange Experiment" in the field. As guest investigator at the Woods Hole Oceanographic Institution, the author could further strengthen the close collaboration. Similar measurements were also conducted in the Heidelberg Aeolotron and in the University of Miami ASIST facility. Thermographic measurements in Miami were carried out by Prof. Peter Minnett (RSMAS/MPO, University of Miami, USA), Dr. Geoffrez Smith (Naval Research Labs, Washington, USA) and Prof. Brian Ward (Center for Coastal Physical Oceanography, Old Dominion University, USA), and the data analysis was conducted in close communication with them.

Through the author's membership in the international Working Group on Surface Fluxes (WGSF) of the World Climate Research Program (WCRP), a close collaboration on all aspects of surface fluxes between the ocean and the atmosphere exists to WGSF chair Dr. Christopher W. Fairall (NOAA, USA), as well as to the following WGSF members Dr. Edgar L. Andreas (USACE, USA), Dr. Bernard Barnier (Institut de Mécanique de Grenoble, France), Dr. Abderrahim Bentamy (IFREMER, France), Dr. Pascale Braconnot (Laboratoire des Sciences du Climat et de l'Environnement, France), Dr. E. Frank Bradley (CSIRO, Australia), Prof. William M. Drennan (University of Miami, USA), Dr. Peter J. Gleckler (Lawrence Livermore National Laboratory, USA), Dr. Sergey K. Gulev (Shirshov Institute of Oceanology, Russia), Dr. Elizabeth C. Kent (Southampton Oceanography Centre, UK), Prof. Gerrit de Leeuw (TNO Physics and Electronics Laboratory, The Netherlands), Prof. Wade R. McGillis (Columbia University, USA), PD Dr. Rolf Philipona (World Radiation Center, Switzerland), Dr. Shawn R. Smith (Florida State University, USA), Dr. Andreas Sterl (Royal Netherlands Meteorological Institute, The Netherlands), Dr. Peter Taylor (Southampton Oceanography

Centre, United Kingdom) and Dr. Robert A. Weller (Woods Hole Oceanographic Institution, USA).

Recently, a collaboration has started with Prof. Detlef Stammer and Dr. Martin Gade (Institute of Oceanography, University of Hamburg, Germany), Dr. Gerhard Peters (Meteorological Institute, University Hamburg, Germany) and Dr. Bernd Schneider (Baltic Sea Research Institute, Rostock-Warnemünde, Germany). Within the SOPRAN project (Surface Ocean Processes in the Anthropocene), joint measurements will be conducted in the Baltic sea in which the novel techniques to measure the transport of energy, momentum and mass will be employed. At the same time gas fluxes will be measured from eddy correlation and waves slopes from radar backscatter. An aim will be taken at a physically based parametrization, that will also allow to estimate transfer velocities from satellite products, thus improving currently available global maps of air-sea gas exchange.

In a collaboration with Prof. Gerhard H. Jirka and Dr. Herlina (Institute for Hydromechanics University of Karlsruhe, Germany), as well as Johannes Gérson Janzen (São Carlos School of Engineering – University of São Paulo, Brazil) active thermographic techniques were applied to research in grid stirred turbulence.

The water relations in plant leaves and the fluid flow of the xylem were measured in the context of a project with the Research Center Jülich. Beyond the scope of this project, refined measurements were conducted in collaboration with Prof. Ulrich Schurr (Institute of Chemistry and Dynamics of the Geosphere ICG-III: Phytosphere, Research Center Jülich, Germany) and Dr. Roland Pieruschka (Carnegie Institution of Washington, Stanford University, USA).

Within the Priority Program on "'Image Measurements in Fluid Mechanics (DFG-SPP1147)"' (JA 395/11-2) novel techniques were developed and tested in microfluidic flow together with Dr. Volker Beushausen and Karsten Roethmann (Laser-Laboratory Göttingen e.V., Germany). Currently, in a collaboration with Dr. Volker Beushausen and Dr. Jochen Scholz (Laser-Laboratory Göttingen e.V., Germany) an extension of the presented techniques to fuel air ratio light induced fluorescence (FAR-LIF) measurements and Ramanography, where only two images are available, is underway. Here a low signal to noise ratio and little temporal information poses new challenges.

Part I

Estimation of Motion

Chapter 2

Models of Motion

2.1 Introduction

The topic of this thesis is to measure and model fluid dynamic processes. These processes are visualized with various imaging techniques, depending on the application. The imaging techniques exhibit high spatial and temporal resolution. Also, they make non-invasive measurements possible, where standard invasive techniques fail. However, these techniques visualize the effect of moving structures in terms of gray value changes in the imager. They present no direct means of measuring fluid dynamic processes. Hence, the task of measuring fluid dynamic processes from image driven techniques represents a classical inverse problem. In contrast to forward problems, in which model parameters are known in advance and a prediction is sought, in inverse problems we try to infer these model parameters from data. The dependence of forward and inverse problems can be broken down to

forward problem:	model parameters	$\rightarrow$	model	$\rightarrow$	prediction of data
inverse problem:	data	$\rightarrow$	model	$\rightarrow$	estimate model parameters

Central to both problems is of course the model. Starting from the model, both forward and inverse problem differ only in the a priory knowledge of model parameters or their estimation from observations. Here, a model can be thought of as a simplified description of observable processes. The models being used in inverse theory should be as simplistic as possible, while still describing the processes with the required accuracy. This is an application of the *lex parsimoniae* stated by Ockham as *"entia non sunt multiplicanda praeter necessitatem"*. Ockham's razor expresses the fact that as few assumptions as possible should be made in order to explain a given phenomenon.

This chapter will present and develop a number of models that will build the basis for solving the inverse problem. Common to all these models is their connection in between motion on the one hand and intensity changes on the other. There is a vast range of different model that can be formulated in the same framework presented in this work. Here, only a short overview will be given of the models used in applications presented in this thesis. Noteworthy

extensions would be multiple motions [Mota et al., 2001; Mühlich and Aach, 2006], such as additive or multiplicative transparent motion. It can be shown that this type of motion problem can be formulated in the same framework. Solutions to all the motion models presented in this chapter will be introduced in Chapter 3.

This chapter is organized as follows: Section 2.2 will present the most basic model of motion and its relation to brightness changes in image sequences. As will be seen, this model assumes constant translation of objects. The complexity of this model can be increased by allowing parametric motion models, presented in Section 2.3. Here the relative motion is formulated by affine transformation in Section 2.3.1 or planar patches in Section 2.3.2. These models can be generalized by formulating them as Lie groups which is done in Section 2.3.3. Section 2.4 will demonstrate how models can be formulated in the presence of multiple spectral channels or color images. Very often in natural scenes or scientific applications, the brightness of object along their trajectories does not remain constant. These types of brightness changes will be addressed in Section 2.5 and formulated in a very general framework in Section 2.5.1. Special expressions will be presented in Sections 2.5.2, 2.5.3 and 2.5.4, where linear brightness changes will be looked at, exponential brightness changes and brightness change due to diffusion, respectively. Section 2.6 will look at range flow and show how 3D velocity data can be formulated in a motion equation for this type of applications. In some scientific applications, integrating a marker over velocity profiles will lead to intensity changes due to the flow. This will be shown in Section 2.7, where results will be presented of such an integration over plane Couette flow in Section 2.7.1 as well as Taylor dispersion in plane Poiseuille flow in Section 2.7.2. These expressions to n-th order profiles will be generalized in Section 2.7.3. This chapter will be concluded with Section 2.8 where a brief summary of motion models will be given.

2.2 Constancy of Gray Values

A very common assumption in optical flow computations is the brightness change constraint equation (BCCE) [Horn and Schunk, 1981]. It is assumed that the image brightness of a scene point remains constant in a spatio-temporal neighborhood. That is the image intensity I at the location (x, y) at time t stays the same in a time interval ∂t during which a translation by $(\partial x, \partial y)$ took place. This brightness constancy model can be formulated as

$$I\left(x + \partial x, y + \partial y, t + \partial t\right) = I\left(x, y, t\right). \tag{2.1}$$

Developing this equation up to first order in a Taylor series expansion leads to

$$I\left(x + \partial x, y + \partial y, t + \partial t\right) = I(x, y, t) + \frac{\partial I}{\partial x}\frac{\mathrm{d}x}{\mathrm{d}t}\partial t + \frac{\partial I}{\partial y}\frac{\mathrm{d}y}{\mathrm{d}t}\partial t + \frac{\partial I}{\partial t}\partial t + \mathcal{O}(\boldsymbol{u}^2). \tag{2.2}$$

The well known brightness change constraint Equation (BCCE) [Fennema and Thompson, 1979; Horn and Schunk, 1981] is then derived by simplifying Equation (2.2) and differentiating with respect to time, leading to

$$\frac{dI}{dt} = \frac{\partial I}{\partial t} + \frac{\partial I}{\partial x}\frac{\mathrm{d}x}{\mathrm{d}t} + \frac{\partial I}{\partial y}\frac{\mathrm{d}y}{\mathrm{d}t} = I_t + (\boldsymbol{u}\boldsymbol{\nabla})I = 0. \tag{2.3}$$

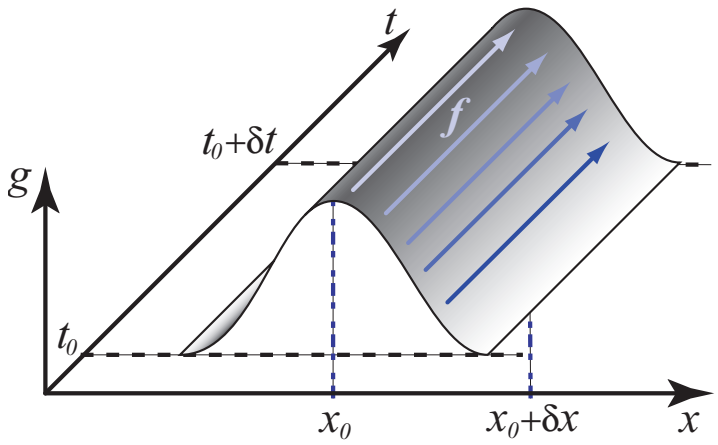

Figure 2.1: *Illustration of the brightness change constraint equation. A one dimensional gray value distribution is moved along the x-axis. During the translation from point x_0 to $x_0 + \delta x$ the gray value distribution stays the same over the period δt. This can be formulated as $dI/dt = 0$.*

With the optical flow $\boldsymbol{u} = [dx/dt, dy/dt]^\top = [u_1, u_2]^\top$, the spatial gradient $\boldsymbol{\nabla} I$ and the partial time derivative $I_t = \partial I/\partial t$. This formulation of the BCCE states that the image brightness $I(\boldsymbol{x}, t)$ at the location $\boldsymbol{x} = [x_1, x_2]^\top$ should change only due to motion, that is, the total derivative of its brightness has to vanish, which is illustrated in Figure 2.1. Schunk [1986] and Verri and Poggio [1989] proved that this assumption holds provided that no illumination changes are present and the surface of the object are Lambertian in nature. In the following it is always assumed that the optical flow is to be computed for two dimensional data. In the case of volumetric or even higher dimensional data, the BCCE of Equation (2.3) and subsequent results can readily be extended by introducing additional terms similar to the two dimensional ones.

Higher order differentials of the gray values can also be formulated to similar constancy equation. For example, the constancy of the gradient as introduced by Uras et al. [1988] can have invariant properties with respect to additive brightness changes along properties. Papenberg et al. [2006] summarized several such constancy constraint equations. They will not be considered in the context of this work. This is due to the fact that in the scientific applications under consideration, the brightness and changes thereof are of physical significance. This information is lost by formulating constancy equations on derivatives of gray values. Also, if intensity changes are not additive, but underly different physical processes such as diffusion, then the gradients change due to this process, making the gradient constancy equation inapplicable. Ways of formulating constraint equations that take such effects into account will be presented in Section 2.5.

2.3 Parametric Motion Models

The formulation of the BCCE in the previous section is generally only satisfied for orthographic projection and pure translational motion parallel to the scene [Beauchemin and Barron, 1995].

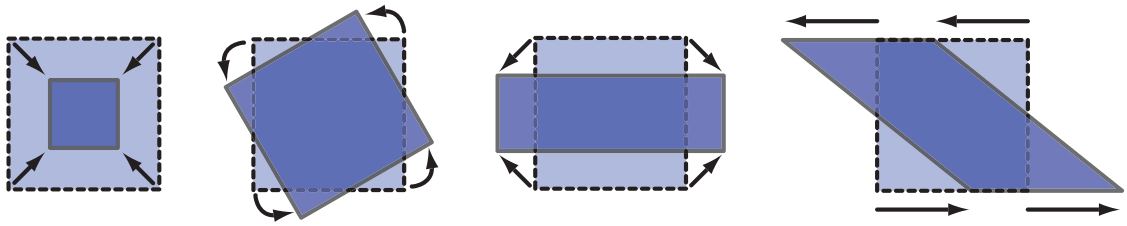

Figure 2.2: *Parameterization of affine flow model. The elementary geometric transformations of divergence, rotation, stretching and shear.*

However, these hypotheses are not met by a number of applications which motivated the investigation of constraints applicable to a wider range of conditions. In this section the BCCE will be extended to cope with an arbitrary motion on the image plane. The prerequisite of constancy of brightness along trajectories still holds. This will be dropped in Section 2.5.

2.3.1 Affine Transformations

It is common in computer vision to model the velocity field $\boldsymbol{u}$ in a local neighborhood by an affine flow model [Black and Anandan, 1996; Farnebäck, 2000; Fleet, 1992]:

$$\boldsymbol{u} = \boldsymbol{t} + \boldsymbol{A}\boldsymbol{x} = \begin{bmatrix} t_1 \\ t_2 \end{bmatrix} + \begin{bmatrix} a_1 & a_2 \\ a_3 & a_4 \end{bmatrix} \begin{bmatrix} x \\ y \end{bmatrix} = \begin{bmatrix} a_1 & a_2 & t_1 \\ a_3 & a_4 & t_2 \end{bmatrix} \begin{bmatrix} x \\ y \\ 1 \end{bmatrix} = \tilde{\boldsymbol{A}} \cdot \tilde{\boldsymbol{x}}, \tag{2.4}$$

where $\boldsymbol{t} = [t_1, t_2]^\top$ represent the constant translation of the center of the neighborhood and $\boldsymbol{x} = [x, y]^\top$ represents the relative position of pixels in the neighborhood to its center. A sketch of the possible transformation described by this model is shown in Figure 2.2.

The parameters of the affine transformation matrix $\boldsymbol{A}$ can be used directly to estimate convergence and divergence of the flow field. This model is a superposition of uniform motion, rotation, dilation and shear. This can be seen by noting that

$$\begin{aligned} div(v) &= \partial_x v_x + \partial_y v_y = \operatorname{trace} \boldsymbol{A} = a_1 + a_4, & shA &= \partial_x v_x - \partial_y v_y = a_1 - a_4 \\ rot(v) &= \partial_x v_y - \partial_y v_x = a_2 - a_3, & shB &= \partial_x v_y + \partial_y v_x = a_2 + a_3 \end{aligned}$$

We can thus superimpose the matrix of affine transformations by

$$\boldsymbol{A} = \frac{1}{2}\left[div(\boldsymbol{v})\boldsymbol{E}_0 + \boldsymbol{Shr}(\boldsymbol{v}) + rot(\boldsymbol{v})\boldsymbol{E}_3\right], \tag{2.5}$$

where $\boldsymbol{Shr}(\boldsymbol{v}) = shA(\boldsymbol{v})\boldsymbol{E}_1 + shB(\boldsymbol{v})\boldsymbol{E}_2$ and

$$\boldsymbol{E}_0 = \begin{bmatrix} 1 & 0 \\ 0 & 1 \end{bmatrix}, \qquad \boldsymbol{E}_1 = \begin{bmatrix} 1 & 0 \\ 0 & -1 \end{bmatrix}$$
$$\boldsymbol{E}_2 = \begin{bmatrix} 0 & 1 \\ 1 & 0 \end{bmatrix}, \qquad \boldsymbol{E}_3 = \begin{bmatrix} 0 & -1 \\ 1 & 0 \end{bmatrix}$$

Inserting the affine motion model into the standard BCCE of Equation (2.3) yields

$$\begin{aligned} 0 &= I_t + \left(\tilde{\boldsymbol{A}} \cdot \hat{\boldsymbol{x}}\right) \nabla I \\ &= \begin{bmatrix} I_x & I_y & xI_x & yI_x & xI_y & yI_y & I_t \end{bmatrix} \cdot \begin{bmatrix} t_1 & t_2 & a_1 & a_2 & a_3 & a_4 & 1 \end{bmatrix}^\top \\ &= \boldsymbol{d} \cdot \boldsymbol{p} = 0. \end{aligned} \tag{2.6}$$

Here subscripts denote spatial derivatives along the coordinates indicated.

2.3.2 Planar Model

Another model used is the one propagated by Waxman and Wohn [1985]. It has been used successfully by Black and Anandan [1996] and assumes that regions of piecewise-smooth image intensities correspond to planar surfaces in a scene. The planarity of local surfaces can be extended to include 2nd order curved surfaces. This kind of model is described by 8 parameters and can be formulated as

$$\begin{aligned} \boldsymbol{u} &= \boldsymbol{t} + \boldsymbol{A}\boldsymbol{x} + \boldsymbol{X}\boldsymbol{a} = \begin{bmatrix} t_1 \\ t_2 \end{bmatrix} + \begin{bmatrix} a_1 & a_2 \\ a_3 & a_4 \end{bmatrix} \begin{bmatrix} x \\ y \end{bmatrix} + \begin{bmatrix} x^2 & xy \\ xy & y^2 \end{bmatrix} \begin{bmatrix} a_5 \\ a_6 \end{bmatrix} \\ &= \begin{bmatrix} a_1 & a_2 & a_5 & 0 & a_6 & t_1 \\ a_3 & a_4 & 0 & a_6 & a_5 & t_2 \end{bmatrix} \cdot \begin{bmatrix} x & y & x^2 & y^2 & xy & 1 \end{bmatrix}^\top = \tilde{\boldsymbol{A}} \cdot \tilde{\boldsymbol{x}}. \end{aligned} \tag{2.7}$$

In both Equations (2.4) and (2.7) the parameter $\boldsymbol{t} = [t_1, t_2]^\top$ represent the neighborhood center velocity whereas the a_i are 1st or 2nd order velocity derivatives.

As shown previously in the case of the affine motion model, the standard BCCE of Equation (2.3) can be extended to include this planar model. This extension results in

$$\begin{aligned} 0 &= I_t + \left(\tilde{\boldsymbol{A}} \cdot \hat{\boldsymbol{x}}\right) \nabla I \\ &= \begin{bmatrix} I_x & I_y & xI_x & yI_x & xI_y & yI_y & x^2I_x + xyI_y & xyI_x + y^2I_y & I_t \end{bmatrix} \\ &\quad \cdot \begin{bmatrix} t_1 & t_2 & a_1 & a_2 & a_3 & a_4 & a_5 & a_6 & 1 \end{bmatrix}^\top \\ &= \boldsymbol{d} \cdot \boldsymbol{p} = 0. \end{aligned} \tag{2.8}$$

Commonly used parameterizations include those that try to model 3D affine motion of planar patches under projective geometry [Tsai and Huang, 1981] or polynomial models that approximate the optical flow field by a variable number of parameters [Karczewicz et al., 1997]. A compilation of different parameterizations can be found in Stiller and Konrad [1999].

2.3.3 Lie Groups

A more general parameterization of the flow field can be derived by replacing the flow vector $\boldsymbol{u}$ by a generalized transformation $\boldsymbol{S}(\boldsymbol{r}, \boldsymbol{a})$ [Garbe et al., 2003b; Haußecker and Spies, 1999]. In this notation $\boldsymbol{a} = [a_1, \ldots, a_p]^\top$ is the p-dimensional parameter vector and $\boldsymbol{S} = [S_1, \ldots, S_n]^\top$

an invertible transformation acting on an element $\boldsymbol{r} = [r_1, \ldots, r_n]^\top$ in the spatio-temporal space $\mathbb{R}^n$, that is

$$\boldsymbol{r} = \boldsymbol{S}(\boldsymbol{r}', \boldsymbol{a}) \quad \text{and} \quad \boldsymbol{r}' = \boldsymbol{S}^{-1}(\boldsymbol{r}, \boldsymbol{a}). \tag{2.9}$$

The generalized transformation $\boldsymbol{S}$ is taken to be infinitely differentiable in $\boldsymbol{r}$ and analytical in $\boldsymbol{a}$. From the above properties of $\boldsymbol{S}$ and $\boldsymbol{r} = \boldsymbol{S}(\boldsymbol{r}, 0)$ it follows that $\boldsymbol{S}$ forms a one-parameter Lie group of transformations [Olver, 1986]. Therefore, the vector $\boldsymbol{r}$ can be expanded in a Taylor series about $\boldsymbol{a} = 0$ as

$$\boldsymbol{r} = \boldsymbol{r}' + \sum_{i=1}^{p} a_i \frac{\partial S(\boldsymbol{r}', \boldsymbol{a})}{\partial a_i}. \tag{2.10}$$

Given a brightness function $I(\boldsymbol{r})$ its dependence on the transformation parameters a_i can be derived to be

$$\frac{\partial I(\boldsymbol{r})}{\partial a_i} = \sum_{j=0}^{n} \frac{\partial I}{\partial r_j} \frac{\partial r_j}{\partial a_i} = \sum_{j=0}^{n} \frac{\partial I}{\partial r_j} \frac{\partial S(\boldsymbol{r}', \boldsymbol{a})}{\partial a_i} = \mathfrak{L}_i I(\boldsymbol{r}), \tag{2.11}$$

where Equation (2.10) was used. The infinitesimal generator of the Lie group $\mathfrak{L}_i$, $i \in \{1, \ldots, P\}$ is defined as

$$\mathfrak{L}_i = \sum_{j=0}^{n} \frac{\partial S_j}{\partial a_i} \frac{\partial}{\partial r_j}. \tag{2.12}$$

Using Equation (2.11) in expanding the brightness function $I(\boldsymbol{r})$ about $\boldsymbol{r}'$ with respect to the parameters a_i yields

$$I(\boldsymbol{r}) = I(\boldsymbol{r}') + \sum_{i=1}^{p} a_i \frac{\partial I(\boldsymbol{r}')}{\partial a_i} = I(\boldsymbol{r}') + \sum_{i=1}^{p} a_i \mathfrak{L}_i I(\boldsymbol{r}') \ . \tag{2.13}$$

With the assumption of brightness conservation $I(\boldsymbol{r}) = I(\boldsymbol{r}')$ this equation reduces to the parametric brightness change constraint equation (PBCCE) given by

$$\sum_{i=1}^{p} a_i \mathfrak{L}_i I(\boldsymbol{r}') = (\mathfrak{L} I)^\top \boldsymbol{a} = 0, \quad \text{with} \quad (\mathfrak{L} I) \in \mathbb{R}^p, \boldsymbol{a} \in \mathbb{R}^p. \tag{2.14}$$

This equation is similar to the traditional BCCE where the spatio-temporal gradient is replaced by the p-dimensional vector of Lie derivatives $\mathfrak{L} g = [\mathfrak{L}_1 g, \ldots, \mathfrak{L}_p I]^\top$. It can easily be shown that the PBCCE reduces to the BCCE for the case of constant translation $\boldsymbol{S}(\boldsymbol{r}, \boldsymbol{a}) = \boldsymbol{r} + \boldsymbol{a}$ with the translation vector $\boldsymbol{a} = [\delta x, \delta y, \delta t]^\top$ and the resulting generators $\mathfrak{L}_1 = \partial/\partial x$, $\mathfrak{L}_1 = \partial/\partial y$ and $\mathfrak{L}_1 = \partial/\partial t$. Also the affine transformation of Equation (2.4) as a special case of this PBCCE can be verified straightforwardly by noting that $\boldsymbol{S}(\boldsymbol{r}, \boldsymbol{a}) = \boldsymbol{A}\boldsymbol{r} + \boldsymbol{t}$ with $\boldsymbol{a} = [a_1, \ldots, a_4, t_1, t_2, 1]^\top$. The infinitesimal generators can than be derived as $\mathfrak{L}_1 = x\partial/\partial x$, $\mathfrak{L}_2 = y\partial/\partial x$, $\mathfrak{L}_3 = x\partial/\partial y$, $\mathfrak{L}_4 = y\partial/\partial y$, $\mathfrak{L}_5 = \partial/\partial x$, $\mathfrak{L}_6 = \partial/\partial y$ and $\mathfrak{L}_7 = \partial/\partial t$. The presented parameterization by Lie groups has previously been successfully used for estimating the optical flow [Duc, 1994, 1997]. This formulation has some practical advantages as a number of transformations can be invariantly decomposed, such as the optical flow induced by perspective projection onto the image plan with added camera rotation [Kanatani, 1990].

2.4 Multi Channel

This approach of estimating motion according to Equation (2.3) is not limited to gray value image sequences. It can readily be extended to spectral image sequences, of which color sequences are a special case. For this type of problem not only the one constraint Equation (2.3) is given at the pixel position as is the case for gray value images. Moreover one such equation results from each spectral channel. For the case of n spectral channels the resulting system of n equations is given by

$$\begin{array}{ccccccccccccccc} u_1 \cdot \frac{\partial F_1}{\partial x} & + & u_2 \cdot \frac{\partial F_1}{\partial y} & + & \frac{\partial F_1}{\partial t} & = & [F_{1,x}, F_{1,y}, F_{1,t}] & \cdot & [u_1, u_2, 1]^\top & = & \boldsymbol{d}_1 & \cdot & \boldsymbol{p}^\top & = & 0 \\ u_1 \cdot \frac{\partial F_2}{\partial x} & + & u_2 \cdot \frac{\partial F_2}{\partial y} & + & \frac{\partial F_2}{\partial t} & = & [F_{2,x}, F_{2,y}, F_{2,t}] & \cdot & [u_1, u_2, 1]^\top & = & \boldsymbol{d}_2 & \cdot & \boldsymbol{p}^\top & = & 0 \\ \vdots & & \vdots & & \vdots & = & \vdots & & \vdots & = & \vdots & & \vdots & = & 0 \\ u_1 \cdot \frac{\partial F_n}{\partial x} & + & u_2 \cdot \frac{\partial F_n}{\partial y} & + & \frac{\partial F_n}{\partial t} & = & [F_{n,x}, F_{n,y}, F_{n,t}] & \cdot & [u_1, u_2, 1]^\top & = & \boldsymbol{d}_n & \cdot & \boldsymbol{p}^\top & = & 0 \end{array} . \tag{2.15}$$

The different spectral channels are denoted by $F_1 \dots F_n$. In color image sequences the channels $[F_1, F_2, F_3]$ are given in the RGB color space by the red, green and blue channel respectively [Ohta, 1989]. Depending on the application it might be beneficial to formulate the problem in a different color space, such as the HSV space, where $[F_1, F_2, F_3]$ correspond to hue, saturation and value [Golland and Bruckstein, 1997]. More general, the $F_1 \dots F_n$ can be the channels of multi spectral image sequences such as those present in remote sensing applications.

In this framework it is also possible to express the output of different operators on image sequences as the different channels $F_1 \dots F_n$. For example, the gradients in x and y direction of an image can be thought of as two such channels F_1 and F_2. According to Equation (2.15) this leads to second derivatives of image intensities. Constraint equations of this type have been proposed by Nagel [1983, 1987] and Tretiak and Pastor [1984]. The resulting equation of this form is given by [Uras et al., 1988]

$$(\boldsymbol{\nabla}\boldsymbol{\nabla} I(\boldsymbol{x}, t))\, \boldsymbol{u}^\top = -\boldsymbol{\nabla} I_t(\boldsymbol{x}, \boldsymbol{t}). \tag{2.16}$$

Formulating the motion model with channels that are representations of filter responses is only beneficial if the resulting channels are linearly independent.

2.5 Changes in Image Intensities

Currently, the BCCE from Equation (2.3) in terms of different parametric models has been extended. All of these motion equation have in common that the brightness of objects has to remain constant along their trajectory. This will lead to errors if brightness changes along motion trajectories occur. A sketch of such a process can be seen in Figure 2.3. Without taking brightness changes into consideration, the displacement vectors point in the wrong direction.

This section will introduce models that will allow changes in image intensities. Because brightness changes are always present in natural scenes, this will increase the accuracy of the

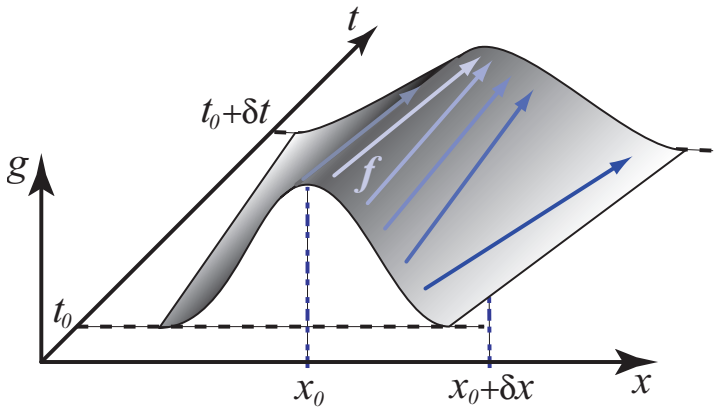

Figure 2.3: *Illustration of the brightness change constraint equation. A one dimensional gray value distribution is moved along the x-axis. During the translation from point x_0 to $x_0 + \delta x$ the gray value distribution is changed according to a diffusion process. The BCCE estimates the optical flow $\boldsymbol{u}$ incorrectly.*

motion models. Also, a number of scientific applications model physically motivated brightness changes. These brightness changes are often more important to the application than the actual motion field $\boldsymbol{u} = [u_1, u_2]^\top$. In Garbe [2001] details concerning these brightness changes can be found. Therefore, a short introduction and a focus more on applications will be given here.

2.5.1 The Extended Brightness Model

In the context of this work the imaged processes change the image brightness according to the underlying physical processes. Rather than just extending the BCCE in order to gain more accurate optical flow fields under changing illumination, the parameter of intensity change have a significant physical meaning. This is the case in heat flux measurements at the sea surface [Garbe et al., 2004] or in quantifying water transport and heat transfer in plant leaves [Garbe et al., 2002d]. A closer look will be taken at these applications in Sections 7.7 and 9 respectively.

In order to make the technique presented in the context of this work applicable to a wide range of scientific applications, a more general extension of the BCCE is chosen [Haußecker et al., 1999; Haußecker and Fleet, 2001; Garbe, 2001]. The brightness of a moving pattern is allowed to change according to an analytical function h, that is

$$I(\boldsymbol{x}) = h(I'(\boldsymbol{x}), \boldsymbol{b}), \quad \text{and} \quad I'(\boldsymbol{x}) = h^{-1}(I(\boldsymbol{x}), \boldsymbol{b}), \tag{2.17}$$

where $h(I(\boldsymbol{x}), \boldsymbol{b})$ is a scalar invertible transformation with the q-dimensional parameter vector $\boldsymbol{b} = (b_1, \ldots, b_q)^\top$ and the identity element $h(I(\boldsymbol{x}), 0) = I(\boldsymbol{x})$. In the case of h being analytical with respect to $\boldsymbol{b}$ the brightness variation can be expanded into a Taylor series around $\boldsymbol{b} = 0$, hence

$$I(\boldsymbol{r}) = I'(\boldsymbol{r}) + \sum_{k=1}^{q} b_k \frac{\partial h}{\partial b_k}. \tag{2.18}$$

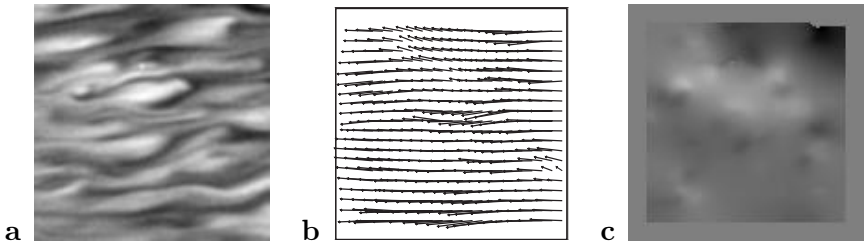

Figure 2.4: *Image from a sequence with the corresponding 2D optical flow and the total derivative of the temperature.*

A generalization of the BCCE, in the following referred to as GBCCE, can be derived by making use of this equation together with Equation (2.13)

$$\begin{aligned} I'(\boldsymbol{x}) - I'(\boldsymbol{x}') &= \sum_{i=1}^{p} a_i \mathfrak{L}_i I(\boldsymbol{x}') \\ \Leftrightarrow\ I(\boldsymbol{x}) - I'(\boldsymbol{x}') &= \sum_{i=1}^{p} a_i \mathfrak{L}_i I(\boldsymbol{r}') - \sum_{k=1}^{q} b_k \frac{\partial h}{\partial b_k} = 0. \end{aligned} \tag{2.19}$$

For the special case of constant brightness ($\boldsymbol{b} = 0$) this equation reduces to the PBCCE from Equation (2.14). In the derivation of Equation (2.19) $I(\boldsymbol{r}) = I'(\boldsymbol{r}')$ is used, which is due to the fact that the initial brightness I shifted from $\boldsymbol{r}$ to $\boldsymbol{r}'$ leads to the primed brightness I' at $\boldsymbol{r}'$.

Equation (2.19) can of course be written in vector notation, reducing to

$$\boldsymbol{d}^\top \boldsymbol{p} = 0, \quad \text{with} \quad \boldsymbol{d} \in \mathbb{R}^{p+q}, \boldsymbol{p} \in \mathbb{R}^{p+q}, \tag{2.20}$$

with the data term $\boldsymbol{d} = \left[(\mathfrak{L}I)^\top, (\boldsymbol{\nabla}_b h)^\top\right]^\top$ and the parameter vector $\boldsymbol{p} = [\boldsymbol{a}^\top, -\boldsymbol{b}^\top]^\top$, where $\boldsymbol{\nabla}_b$ represents the gradient with respect to the parameters $\boldsymbol{b}$.

With the formulation of the generalized brightness change constraint Equation (2.20) it is now possible to estimate reliable optical flow in applications where the BCCE failed due to its limitations. Moreover, in scientific applications the image intensity change might be due to physical phenomena, the parameters of which can be estimated very elegantly according to Equation (2.20).

2.5.2 Linear Brightness Change

The simplest model of brightness change is that of a locally linear change over time. This is achieved by requiring that

$$I\left(x + \partial x, y + \partial y, t + \partial t\right) = I\left(x, y, t\right) + c\left(x, y, t\right) \partial t. \tag{2.21}$$

This type of brightness change can widely be used since it presents a first approximation if no further knowledge about the intensity change can be found.

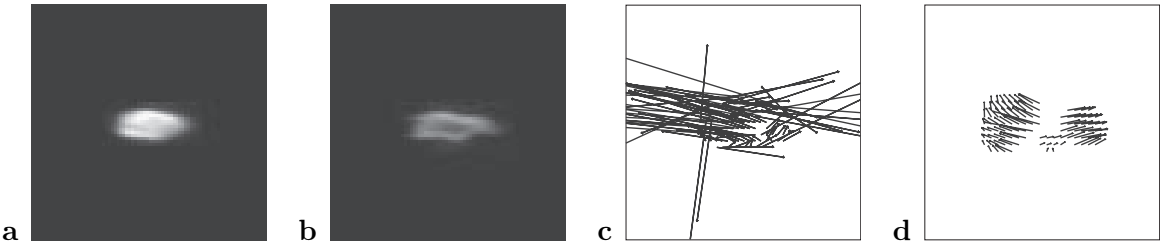

Figure 2.5: *Exponentially decaying heat spot at a wavy water surface. In* **a** *and* **b** *are the 1st and 9th image of a sequence. The optical flow field computed from the standard BCCE is shown in* **c**, *and that, estimated with an exponential decay model, is shown in* **d**.

For constant translation the coordinate transform $\boldsymbol{S}$ in Equation (2.9) is given as

$$\boldsymbol{S}(\boldsymbol{r}, \boldsymbol{a}) = \boldsymbol{r} + \boldsymbol{a}, \tag{2.22}$$

where the parameter of the transformation $\boldsymbol{a} = (\delta x, \delta y, \delta t)^\top$ denotes the translation vector to be estimated. Following Equation (2.12) the infinitesimal generators are given as

$$\mathfrak{L}_1 = \frac{\partial}{\partial x}, \quad \mathfrak{L}_2 = \frac{\partial}{\partial y} \quad \text{and} \quad \mathfrak{L}_3 = \frac{\partial}{\partial t} \tag{2.23}$$

and the brightness change function h as

$$h(I(\boldsymbol{r}), \boldsymbol{b}) = c \cdot \boldsymbol{b}. \tag{2.24}$$

Consequently $\partial h(I(\boldsymbol{r}), \boldsymbol{b}) / \partial \boldsymbol{b} = c$ and the GBCCE (2.20) can be formulated yielding

$$\boldsymbol{d}^\top \boldsymbol{p} = [-1, I_x, I_y, I_t] \cdot [c, u_1, u_2, 1]^\top = 0, \tag{2.25}$$

where the subscripts denote partial derivatives.

This equation of linear brightness change was first introduced by Negahdaripour and Yu [1993]. It allows accurate optical flow computations under nonuniform illumination [Nomura et al., 1995] or in scenes with a moving light source [Haußecker and Fleet, 2001]. When no further information is available regarding the physical processes of lightness change, linear changes present a good first order approximation.

For measuring transport processes at the air-sea interface, this type of motion equation was used for measuring the net heat flux at the air-sea interface [Garbe et al., 2003b, 2004]. This will be presented in Section 7.7.2. An example of such a motion estimation can be seen in Figure 2.4. It has also been successfully applied for optical flow computations in range data, that is on images where distances to the imaging system are coded as gray values [Spies, 2001; Barron and Spies, 2001; Garbe et al., 2002e]. This type of problem will be introduced in Section 2.6.

2.5.3 Exponential Decay

A more elaborate model of brightness change than the linear model is that of exponentially decreasing intensities. This type of model was first used by Haußecker et al. [1999] to measure

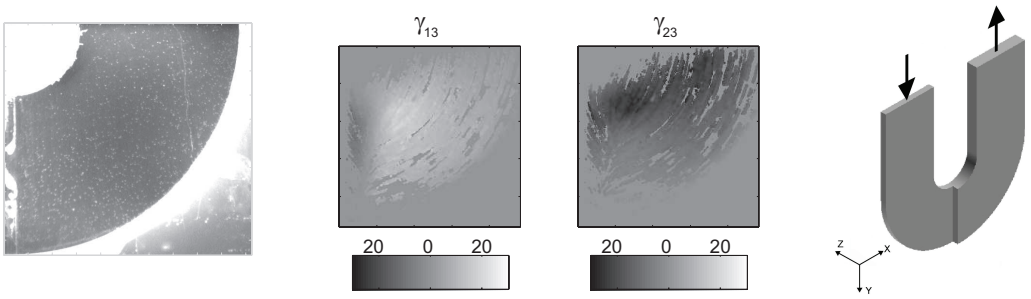

Figure 2.6: *Fluid flow in an U pipe. Depth is measured through exponential decay of Lambert-Beer's law. This allows to measure 3D velocity from Equation (2.27). Pictures taken from Jehle [2007].*

a decaying heat spot at the sea surface. This can be seen in Figure 2.5. Another important application of this type of model is the visualization of chemical reactions. On global scales, satellites can measure chemical species in our atmosphere, the motion of which has then to be estimated with an exponential decay model. On smaller scales, the exponential decay can be used when light is attenuated due to Lambert-Beer's law. One application will be presented in Section 7.8.2, where the motion of heated water parcels is measured from infrared thermography. Another application in the visible spectrum is presented by Jehle [2007]. Here, light of particles is attenuated by a special dye in the fluid. The attenuation follows again Lambert-Beer's law and can be directly correlated to the depths of particles inside the fluid. Results of this technique are shown in Figure 2.6.

The differential equation for an exponential decay of the brightness is given by $H(I_0, t, a) = I_0 \exp(-\kappa t)$. Together with Equation (2.19) this leads to the following motion model

$$f(I_0, t, \kappa) = \frac{\mathrm{d}I}{\mathrm{d}t} = -\kappa I_0 \exp(-\kappa t) = -\kappa I. \tag{2.26}$$

This equation can be expressed in vector notation, leading to

$$\boldsymbol{d}^\top \boldsymbol{p} = [\kappa, I_x, I_y, I_t] \cdot [I, u_1, u_2, 1]^\top = 0. \tag{2.27}$$

Partial deprivates are denoted by subscripts and κ is the constant of exponential decay.

2.5.4 Diffusion Processes

Diffusion is the process by which matter is transported from one part of a system to another due to random molecular motions driven by a concentration gradient. In the transport of heat by conduction, energy is also transported by random molecular motions, where the transfer comes about due to a temperature gradient. As can be deducted by intuition there exists a strong analogy between the two processes. This was first recognized by Fick [1855], who derived diffusion on a quantitative basis by adopting the mathematical framework of heat conduction derived earlier by Fourier [1822]. The theory of diffusion in *isotropic substances* is therefore based on the hypothesis that the rate of transfer of the diffusing substance through

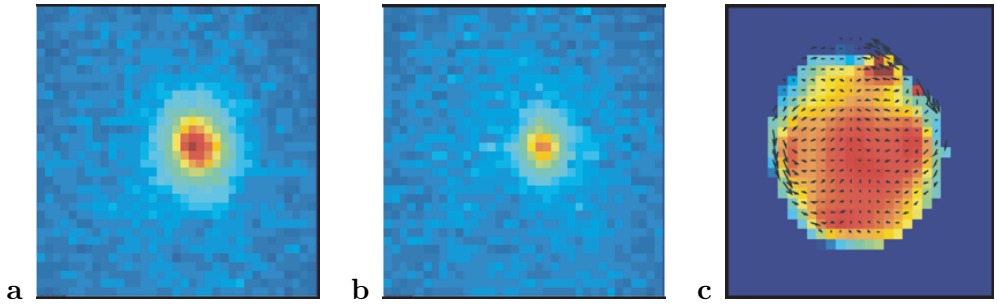

Figure 2.7: *Isotropic diffusion of heat in a polymer heated with a laser. In* **a** *and* **b** *two frames of the sequence are shown and in* **c** *the computed diffusivity and optical flow field. The images were recorded with an infrared camera.*

a unit area of a section, also referred to as the *flux of the substance* $\boldsymbol{j}$, is proportional to the concentration gradient measured normal to the section, that is

$$\boldsymbol{j} \;=\; -D\boldsymbol{\nabla}C. \tag{2.28}$$

In this equation, which is also known as *Fick's First Law*, the concentration gradient of the diffusing substance is denoted by $\boldsymbol{\nabla}C$ and the *diffusion coefficient* by D.

Fick's Second Law describes the non-steady state. The rate of change of a concentration in a given volume is given by the efflux through the volume's boundary. This results to

$$\frac{\partial C}{\partial t} = \boldsymbol{\nabla}\left(D\boldsymbol{\nabla}C\right) = D\Delta C, \tag{2.29}$$

where $\Delta I = (\partial^2 I/\partial x^2 + \partial^2 I/\partial y^2)$ is the Laplace operator. The last transform is valid only for a scalar, isotropic diffusivity D.

In digital image processing, the gray values correspond to the concentration C in Equation (2.29). The corresponding equation is then given by

$$\begin{bmatrix} -\Delta I & I_x & I_y & I_t \end{bmatrix} \cdot \begin{bmatrix} D & u_1 & u_2 & 1 \end{bmatrix} = \boldsymbol{D}\cdot\boldsymbol{p} = 0, \tag{2.30}$$

where D is the constant of diffusivity. An example of such a process is the conduction of heat in an isotropic material. Results of such an image sequence recorded with an infrared camera are presented in Figure 2.7.

The case of a direction dependent diffusion, the constant of diffusivity is in fact a tensor $\boldsymbol{D}$. Therefore, the last simplification in Equation (2.29) is not valid. This yields

$$I_x \cdot u_1 + I_y \cdot u_2 + I_t - \boldsymbol{\nabla}\left(\boldsymbol{D}\cdot\boldsymbol{\nabla}\right) I = 0, \tag{2.31}$$

with the anisotropic diffusion tensor $\boldsymbol{D}$. This tensor is given by

$$\boldsymbol{D} = \begin{bmatrix} d_{00} & d_{01} \\ d_{10} & d_{11} \end{bmatrix} = \begin{bmatrix} d_{00} & d_{10} \\ d_{10} & d_{11} \end{bmatrix}, \tag{2.32}$$

where use was made of the fact that the diffusion tensor $\boldsymbol{D}$ is a symmetric tensor, that is $d_{ij} = d_{ji}$. Inserting this expression in Equation (2.31) leads to the following vector equation

$$\begin{bmatrix} I_x & I_y & -I_x x & -I_y y & -2I_x y & I_t \end{bmatrix} \cdot \begin{bmatrix} u_1 & u_2 & d_{00} & d_{11} & d_{10} & 1 \end{bmatrix}^\top = 0. \tag{2.33}$$

2.6 Range Flow

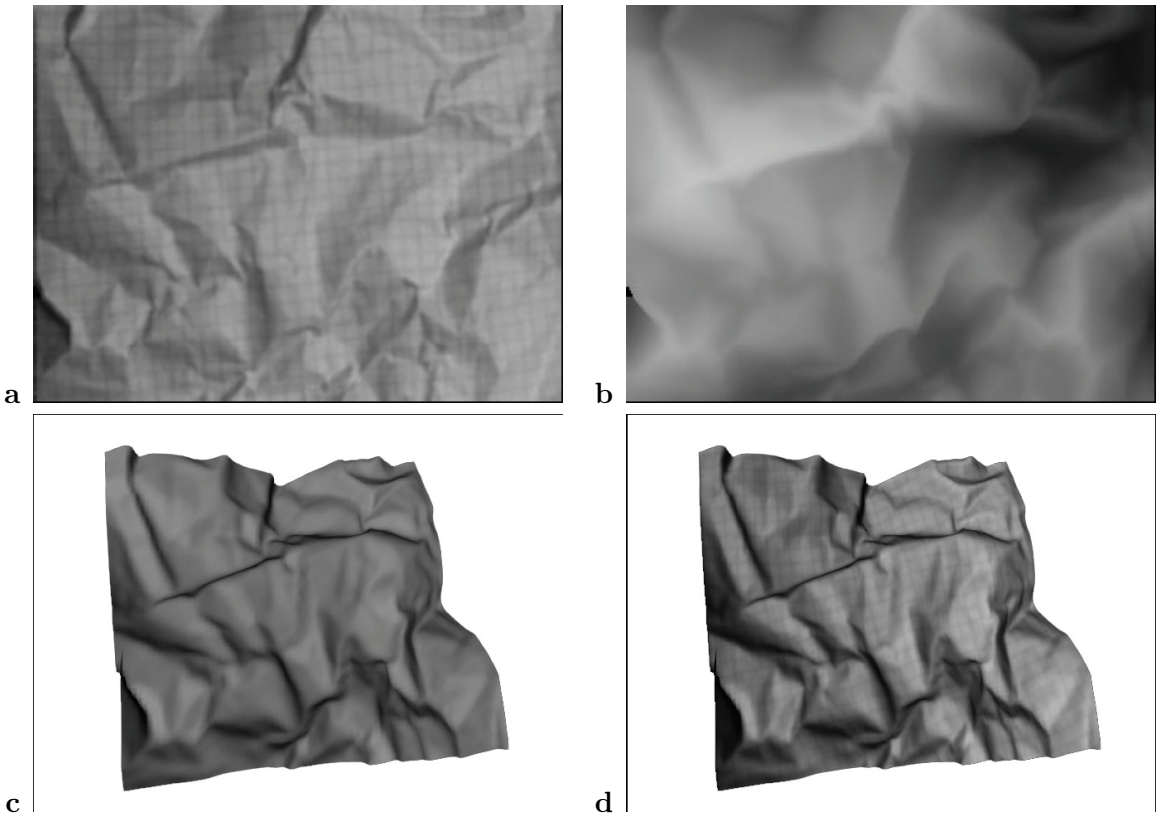

Figure 2.8: ***a*** *shows the intensity data of crumbled paper and* ***b*** *the corresponding range data. A rendered image of the range data is shown in* ***c****, while the same with the projected intensity data is shown in* ***d****.*

Range images provide the three-dimensional shape of the sensed object surfaces in the field of view. This geometric information has turned out to be very useful for a variety of vision tasks, such as segmentation, object recognition, industrial inspection, reverse engineering and collision detection. Range data are 2D+t image sequences, encoding the distance from the range sensor to the objects in gray values. Range sensors can be highly accurate scanning laser systems, but also novel instantaneous systems such as *photonic mixer device* (PMD) cameras are becoming increasingly popular [Schwarte et al., 1999].

The instantaneous velocity field that describes the motion of a deformable surface has been denoted *range flow* when derived from sequences of range data sets [Yamamoto et al., 1993]. Together with the 3D structure the range flow field can be used to study the dynamic changes

of such surfaces.

A time varying surface may be viewed as a depth function $Z(X, Y, t)$. If the object under consideration is made up of local planar patches then this function can be expressed by its first order Taylor series expansion as:

$$Z(X, Y, t) = Z_0(t) + Z_X X(t) + Z_Y Y(t) \ , \tag{2.34}$$

where the Z_X, Z_Y denote the partial derivatives with respect to X and Y respectively. Here X, Y are the local world coordinates around the point of interest. The change in depth with time then becomes:

$$\frac{\mathrm{d}Z}{\mathrm{d}t} = \frac{\partial Z_0}{\partial t} + Z_X \frac{\mathrm{d}X}{\mathrm{d}t} + Z_Y \frac{\mathrm{d}Y}{\mathrm{d}t} + X \frac{\mathrm{d}Z_X}{\mathrm{d}t} + Y \frac{\mathrm{d}Z_Y}{\mathrm{d}t} \ . \tag{2.35}$$

Under the assumption that the infinitesimal motion of the patch is a pure translation, i.e. the slope does not change ($\frac{\mathrm{d}Z_X}{\mathrm{d}t} = \frac{\mathrm{d}Z_Y}{\mathrm{d}t} = 0$), this can be written as:

$$U_3 = Z_X U_1 + Z_Y U_2 + Z_t \ . \tag{2.36}$$

The local displacements form the range flow field denoted by: $\boldsymbol{U} = [U_1 \ U_2 \ U_3]^T = \frac{\mathrm{d}}{\mathrm{d}t}[X \ Y \ Z]^\top$. Equation (2.36) is called the *range flow constraint equation* [Yamamoto et al., 1993]. The same equation has also been termed the *elevation rate constraint equation* [Horn and Harris, 1991]. We identify the general constraint equation:

$$\boldsymbol{d}_z \cdot \boldsymbol{p}^\top = 0, \quad \text{with} \quad \boldsymbol{d}_z = [Z_X \ Z_Y \ -1 \ Z_t]^\top, \boldsymbol{p} = [U_1 \ U_2 \ U_3 \ 1]^\top \ . \tag{2.37}$$

In order to evaluate the range flow motion constraint Equation (2.36) the derivatives of the depth function with respect to world coordinates have to be computed. This is not entirely straightforward for unevenly sampled data. For moderate inclination angles the derivatives can however be approximated by derivative filters in the image domain [Spies et al., 2002b].

Apart from the 3D structure information discussed so far, optical range sensors also return an intensity value of the observed surface. An example of such range data together with the intensity data is shown in Figure 2.8. Clearly, all the available information should be exploited for the motion model. In order to derive another constraint equation it is reasonable to assume that the intensity of an observed point remains the same for moderate depth changes. Thus, all changes in intensity are attributed to motion in the horizontal plane, similar to the optical flow model as presented in Section 2.2. This yields another constraint equation:

$$0 = I_X U_1 + I_Y U_2 + I_t \quad \rightarrow \quad \boldsymbol{d}_I = [I_X \ I_Y \ 0 \ I_t]^\top \ ; \quad \boldsymbol{p} = [U_1 \ U_2 \ U_3 \ 1]^\top \ . \tag{2.38}$$

Because it was assumed that the intensity is not altered by changes in the distance, it is not possible to infer any information about the vertical motion U_3. However, the intensity constraints both U_1 and U_2. We can thus combine the two equations of motion (2.37) and (2.38) by a weighted adding, leading to

$$\begin{aligned} \boldsymbol{d}_z \cdot \boldsymbol{p}^\top &= 0, \quad \text{with} \quad \boldsymbol{p} = [U_1 \ U_2 \ U_3 \ 1]^\top \quad \text{and} \\ \boldsymbol{d} &= \boldsymbol{d}_z + \lambda \boldsymbol{d}_I = [Z_X + \lambda I_x, Z_Y + \lambda I_y, -1, Z_t + \lambda I_t]^\top \ , \end{aligned} \tag{2.39}$$

where λ is a scalar used for weighting the intensity channels against the depth channels. This weighting can be important when the two channels are corrupted by noise of different magnitude.

2.7 Flow Profiles

2.7.1 Plane Couette Flow

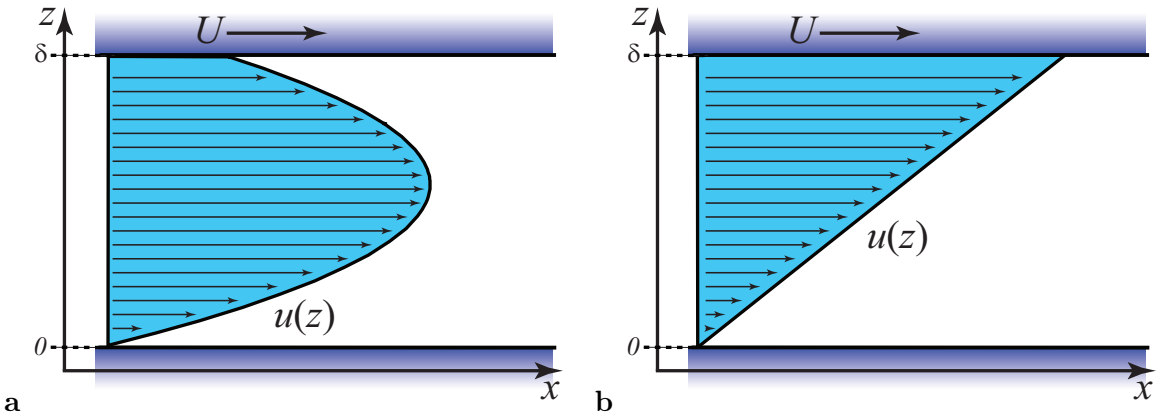

Figure 2.9: *Flow between parallel plates. The bottom plate is stationary, the upper one moving to the right at the velocity U. In* **a** *an additional pressure gradient $dp/dx < 0$ is driving the fluid, in* **b** *Plane Couette flow is shown ($dp/dx = 0$).*

The equation of motion for a flow of uniform density ρ is given by the Navier-Stokes equation for an incompressible fluid [Kundu, 1990]:

$$\frac{d\boldsymbol{u}}{dt} = \boldsymbol{g} - \frac{1}{g}\nabla p + \frac{\mu}{\rho}\nabla^2\boldsymbol{u}, \tag{2.40}$$

where μ is the viscosity and $\nu = \mu/\rho$ is the kinematic viscosity. $\boldsymbol{g}$ is the acceleration of gravity and ∇p is a pressure gradient incident on the fluid. $\boldsymbol{u}$ is the fluid velocity we are interested in. If the body of fluid is at rest, the pressure is hydrostatic ($\boldsymbol{g}\rho = \nabla p_s$), resulting in

$$\frac{d\boldsymbol{u}}{dt} = -\frac{1}{\rho}\nabla p_d + \nu\nabla^2\boldsymbol{u}, \tag{2.41}$$

where $p_d = p - p_s$ is the pressure change due to dynamic effects.

Due to the nonlinear advection term $\boldsymbol{u}\nabla\boldsymbol{u}$ in the Navier Stokes equation, this equation can be solved in closed form for a few special cases only. In general, exact solutions are possible for vanishing nonlinear advection term [Kundu, 1990]. An example of such a special case is the developed flow between infinite parallel plates.

Such a flow is generally driven by a combination of an externally imposed pressure gradient and the motion of the upper plate at uniform velocity U, as shown in Figure 2.9. The two

plates are separated by the distance δ. The 2D configuration of the flow requires $\partial w/\partial y = 0$. In the developed flow, characteristics are also invariant along the x direction, so that continuity requires also $\partial w/\partial z = 0$. Since at the boundary $w = 0$ at $z = 0$, it follows that the flow is parallel to the walls or $w(z) = 0$. The x- and z-momentum equations are then given by

$$0 = -\frac{1}{\rho}\frac{\partial p}{\partial x} + \nu\frac{d^2u}{dz^2} \tag{2.42}$$

$$0 = -\frac{1}{\rho}\frac{\partial p}{\partial z}. \tag{2.43}$$

Integrating the x momentum equation twice leads to

$$0 = -\frac{z^2}{2}\frac{dp}{dx} + \mu u + az + b. \tag{2.44}$$

p is a function of x alone, which allows to write $\partial p/\partial x = dp/dx$. The constants of integration a and b have to be solved from the boundary conditions of the flow. From the lower boundary condition $u(0) = 0$ at $z = 0$, b is required to be $b = 0$. The upper boundary $u(\delta) = U$ at $z = \delta$ leads to $a = \delta(dp/dx)/2 - \mu U/\delta$. This results in the equation

$$u(z) = \frac{z \cdot U}{\delta} - \frac{z}{2\mu}\frac{dp}{dx}(\delta - z). \tag{2.45}$$

From the knowledge of this velocity the volume rate of flow per unit width of the channel Q and the mean velocity $< u >$ as well as the shear stress τ can be estimated to

$$Q = \int_0^\delta u dz = \frac{\delta}{2}U - \frac{\delta^3}{12\mu}\frac{dp}{dx} = \frac{\delta}{2}U\left[1 - \frac{\delta^2}{6\mu U}\frac{dp}{dx}\right] \tag{2.46}$$

$$< u > \equiv \frac{Q}{\delta} = \frac{U}{2}\left[1 - \frac{\delta^2}{6\mu U}\frac{dp}{dx}\right] \tag{2.47}$$

$$\tau = \mu\frac{du}{dz} = \frac{\mu U}{\delta} - \frac{dp}{dx}(\delta - z). \tag{2.48}$$

In the case of plane Couette flow, illustrated in Figure 2.9**b**, the flow is driven by the motion of the upper plate alone, without any externally imposed pressure gradient. For this case, Equations (2.45) - (2.48) reduce to

$$u(z) = \frac{z \cdot U}{\delta}, \qquad < u > = \frac{U}{2} \tag{2.49}$$

$$\tau = \frac{\mu U}{\delta}, \qquad Q = \frac{\delta}{2}U \tag{2.50}$$

Looking at a slight modification of the above configuration, a more general case would be that both plates are moving. The one on top (at $z = \delta$ were δ is the separation of the plates) is moving with the velocity $u(z = \delta) = U_\delta$, the bottom one at $z = 0$ is no longer stationary but moving with the velocity $u(z = 0) = U_0$. This slight change in the boundary conditions leads to the following expression for a and b in Equation (2.44):

$$a = \frac{\mu}{\delta}(U_0 - U_\delta) + \frac{\delta}{2}\frac{dp}{dx}, \quad \text{and} \quad b = -\mu U_0. \tag{2.51}$$

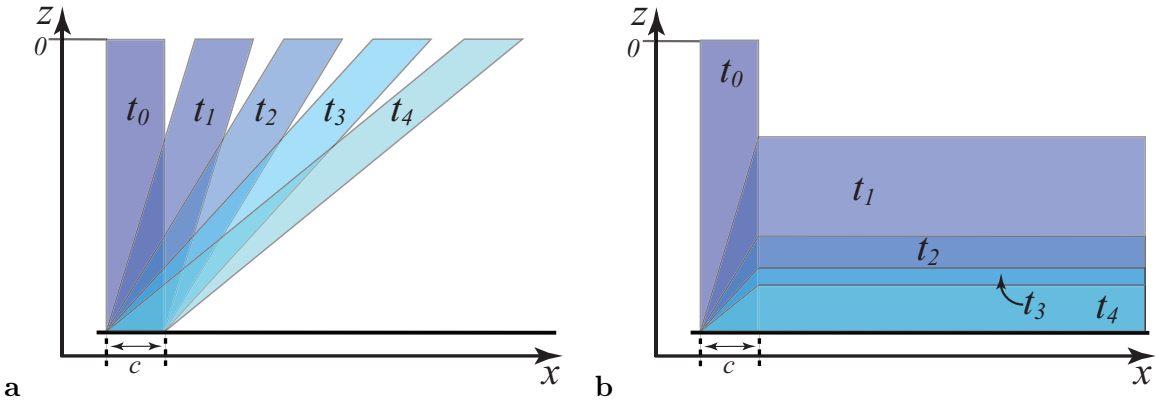

Figure 2.10: *Sketch of a marker in plane Couette Flow written with at time t_0 in subsequent time steps $t_1 - t_4$ in* ***a****. The marker is sheared due to the flow. Shown in* ***b*** *is the depth integration of the marker, as visualized with the camera.*

This leads to the velocity profile $u(z)$ to be given by

$$u(z) = \frac{z}{\delta}\left(U_\delta - U_0\right) + U_0 - \frac{z}{2\mu}\frac{dp}{dx}\left(\delta - y\right), \tag{2.52}$$

and the derived quantities Q, $< u >$ and τ by

$$Q = \int_0^\delta u(z)\, dz = \frac{\delta}{2}\left(U_\delta + U_0\right) - \frac{\delta^3}{12\mu}\frac{dp}{dx} \tag{2.53}$$

$$< u > \equiv \frac{Q}{\delta} = \frac{1}{2}\left(U_\delta + U_0\right) - \frac{\delta^2}{12\mu}\frac{dp}{dx} \tag{2.54}$$

$$\tau = \mu\frac{du}{dz} = \frac{\mu}{\delta}\left(U_\delta - U_0\right) - \frac{1}{2}\frac{dp}{dx}\left(\delta - 2z\right). \tag{2.55}$$

It is evident that these equations make sense as they reduce to Equations (2.45)- (2.48) for $U_0 = 0$. Also, the motion of the lower plate can be thought of as a change in the frame of reference, which leaves the gradients untouched.

In the event that no external pressure is driving the flow, that is $dp/dx = 0$, Equations (2.52) - (2.55) simplify to

$$u(z) = \frac{z}{\delta}\left(U_\delta - U_0\right) + U_0, \qquad < u > = \frac{1}{2}\left(U_\delta + U_0\right) \tag{2.56}$$

$$\tau = \frac{\mu}{\delta}\left(U_\delta - U_0\right), \qquad Q = \frac{\delta}{2}\left(U_\delta + U_0\right). \tag{2.57}$$

Plane Couette flow might seem of academic interest only. However, it is a very good approximation of a number of shear driven flows. It can be used to describe the velocity structure at the wind driven sheared interface between atmosphere and ocean, as will be presented in Section 7.8. The model of plane Couette flow is an even better approximation of the air-water boundary condition in the event of a surfactant covered interface. This is due to the fact that surfactants suppress waves and can be thought of as a rigid interface.

For a number of scientific and industrial applications, it is of interest to accurately measure the flow and velocity profile of the plane Couette flow. This is a straight forward task when the flow is accessible from the side (along the y-axis in Figure 2.9). In this case the velocity can be measured at a range between the two plates and the gradient with respect to z computed.

Very often, it is not possible to measure the fluid flow in this fashion, since the flow is not accessible from the side. This can either be due to the minute separation of the plates in microfluidic applications or because a very small boundary layer is modulated by relatively high waves at the air-water interface. Under these circumstances, it might be necessary to measure the flow through either the top of bottom plate in technical applications or from the above the air-water interface. As in most fluid flow applications, a marker has to be introduced to visualize the flow. In microfluidic flows this can be done with caged dyes, which will be discussed in Chapter 8. Heat can also be used as a marker visualized with infrared cameras. This technique will be pursued in Section 7.8. The problem of using these techniques is that the marker is not visualized in one well defined layer between the two plates. Moreover, due to experimental constraints, the marker is integrated across the distance separating the two plates. Due to this integration, the markers appear to be smeared by the motion, a process that is also known as Taylor dispersion in the case of parabolic profiles (cf Section 2.7.2). In order to estimate motion correctly under these circumstances, this integration of the marker over the separation of the plates has to be modeled adequately.

As has been shown earlier, the velocity profile in plane Couette flow is given by Equation (2.49) in the case of stationary plate at the bottom of the flow ($v(z = 0) = 0$) and by Equation (2.56) otherwise. This leads to the following time dependence of the position of a marker attached to the flow at $t = t_0 = 0$ for both cases, respectively:

$$x_{U_0=0}(z,t) = \frac{z}{\delta} U \cdot t = \frac{z}{\mu} \tau \cdot t \quad \text{and} \tag{2.58}$$

$$x_{U_0}(z,t) = \frac{z}{\delta}(U_\delta - U_0) \cdot t + U_0 \cdot t = \frac{z}{\mu} \tau \cdot t + U_0 \cdot t. \tag{2.59}$$

It shall be assumed that the fluid elements are marked at time $t_0 = 0$ with an appropriate technique. Section 8 will present such a technique relying on the activation of caged dyes with a XeF Excimer laser. In Sections 7.8 and 9 we will heat up water parcels with ca CO_2 laser and visualize them with an infrared camera. Without taking the Lamert-Beer law into consideration and thus no attenuation with depth, the marker highlights a homogeneous three dimensional structure inside the viscous boundary layer. A sketch of such a structure is presented in Figure 2.10**a**.

Once the structure is written at time t_0, it is sheared due to the velocity profile as indicated in the same figure in successive time steps $t_1 - t_4$. In the imaging process the dimension of depth z is lost through integration. The projection of intensities I onto the surface at $z = \delta$

is given by

$$I_{U_0=0}(x,t) = \int_{\frac{\delta\cdot(x-c)}{U\cdot t}}^{\frac{\delta\cdot x}{U\cdot t}} 1\, dz = \frac{x\cdot\delta}{t\cdot U} - \frac{(x-c)\cdot\delta}{t\cdot U} = \frac{c\cdot\delta}{t\cdot U} = \frac{\mu\cdot c}{t\cdot\tau} \quad \text{and} \tag{2.60}$$

$$\begin{aligned} I_{U_0}(x,t) &= \frac{x\cdot\delta}{t\,(U_\delta - U_0)} - \frac{U_0\cdot\delta}{U_\delta - U_0} - \frac{(x-c)\cdot\delta}{t\,(U_\delta - U_0)} + \frac{U_0\cdot\delta}{U_\delta - U_0} \\ &= \frac{c\cdot\delta}{t\,(U_\delta - U_0)} = \frac{\mu\cdot c}{t\cdot\tau}. \end{aligned} \tag{2.61}$$

Here c denotes the width of the area marked, as can be seen in Figure 2.10. The expression for τ was used from Equation (2.50) and (2.57), respectively.

From Equations (2.60) and (2.61) it becomes apparent, that in terms of the visualized intensity structures I, both cases of boundary conditions ($u(z=0)=0$ and $u(z=0)=U_0$) can be treated identically. The only exception is that in the case of a moving bottom "plate", the intensities I_{U_0} only depend on the relative velocity $\Delta U = U_0 - U_\delta$. This is ostensivly clear, since only the frame of reference has changed due to the motion of the bottom boundary at $z=0$. In the following one only needs to be concerned with the case of stationary bottom boundary condition, knowing that all needed to do is replace U by $U_\delta - U_0$ for the other case.

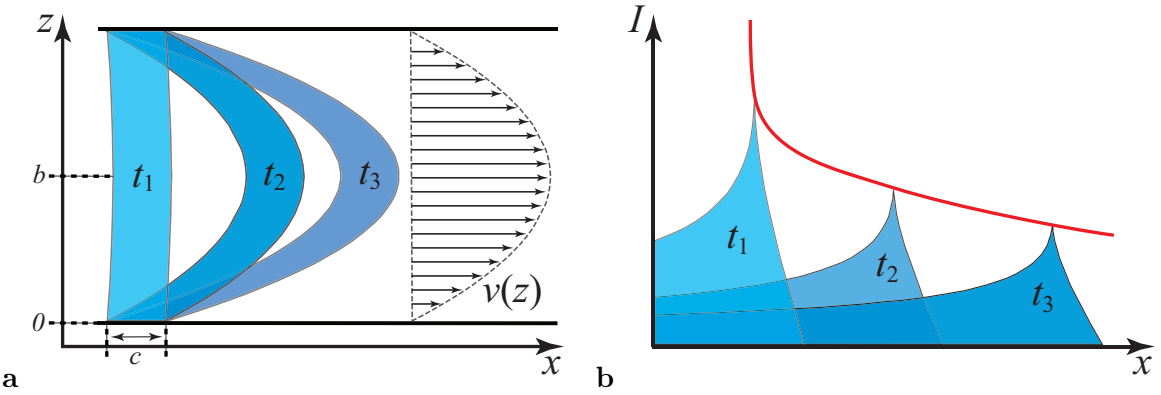

Figure 2.11: *A sketch of the intensity profile of the dye for a Poiseuille flow at three times t_1-t_3 is shown in* ***a*** *together with the velocity profile $v(z)$. The projection of these profiles onto one plate as seen by the camera is shown in* ***b****.*

Differentiating Equation (2.60) with respect to time leads to

$$\frac{dI}{dt} = \frac{d}{dt}\left(\frac{c\cdot\delta}{t\cdot U}\right) = -\frac{1}{t}I. \tag{2.62}$$

Estimating the velocity of the intensity structures subject to a plane Couette type shear flow with a linear velocity gradient can thus be computed by solving the differential equation $dI/dt = -(t)^{-1}I$ which can be written in an extension of the BCCE as

$$\frac{dI}{dt} = u_1\frac{\partial I}{\partial x} + u_2\frac{\partial I}{\partial y} + \frac{\partial I}{\partial t} = -\frac{1}{t}I. \tag{2.63}$$

Rewriting this equation in vector notation leads to

$$\frac{dI}{dt} = d^\top \cdot p = \begin{bmatrix} \frac{1}{t}I & \frac{\partial I}{\partial x} & \frac{\partial I}{\partial y} & \frac{\partial I}{\partial t} \end{bmatrix} \cdot \begin{bmatrix} 1 & u_1 & u_2 & 1 \end{bmatrix}^\top = 0 \,. \tag{2.64}$$

This equation can be thought of as the motion equation of density structures visualized through integration across a plane Couette type flow. Later on in Section 3 it will be shown how this model can be used to estimate motion from it. An application will be presented in Section 7.8.

2.7.2 Plane Poiseuille Flow

An expression for plane Couette flow has been developed in the previous section. In this type of flow a fluid between two plates is driven by the relative motion of them. It was assumed that no pressure difference was present. In Poiseuille flow, the configuration is again similar. Once more, a fluid is bounded by two infinite plates separated by a distance $\delta = 2 \cdot b$. However, for Poiseuille flow both plates are stationary ($U_\delta = U_0 = U = 0$) and the flow is driven only by a pressure difference dp/dx. In this configuration, Equation (2.45) reduces to

$$u(z) = -\frac{z}{2\mu}\frac{dp}{dx}(\delta - z) = -\frac{z}{\mu}\frac{dp}{dx}\left(b - \frac{z}{2}\right) = \frac{a}{2}z^2 - a \cdot b \cdot z \quad \text{with} \quad a = \frac{1}{\mu}\frac{dp}{dx}. \tag{2.65}$$

This type of flow and the associated quantities are visualized in the sketch of Figure 2.11 **a**.

The maximum velocity $v_{\max}$ of the flow is given at the center in between the two plates at $x = b$. This velocity and the mean velocity $\langle v(y) \rangle$ are thus given by

$$v_{\max} = v(b) = -\frac{a}{2} \cdot b^2, \tag{2.66}$$

$$v_{\text{mean}} = \langle v(z) \rangle = \frac{1}{2b}\int_0^{2b} v(z)dz = -\frac{a}{3} \cdot b^2 = \frac{2}{3}v_{\max}. \tag{2.67}$$

The shear stress τ is found by setting $U = 0$ in Equation (2.48) which leads to

$$\tau = \frac{dp}{dx}(z - \delta) \,. \tag{2.68}$$

Similar to plane Couette flow as presented in Section 2.7.1, plane Poisseuille flow has a broad range of applications, especially in microfluidics, as will be presented in Chapter 8. In these types of applications it is important to measure the velocity of fluid parcels in between parallel plates. However, due to the boundary conditions of the microfluidic devices, it is not possible to visualize the cross section of the flow. A marker such as a caged dye is introduced into the fluid and a pattern is written to the fluid a time $t = 0$. In later times, this structure is sheared by the paraboloid velocity profile developed by the Poiseuille flow. The 2D cut of this process is shown for three time steps t_1-t_3 in Figure 2.11**a**. Through this projection, it appears as though the structure written to the fluid is smeared in the direction of the fluid flow over time. This process which might appear similar to anisotropic diffusion is also known

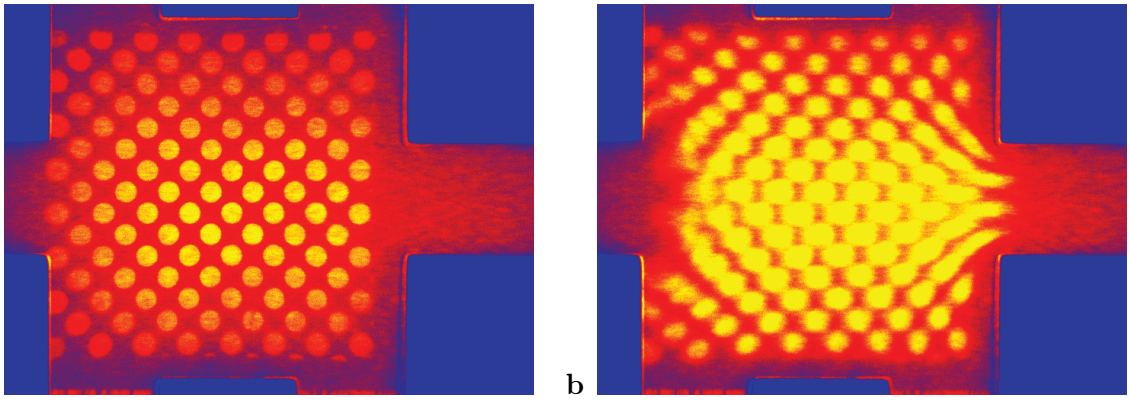

Figure 2.12: *In* **a** *and* **b** *two frames of a microfluidic image sequences are shown. The implication of Taylor dispersion can clearly be observed. Structures seem to diffuse in the direction of fluid flow.*

as *Taylor dispersion* [Taylor, 1954]. An image of this type of process can be seen in Figure 2.12.

The marker is visualized through one of the plates, leading to an integration of the dye with respect to depth z. This results in

$$I = \int_{b\pm\sqrt{b^2+\frac{2x}{at}}}^{b\pm\sqrt{b^2+\frac{2(x+c)}{at}}} 1dz = \sqrt{\left\| b^2 + \frac{2\cdot(c+x)}{a\cdot t} \right\|} - \sqrt{\left\| b^2 + \frac{2\cdot x}{a\cdot t} \right\|}. \tag{2.69}$$

This analytic function is visualized in the sketch in Figure 2.11**b**.

The maximum of the projected intensity is given by

$$I_{\max} = \sqrt{\left\| \frac{2\cdot c}{a\cdot t} \right\|}. \tag{2.70}$$

The location of this intensity maximum $x_{\max}$ can be found to be

$$x_{\max} = -\frac{a}{2}\cdot b^2 \cdot t \tag{2.71}$$

and subsequently the velocity of the intensity maximum to

$$v_{\max} = \frac{\partial x_{\max}}{\partial t} = -\frac{a}{2}\cdot b^2. \tag{2.72}$$

By comparing this equation with the expression of the maximum velocity from the velocity profile in Equation (2.66) it becomes apparent, that the velocity of the intensity maximum is equivalent to the velocity halfway in between the two plates. This result is not surprising, as the intensity maximum of the projection is collocated to the trailing edge of the written structures halfway in between the plates. This can easily be seen in Figure 2.11**b**.

The projected intensity structure is given by Equation (2.69). This structure can be developed in a Taylor series around $t = 0$. This results in

$$I = \sqrt{\frac{2}{t}}\left(\sqrt{\frac{c+x}{a}} - \sqrt{\frac{x}{a}}\right) + \frac{b^2\sqrt{t}}{2\sqrt{2}}\left(\sqrt{\frac{a}{c+x}} - \sqrt{\frac{a}{x}}\right) + \mathcal{O}\left(t^{3/2}\right). \tag{2.73}$$

Differentiating the first term of the expansion in time leads to

$$\frac{dI}{dt} = \frac{d}{dt}\left(\sqrt{\frac{2}{t}}\left(\sqrt{\frac{c+x}{a}} - \sqrt{\frac{x}{a}}\right)\right) = -\frac{1}{2t}I. \tag{2.74}$$

Estimating the velocity of the intensity structures subject to Taylor dispersion can thus be computed by solving the differential

$$\frac{dI}{dt} = u_1\frac{\partial I}{\partial x} + u_2\frac{\partial I}{\partial y} + \frac{\partial I}{\partial t} = -\frac{1}{2t}I. \tag{2.75}$$

This linear differential equation can be rewritten in vector notation which leads to

$$\frac{dI}{dt} = d^\top \cdot p = \begin{bmatrix} \frac{1}{2t}I & \frac{\partial I}{\partial x} & \frac{\partial I}{\partial y} & \frac{\partial I}{\partial t} \end{bmatrix} \cdot \begin{bmatrix} 1 & u_1 & u_2 & 1 \end{bmatrix}^\top = 0. \tag{2.76}$$

This equation can then be solved by the algorithm presented in Section 3.3.

2.7.3 n-th Order Velocity Profiles

For a number of fluid flow configuration, the velocity profile can be approximated to leading order by

$$u(z) = A \cdot z^n, \tag{2.77}$$

where A is a term independent of z and t. The integration across the profile results in

$$I = \int_{\sqrt[n]{\frac{x-c}{A\cdot t}}}^{\sqrt[n]{\frac{x}{A\cdot t}}} 1 \,\mathrm{d}z = \sqrt[n]{\frac{x}{A\cdot t}} - \sqrt[n]{\frac{x-c}{A\cdot t}}. \tag{2.78}$$

Differentiating this expression with respect to time leads directly to the following differential equation

$$\frac{dI}{dt} = u_1\frac{\partial I}{\partial x} + u_2\frac{\partial I}{\partial y} + \frac{\partial I}{\partial t} = -\frac{1}{n\cdot t}I, \tag{2.79}$$

which can be written in vector notation giving

$$\frac{dI}{dt} = d^\top \cdot p = \begin{bmatrix} \frac{1}{nt}I & \frac{\partial I}{\partial x} & \frac{\partial I}{\partial y} & \frac{\partial I}{\partial t} \end{bmatrix} \cdot \begin{bmatrix} 1 & u_1 & u_2 & 1 \end{bmatrix}^\top = 0. \tag{2.80}$$

It is quite easy to see that this is a generalization of the previous cases of plane Couette flow from Section 2.7.1 ($n = 1$), compared to Equation (2.63) and (2.64) and of plane Poiseuille flow introduced in Section 2.7.2 ($n = 2$), compared to Equations (2.75) and (2.76).

The both relevant flow configuration between parallel plates discussed so far have been plane Couette flow and plane Poiseuille flow. It might seem superfluous to expand the model to n-th order. However, there are flows for wich higher order flow profiles are relevant. In Figure 2.13**a** the velocity profiles for a range of higher order models is sketched. It becomes apparent, that the central part of the profile becomes increasingly flat. Choosing ever higher

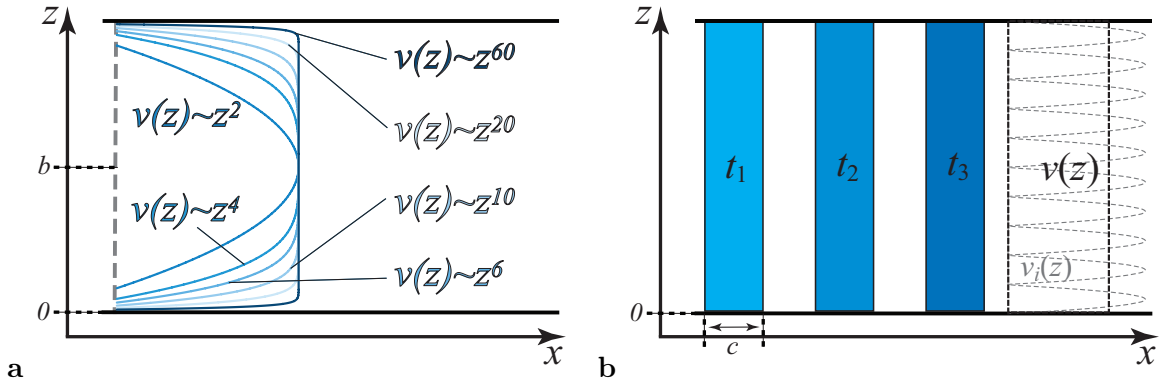

Figure 2.13: *In* **a** *a sketch of velocity profiles* $v(z) \sim z^n$ *with* $n \in \{2, 4, 6, 10, 20, 60\}$. *The higher the order* n *the better the approximation of a constant profile as shown in* **b**. *In the xylem of plants, the flow can be approximated by a number of small hollow tubes with a Poiseuille flow in between, as shown in* **b**. *The resulting velocity profile is a constant one.*

order up to $n \overset{\lim}{\longrightarrow} \infty$, we end up with a constant velocity profile with sharp edges. As we will learn, this is precisely the model chosen for the velocity profiles in the xylem of plants. This model is shown in Figure 2.13**b**. In this application, we try to measure water flows inside the xylem. This will be explained in detail in Section 9.

It is interesting to note that the motion Equations (2.79) and (2.80) reduce to

$$\frac{dI}{dt} = u_1 \frac{\partial I}{\partial x} + u_2 \frac{\partial I}{\partial y} + \frac{\partial I}{\partial t} = -\frac{1}{n \cdot t} I, \quad \text{and} \quad n \overset{\lim}{\to} \infty \quad \frac{dI}{dt} = 0, \tag{2.81}$$

which is the standard BCCE which was already introduced in Section 2.2. This means that in the case of a constant velocity profile with depth, integration over depth does not matter and the standard BCCE can be used for estimating velocities of projected quantities. Intuitively this does make sense, indicating the value of expanding the motion models to n-th order profiles.

2.8 Conclusion

In this chapter, a number of different motion models were presented. These model connect the motion of object in the scene with gray value changes in the acquired image sequences. The applicability of each model will depend on the specific scene or imaged data at hand. A number of scientific applications will be introduced in the second part of this thesis, where the models of this chapter will be used.

The models that were introduced can be divided into two groups, depending on the feature they are addressing:

1. Models that parameterize motion within the local neighborhood

2. Change of brightness along trajectories of objects.

For the group 1, a very general model based on Lie groups was introduced, as well as its special cases of affine and planar transformation. For case 2, a general extension of the BCCE was presented that allows to formulate the brightness change along trajectories as partial differential equations. Special cases include linear brightness change, exponential decay and brightness change due to diffusion processes. Also, being introduced was the estimation of range flow from range data, which is very similar to the linear brightness change model presented previously. Integration of a marker over a flow profile will also lead to an apparent brightness change in the objects. This brightness change is very similar in appearance to anisotropic diffusion. Expressions for first and second order flow profile have been developed as well as general n-th order profiles. Applications of these models will be presented in Sections 7.8, 8 and 9. Also, the motion models to n-dimensional data in the case of spectral image sequences have been extended. Here, color sequences present a special case of $n = 3$.

The models are formulated as linear partial differential equations. Combinations of any of the presented models are thus easily achievable. The model parameter can be estimated in a very general framework, which will be introduced in the next chapters.

Chapter 3

Gradient Based Techniques

3.1 Introduction

Moving objects in a scene will cause image brightness changes. In motion estimation, one tries to infer the displacement of patterns from the change in gray values the motion caused. This represents a classical inverse problem. Menke [1989] defines inverse theory as "an organized set of mathematical techniques for reducing data to obtain useful information about the physical world on the basis of inferences drawn from observations." This definition emphasizes the three foundations of inverse theory:

- data, corrupted by noise, or "inferences drawn from observations",
- a model, or "useful information about the physical world" and
- estimation of model parameters or "mathematical techniques for reducing data".

In the context of motion estimation, data is given in the form of image sequences $I(\boldsymbol{x}, t)$ or responses to filters thereof. Useful models will depend on the application at hand. In Chapter 2 a number of applicable models have been introduced. Common to all these models is, that they are linear models in their parameters and that they can be formulated as a vector product in between a data vector $\boldsymbol{d}$ and a parameter vector $\boldsymbol{p}$. A very basic model often used is the brightness change constraint equation (BCCE) from Equation (2.3):

$$\frac{dI}{dt} = u_1 \frac{\partial I}{\partial x} + u_2 \frac{\partial I}{\partial y} + \frac{\partial I}{\partial t} = \boldsymbol{d}^\top \cdot \boldsymbol{p} = 0, \quad \text{with} \quad \boldsymbol{d} = [I_x, I_y, I_t]^\top \text{ and } \boldsymbol{p} = [u_1, u_2, 1]^\top . \quad (3.1)$$

Here subscripts I_n denote partial derivatives of I in the direction of n.

In inverse theory, or motion estimation for that matter, one seeks to compute model parameters $\boldsymbol{p}$ from observations $\boldsymbol{d}$. This task is not as easy as it might appear on first sight. First of all, it is not possible to observe the true data $\boldsymbol{d}_0$, but only the observations corrupted by noise $\boldsymbol{n}$, thus $\boldsymbol{d} = \boldsymbol{d}_0 + \boldsymbol{n}$. The structure of the noise has to be taken into account in order to gain unbiased estimates of the parameter vector [Garbe et al., 2002e; Jähne and Garbe, 2003].

The main obstacle of inferring the model parameters $\boldsymbol{p}$ from the noisy data $\boldsymbol{d}$ is that this problem is an ill-posed one. In contrast, a well-posed problem as defined by Hadamard [1902] has to have the following properties:

1. A solution exists
2. The solution is unique
3. The solution depends continuously on the data, in some reasonable topology.

Even though generally a solution will exist to Equation (3.1), it surely cannot be unique. This is due to the fact that one tries to find $p \geq 2$ model parameters from only one constraint equation. This represents a manifestation of the aperture problem that will be introduced in Section 3.2.1.

The inverse problem of motion estimation can only be solved by introducing additional constraint equations. It is difficult to find universally valid constraints. However, it is observed that motion vectors should not change drastically from one image location to the next. This is especially the case in image locations representing the same object. Here, the motion field can be assumed to change only gradually. This gradual change in the motion field can be formulated as a smoothness constraint. Two distinctly different ways of formulating this smoothness constraint exist. The first one was conceived by Lucas and Kanade [1981]. They assumed the parameters $\boldsymbol{p}$ to remain locally constant in a small neighborhood. This formulation of the smoothness constraint leads to an overdetermined system of equations which can be solved in the formalism of parameter estimation. This type of motion estimator will be presented in Section 3.3. In contrast to this local formulation of the smoothness constraint, smoothness can also be stipulated globally, as was first demonstrated by Horn and Schunk [1981] in a variational framework. This type of estimator will be presented in Section 3.5. As will be shown, both approaches initially had their strong advantages and disadvantages. This has lead to intensive research in both types of motion estimators, leading ultimately to a merger of these approaches [Spies and Garbe, 2002; Bruhn et al., 2005], which will be presented in Section 3.5.4.

This chapter is organized as follows: In Section 3.2 two fundamental problems in motion estimation will be discussed, namely the aperture problem in Section 3.2.1 and the problem of occlusions in Section 3.2.2. In Section 3.3 the technique of estimating motion in a local framework from the models presented in Chapter 2 will be introduced. This technique, also known as the structure tensor approach, can be thought of as a special case of parameter estimation. Therefore, in Section 3.4 a general parameter estimation framework will be presented. It will be shown that depending on the motion model used, different estimators result in unbiased estimates. In Section 3.5 a different class of estimators will be presented. Here, motion will not be estimated in a local neighborhood, but in a variational approach which takes the complete image sequence into consideration.

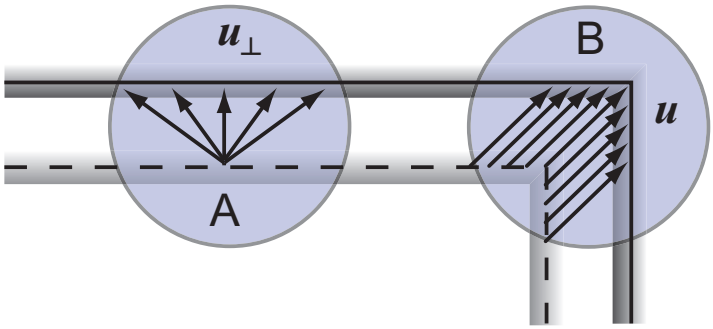

Figure 3.1: *The aperture problem illustrated by a moving edge. The edge is moved from the initial (dotted line) to the final location (solid line). In the neighborhood* **A** *an aperture problem is present and only the minimum norm solution* $\boldsymbol{u}_\perp$ *in the direction of the gradient can be estimated. In the neighborhood* **B** *enough structure (corner) is present to estimate the full flow* $\boldsymbol{u}$*.*

3.2 Problems of Motion Estimation

3.2.1 The Aperture Problem

As was shown in the previous section, mathematically the BCCE forms an ill posed problem. For the p unknowns of the parameter vector $\boldsymbol{p} \in \mathbb{R}^p$ only one constraint equation has been formulated. The number of free parameters p will depend on the model used. In Section 2 several possible models have been presented. For the simplest model of pure translation, the optical flow $\boldsymbol{u} = [u_1, u_2]^\top$ represents $p = 2$ unknowns of translation along the x and y axis. However, from this one constraint equation, only the motion component $\boldsymbol{u}_\perp$ in the direction of the local gradient can be estimated, an incident known as the *aperture problem* [Ullman, 1979]. This orthogonal motion can be derived from the BCCE in Equation (3.1) as

$$\boldsymbol{u}_\perp = -\frac{I_t(\boldsymbol{x},t)\boldsymbol{\nabla} I(\boldsymbol{x},t)}{||\boldsymbol{\nabla} I(\boldsymbol{x},t)||_2^2}, \tag{3.2}$$

where I_t is the partial derivative of the image intensity with respect to time and $||\cdot||_2$ is the L-2 norm. ∇I represents the spatial gradient. This expression turns out to be equivalent to the non-generic TLS problem presented in Equation (3.30) of Section 3.4.2.

By itself, the aperture problem cannot be solved. This becomes apparent by looking at Figure 3.1. If locally only a straight edge is seen, no information regarding motion along this edge can be extracted. Full information can only be derived from analyzing a local neighborhood where enough structure along all directions is available, at corners for example. Thus, from one point alone full motion cannot be computed, only by relating information from neighboring pixel the aperture problem can be resolved. By incorporating information from neighboring pixel it is assumed, that the motion of these pixel is related in some way, which represents a second assumption besides the motion model. Two distinctly different formulations to solve the aperture problem will be detailed later on in this chapter.

3.2.2 Occlusion in Image Sequences

The occlusion problem has been widely studied in the context scene reconstruction from stereo images [Geiger et al., 1995; Lin and Tomasi, 2004]. In this context, the detection of the occluded areas is very important to improve the dense disparity map and the quality of 3D reconstruction. Occlusions are defined to be regions in one image that have no match in the other image for a stereoscopic image pair [Geiger et al., 1995]. The same holds true for an image sequence, where an occlusions is defined as a region in one image that has no match in the other one. However, contrasting stereo vision, in motion analysis often more than two frames are available. The definition of occlusions is thus extended to this case, stating that an occlusion is an area which has no match in all of the frames included in the motion estimation. For example, if for a gradient approach a 5 tap temporal gradient filter is used, then an occlusion would be defined as a region that is not apparent in all of these 5 frames.

Occlusions have gained importance in the context of layer representation of image sequences and their extraction [Wang and Adelson, 1994; Tao et al., 2002; Smith et al., 2004; Xiao and Shah, 2005]. It is also important to detect these occlusions, as they might potentially corrupt the image estimation. Measures for detecting this type of areas in scenes will be described in Chapter 5. A motion estimator was presented by Silva and Santos [2001] that is based on the effect of occlusions to estimate ego-motion.

In the context of this work, occlusions do not play an important role. In most scientific applications and especially in those of fluid dynamics, this problem can be avoided. Therefore, this problem will not be addressed in the following.

3.3 Tensor Based Motion Estimation

The aperture problem can be solved by an approach introduced by Lucas and Kanade [1981] and Lucas [1984]. They assume the motion patterns to be constant in a local neighborhood. From this assumption follows directly that the constraint can be pooled over this neighborhood. The optical flow problem can then be solved using a weighted ordinary least squares estimator (see Section 3.4.2):

$$\text{minimize } e(\boldsymbol{u}) = \sum_{\boldsymbol{x}\in\mathcal{N}} w(\boldsymbol{x}) \left(\boldsymbol{\nabla} I(\boldsymbol{x},t)\cdot\boldsymbol{u} + I_t(\boldsymbol{x},t)\right)^2, \tag{3.3}$$

where $w(\boldsymbol{x})$ denotes a window function that determines the support of the estimator, $\mathcal{N}$ the local spatial neighborhood and $e(\boldsymbol{u})$ is the residual of the fit. In practical applications, the window function w is realized by a Gaussian smoothing kernel, although different weighting functions are conceivable such as robust formulations based on M-estimators [Huber, 1980]. Here the rationale is to weight constraints in the center of the neighborhood higher and to give them a stronger influence on the estimation. This is due to the fact that the assumption of locally constant parameters is usually better met close to the central pixel.

The solution to the problem of Equation (3.3) can be found by setting the derivatives of

$\boldsymbol{e}$ with respect to the parameters $\boldsymbol{u}$ to zero, leading to

$$\frac{\partial e(\boldsymbol{u})}{\partial u_1} = \sum_{\boldsymbol{x}\in\mathcal{N}} w(\boldsymbol{x}) \left(u_1 I_x^2 + u_2 I_x I_y + I_x I_t\right) \stackrel{!}{=} 0 \tag{3.4}$$

$$\frac{\partial e(\boldsymbol{u})}{\partial u_2} = \sum_{\boldsymbol{x}\in\mathcal{N}} w(\boldsymbol{x}) \left(u_2 I_y^2 + u_1 I_x I_y + I_y I_t\right) \stackrel{!}{=} 0 \tag{3.5}$$

which can be rewritten in matrix form as

$$\begin{aligned} \boldsymbol{A}\cdot\boldsymbol{u} &= \boldsymbol{b} \quad \text{with} \quad \boldsymbol{A}\in\mathbb{R}^{2\times 2}, \boldsymbol{u}\in\mathbb{R}^2 \text{ and } \boldsymbol{b}\in\mathbb{R}^2 \quad \text{given by} \\ \boldsymbol{A} &= \begin{bmatrix} \sum w I_x^2 & \sum w I_x I_y \\ \sum w I_x I_y & \sum w I_y^2 \end{bmatrix} = \begin{bmatrix} \mathcal{B}*(I_x\cdot I_x) & \mathcal{B}*(I_x\cdot I_y) \\ \mathcal{B}*(I_x\cdot I_y) & \mathcal{B}*(I_y\cdot I_y) \end{bmatrix} \\ \boldsymbol{b} &= -\begin{bmatrix} \sum w I_x I_t \\ \sum w I_y I_t \end{bmatrix} = -\begin{bmatrix} \mathcal{B}*(I_x\cdot I_t) \\ \mathcal{B}*(I_y\cdot I_t) \end{bmatrix}. \end{aligned} \tag{3.6}$$

Here, $(I_x\cdot I_x)$ denote point wise multiplication of the partial derivatives, $*$ indicates a convolution and $\mathcal{B}$ denotes a smoothing with an appropriate kernel, such as a binomial kernel as an approximation of the Gaussian kernel. The size of the binomial kernel, or the support of the Gaussian, are equivalent to the size of the local spatial-temporal integration.

Given that the matrix $\boldsymbol{A}$ has full rank, that is its determinant $\det\boldsymbol{A}\neq 0$, the solution $\hat{\boldsymbol{u}}$ to this problem is readily given as

$$\hat{\boldsymbol{u}} = \boldsymbol{A}^{-1}\boldsymbol{b} = -\frac{1}{\det\boldsymbol{A}} \begin{bmatrix} \mathcal{B}*(I_y\cdot I_y) & -\mathcal{B}*(I_x\cdot I_y) \\ -\mathcal{B}*(I_x\cdot I_y) & \mathcal{B}*(I_x\cdot I_x) \end{bmatrix} \cdot \begin{bmatrix} \mathcal{B}*(I_x\cdot I_t) \\ \mathcal{B}*(I_y\cdot I_t) \end{bmatrix} \tag{3.7}$$

$$= \frac{1}{\mathcal{B}(I_xI_y)^2 - \mathcal{B}(I_xI_x)\mathcal{B}(I_yI_y)} \begin{bmatrix} \mathcal{B}(I_yI_y)\mathcal{B}(I_xI_t) - \mathcal{B}(I_xI_y)\mathcal{B}(I_yI_t) \\ \mathcal{B}(I_xI_x)\mathcal{B}(I_yI_t) - \mathcal{B}(I_xI_y)\mathcal{B}(I_xI_t) \end{bmatrix}. \tag{3.8}$$

It is evident that this estimation of the velocity field $\hat{\boldsymbol{u}}$ can be implemented very efficiently, as only the three spatio-temporal gradients of the image sequence I have to be computed. Then, five point wise multiplications of these gradients have to be performed and the results convoluted with a smoothing filter. On the resulting date, five multiplications and three additions have to be performed.

This algorithm was first introduced by Lucas and Kanade [1981] and is based on a weighted ordinary least squares fit (OLS) of the motion model to an overdetermined set of equations. This has some implications for an unbiased estimate on the noise distribution of the spatio-temporal derivatives as will be demonstrated in Section 3.4.1.

Generally, all the spatio-temporal gradients of image intensity will be erroneous which introduces a bias in the estimation via OLS [Jähne and Garbe, 2003] (see Section 3.4.1). In performance analyses it has been shown that the estimated velocities tend to lower values for $\hat{\boldsymbol{u}}$ in the presence of noise. Thus it is preferable to solve the system of linear Equations (3.3) in the weighted total least squares framework of Section 3.4.2 [Chu and Delp, 1989]. This approach of solving the motion parameters is generally known as the *structure tensor technique*. The structure tensor was first introduced by Bigün and Granlund [1987] for detecting linear

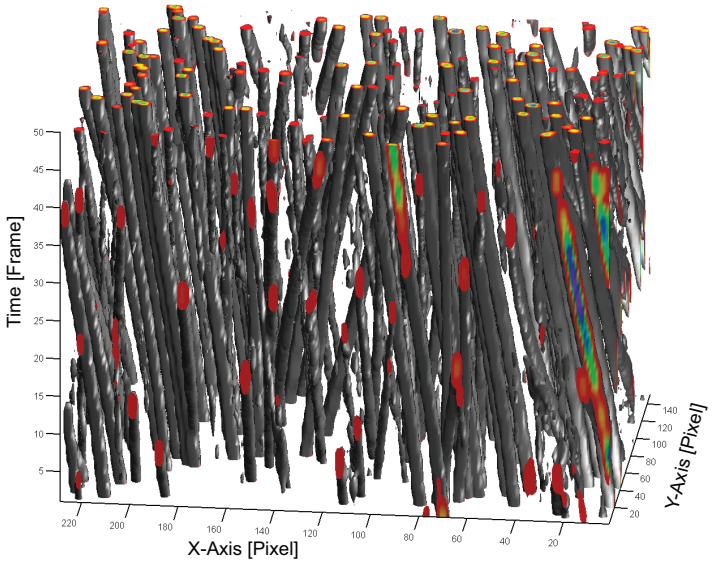

Figure 3.2: *A time sequence of particle images, visualized as a 2D+t volume. The trajectories of the particles can clearly be seen as particle "tubes". The velocity is directly related to the orientation of these structures.*

symmetries in 2D images. As it turns out, 2D motion can be thought of as an oriented structure in 2D+t. This idea is visualized in Figure 3.2. The concept of the 2D structure tensor can thus readily be extended to 3D, leading to the minimization of

$$\text{minimize } e(\boldsymbol{w}) = \sum_{\boldsymbol{x}\in\mathcal{N}} w(\boldsymbol{x}) \left(\boldsymbol{\nabla}_{xt} I(\boldsymbol{x},t) \cdot \boldsymbol{w}\right)^2, \quad \text{with} \quad \boldsymbol{w} = \begin{bmatrix} \boldsymbol{u} \\ 1 \end{bmatrix}, \tag{3.9}$$

where $\boldsymbol{\nabla}_{xt}$ represents the spatio-temporal gradient. In order to avoid the trivial solution $\boldsymbol{w} \equiv 0$ the additional constraint $\boldsymbol{w}^\top \boldsymbol{w} \stackrel{!}{=} 1$ has to be imposed on $\boldsymbol{w}$. As will be shown in Section 3.4.2 this minimization will lead to the following quadratic form $e(\boldsymbol{w}) = \boldsymbol{w}^\top \boldsymbol{J} \boldsymbol{w}$, which reduces to the following eigenvalue equation by incorporating the constraint on the norm of $\boldsymbol{w}$:

$$e(\boldsymbol{w}) = \boldsymbol{w}^\top \boldsymbol{J} \boldsymbol{w} = \boldsymbol{w}^\top \lambda \boldsymbol{w} = \lambda, \tag{3.10}$$

where λ is an eigenvector of the symmetric matrix $\boldsymbol{J}$. Thus, $e(\boldsymbol{w})$ is minimized by the smallest eigenvalue λ_n of the structure tensor $\boldsymbol{J}$. The solution of the motion estimation problem in the structure tensor formalism can thus be solved by performing an eigensystem analysis of the structure tensor $\boldsymbol{J}$ given by

$$\boldsymbol{J} = \begin{bmatrix} \mathcal{B} * (I_x \cdot I_x) & \mathcal{B} * (I_x \cdot I_y) & \mathcal{B} * (I_x \cdot I_t) \\ \mathcal{B} * (I_x \cdot I_y) & \mathcal{B} * (I_y \cdot I_y) & \mathcal{B} * (I_y \cdot I_t) \\ \mathcal{B} * (I_x \cdot I_t) & \mathcal{B} * (I_y \cdot I_t) & \mathcal{B} * (I_t \cdot I_t) \end{bmatrix}, \tag{3.11}$$

which can also be thought of as the correlations of the weighted gradients of I. The sought solution is then given by the eigenvector $\boldsymbol{e}_n$ to the smallest eigenvalue λ_n. Comparing this

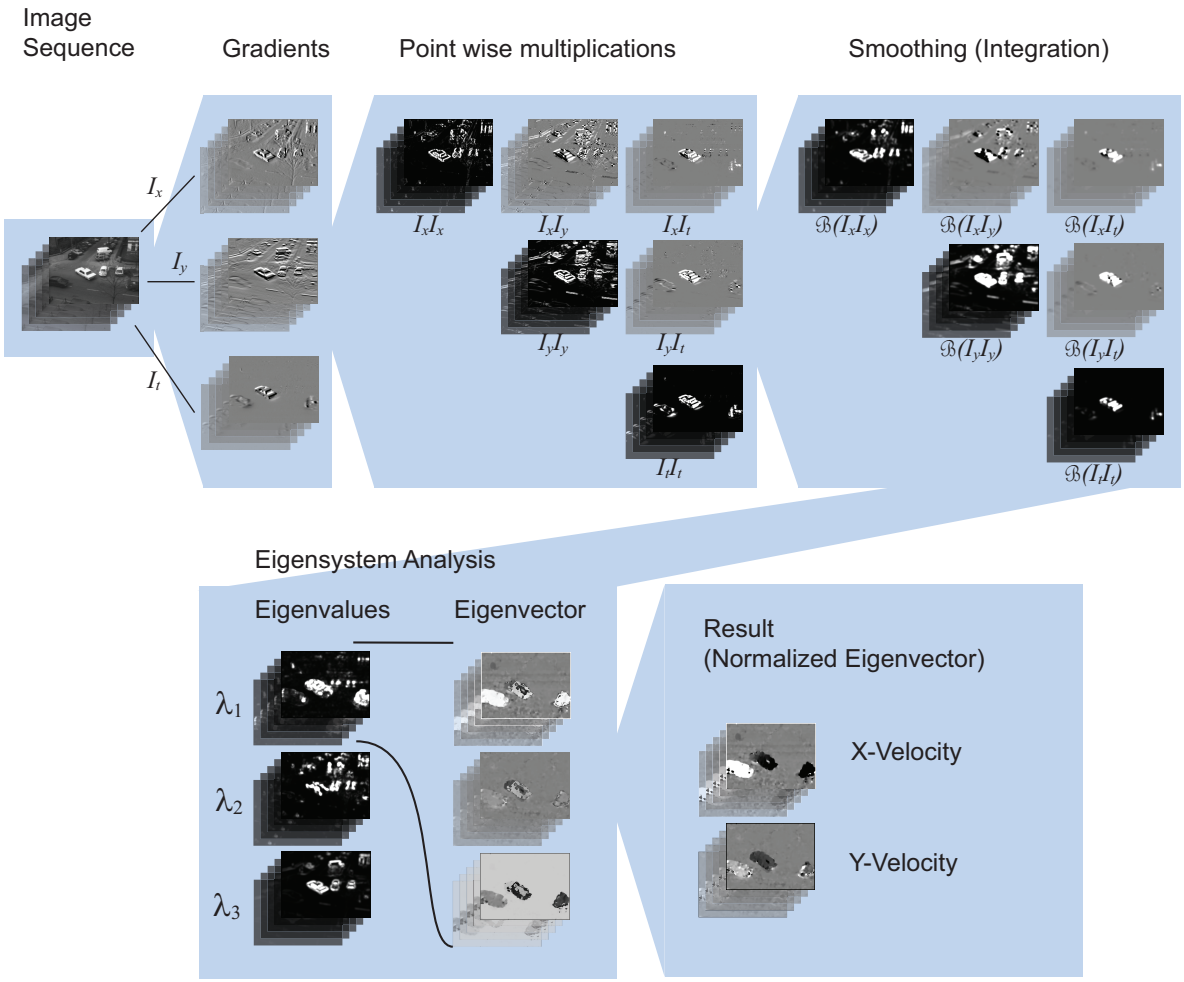

Figure 3.3: *The different steps for motion estimation from structure tensor.*

eigenvector to $\boldsymbol{w}$ from Equation (3.9) it becomes clear that the eigenvector has to be rescaled so that the last component is unity, thus

$$\boldsymbol{w} = \begin{bmatrix} \boldsymbol{u} \\ 1 \end{bmatrix} = \frac{\boldsymbol{e}_n}{e_{n,n}}. \tag{3.12}$$

This procedure of estimating motion from the structure tensor approach is sketched in Figure 3.3. This approach of solving the aperture problem in a local neighborhood is similar to parameter estimation in a total least squares sense (TLS) formulated from normal equations, as shall be detailed in Section 3.4.2.

The two presented approaches of solving the inverse problem of motion estimation from image sequences is only viable if enough intensity structure is present in the neighborhood. If for example all gradients are parallel to one another, still only the component of the optical flow in the direction of this gradient can be computed following Equation (3.2). This problem of the aperture problem on 1D directed structures was detailed in Section 3.2.1. It is important for optical flow computations to detect these regions where the aperture problem could not

be solved and treat the solution accordingly. By using the estimators based on the total least squares principle a measure for the aperture problem is available. Without enough intensity structure in the neighborhood the data matrix will be rank deficient and hence no unique solution can be found. In this case the non-generic solution can be estimated as outlined in Section 3.4.2. The analogy between the aperture problem in optical flow computations and the non-generic case in parameter estimation will become apparent later on. Different confidence and type measures of the motion estimates will be presented in Chapter 5. A very simple method is to analyze the eigenvalues and hence the rank of the tensor $\boldsymbol{J}$. Four cases can be discriminated:

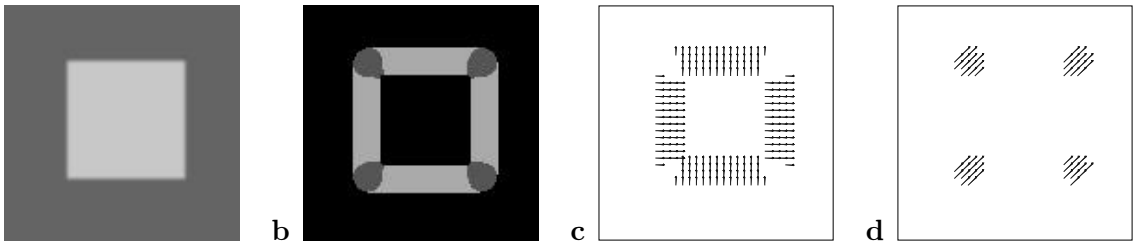

Figure 3.4: *Moving square example:* **a** *image data,* **b** *type of flow (black: trace to small, light grey: linear dependency and dark grey: full estimate possible),* **c** *normal flow and* **d** *full flow.*

$\text{rank}(\boldsymbol{J}) = 3$	$\lambda_1, \lambda_2, \lambda_1 \gg 0$	no coherent motion, estimation not possible
$\text{rank}(\boldsymbol{J}) = 2$	$\lambda_1, \lambda_2 \gg \lambda_1 \approx 0$	full motion can be estimated
$\text{rank}(\boldsymbol{J}) = 1$	$\lambda_1 \gg \lambda_2, \lambda_1 \approx 0$	aperture problem, computation of normal velocities
$\text{rank}(\boldsymbol{J}) = 0$	$1 \gg \lambda_1, \lambda_2, \lambda_1 \approx 0$	no gray value structures, no estimation possible

An example of this analysis is presented in Figure 3.4. The full flow can only be estimated at the corners, where $\text{rank}(\boldsymbol{J}) = 2$. On edges ($\text{rank}(\boldsymbol{J}) = 1$) only the normal component can be estimated. In the background, no greyvalue structuer is present, resulting in $\text{rank}(\boldsymbol{J}) = 0$.

The results for computing the optical flow from Equation (3.3) can be stabilized and made more accurate by not only considering a spatial neighborhood $w(\boldsymbol{x})$ but also taking temporal information into account and extending the weighting to the time domain $w(\boldsymbol{x}, t)$ [Jähne, 1993, 1997]. This is the approach chosen in this work to solve the problem of optical flow estimation.

Up to now only the most simple motion model of pure translation and constant brightness along the trajectory of the moving structure was considered. This is the model formulated in the BCCE of Equation (3.1). In Section 2 much more complex and realistic models of motion have been introduced. It was shown that all these models can be formulated in the same fashion as a vector product of a data and parameter term of the type

$$\boldsymbol{d}^\top \cdot \boldsymbol{p} = 0, \quad \text{with} \quad \boldsymbol{d}, \boldsymbol{p} \in \mathbb{R}^{p+1}. \tag{3.13}$$

Since the BCCE is just a special case of this formulation, it can be seen that here $\boldsymbol{w} \equiv \boldsymbol{p}$ and likewise this constraint can be pooled in a local spatio-temporal neighborhood, leading to

$$\boldsymbol{W}\boldsymbol{D} \cdot \boldsymbol{p} = 0, \quad \text{with} \quad \boldsymbol{D} \in \mathbb{R}^{m \times (p+1)}, \boldsymbol{W} \in \mathbb{R}^{m \times m} \text{ and } \boldsymbol{p} \in \mathbb{R}^{p+1}. \tag{3.14}$$

Here $\boldsymbol{W}$ denotes the weighting matrix.

Again, the quadratic form of this system of equations can be formulated, leading to the p-dimensional structure tensor

$$\boldsymbol{J} = \boldsymbol{D}^\top \boldsymbol{W}^\top \boldsymbol{W} \boldsymbol{D}, \quad \text{with} \quad \boldsymbol{J} \in \mathbb{R}^{(p+1)\times(p+1)}. \tag{3.15}$$

The parameter $\boldsymbol{p}$ can be estimated in the same fashion as shown for the two parameters of the BCCE. Again, an eigensystem analysis is performed and the parameter vector $\boldsymbol{p}$ is computed from the eigenvector $\boldsymbol{e}_n$ to the smallest eigenvalue λ_n. This shows, that the model best suited to the problem can freely be chosen in the spirit of Section 2. The correct choice of the motion model is of course essential for an accurate estimation of the motion field $\boldsymbol{u}$. This point is emphasized in an illustration of the result of different motion models. They are applied to image sequences of a Gaussian changing brightness according to diffusion and exponential decay which is presented in Figure 3.5.

It has been shown in both the Equations (3.3) and (3.9), that the estimation of motion in the tensor based approach leads to finding model parameters from an over-determined set of equations. In order to better understand advantages and disadvantages of the different techniques, the tensor based motion estimators will be embedded into a general parameter estimation framework. This will lead to finding unbiased estimators depending on the motion model used.

3.4 Parameter Estimation

In this section a general parameter estimation framework be the main focus. Depending on the motion model used, different estimators will lead to unbiased estimates. These estimators have been presented in great detail in Garbe [2001]. Therefore only a short account will be given here.

3.4.1 Ordinary Least Squares Parameter Estimation

Parameter estimation by means of ordinary least square (OLS) was introduced by *Euler* in the 18th century when he successfully predicted the movement of celestial bodies. It has been used extensively in many fields of sciences as well as in computer vision [Lawson and Hanson, 1974; Menke, 1989]. The p parameters $\boldsymbol{x}$ of the model are given as $\boldsymbol{x} = (x_1, x_2, \ldots, x_p)^\top$. The model will differ for the problem under consideration. It can generally be written as $b_i = a_{1i} \cdot x_1 + a_{2i} \cdot x_2 + \cdots + a_{pi} \cdot x_p$, where $i \in \{1, 2, \ldots, n\}$ represent n data points. In vector notation this set of equations can be formulated as $\boldsymbol{A}\boldsymbol{x} = \boldsymbol{b}$, relating the parameter vector $\boldsymbol{x} \in \mathbb{R}^p$ in the model and the observation vector $\boldsymbol{b} \in \mathbb{R}^n$. This type of model is commonly referred to as the *Gauss-Markoff model*, in which one assumes that the expected values of the observations $\boldsymbol{b}$ are linear combinations of the given coefficients $\boldsymbol{A}$ and the unknown parameters $\boldsymbol{x}$ [Koch, 1988].

In a least squares framework the sought parameter vector $\boldsymbol{x}^{\text{est}}$ solves the model Equation approximately, where the goodness of the approximation is defined by the residual $\text{res}(\boldsymbol{x})$ for

	constant	exponential	diffusion
constant	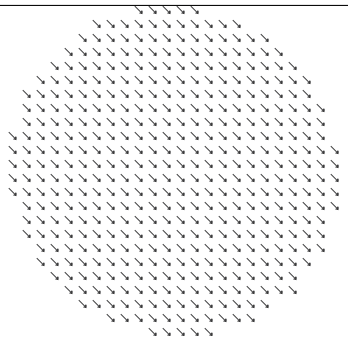	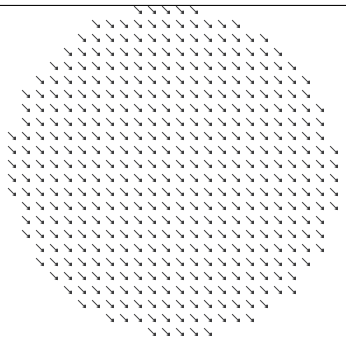	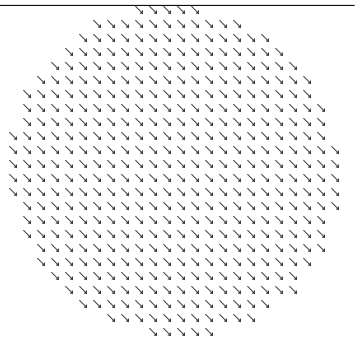
	$E_f = (6.5 \pm 7.9) \cdot 10^{-4}$ no brightness change	$E_f = (1.4 \pm 1.7) \cdot 10^{-2}$ $E_k = (6.7 \pm 8.2) \cdot 10^{-4}$	$E_f = (1.1 \pm 1.1) \cdot 10^{-3}$ $E_D = (4.8 \pm 5.9) \cdot 10^{-3}$
exponential	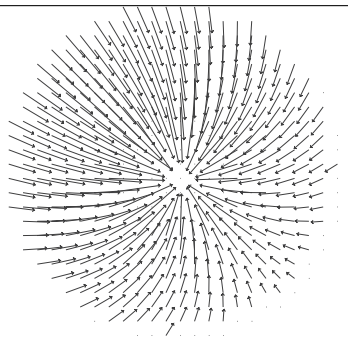	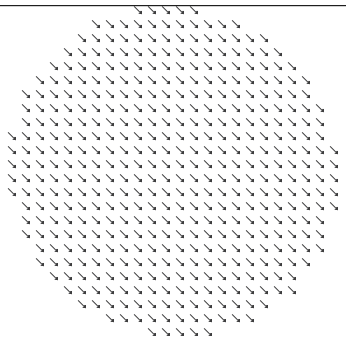	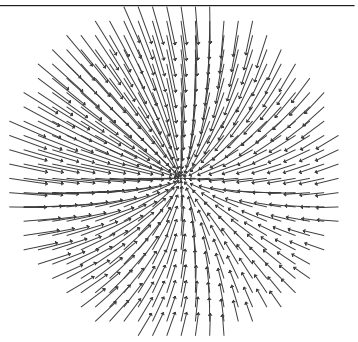
	$E_f = (4.7 \pm 2.6) \cdot 10^{1}$ no brightness change	$E_f = (3.7 \pm 3.3) \cdot 10^{-2}$ $E_k = (2.1 \pm 1.1) \cdot 10^{-1}$	$E_f = (1.9 \pm 1.0) \cdot 10^{1}$ $E_D = (5.3 \pm 0.9) \cdot 10^{4}$
diffusion	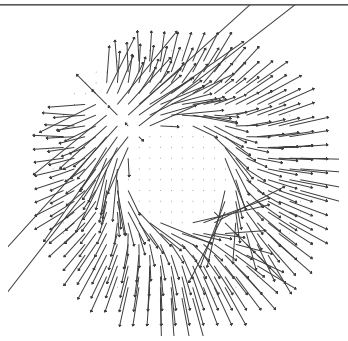	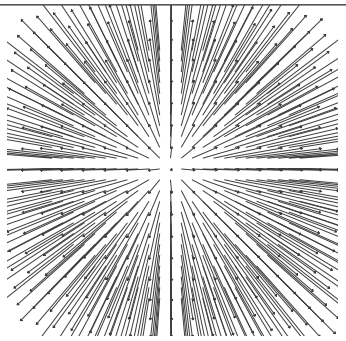	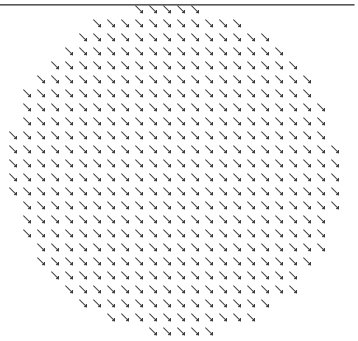
	$E_f = (0.5 \pm 1.2) \cdot 10^{3}$ no brightness change	$E_f = (5.8 \pm 1.5) \cdot 10^{2}$ $E_k = (1.0 \pm 0.0) \cdot 10^{2}$	$E_f = (1.2 \pm 0.5) \cdot 10^{-1}$ $E_D = (6.7 \pm 3.5) \cdot 10^{-2}$

Figure 3.5: *Results of different parameterized brightness constraint models (columns) used to estimate motion and brightness change parameters of test sequences (rows) with constant brightness, exponential decay, and diffusion, respectively. Every sequence is evaluated with all three models. Errors are given for the estimated optical flow field (E_f) and for the model parameters (exponential decay constant E_k, and diffusion constant E_D). All errors are relative errors (in per cent) and show the mean and standard deviation across an area thresholded by the confidence measure.*

the parameter vector $\boldsymbol{x}$ in the L_2 norm:

$$\text{res}(\boldsymbol{x}^{\text{est}}) = \boldsymbol{e}^\top \boldsymbol{e} = ||\boldsymbol{A}\boldsymbol{x}^{\text{est}} - \boldsymbol{b}||_2 = \left[\boldsymbol{A}\boldsymbol{x}^{\text{est}} - \boldsymbol{b}\right]^\top \left[\boldsymbol{A}\boldsymbol{x}^{\text{est}} - \boldsymbol{b}\right]. \tag{3.16}$$

The method of OLS is based on the premiss that the residual res defined in Equation (3.16) is at a minimum for the estimated parameter vector $\boldsymbol{x}^{\text{est}}$. This leads to the definition of the ordinary least squares problem:

Definition 1 *Given an over determined set of n linear Equations $\boldsymbol{A}\boldsymbol{x} = \boldsymbol{b}$ with $\boldsymbol{A} \in \mathbb{R}^{n\times p}$, $\boldsymbol{b} \in \mathbb{R}^n$ and the sought parameter vector $\boldsymbol{x} \in \mathbb{R}^p$. The OLS problem seeks to*

$$\begin{aligned} &\textit{minimize} \quad ||\boldsymbol{b} - \boldsymbol{b}^{\text{est}}||_2, \quad \textit{with} \quad \boldsymbol{b}, \boldsymbol{b}^{\text{est}} \in \mathbb{R}^n \\ &\textit{subject to} \quad \boldsymbol{b}^{\text{est}} \in \text{range}(\boldsymbol{A}). \end{aligned} \tag{3.17}$$

Any minimizing $\boldsymbol{x}^{\text{est}}$ is called a linear ordinary least squares solution of the set $\boldsymbol{A}\boldsymbol{x} \approx \boldsymbol{b}$.

The *range* of a matrix $\boldsymbol{A}$ is defined as the subspace given by [Golub and van Loan, 1996]:

$$\text{range}(\boldsymbol{A}) = \left\{\boldsymbol{y} \in \mathbb{R}^n, \boldsymbol{A} \in \mathbb{R}^{n\times p} : \boldsymbol{y} = \boldsymbol{A}\boldsymbol{x} \text{ for some } \boldsymbol{x} \in \mathbb{R}^p\right\}. \tag{3.18}$$

It is known from elementary calculus that the minimum of a function is found by setting its derivatives with respect to the parameters to zero and solving the resulting equations. Performing these calculations for Equation (3.16) results in $\boldsymbol{A}^\top\boldsymbol{A}\boldsymbol{x} - \boldsymbol{A}^\top\boldsymbol{b} = 0$. Assuming that $\left(\boldsymbol{A}^\top\boldsymbol{A}\right)^{-1}$ exists, the sought OLS solution of the problem $\boldsymbol{A}\boldsymbol{x} = \boldsymbol{b}$ is then given by

$$\boldsymbol{x}^{\text{est}} = \left(\boldsymbol{A}^\top\boldsymbol{A}\right)^{-1}\boldsymbol{A}^\top\boldsymbol{b}. \tag{3.19}$$

In the literature the matrix $(\boldsymbol{A}^\top\boldsymbol{A})^{-1}\boldsymbol{A}^\top$ is commonly referred to as the *Moore-Penrose* Inverse [Koch, 1988; Groetsch, 1993].

Gauss [1823] showed that the OLS estimate $\boldsymbol{x}$ has the smallest variance in the class of estimation methods, which display no systematic errors in the estimates (no bias) and whose estimates are linear functions of $\boldsymbol{b}$.

Apart from the estimated parameter vector $\boldsymbol{x}^{\text{est}}$ another important entity of characterizing the model and its estimation is the covariance matrix Σ. The covariance matrix Σ (also known as the variance-covariance or dispersion matrix) is defined as [Mardia et al., 1979]

$$\Sigma = \left\langle \left(\boldsymbol{x} - \langle\boldsymbol{x}\rangle\right)\left(\boldsymbol{x} - \langle\boldsymbol{x}\rangle\right)^\top \right\rangle, \tag{3.20}$$

where $\langle\cdots\rangle$ denotes the expectation value, that is

$$\langle x_i\rangle = \int_\infty^\infty x_i p(\boldsymbol{x})\mathrm{d}\boldsymbol{x} \quad \text{with} \quad i = 1, \ldots, p, \tag{3.21}$$

where $p(\boldsymbol{x})$ is the probability density function of $\boldsymbol{x}$. From this definition follows, that for a linear system of Equations $\boldsymbol{b} = \boldsymbol{A}\boldsymbol{x} + \boldsymbol{v}$ the covariance matrix Σ can be computed as [Koch, 1988]

$$\Sigma(\boldsymbol{b}) = \boldsymbol{A}\ \Sigma(\boldsymbol{x})\ \boldsymbol{A}^\top. \tag{3.22}$$

Intuitively this equation is straight forward to understand as a linear system of equations can be thought of as a transformation between coordinate systems. The same transformation must then be applied to the covariance matrix as well, which is given by Equation (3.22).

The covariance matrix for the OLS estimator can then be derived by considering the expression for the estimated parameter $\boldsymbol{p}$ from Equation (3.19), that is

$$\Sigma(\boldsymbol{x}) = \sigma_b^2 \left(\boldsymbol{A}^\top \boldsymbol{A} \right)^{-1}. \tag{3.23}$$

The use of OLS in digital image processing applications has the major advantage that it can be interpreted as a linear shift-invariant filter (LSI) [Jähne, 1999]. This allows for the implementation to rely on common digital image processing techniques and thus enables for a very fast estimation of the parameters.

3.4.2 Total Least Squares

Although the term 'Total Least Squares' appeared only recently [Golub and van Loan, 1980] this method of parameter estimation is not new and is known in statistical literature under the term *orthogonal regression* or *errors-in-variables regression*. The univariate line fitting problem ($\alpha + a \cdot x = b$) already appeared in the 19th century [Adcock, 1878]. Assuming that the errors of the observations are independently and identically distributed with zero mean and covariance matrix $\sigma \mathbb{1}$, it can be proven that the TLS solution estimates the true parameter values $\boldsymbol{p}$ consistently [Gallo, 1982; Gleser, 1981]. This means that the estimated parameter vector $\boldsymbol{p}^{\text{est}}$ converges to the true vector $\boldsymbol{p}$ as the number of observations n tends to infinity. Furthermore it can be shown that this property of TLS estimates does not depend on any assumed distribution of the errors. This strongly contrasts the behavior of OLS estimates which are inconsistent in the presence of non Gaussian noise [Gelb, 1974]. Although there exists a formal equivalence between OLS and TLS [Lemmerling et al., 1998], one should not confuse the two estimates as both will lead to different solutions. A geometric interpretation of the two estimators will be presented in Section 3.4.3.

The underlying assumption in OLS is that the errors only occur in the vector $\boldsymbol{b}$ and that the matrix $\boldsymbol{A}$ is exactly known (see Section 3.4.1). While for some application this prerequisite may hold, in a number of scientific applications and especially digital image processing the data matrix $\boldsymbol{A}$ is also effected by measurement or sampling errors. These errors are taken into account by perturbing not only $\boldsymbol{b}$ but $\boldsymbol{A}$ as well and formulating the TLS problem:

Definition 2 *Given an over determined set of n linear equations $\boldsymbol{A}\boldsymbol{x} = \boldsymbol{b}$ with $\boldsymbol{A} \in \mathbb{R}^{n \times p}$, $\boldsymbol{b} \in \mathbb{R}^n$ and the sought parameter vector $\boldsymbol{x} \in \mathbb{R}^p$. In the TLS problem it is then tried to*

$$\begin{aligned} &\textit{minimize} \quad || \, [\boldsymbol{A}, \boldsymbol{b}] - \left[\tilde{\boldsymbol{A}}, \tilde{\boldsymbol{b}}\right] \, ||_F, \quad \left[\tilde{\boldsymbol{A}}, \tilde{\boldsymbol{b}}\right] \in \mathbb{R}^{n \times (p+1)} \\ &\textit{subject to} \quad \tilde{\boldsymbol{b}} \in \text{range}(\tilde{\boldsymbol{A}}). \end{aligned} \tag{3.24}$$

Any $\boldsymbol{x}$ satisfying $\tilde{\boldsymbol{A}}\boldsymbol{x} = \tilde{\boldsymbol{b}}$ is called a solution to the TLS problem for a minimizing $[\tilde{\boldsymbol{A}}, \tilde{\boldsymbol{b}}]$.

In the above definition $||\cdot||_F$ denotes the Frobenius norm, that is $||\boldsymbol{A}||_F = \sqrt{\sum_i \sum_j |a_{ij}|^2}$. The range of a matrix $\boldsymbol{A}$ was defined in Section 3.4.1. The TLS problem can be reduced to a singular value analysis due to the *Eckart-Young-Mirsky matrix approximation theorem* which can be stated as follows [Van Huffel and Vandewalle, 1991]:

Theorem 1 *Given a matrix $\boldsymbol{A} \in \mathbb{R}^{n\times p}$ with its singular value decomposition $\boldsymbol{A} = \sum_{i=1}^{r} \lambda_i \boldsymbol{u}_i \boldsymbol{v}_i^\top$, $r = \text{rank}(\boldsymbol{A})$ and a matrix $\boldsymbol{B} \in \mathbb{R}^{n\times p}$ with $k = \text{rank}(\boldsymbol{B})$. If $k < r$, $\boldsymbol{A}_k = \sum_{i=1}^{k} \lambda_i \boldsymbol{u}_i \boldsymbol{v}_i^\top$ it can be shown that*

$$\min \quad ||\boldsymbol{A} - \boldsymbol{B}||_F = ||\boldsymbol{A} - \boldsymbol{A}_k||_F = \sqrt{\sum_{i=k+1}^{p} \lambda_i^2}, \quad p = \min\{n, p\}, \tag{3.25}$$

and

$$\min \quad ||\boldsymbol{A} - \boldsymbol{B}||_2 = ||\boldsymbol{A} - \boldsymbol{A}_k||_2 = \lambda_{k+1}. \tag{3.26}$$

The reader is referred to Eckhart and Young [1936] and Mirsky [1960] for the proof of this theorem.

The connection between the TLS problem and the Eckhart-Young-Mirsky theorem from Equation (3.25) comes about by writing the set of n linear equation in the form

$$[\boldsymbol{A}, \boldsymbol{b}] \begin{bmatrix} \boldsymbol{x} \\ -1 \end{bmatrix} = 0, \tag{3.27}$$

and thus embedding the space spanned by the matrix $\boldsymbol{A}$ in the one spanned by $[\boldsymbol{A}, \boldsymbol{b}]$. The SVD of $[\boldsymbol{A}, \boldsymbol{b}]$ is given by $[\boldsymbol{A}, \boldsymbol{b}] = \boldsymbol{U}\Lambda\boldsymbol{V}$ with $\Lambda = \text{diag}(\lambda_1, \ldots, \lambda_{n+1})$. If $\lambda_{n+1} \neq 0$, then $\text{rank}[\boldsymbol{A}, \boldsymbol{b}] = n + 1$. Consequently, the space $\mathcal{S}$ generated by the rows of $[\boldsymbol{A}, \boldsymbol{b}]$ is $\mathcal{S} \in \mathbb{R}^{n+1}$. All solutions to the TLS problem lie in the null space $\mathcal{N}$ orthogonal to the space $\mathcal{S}$. The set of Equations (3.27) is incompatible and for a solution of the TLS problem to be found, the rank of $[\boldsymbol{A}, \boldsymbol{b}]$ has to be reduced to $\text{rank}[\boldsymbol{A}, \boldsymbol{b}] = n$ which results in a one dimensional space $\mathcal{N}$. Using the Eckhart-Young-Mirsky theorem the best rank n approximation $[\tilde{\boldsymbol{A}}, \tilde{\boldsymbol{b}}]$ of $[\boldsymbol{A}, \boldsymbol{b}]$ is given by $[\tilde{\boldsymbol{A}}, \tilde{\boldsymbol{b}}] = \boldsymbol{U}\tilde{\Lambda}\boldsymbol{V} = \sum_{i=1}^{n+1} \lambda_i \boldsymbol{u}_i \boldsymbol{v}_i^\top$ with $\tilde{\Lambda} = \text{diag}(\lambda_1, \ldots, \lambda_n, \lambda_{n+1})$ and the singular values $\lambda_1 > \lambda_2 > \cdots > \lambda_n > \lambda_{n+1} \approx 0$. The TLS problem in Equation (3.24) can thus be written as

$$\begin{array}{lllll} \min & ||\,[\boldsymbol{A}, \boldsymbol{b}] - \left[\tilde{\boldsymbol{A}}, \tilde{\boldsymbol{b}}\right]||_F & = & \lambda_{n+1}, \quad \text{with} \quad \text{rank}\left[\tilde{\boldsymbol{A}}, \tilde{\boldsymbol{b}}\right] = n \\ \text{and} & [\boldsymbol{A}, \boldsymbol{b}] - \left[\tilde{\boldsymbol{A}}, \tilde{\boldsymbol{b}}\right] & = & \lambda_{n+1}\boldsymbol{u}_{n+1}\boldsymbol{v}_{n+1}^\top. \end{array} \tag{3.28}$$

The approximate equation $\left[\tilde{\boldsymbol{A}}, \tilde{\boldsymbol{b}}\right] \left[\boldsymbol{x}^\top, -1\right]^\top$ is now compatible with the solution given by the one-dimensional space $\mathcal{N}$ orthogonal to $\mathcal{S}$, spanned by $\boldsymbol{v}_{n+1}$. The TLS solution is then obtained by scaling $\boldsymbol{v}_{n+1}$ so that its last component is -1, that is

$$\begin{bmatrix} \boldsymbol{x} \\ -1 \end{bmatrix} = -\frac{1}{\boldsymbol{v}_{n+1,n+1}} \boldsymbol{v}_{n+1}, \quad \text{for} \quad \boldsymbol{v}_{n+1,n+1} \neq 0. \tag{3.29}$$

In case that $\boldsymbol{v}_{n+1,n+1} = 0$ the above procedure cannot be conducted. However, this does not pose any limitation, as $\boldsymbol{v}_{n+1,n+1} = 0$ means that $[\boldsymbol{A}, \boldsymbol{b}]$ is of rank n already and the vector $\boldsymbol{v}_{n+1}$ is in the space $\mathcal{N}$. The solution is said to be *non-generic* as the space $\mathcal{N}$ is m-dimensional with $m > 1$. This case will be treated in the next section. It can be shown that there exists one unique solution to the TLS problem given by equation (3.29) if and only if $[\boldsymbol{A}, \boldsymbol{b}]$ has full column rank [Van Huffel and Vandewalle, 1991].

The basic principle in the TLS problem is then, that the noisy data matrix $\boldsymbol{D} = [\boldsymbol{A}, \boldsymbol{b}]$ is modified with minimal effort into a matrix $\tilde{\boldsymbol{D}} = [\tilde{\boldsymbol{A}}, \tilde{\boldsymbol{b}}]$ that is close to the original matrix in the Frobenius norm. The approximated matrix is rank-deficient so that its columns are linearly related. In this approach all the data are modified in contrast to the OLS approach where only one column of $\boldsymbol{D} = [\boldsymbol{A}, \boldsymbol{b}]$ is modified.

Solution of the Non-generic Total Least Squares Problem

In the previous section it was shown that there exists a unique solution to the TLS problem only if $\boldsymbol{v}_{p+1,p+1} \neq 0$. However, this may not always be the case and the problem is said to be non-generic [Van Huffel and Vandewalle, 1988]. When trying to find a solution to the non-generic TLS problem one has to distinguish between two cases:

1. The set of equations is highly conflicting and thus $\lambda_n \approx \lambda_{n+1} \gg 0$.
2. The matrix $\boldsymbol{A}$ is rank deficient and thus $\lambda_1 > \lambda_2 > \cdots > \lambda_k \approx \cdots \approx \lambda_{p+1} \approx 0$, with $k < p$.

The case 1 can easily be detected by introducing a threshold on the smallest singular value for which $\boldsymbol{v}_{p+1,p+1} \neq 0$. If this singular value is large it can be concluded that the data are not sufficiently closely approximated by the model assumption in which case either the model needs to be refined or, where this is not possible, the problem can be rejected as irrelevant from the linear modeling point of view.

Much more interesting in the context of this work is the case 2. It is analogous to the aperture problem in optical flow computations that was introduced in Section 3.2.1. As the space $\mathcal{N}$ is of dimension higher than one, all linear combinations of the vectors spanning this space are solutions to the TLS problem. In terms of stability and minimal sensitivity the only sensible solution to the TLS problem will be that solution with minimal norm. It can be shown that the solution, that is minimal in the L_2 norm, is also minimal in the Frobenius norm [Van Huffel and Vandewalle, 1991]. The minimum norm TLS solution can then be formulated as follows [Van Huffel, 1992]:

Definition 3 *Given* $(\boldsymbol{A}, \boldsymbol{b})$ *with the SVD* $(\boldsymbol{A}, \boldsymbol{b}) = \sum_{i=1}^{p+1} \lambda_i \boldsymbol{u}_i \boldsymbol{v}_i^\top$ *and assuming* $\lambda_k > \lambda_{k+1} \approx \cdots \approx \lambda_{p+1}$ *with* $k \leq p$. *If not all* $\boldsymbol{v}_{p+1,i} = 0$, $i = k+1, \ldots, p+1$, *then the minimum norm TLS solution* $\tilde{\boldsymbol{x}}$ *is given by*

$$\tilde{\boldsymbol{x}} = -\frac{\sum_{i=k+1}^{p+1} \boldsymbol{v}_{p+1,i} \cdot [\boldsymbol{v}_{1,i}, \ldots \boldsymbol{v}_{p,i}]^\top}{\sum_{i=k+1}^{p+1} \boldsymbol{v}_{p+1,i}^2} = -\frac{\sum_{i=1}^{k} \boldsymbol{v}_{p+1,i} \cdot [\boldsymbol{v}_{1,i}, \ldots \boldsymbol{v}_{p,i}]^\top}{1 - \sum_{i=1}^{k} \boldsymbol{v}_{p+1,i}^2}. \tag{3.30}$$

Thus, the solution can be expressed as a linear combination of the "reduced" eigenvectors $\hat{\boldsymbol{b}}_k = \frac{1}{1-\sum_{i=1}^{k} \boldsymbol{v}_{p+1,i}^2} [\boldsymbol{v}_{1,1}, \dots \boldsymbol{v}_{p,k}]^\top$. The validity of this minimum norm solution to optical flow estimations is shown in Spies et al. [2002a, 2003], while the reader is referred to Van Huffel and Vandewalle [1988] and Van Huffel and Vandewalle [1991] for a proof of the minimum norm solution given in Equation (3.30). The results obtained in this section for the minimum norm solution to the TLS problem also hold true for the OLS problem and can be applied without any modifications [Wei, 1992].

TLS Estimates from Normal Equations

As stated before the key difference between TLS and OLS is that in TLS all the elements in the noisy data matrix $\boldsymbol{D} = (\boldsymbol{A}, \boldsymbol{b})$ are modified. This contrasts the OLS problem in which only one column of $\boldsymbol{D} = (\boldsymbol{A}, \boldsymbol{b})$ is modified.

This property of the TLS problem can of course not only be stated as previously in Equation (3.24). Other formulations can be used of which especially the formulation of normal equations is commonly used in computer vision and referred to as the structure tensor [Bigün and Granlund, 1987; Haußecker et al., 1999]. This formulation of the TLS problem is also known as the orthogonal L_2 approximation problem [Van Huffel and Vandewalle, 1991] which can be stated as follows:

Definition 4 *Given a data matrix $\boldsymbol{D} \in \mathbb{R}^{n \times (p+1)}$. We then seek to*

$$\begin{aligned} &\textit{minimize} && ||\boldsymbol{e}|| = ||\boldsymbol{D}\boldsymbol{p}||_2, \quad \boldsymbol{p} \in \mathbb{R}^p \\ &\textit{subject to} && \boldsymbol{p}^\top \boldsymbol{p} = 1, \end{aligned} \tag{3.31}$$

with the vector of residuals $\boldsymbol{e} = \boldsymbol{D}\boldsymbol{p}$. The constraint has to be posed on the parameter vector $\boldsymbol{p}$ to avoid the trivial solution $\boldsymbol{p} = 0$.

The orthogonal L_2 approximation problem in Equation (3.31), incorporating the constraint, can be solved by means of a Lagrange multiplier, minimizing

$$\boldsymbol{f} = \arg\min L(\boldsymbol{p}, \lambda), \quad L(\boldsymbol{p}, \lambda) = \boldsymbol{p}^\top \boldsymbol{J} \boldsymbol{p} + \lambda \left(1 - \boldsymbol{p}^\top \boldsymbol{p}\right), \quad \text{with} \quad \boldsymbol{J} = \boldsymbol{D}^\top \boldsymbol{D}, \tag{3.32}$$

where $\boldsymbol{J} \in \mathbb{R}^{p \times p}$. The functional $L(\boldsymbol{p}, \lambda)$ is minimized, when the partial derivatives with respect to all parameters are equal to zero, that is

$$\frac{\partial L(\boldsymbol{p}, \lambda)}{\partial p_i} = 2 \sum_{k=1}^{p} J_{ik} p_k - 2\lambda p_i = 0, \quad i \in \{1, 2, ..., p\}. \tag{3.33}$$

This system of Equations can be written in vector form, leading to

$$\boldsymbol{J}\boldsymbol{p} = \lambda \boldsymbol{p}. \tag{3.34}$$

Therefore, the solution to the minimization problem of Equation (3.31) is reduced to an eigenvalue problem of the symmetric matrix $\boldsymbol{J}$, as can be shown by use of Equation (3.34):

$$\min ||\boldsymbol{D}\boldsymbol{p}||_2 = \boldsymbol{p}^\top \boldsymbol{J} \boldsymbol{p} = \boldsymbol{p}^\top \lambda \boldsymbol{p} = \lambda. \tag{3.35}$$

Consequently, the eigenvector $\boldsymbol{e}_n$ to the smallest eigenvalue λ_n of $\boldsymbol{J}$ is the sought after solution to this minimization problem.

The appeal of this formulation of the TLS problem is its equivalences in classical mechanics as the *moment of inertia tensor* [Goldstein, 1980; Landau and Lifschitz, 1990] or in digital image processing as the structural tensor [Bigün et al., 1991] in orientation analysis. Here the eigenvalue analysis represents a rotation of the tensor along its axis of smallest inertia or along its predominant texture. In this context the parameter estimation can be thought of as an orientation analysis, which offers an intuitive interpretation in optical flow computations as has been shown in Section 3.3.

For the eigenvalue analysis Jacobi transformations of symmetric matrices [Press et al., 1992] can be employed. This method has the advantage of being very simple and foolproof. Performance wise it is not competitive with the symmetric QR algorithm, even though it converges quadratically. The poorer performance is noticeable for matrices of order greater than about 10 [Press et al., 1992], which is not that common in optical flow computations. Much more efficient algorithms will be presented in Chapter 4, that allow to perform these optical flow computations in real time.

Weighted Total Least Squares

In the formulation of the TLS problem from the previous sections the rows in the data matrix were treated equal. This may not always be beneficial. In optical flow computations the observations are weighted differently depending on their relative location in a local neighborhood (see Section 3.3). When working with the robust estimators such as M-estimators [Huber, 1981], the observations must be weighted according to a weight function of their residuals. Guillaurne et al. [1998] weight the observations differently to derive an estimator for linear time-invariant multivariable systems with maximum likelihood estimators. All these shortcomings in the previous formulation of the TLS problem call for an extension thereof, called weighted total least squares (WTLS). It can be formulated as follows:

Definition 5 *Given an over determined set of n linear Equations* $\boldsymbol{A}\boldsymbol{x} = \boldsymbol{b}$ *with* $\boldsymbol{A} \in \mathbb{R}^{n\times p}$, $\boldsymbol{b} \in \mathbb{R}^n$ *and a parameter vector* $\boldsymbol{x} \in \mathbb{R}^p$ *as well as a weight matrix* $\boldsymbol{W} \in \mathbb{R}^{n\times n}$. *In the WTLS problem it is then tried to*

$$\begin{aligned} \textit{minimize} \quad & || \left(\boldsymbol{W}[\boldsymbol{A}, \boldsymbol{b}]\right) - \left(\boldsymbol{W}[\tilde{\boldsymbol{A}}, \tilde{\boldsymbol{b}}]\right) ||_F, \\ \textit{with} \quad & \left[\tilde{\boldsymbol{A}}, \tilde{\boldsymbol{b}}\right] \in \mathbb{R}^{n\times(p+1)},\ \boldsymbol{W} = \operatorname{diag}(w_1, \ldots, w_n), \\ \textit{subject to} \quad & \tilde{\boldsymbol{b}} \in \operatorname{range}(\tilde{\boldsymbol{A}}). \end{aligned} \tag{3.36}$$

When comparing the WTLS problem with the TLS problem of Equation (3.24) it becomes apparent, that the TLS is just a special case of the WTLS with the weighting matrix $\boldsymbol{W} = \mathbb{1}$. Therefore, one can write $\boldsymbol{A}' \leftarrow \boldsymbol{W}\boldsymbol{A}$ and $\boldsymbol{b}' \leftarrow \boldsymbol{W}\boldsymbol{b}$ and use the transformed matrix $[\boldsymbol{A}', \boldsymbol{b}']$ instead of $[\boldsymbol{A}, \boldsymbol{b}]$ in the TLS problem of Section 3.4.2. All the results, limitations and algorithms derived for the TLS problem can thus be readily transferred to the WTLS problem.

Implementation of the TLS Estimator

In this section the actual implementation used for the TLS estimator in the context of this work is outlined. Basically two distinct implementations are conceivable. The difference in between them depends by large on the formulation of the TLS problem in terms of a matrix approximation or normal equations and the subsequent singular value or eigenvalue analysis respectively. In the formulation of normal equation an eigenvalue analysis on a symmetric square matrix $\boldsymbol{J} = \boldsymbol{D}^\top \boldsymbol{D}$ has to be performed where the method of choice are Jacobi rotations [Press et al., 1992]. For the matrix approximation formulation a singular value analysis in terms of a singular value decomposition (SVD) has to be performed. For a comprehensive overview of developments in the field of SVD the reader is referred to van der Vorst and Golub [1997].

The main disadvantage of the formulation of orthogonal equations and an subsequent eigenvalue analysis is concerned with the forming of the matrix $\boldsymbol{J}$ by an outer product. Due to this outer product information is lost when calculating $\boldsymbol{D}^\top \boldsymbol{D}$ due to roundoff errors, which may be quite significant when combining entities of different magnitude [Björck, 1990]. Also, small perturbations in the outer product have a much more dominant effect on the solution than perturbations of the same size in the matrix $\boldsymbol{D}$. A more thorough perturbation analysis shows that normal equation solution depends on the square of the condition number of $\boldsymbol{D}$. This condition number κ of a matrix $\boldsymbol{A}$ is defined as

$$\kappa(\boldsymbol{A}) = ||\boldsymbol{A}||_2 \cdot ||\boldsymbol{A}^I||_2 = \lambda_1/\lambda_r \ , \tag{3.37}$$

where the pseudoinverse is termed as $\boldsymbol{A}^I$, the biggest singular value is given by λ_1 and the smallest one by λ_r respectively. It follows that the condition number $\kappa(\boldsymbol{A}) = \infty$ for singular matrices $\boldsymbol{A}$. If $\kappa(A)$ is large, then $\boldsymbol{A}$ is said to be an ill-conditioned matrix.

Although the cyclic Jacobi method converges quadratically [Golub and van Loan, 1996], it is not competitive with the symmetric QR algorithm. The big advantage of the Jacobi rotations is, that it can compute the eigenvalues with a smaller relative error if $\boldsymbol{J}$ is positive definite [Demmel and Veseliç, 1992]. In the context of this work the relative error of the eigenvalues is not that crucial however, as generally only the eigenvectors to the smallest eigenvalue make up the solution parameter vector. An efficient real time solution to the eigensystem analysis, based on the formulation of normal equations will be presented in Chapter 4.

3.4.3 Geometric Interpretation

The key difference between the OLS and TLS estimators is best illustrated geometrically. From the formulation of the TLS problem $(\boldsymbol{A}, \boldsymbol{b})(\boldsymbol{x}^\top, -1)^\top = \boldsymbol{D}\boldsymbol{p} = 0$ it is straight forward to verify that the solution to Equation (3.31) is given by

$$\frac{||\boldsymbol{D}\boldsymbol{p}||_2}{||\boldsymbol{p}||_2} = \sum_{i=1}^{n} \frac{\left(\boldsymbol{a}_i^\top \boldsymbol{x} - b_i\right)^2}{\boldsymbol{x}^\top \boldsymbol{x} + 1} = \lambda_{p+1}, \tag{3.38}$$

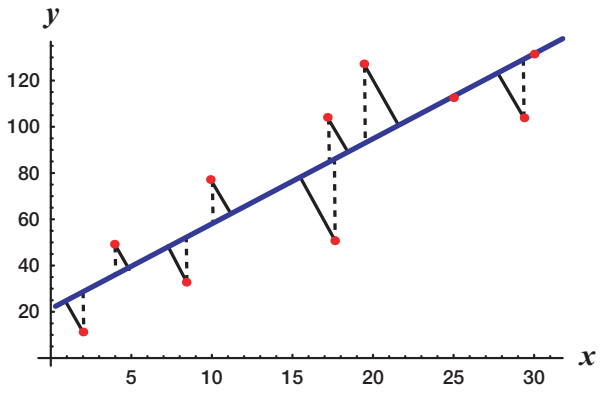

Figure 3.6: *The geometric interpretation of OLS versus TLS. The TLS tries to find the closest subspace $\mathcal{P}_x$ to the data points which is equivalent to minimizing the orthogonal distances (solid lines), whereas OLS tries to minimize the vertical distances (dotted lines).*

where $\boldsymbol{a}_i^\top = [a_{i,1}, \ldots, a_{i,p}]$ is the ith row of $\boldsymbol{A}$. It can be derived quite easily from basic linear algebra that the quantity

$$\frac{\left(\boldsymbol{a}_i^\top \boldsymbol{x} - b_i\right)^2}{\boldsymbol{x}^\top \boldsymbol{x} + 1} \tag{3.39}$$

is the square of the distance from $(\boldsymbol{a}_i^\top, \boldsymbol{b})^\top \in \mathbb{R}^{p+1}$ to the nearest point in the hyperplane $\mathcal{P}_x$ defined by

$$\mathcal{P}_x = \left\{ \left[\begin{array}{c} \boldsymbol{a} \\ b \end{array} \right] \middle| \boldsymbol{a} \in \mathbb{R}^p, b \in \mathbb{R}, b = \boldsymbol{x}^\top \boldsymbol{a} \right\}. \tag{3.40}$$

Thus from Equation (3.38) the TLS solution can be interpreted as minimizing the sum of squared orthogonal distances from n observations to the hyperplane $\mathcal{P}_x$. This is in contrast to the OLS estimator, which only tries to minimize the sum of squared vertical distances by minimizing $||\boldsymbol{b} - \boldsymbol{b}^{\text{est}}||_2$ (see Equation 3.17), which is illustrated in Figure 3.6.

3.4.4 Mixing Least Squares and Total Least Squares

In Section 3.4.2 it was stated that the estimated parameter vector $\boldsymbol{p}^{\text{est}}$ converges to the true vector $\boldsymbol{p}$ in the case of independently and identically distributed errors in the observations. That means that all observations should have the same standard deviation σ, which can be achieved by scaling the data accordingly [Mühlich and Mester, 1999; Mester and Mühlich, 2001]. However, there are instances when one column in the data matrix is known *exactly*, that it is not subject to any errors. This is the case in intercept models of the form

$$c + a_1 x_1 + \cdots + a_m x_m = b. \tag{3.41}$$

Such a model gives rise to an overdetermined set of equations of the form

$$[1_N; \boldsymbol{A}] \left[\begin{array}{c} c \\ \boldsymbol{x} \end{array} \right] = b, \tag{3.42}$$

where 1_N is first column of the data matrix that is exactly known ($1_N = [1, \ldots, 1]^\top$).

The accuracy of the estimated parameters can be maximized by requiring that the exactly known columns in the data matrix be unperturbed [Van Huffel and Vandewalle, 1991; Björck, 1990]. This can be achieved by reformulating the TLS problem in a more general form by mixing OLS and TLS:

Definition 6 *Given a set of n linear Equations with p unknown parameters* $\boldsymbol{x}$

$$[\boldsymbol{A}_1, \boldsymbol{A}_2]\, \boldsymbol{x} = \boldsymbol{b}, \quad \text{with} \quad \boldsymbol{A}_1 \in \mathbb{R}^{n \times p_1}, \boldsymbol{A}_2 \in \mathbb{R}^{n \times p_2}, \boldsymbol{x} \in \mathbb{R}^p, \boldsymbol{b} \in \mathbb{R}^n, \tag{3.43}$$

and $p_1 + p_2 = p$. *The mixed OLS-TLS problem then seeks to minimize*

$$\begin{aligned} \min \quad & \left([\boldsymbol{A}_2, \boldsymbol{b}]\, \boldsymbol{p}_2\right)^2 \\ \textit{subject to} \quad & [\boldsymbol{A}_1, \boldsymbol{A}_2]\, \boldsymbol{x} = \boldsymbol{A}_1 \boldsymbol{x}_1 + \boldsymbol{A}_2 \boldsymbol{x}_2 = \boldsymbol{b}, \end{aligned} \tag{3.44}$$

where $\boldsymbol{p} = \left[\boldsymbol{x}^\top, -1\right]^\top$, $\boldsymbol{p}_2 = \left[\boldsymbol{x}_2^\top, -1\right]^\top$ *and* $\boldsymbol{x} = \left[\boldsymbol{x}_1^\top, \boldsymbol{x}_2^\top\right]^\top$.

In the specific example of Equation (3.41) $p_1 = 1$ and $p_2 = m$, Equation (3.44) can thus be depicted as first finding a TLS solution on the reduced subspace of erroneous observations and then choosing from this set the one solution that solves the Equations of unperturbed data exactly. The implementation of this estimator and performance improvements are detailed in Section 4.3.1.

In the event of all observations $\boldsymbol{A}$ being known exactly, the OLS-TLS solution reduces to the OLS solution, while at the other extreme of only erroneous data the problem reduces to the TLS problem. By varying p_1 from zero to p the formulation of equation (3.44) can thus handle OLS, TLS or any mixtures of the two.

3.5 Regularization of Parameter

In the previous section the ill posed problem of motion estimation from image sequences was solved in the spirit of Lucas and Kanade [1981]. Assuming that the parameters of the motion model are locally smooth, an overdetermined system was derived by pooling the constraints in a local neighborhood. The smoothness of parameters can also be formulated globally on the image sequence. Generally, this global smoothness constraint is formulated continuously in a variational framework. The estimation of motion was formulated by Horn and Schunk [1981] as

$$\int_D \left((\boldsymbol{\nabla} I \cdot \boldsymbol{u} + I_t)^2 + \lambda^2 \left(\boldsymbol{\nabla} \boldsymbol{u}\right)^\top \left(\boldsymbol{\nabla} \boldsymbol{u}\right) \right) \mathrm{d}\boldsymbol{x}, \tag{3.45}$$

where $\boldsymbol{x} = (x_1, x_2)^\top$, $\boldsymbol{\nabla} \boldsymbol{u} = (\partial u_1 / \partial x_1, \partial u / \partial x_2)^\top$ and λ is a parameter that controls the smoothness of the optical flow $\boldsymbol{u}$. The solution of $\boldsymbol{u}$ is given as a set of Gauss-Seidel equations which are solved iteratively through standard numerical routines. By employing multiscale stochastic algorithms the regularization scheme of Equation (3.45) can be solved non-iteratively with the added benefit of gaining confidence measures in terms of multiscale error

covariance statistics [Luettgen et al., 1994]. This basic approach by Horn and Schunk [1981] can be extended in a number of different ways. In the following, a number of such extensions will be outlined. First the basic calculus of variations will be outlined, followed by an introduction to possible data and smoothness terms.

3.5.1 Calculus of Variations

From basic variational calculus follows the following energy functional over a Lagrange function L:

$$E(\boldsymbol{p}) = \int_{\Omega} L(\boldsymbol{p}, \nabla\boldsymbol{p}, \boldsymbol{d}, \nabla\boldsymbol{d})\ dx_1 dx_2 dt\ . \tag{3.46}$$

The solution vector $\boldsymbol{p}$ that minimizes E has to fulfill the Euler-Lagrange equations:

$$\frac{\partial L}{\partial p_i} - \frac{\mathrm{d}}{\mathrm{d}x_1}\frac{\partial L}{\partial (p_i)_{x_1}} - \frac{\mathrm{d}}{\mathrm{d}x_2}\frac{\partial L}{\partial (p_i)_{x_2}} - \frac{\mathrm{d}}{\mathrm{d}t}\frac{\partial L}{\partial (p_i)_{t}} = 0\ ; \quad i = 1 \ldots p\ . \tag{3.47}$$

Here the indices x_1, x_2, t denote partial differentiation with respect to x_1, x_2, t. Apart from the sought parameters, L can also depend on a set of data values $\boldsymbol{d}$ that may include the coordinates or functions thereof. Equation (3.47) gives p partial differential equations in the p parameters to be estimated. For every pixel such a system of equations exists and in special cases the resulting sparse matrix equation $\boldsymbol{Ap} = \boldsymbol{b}$ can be solved by the use of standard iterations $\boldsymbol{M}\boldsymbol{p}^{k+1} = \boldsymbol{N}\boldsymbol{p}^{k} + \boldsymbol{b}$, where $\boldsymbol{A} = \boldsymbol{M} - \boldsymbol{N}$ is a suitable splitting of the matrix $\boldsymbol{A}$ [Golub and van Loan, 1996]. Another numerical approach considers these equations to be the steady state of a diffusion reaction system [Schnörr and Weickert, 2000]:

$$\frac{\partial p_i}{\partial s} = \frac{\partial L}{\partial p_i} - \frac{\mathrm{d}}{\mathrm{d}x_1}\frac{\partial L}{\partial (p_i)_{x_1}} - \frac{\mathrm{d}}{\mathrm{d}x_2}\frac{\partial L}{\partial (p_i)_{x_2}} - \frac{\mathrm{d}}{\mathrm{d}t}\frac{\partial L}{\partial (p_i)_{t}}\ ; \quad i = 1 \ldots p\ . \tag{3.48}$$

Where s denotes diffusion time or scale parameter. Discretization of $\partial_s p_i$ by finite differences results in the standard explicit Euler forward evaluation scheme.

The function L defines the problem at hand. For example in mechanics this Lagrange function is given in its natural form as $L = T - U$ with a kinetic Energy T and a potential energy U [Goldstein, 1980; Landau and Lifschitz, 1990]. In computer vision, often the Lagrange function is expressed in terms of a data (D) and smoothness (V) term: $L = D + \alpha V$. The data term D is commonly also referred to as the fidelity term. The constant α is a regularization parameter that controls the relative influence of the two terms.

There exists a unique minimizer $\boldsymbol{p}$ for $E(\boldsymbol{p})$ when E is a convex functional [Schnörr, 1999]. Assume the energy functional can be written as a quadratic form:

$$E(\boldsymbol{p}) = \frac{1}{2}a(\boldsymbol{p}, \boldsymbol{p}) - f(\boldsymbol{p}) + c\ , \tag{3.49}$$

with a bilinear form $a(\cdot,\cdot) : \mathbb{R}^p \times \mathbb{R}^p \to \mathbb{R}$, a linear form $f(\cdot) : \mathbb{R}^p \to \mathbb{R}$ and a constant term c. Then $E(\boldsymbol{p})$ is strictly convex and a unique solution exits, if [Hackbusch, 1986; Schnörr, 1991]:

$$a(\boldsymbol{p}, \boldsymbol{p}) \geq C|\boldsymbol{p}| \quad \forall \boldsymbol{p} \in \mathbb{R}^p\ , \tag{3.50}$$

with a positive constant $C > 0$. All the smoothness terms considered here are positive definite bilinear forms in the derivatives of $\boldsymbol{d}$. Hence it is sufficient to show that Equation (3.50) holds for the data term alone in order to prove the existence of a unique solution.

3.5.2 Data Constraints

In this section, the focus will lie on different formulations of possible data terms. After stating the standard versions, a novel constraint that utilizes the nature of the previously determined TLS solution, will be introduced. This constraint has been previously published in Spies and Garbe [2002]. In the following an estimate of the parameter field $\boldsymbol{p} = [p_1, \ldots, p_p]^T$, with $\boldsymbol{p} \in \mathbb{R}^p$ is sought. For numerical reasons, the parameters should all lie in roughly the same range. Here it is assumed that a normalization toward this end has already been performed. In places, where the parameters have been estimated from the above TLS procedure, these estimates are denoted $\tilde{\boldsymbol{x}}$, obtained from Equation (3.30).

Parameter Constraint Equation

One example of a parameter constraint equation was given in the original Horn and Schunk [1981] formulation presented in Equation (3.45). There, the standard motion constraint equation from Section 2.2 was used. This assumption of brightness constancy is currently used in most variational algorithms [Horn and Schunk, 1981; Nagel and Enkelmann, 1986; Schnörr, 1993; Alvarez et al., 2000; Bruhn et al., 2005; Papenberg et al., 2006]. While some of these approaches make use of very elaborate smoothness constraints, the data constraint remains the same. The interested reader is referred to Schnörr and Weickert [2000] and Weickert and Schnörr [2001] for a discussion of possible smoothness constraints. As has been outlined earlier, using such a simple model which is only a crude approximation, will lead to inaccuracies. Moreover, for a number of scientific applications, the other model parameters beside translational movement can be just as important.

A straight forward extension of this simple constraint equation is to include any of the other motion models introduced in Section 2. Due to the same structure as the standard BCCE, they can equally be applied to this variational framework. The range flow model from Section 2.6 has already been extended into a variational framework by Barron and Spies [2000, 2001].

Following Equation (3.45), the fidelity term D can be formulated from the different motion models according to

$$D = (\boldsymbol{d}^T \cdot \boldsymbol{p})^2 \quad \text{with} \quad \boldsymbol{d}, \boldsymbol{p} \in \mathbb{R}^p \; . \tag{3.51}$$

Note that here the L^2 norm is always used. This is of course not the only possible choice. Other norms may have more desirable features with respect to outliers for example. Here functionals such as those from M-estimators might be preferable [Huber, 1980].

TLS Subspace Constraint

The main advantage of using a variational framework as opposed to the local TLS approach is, that 100% dense parameter fields result from this technique. This is inherent to the variational approach where globally smooth parameter fields are assumed. Due to motion discontinuities at object boundaries, the assumption of globally smooth fields can be relaxed to piecewise smooth parameter fields, as will be detailed in Chapter 6.

Here, it will be shown how dense parameter fields can be derived from the TLS solution and derivations thereof as presented in Section 3.4. In this context, it makes sense to exploit the information about the local data structure obtained from the structure tensor.

The dimensionality of the problem is p dimensions from the sought parameter vector $\boldsymbol{p} \in \mathbb{R}^p$. It should be noted that the p dimensional problem is embedded into a $p+1$ dimensional space in TLS estimation. As has been shown in Section 3.4.2, the resulting TLS estimate might not necessarily have a full dimensional solution. This is the case when only the minimal norm solution is available, for example when the aperture problem is present. Under those conditions, only a reduced set of eigenvectors forms a basis for the desired solution. This basis needs not necessarily to be orthogonal.s

$$\hat{\boldsymbol{b}}_i = \frac{1}{\sum_{k=1}^{p} e_{i,k}^2} \begin{bmatrix} e_{i,1} \\ \vdots \\ e_{i,p} \end{bmatrix} . \tag{3.52}$$

Using this notation, a transformation $\boldsymbol{P}$ is define which projects onto the subspace that was determined by the TLS algorithm. The basis of this subspace are the reduced eigenvectors to the non-vanishing eigenvalues:

$$\boldsymbol{P} = \boldsymbol{B}_k \boldsymbol{B}_k^T \quad \text{where} \quad \lambda_1 \geq \ldots \geq \lambda_k > \lambda_{k+1} \approx \ldots \approx \lambda_p + 1 \approx 0 , \tag{3.53}$$

$$\boldsymbol{B}_k = [\hat{\boldsymbol{b}}_1 \ \ldots \ \hat{\boldsymbol{b}}_k] . \tag{3.54}$$

Let $\boldsymbol{q}$ be the parameter vector computed from the TLS estimate. Each estimated parameter vector $\boldsymbol{q}$ restricts the solution within this subspace. Therefore, it is required that the regularized solution $\boldsymbol{p}$ is close to this TLS estimate $\boldsymbol{q}$ in a least squares sense:

$$D = \omega \left(\boldsymbol{P}\boldsymbol{p} - \boldsymbol{q} \right)^2 . \tag{3.55}$$

At locations, where no solution has been computed, no such data term exists. This case is readily taken into account by using an appropriate confidence measure ω. A number of different confidence measures are detailed in Chapter 5.

It is sometimes desirable to use an orthogonal basis as then the variation of $\boldsymbol{p}$ is restricted to the orthogonal complement of the TLS subspace. Such a basis system is easily computed by successive orthogonalization [Bronstein and Semendjajew, 1989]:

$$\hat{\boldsymbol{a}}_1 = \hat{\boldsymbol{b}}_1 \quad \text{and} \quad \hat{\boldsymbol{a}}_k = \frac{\boldsymbol{a}_k}{|\boldsymbol{a}_k|} \quad \text{with} \quad \boldsymbol{a}_k = \hat{\boldsymbol{b}}_k - \sum_{i=1}^{k-1} \frac{\hat{\boldsymbol{b}}_k^T \hat{\boldsymbol{a}}_i}{\hat{\boldsymbol{a}}_i^T \hat{\boldsymbol{a}}_i} \hat{\boldsymbol{a}}_i . \tag{3.56}$$

A conceptually similar data term using the orthogonal projection on a subspace of an OLS solution based on multiple constraints at the same pixel has been given by Schnörr [1993]. The considered data term Equation (3.55) can be written in the form of Equation (3.49) with

$$a(\boldsymbol{p},\boldsymbol{p}) = 2\int \omega_c\, \boldsymbol{p}^T\boldsymbol{P}^T\boldsymbol{P}\boldsymbol{p}\,, \quad f(\boldsymbol{p}) = 2\int \omega_c\, \boldsymbol{q}^T\boldsymbol{P}\boldsymbol{p} \quad \text{and} \quad c = \int \omega_c\, \boldsymbol{q}^T\boldsymbol{q}\,. \tag{3.57}$$

Under extreme conditions, TLS estimates can be very sparse under unfavorable conditions. An extreme case would be to have a full solution at just one point $\boldsymbol{x}_0$ and no solution everywhere else. At this location one then has $\boldsymbol{P} = \mathbb{1}$ and the bilinear form becomes: $a(\boldsymbol{p},\boldsymbol{p}) = 2\omega\,\boldsymbol{p}^T\boldsymbol{p}$. As a full flow solution implies $\omega > 0$ the condition Equation (3.50) is satisfied with $C = \frac{1}{2\omega}$. Because $a(\boldsymbol{p},\boldsymbol{p})$ is positive definite the argument still holds when there are further places where a TLS solution $\boldsymbol{q}$ is available. Thus it can be concluded that the existence of a single full flow estimate is sufficient for a unique regularized solution to exist. Of course, a dense solution based on just a single full flow estimate does in most cases not capture the underlying real parameter field. Therefore, confidence measures are important, that do not only assume smoothness of the parameter field. A number of possible confidence measures are presented in Chapter 5.

Combined Local Global Estimator

Recently, a combined local-global estimator (CLG) has been proposed by Bruhn et al. [2005]. The CLG approach of motion estimation does not perform TLS estimation as a preprocessing step. Instead, in this method the quadratic form is minimized directly by the optimization procedure. Thus, the fidelity term becomes

$$D = \boldsymbol{u}(\boldsymbol{x})^T\boldsymbol{J}\boldsymbol{u}(\boldsymbol{x}). \tag{3.58}$$

Here, J is the well known structure tensor from Equation (3.11). Obviously this energy is minimized if $\boldsymbol{u}(\boldsymbol{x})$ is equivalent to the eigenvector with the smallest eigenvalue. One advantage of this method is its continuous character: The more a flow vector is similar to the correct one, the smaller the energy becomes. The disadvantage, with respect to the TLS method described above, is that this term is less constrained. Information concerning the local spatio-temporal gray value structure cannot be used in the estimate. With the TLS subspace constraint from the previous section, one has more control over problematic image regions. This can lead to better results under certain conditions [Kondermann et al., 2007].

3.5.3 Smoothness Constraints

There is a large variety of smoothness constraints or regularizers that have been proposed for optical flow estimation. In a recent summary Schnörr and Weickert [2000] and Weickert and Schnörr [2001] showed the connection between such variational approaches and the corresponding diffusion processes. In the context of tensor-driven diffusion it is worth mentioning that Alvarez et al. [1999] showed that the oriented smoothness approach [Nagel and Enkelmann, 1986] can be interpreted as a tensor-driven anisotropic diffusion process. Here the three different types of smoothness constraints will be stated.

The Membrane Model

In their pioneering work Horn and Schunk [1981] introduced a homogenous regulariser for optical flow computation. Translated into the m parameter estimation framework this results in the following smoothness term:

$$V = \sum_{i=1}^{m} (\nabla p_i)^2 \ . \tag{3.59}$$

Apart from this membrane model higher order smoothness terms such as a thin-plate could be employed as well [Terzopoulos, 1986]. The above smoothness term usually considers only spatial neighborhoods ($\nabla = [\partial x, \partial y]^T$), however this is easily extended to enforce temporal smoothness as well ($\nabla = [\partial x, \partial y, \partial t]^T$).

Clearly such a regularizer produces undesirable results at discontinuities which are smoothed across. However if the considered application produces smooth and continuous parameters a membrane model is admissible. This is the case for many scientific applications. Therefore this case will be discussed in more detail in Section 3.5.4.

There are a number of extensions to the standard membrane model such as first order and second order div-curl regularizers [Suter, 1993, 1994; Gupta and Prince, 1996]. Recently, discrete orthogonal decompositions have been proposed for the estimation of solenoidal (divergence-free) image flows [Yuan et al., 2005]. An approach for allowing discontinuous piecewise smooth flow fields will be detailed in Chapter 6.

Projected Smoothness

In the above formulation a smooth parameter field was obtained whose overall smoothness is regulated by the smoothness parameter α. While a large smoothness parameter guarantees fast convergence a smaller value is preferred in order to give more influence to the data term. A practical approach might be to first run the algorithm for a while with a large α to close any gaps. Afterwards, one then can obtain the final result through additional iterations with a smaller value. The same could be obtained in a more automated manner by reducing α after each time step until it reaches the desired small value. This obviously implies the use of a fixed minimal number of iterations.

If one has already defined the subspace in which the TLS solution lies, it makes sense to smooth this subspace differently from its orthogonal complement. While a strong smoothing in the orthogonal space is desirable in order to spread the missing information, only little smoothing is required for the already available solution in order to stabilize results. This idea motivates the following smoothness term:

$$V = \psi \sum_{i=1}^{m} (\nabla (\boldsymbol{P}\boldsymbol{p})_i)^2 + (1-\psi) \sum_{i=1}^{m} (\nabla (\boldsymbol{P}^{\perp}\boldsymbol{p})_i)^2 \ . \tag{3.60}$$

Where the orthogonal projection matrix is given by $\boldsymbol{P}^{\perp} = \mathbb{1} - \boldsymbol{P}$. The relative smoothness between the two orthogonal subspaces is regulated by the parameter ψ. Because an orthogonal

projection is required in this case, the orthogonal and normalized basis $\hat{\boldsymbol{a}}_i$ from Equation (3.56) is used to construct the projection matrix.

Note that it makes no sense to use such a smoothness constraint when the TLS subspace data constraint is used. In this case there is no data constraint in the orthogonal subspace. Any smoothing parameter will thus cancel out. Hence in this combination, the membrane model does already ensure a different smoothing of the two subspaces which is readily modeled by α. This will become more apparent in Section 3.5.4.

Anisotropic Diffusion

So far, only linear isotropic smoothness terms have been considered. The smoothing can be made nonlinear by varying the smoothness strength locally. For example, one can replace the global constraints α and ψ by a function that depends on a confidence measure of the flow estimates (see Chapter 5). This is directly related to a nonlinear image diffusion approach where the smoothing strength is based on the gradient magnitude, which has originally been termed somewhat misleadingly anisotropic diffusion [Perona and Malik, 1990].

A truly anisotropic approach varies the smoothing strength not only locally but also smoothes differently in other directions (on the data array). A nonlinear anisotropic regularizer can be defined as follows:

$$V = \sum_{i=1}^{3} \mu_i \sum_{k=1}^{p+1} (\hat{\boldsymbol{e}}_i^T \nabla p_k)^2 \ . \tag{3.61}$$

This smoothness term restricts the variation of the parameter vector along the spatio-temporal directions given by the $\hat{\boldsymbol{e}}_i$ according to the μ_i. If the $\hat{\boldsymbol{e}}_i$ are chosen as the eigenvectors of the structure tensor and the smoothing strength μ_i based on the eigenvalues of the tensor, one obtains the anisotropic method similar to Weickert and Schnörr [2001].

3.5.4 Subspace Constraint and Membrane Model

In this section, the combined subspace constraint fidelity term combined with the simple membrane smoothness term will be discussed. It has been presented in Spies and Garbe [2002]. In the scientific applications, either motion discontinuities are absent (Section 7) or can easily be segmented (Section 8). Thus only the membrane smoothness model is considered here. For more complex applications, an advanced variational approach will be presented in Chapter 6.

Combining the data Equation (3.55) and smoothness Equation (3.59) constraints in the considered support Ω yields the following minimization problem :

$$\int_{\Omega} \underbrace{\left\{ \omega \left(\boldsymbol{P}\boldsymbol{p} - \boldsymbol{q} \right)^2 + \alpha \sum_{i=1}^{m} (\nabla p_i)^2 \right\}}_{L(\boldsymbol{p}, \nabla \boldsymbol{p})} dxdy \rightarrow \min \ , \tag{3.62}$$

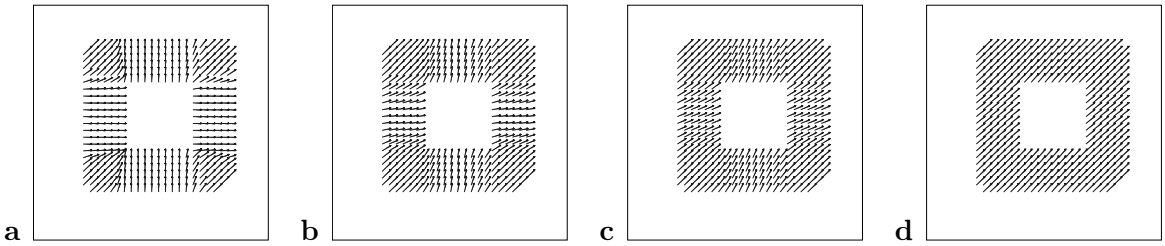

Figure 3.7: *Moving square optical flow after* **a** *10,* **b** *100,* **c** *200 and* **d** *500 iterations.*

where α controls the influence of the smoothness term. Using vector notation the Euler-Lagrange equations can be written as follows:

$$\frac{\partial L}{\partial \boldsymbol{p}} - \frac{\mathrm{d}}{\mathrm{d}x}\frac{\partial L}{\partial(\boldsymbol{p}_x)} - \frac{\mathrm{d}}{\mathrm{d}y}\frac{\partial L}{\partial(\boldsymbol{p}_y)} = 0 \ . \tag{3.63}$$

Computing the derivatives yields:

$$2\omega \boldsymbol{P}(\boldsymbol{P}\boldsymbol{p} - \boldsymbol{q}) - 2\alpha\left[\frac{\mathrm{d}}{\mathrm{d}x}(\boldsymbol{p}_x) + \frac{\mathrm{d}}{\mathrm{d}y}(\boldsymbol{p}_y)\right] = 0 \ . \tag{3.64}$$

Introducing the Laplacian $\Delta\boldsymbol{p} = \boldsymbol{p}_{xx} + \boldsymbol{p}_{yy}$ this becomes:

$$\omega\boldsymbol{P}\boldsymbol{p} - \omega\boldsymbol{P}\boldsymbol{q} - \alpha\Delta\boldsymbol{p} = 0 \ , \tag{3.65}$$

where the idempotence of the projection matrix $\boldsymbol{P}\boldsymbol{P} = \boldsymbol{P}$ is used. The Laplacian can be approximated as $\Delta\boldsymbol{p} = \bar{\boldsymbol{p}} - \boldsymbol{p}$, where $\bar{\boldsymbol{p}}$ denotes a local average [Jähne, 1995]. Using this approximation leads to

$$(\omega\boldsymbol{P} + \alpha\mathbb{1})\ \boldsymbol{p} = \alpha\bar{\boldsymbol{p}} + \omega\boldsymbol{P}\boldsymbol{q} \ . \tag{3.66}$$

This now enables an iterative solution to the minimization problem. One introduces $\boldsymbol{A} = \omega\boldsymbol{P} + \alpha\mathbb{1}$ and computes an update $\boldsymbol{p}^{k+1}$ from the solution at step k from:

$$\boldsymbol{p}^{k+1} = \alpha\boldsymbol{A}^{-1}\bar{\boldsymbol{p}}^k + \omega\boldsymbol{A}^{-1}\boldsymbol{P}\boldsymbol{q} \ . \tag{3.67}$$

Initialization can be done by using the TLS solution $\boldsymbol{p}^0 = \boldsymbol{q}$, where available. Note that Equation (3.67) converges ($\boldsymbol{p}^{k+1} = \boldsymbol{p}^k$) when Equation (3.66) is satisfied, i.e. when Equation (3.62) is minimized. The matrix $\boldsymbol{A}^{-1}$ only has to be computed once and is given by:

$$\boldsymbol{A}^{-1} = \alpha^{-1}\left(\mathbb{1}_m - \frac{\omega}{\alpha+\omega}\boldsymbol{P}\right) \ . \tag{3.68}$$

In order to verify that $\boldsymbol{A}^{-1}\boldsymbol{A} = \mathbb{1}$ only the idempotence of the projection matrix is needed, hence Equation (3.68) also holds when the basis vectors are not orthogonalized. Inserting Equation (3.68) into Equation (3.67) yields:

$$\boldsymbol{p}^{k+1} = \bar{\boldsymbol{p}}^k - \frac{\omega}{\alpha+\omega}\boldsymbol{P}\bar{\boldsymbol{p}}^k + \frac{\omega}{\alpha+\omega}\boldsymbol{P}\boldsymbol{q} \ , \tag{3.69}$$

where also the idempotence of $\boldsymbol{P}$ was used. From $\mathbb{1} = \boldsymbol{P} + \boldsymbol{P}^\perp$ the two subspaces can be separated:

$$\boldsymbol{p}^{k+1} = \boldsymbol{P}^\perp\bar{\boldsymbol{p}}^k + \frac{1}{\alpha+\omega}\boldsymbol{P}(\alpha\bar{\boldsymbol{p}}^k + \omega\boldsymbol{q}) \ . \tag{3.70}$$

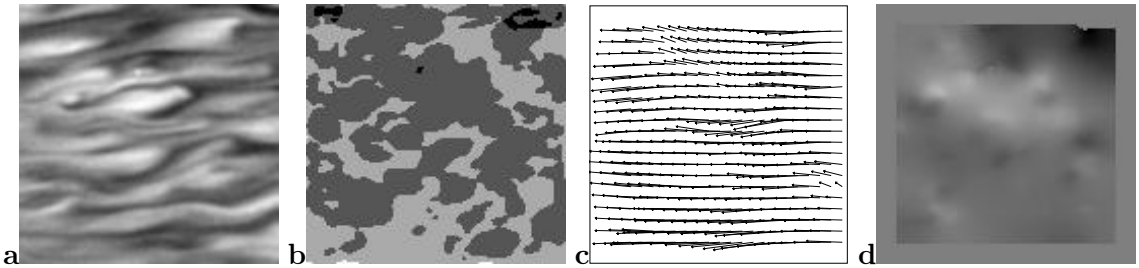

Figure 3.8: *IR sequence of the water surface:* **a** *original image,* **b** *map indicating the type of flow (black: $tr(\boldsymbol{J}) < \tau_1$, white: $k = p - 2$, light grey: $k = p - 1$, dark grey: $k = p$),* **c** *velocity field and* **d** *source term (temperature change)* $[-0.5, 0.5]K/frame$.

In the orthogonal subspace, where no initial TLS solution is available, the local average is used. In the subspace determined by the TLS solution the iterative update is given by a weighted mean of the local average and the originally available solution. The weights are determined by the regularization constant α and the confidence measure ω respectively. Notice that the choice of α only regulates the amount of smoothing in the TLS subspace and has no effect in the orthogonal subspace.

The effect of this regularization on the example of Figure 3.4 is shown in Figure 3.7 ($\alpha = 10$). Initially the flow field is dominated by the normal flows. With increasing iterations the full flow information spreads out until a dense full flow field is obtained. Here the trace is used to mask the area Ω.

As stated above some of the minimum norm parameters can be unreliable when there is a difference in magnitude between the parameters. This can be accounted for by choosing different confidence values ω_i for each parameter p_i in Equation (3.69):

$$\omega_i = \begin{cases} c_i\,\omega & \text{if } q < n-1 \\ \omega & \text{else} \end{cases} . \tag{3.71}$$

Where c_i is a factor reflecting the confidence that the parameter p_i is reliably computed in the minimum norm solutions. In the same way, also a different smoothing strength α_i can be chosen for the different parameters. This is particularly interesting for higher order models in which one smoothing strength $\alpha_{\boldsymbol{u}}$ is set for the motion field and another one can be used for the parameter modeling brightness change.

This framework can of course be applied to the applications presented in Part II of this thesis. One such application is to estimate net heat fluxes at the air-water interface. Using infrared cameras to view the water surface gives a direct way to study the heat exchange Garbe et al. [2002a]. Here a linear source term is used to capture the rate of temperature change, as will be explained in detail in Chapter 7. An example is given in Figure 3.8 where it can be seen that the temperature change (Figure 3.8**d**) does not seem to be correlated to either the original temperature distribution (Figure 3.8**a**) nor the velocity field (Figure 3.8**c**). Note that in this example there are large areas where it is not possible to compute a full parameter field initially (Figure 3.8**b**). These areas are successfully closed from regularizing the parameter fields.

3.6 Conclusion

In this chapter a framework for the computation of motion from image sequences has been presented. Solving this inverse problem starts with formulating a suitable model which relates brightness changes to motion. A number of models have been presented in Chapter 2. It was shown that the problem of motion estimation is ill posed without any additional constraints. This is due to the aperture problem, which is one fundamental problem in motion estimation as is the problem of occlusions. Two approaches of solving the aperture problem were presented. The first one assumes local constancy of model parameters, the second one global smoothness.

The local approach of estimating motion is also known as structure tensor approach. IT was shown that this approach is closely related to a parameter estimation framework. Depending on the motion model and the data terms, different estimators present optimal results. It was shown that the ordinary least squares (OLS) estimator is a maximum likelihood estimator in the case of iid Gaussian noise on the observations. The bias of this estimator in the case of errors in all variables was circumvented with the introduction of the total least squares estimator (TLS). In a number of models, such as linear regression with intersect, some columns will be known without any errors. This leads to an error in TLS estimates which assumes all observations to be perturbed by the same iid Gaussian noise. A more accurate estimation is gained by the introduction of a mixes ordinary least squares - total least squares estimator (mixed OLS-TLS), which computes the parameters of the perturbed data matrix in a total least squares sense and the exactly known columns by means of ordinary least squares estimation.

One significant drawback of local estimators can be that their estimated parameter fields are generally not dense. Therefore an algorithm was presented that allows to regularize parameter fields in a variational approach. All available information concerning the local spatio-temporal gray value structures is used in the regularization process.

The presented framework for parameter estimation represents an ideal tool for applying the motion models from Chapter 2 to a wide range of applications. This framework can readily be extended to estimators from robust statistics as has been shown in Garbe and Jähne [2001]. These estimators have been presented in detail in Garbe [2001]. Therefore they were not mentioned explicitly in this thesis.

Chapter 4

Real Time Performance

4.1 Introduction

In previous chapters, different motion models have been presented which could be solved in a total least squares (TLS) framework. These models can be used for a number of scientific applications such as in microfluidics [Garbe et al., 2006, 2008], in thermopgraphy [Garbe et al., 2003c] in botany [Garbe et al., 2002d,c, 2007c] and in environmental physics [Garbe and Jähne, 2001; Garbe et al., 2002b, 2003b, 2004, 2007a], to name but a few. For most of these applications, long image sequences at high framerates need to be recorded in order to analyze the processes of interest fully. It is important to estimate the model parameter from these large amounts of data quickly and efficiently. Form some application, a real time analysis is necessary to facilitate instant feedback during the measurement.

These requirements will be addressed in this chapter. Fast and efficient algorithms for performing TLS estimates will be presented as well as an extension to the mixed OLS-TLS estimator from Section 3.4.4. Only these algorithmic extensions make a fast implementation in real time feasible. They are also presented in Garbe and Strzodka [2007]. To take advantage of the processing power of modern graphics processing units or GPUs in form of standard graphics cards, the algorithms have been implemented on this hardware. This accelerates execution time by a factor of 4.5 by employing a data-stream based computer paradigm, as has been shown by Strzodka and Garbe [2004]. This allows high throughput for large data volumes to be processed in parallel.

This chapter is organized as follows: In Section 4.2 the structure tensor approach for estimating motion from gradients of image sequences will be recapitulated. The extension of this approach to linear brightness changes and estimation of Range Flow will be discusses in Section 4.3, where also an optimal solution of this motion model both in terms of accuracy and efficiency will be presented. The solution boils down to performing an eigenvalue analysis of an 3×3 matrix, which can be conducted extremely fast, as will be shown in Section 4.4. Here a technique based on the minors of the structure tensor will be presented in Section 4.4.1, one based on Partial Total Least Squares in Section 4.4.2 and one on an analytical solution of the eigenwert problem in Section 4.4.3. The performance of the algorithms presented will

be analyzed in Section 4.5. In Section 4.6 an implementation on standard graphics hardware will be presented that makes a speedup by a factor of 5 feasible. This highly parallel stream based implementation is applied to pedestrian scenes and to a medical application.

4.2 The Classical Structure Tensor Approach

The approach of estimating optical flow with the structure tensor approach was presented in Section 3.3. Essentially, this approach is equivalent to TLS parameter estimation from normal equations as introduced in Section 3.4.2. Principally, the approach consists of two parts:

1. building the structure tensor from the input image sequence
2. performing an eigensystem analysis of the tensor

In literature, a lot of effort has been put into constructing the structure tensor as efficiently as possible. In the approach presented in this thesis, Jähne [1993] is followed in constructing the tensor from intensity gradients as opposed to responses of Gabor or quadrature filters [Knutsson and Granlund, 1983; Bigün et al., 1991; Granlund and Knutsson, 1995; Bigün, 2006]. Gradients are computed from optimized, separable filters [Jähne et al., 1999; Scharr, 2006], which can be achieved very efficiently. The computation of these gradients can be conducted with 15 multiplications and 12 additions per pixel and gradient for 5x5x5 filter kernels. Thus, for the computation of these three gradients take 45 multiplications and 36 additions. Next the tensor elements are computed from point wise multiplication of these gradients. The integration of the structure tensor is then conducted by smoothing the tensor elements with separable binomial filters as approximations to Gaussians. These steps were sketched in Figure 3.3. When integration is performed only spatially with a separable 9x9 smoothing filter, the complete structure tensor can be computed with 159 multiplications and 132 additions, including the computation of the gradients. Thus, the six different elements of the symmetric structure tensor are computed at a cost of 291 floating point operations (FLOP).

In order to estimate motion from the structure tensor, an eigenvalue analysis has to be performed on this symmetric tensor. Standard techniques for performing the eigensystem analysis can be computationally quite expensive. For example, Jacobi rotations require $7 \cdot n^3$ floating point operations per sweep [Barlow, 2002], thus 189 FLOP for a 3×3 structure tensor. Usually five to ten sweeps are required for converging to a solution. Performing the eigenvalue analysis with Jacobi rotations is thus much more expensive than computing the structure tensor. A faster algorithm of estimating the eigensystem of the structure tensor would be performing a bidiagonal reduction followed by an QR factorization. An algorithm of this type requires $20 \cdot n^3$ floating point operations in total [Barlow, 2002], or 540 FLOP in the case of the 3×3 structure tensor. This is still more expensive than constructing the structure tensor. Hence, significant speed improvements are possible by reducing the complexity of the eigensystem analysis. Efficient ways of computing this eigensystem will be presented in Section 4.4.

4.3 Extension: Linear Brightness Change and Range Flow

In image sequences, moving objects with linear brightness change are very common. The stringent brightness change constraint equation (BCCE) requires object intensities to remain constant, which is hardly ever truly the case. Even if it can be guaranteed that the illumination source remains constant, motion toward or away from this source will lead to changes in the intensity as visualized by the camera. Departures from the idealized Lambertian surface of real objects will further constrict the BCCE.

Incorporating linear brightness changes into the BCCE significantly improves accuracy and the applicability of the motion estimator. The rationale is of course that a number of brightness changes can be modeled by such a linear source term. Also, for more complex brightness changes, a linear source term presents a first order approximation, which van be seen by expanding the equation into a Taylor series expansion. The resulting constraint equation and some applications were given in Section 2.5.2. A straight forward derivation led to Equation (2.25):

$$\boldsymbol{d}^\top \boldsymbol{p} = [-1, I_x, I_y, I_t] \cdot [c, u_1, u_2, 1]^\top = 0. \tag{4.1}$$

On first sight, this equation of linear brightness change along the trajectory of a moving object is quite dissimilar to moving objects in range data. Range data are 2D+t image sequences, encoding the distance from the range sensor to the objects in gray values. Range sensors can be highly accurate scanning laser systems, but also novel insantaneous systems such as PMD cameras are becoming increasingly popular [Schwarte et al., 1999]. The constraint equation for range flow was derived and formulated in Section 2.6, resulting in Equation (2.37):

$$\boldsymbol{d}^\top \cdot \boldsymbol{p} = [-1 \; Z_X \; Z_Y \; Z_t] \cdot [U_3 \; U_1 \; U_2 \; 1]^\top = 0. \tag{4.2}$$

Comparing Equations (4.1) and (4.2) it becomes apparent, that both problems are mathematically formulated in the same way, only the interpretation is different. While in Equation (4.1) the parameter c is interpreted as linear brightness change along the trajectory of moving objects, it denotes the velocity U_3 towards or away from the range sensor. Due to the similar formulation, both problems can be solved with the same estimators. In the following, the focus will be on efficiently solving the problem of Equation (4.1), keeping in mind that results and algorithms apply equally for estimating range flow.

4.3.1 Mixed OLS-TLS Minimization

Similar to the standard structure tensor approach presented in Section 3.3, it is assumed that motion parameters remain locally constant. Hence, the constraint equations (4.2) and (4.1) can be pooled over a local neighborhood, leading to

$$\begin{bmatrix} -1 & I_{x,1} & I_{y,1} & I_{t,1} \\ -1 & I_{x,2} & I_{y,2} & I_{t,2} \\ \vdots & \vdots & \vdots & \vdots \\ -1 & I_{x,n} & I_{y,n} & I_{t,n} \end{bmatrix} \cdot \begin{bmatrix} c \\ u_1 \\ u_2 \\ 1 \end{bmatrix} = \boldsymbol{D} \cdot \boldsymbol{p} = 0, \quad \text{with} \quad \boldsymbol{D} \in \mathbb{R}^{n \times 4},\ \boldsymbol{p} \in \mathbb{R}^4. \tag{4.3}$$

Proceeding in the standard structure tensor approach, this would lead to $\boldsymbol{J} = \boldsymbol{D}^\top \boldsymbol{D} \in \mathbb{R}^{4\times 4}$. Computing the structure tensor $\boldsymbol{J}$ in this fashion has two significant drawbacks:

1. As presented in Section 3.4.4, the noise structure in the data terms is not reflected by the total least squares (TLS) estimator [Van Huffel, 1992], implied by the structure tensor approach. This will lead to a bias in the estimates [Garbe et al., 2002e].
2. The eigensystem analysis of a 4×4 matrix can be performed much less efficient than that of a 3×3 matrix.

To address the problem of introducing a bias by solving the system of equations (4.3) in a TLS sense, it has to be solved in a mixed ordinary-total least squares sense (mixed OLS-TLS) [Garbe et al., 2002e]. The basic algorithm has been introduced in Section 3.4.4.

In Section 3.4.4 the mixed OLS-TLS estimator was defined as:

Definition 7 *Given a set of n linear Equations with p unknown parameters $\boldsymbol{x}$*

$$[\boldsymbol{A}_1, \boldsymbol{A}_2]\, \boldsymbol{x} = \boldsymbol{b}, \quad \text{with} \quad \boldsymbol{A}_1 \in \mathbb{R}^{n\times p_1}, \boldsymbol{A}_2 \in \mathbb{R}^{n\times p_2}, \boldsymbol{x} \in \mathbb{R}^p, \boldsymbol{b} \in \mathbb{R}^n, \tag{4.4}$$

and $p_1 + p_2 = p$. The mixed OLS-TLS problem then seeks to minimize

$$\begin{aligned} \min \quad & \left([\boldsymbol{A}_2, \boldsymbol{b}]\, \boldsymbol{p}_2\right)^2 \\ \textit{subject to} \quad & [\boldsymbol{A}_1, \boldsymbol{A}_2]\, \boldsymbol{x} = \boldsymbol{A}_1 \boldsymbol{x}_1 + \boldsymbol{A}_2 \boldsymbol{x}_2 = \boldsymbol{b}, \end{aligned} \tag{4.5}$$

where $\boldsymbol{p} = \left[\boldsymbol{x}^\top, -1\right]^\top$, $\boldsymbol{p}_2 = \left[\boldsymbol{x}_2^\top, -1\right]^\top$ and $\boldsymbol{x} = \left[\boldsymbol{x}_1^\top, \boldsymbol{x}_2^\top\right]^\top$.

In the specific example of Equation (4.3) $p_1 = 1$ and $p_2 = m$. Equation (4.5) can thus be depicted as first finding a TLS solution on the reduced subspace of erroneous observations and then choosing from this set the one solution that exactly solves the Equations of unperturbed data.

The implementation of the mixed OLS-TLS estimator is quite straight forward. The columns of the data matrix A are permuted by the permutation matrix $\boldsymbol{P}$ in such a way, that the submatrix $\boldsymbol{A}_1$ contains the p_1 exactly known observations, that is

$$\boldsymbol{A} \cdot \boldsymbol{P} = [\boldsymbol{A}_1, \boldsymbol{A}_2], \text{ where } \boldsymbol{A} \in \mathbb{R}^{n\times p}, \boldsymbol{A}_1 \in \mathbb{R}^{n\times p_1}, \boldsymbol{A}_2 \in \mathbb{R}^{n\times p_2}, \boldsymbol{P} \in \mathbb{R}^{p\times p}. \tag{4.6}$$

This is followed by a QR factorization of the matrix $[\boldsymbol{A}_1, \boldsymbol{A}_2, \boldsymbol{b}]$, thus

$$[\boldsymbol{A}_1, \boldsymbol{A}_2, \boldsymbol{b}] = \boldsymbol{Q} \begin{bmatrix} \boldsymbol{R}_{11} & \boldsymbol{R}_{12} \\ \boldsymbol{0} & \boldsymbol{R}_{22} \end{bmatrix}, \tag{4.7}$$

with $\boldsymbol{Q}$ being orthogonal and $\boldsymbol{R}_{11}$ upper triangular.

Then the TLS solution for the sub system of Equations $\boldsymbol{R}_{22}\boldsymbol{p}_2 = 0$ is computed according to the algorithm presented in Section 3.4.2. With the known estimate of $\boldsymbol{p}_2$ the system of equations $\boldsymbol{R}_{11}x_1 + \boldsymbol{R}_{12}\boldsymbol{p}_2 = 0$ is solved for x_1 by back-substitution. The parameter vector $\boldsymbol{p} = \left[x_1^\top, \boldsymbol{p}_2^\top\right]^\top$ has then to be transformed back reversing the initial permutations of the columns by $\boldsymbol{p} \leftarrow \boldsymbol{P}^{-1}\boldsymbol{p}$.

With this solution of Equation (4.3) in the mixed OLS-TLS framework, the two issues of estimating the parameters in a TLS directly are resolved. The bias introduced by the wrong assumption of iid noise on the data is no longer present. Furthermore, the TLS estimate has to be performed on the resulting submatrix $\boldsymbol{R}_{22} \in \mathbb{R}^{n\times 3}$ only. The advantage of performing a eigenvalue analysis on the 3×3 matrix $\boldsymbol{R}_{22}^\top \cdot \boldsymbol{R}_{22} \in \mathbb{R}^{3\times 3}$ as opposed to performing one on the 4×4 matrix $\boldsymbol{A}^\top \cdot \boldsymbol{A} \in \mathbb{R}^{4\times 4}$ is offset by the additional computational cost of performing a QR factorization. A reduction of this complexity is essential for increasing performance to real time.

For the mixed OLS-TLS estimator, it is essential to bring the first column in the form $[\ 1 \quad \mathbf{0}\ ]^\top$ where $\mathbf{0}$ denotes the zero vector $\mathbf{0} \in \mathbb{R}^{n-1}$. This can readily be achieved by performing a single Householder reflection [Householder, 1958] instead of a time consuming full QR decomposition. This Householder transform leads to the following system of equations:

$$\begin{aligned} \boldsymbol{H}\cdot\boldsymbol{D}\cdot\boldsymbol{p} &= \boldsymbol{H}\cdot\begin{bmatrix} \mathbf{1} & \boldsymbol{A}_2 & \boldsymbol{b}\end{bmatrix}\cdot\boldsymbol{p} = \begin{bmatrix} 1 & \boldsymbol{R}_{12} \\ \mathbf{0} & \boldsymbol{R}_{22}\end{bmatrix}\cdot\boldsymbol{p} = 0, \quad \text{with} \\ \boldsymbol{R}_{12} &= \begin{bmatrix} \langle\boldsymbol{A}_2\rangle & \langle\boldsymbol{b}\rangle\end{bmatrix} \quad \text{and} \quad \boldsymbol{R}_{22} = \begin{bmatrix} \boldsymbol{A}_2 - \langle\boldsymbol{A}_2\rangle & \boldsymbol{b} - \langle\boldsymbol{b}\rangle\end{bmatrix}, \end{aligned} \tag{4.8}$$

where $\boldsymbol{H}$ is the Householder matrix $\boldsymbol{H} = \mathbb{1} - 2\boldsymbol{v}\boldsymbol{v}^\top/\boldsymbol{v}^\top\boldsymbol{v}$, the Householder vector is $\boldsymbol{v} = [\sqrt{n}-1, -1, \ldots, -1]^\top \in \mathbb{R}^n$ is and $\mathbb{1}$ is the identity matrix. The column mean of $\boldsymbol{A}_2$ and $\boldsymbol{b}$ are denoted with $\langle\boldsymbol{A}_2\rangle$ and $\langle\boldsymbol{b}\rangle$ respectively. The reduction of the Householder reflection to the column mean of $\boldsymbol{A}_2$ and $\boldsymbol{b}$ for $\boldsymbol{R}_{12}$ and the difference in between the entries of $[\boldsymbol{A}_2\ \boldsymbol{b}]$ and the column mean $\langle\boldsymbol{A}_2\rangle$ and $\langle\boldsymbol{b}\rangle$ for $\boldsymbol{R}_{22}$ can be seen from the special form of $\boldsymbol{H}$ which is given by

$$\boldsymbol{H} = \begin{bmatrix} \sqrt{n} & 1/\sqrt{n} & 1/\sqrt{n} & \ldots & 1/\sqrt{n} \\ 1/\sqrt{n} & 1-1/(n-\sqrt{n}) & 1/(\sqrt{n}-n) & \ldots & 1/(\sqrt{n}-n) \\ 1/\sqrt{n} & 1/(\sqrt{n}-n) & 1-1/(n-\sqrt{n}) & \ldots & 1/(\sqrt{n}-n) \\ \vdots & \vdots & \vdots & \ddots & \vdots \\ 1/\sqrt{n} & 1/(\sqrt{n}-n) & 1/(\sqrt{n}-n) & \ldots & 1-1/(n-\sqrt{n}) \end{bmatrix}. \tag{4.9}$$

From Equation (4.8) it is evident that the parameters $\boldsymbol{p}_2 \in \mathbb{R}^{p-1}$ need to be estimated from the submatrix $\boldsymbol{R}_{22}$ in a TLS sense. The remaining parameter x_1 can then be computed by back-substituting $x_1 = \boldsymbol{R}_{12}\cdot\boldsymbol{p}_2$. The structure tensor is thus constructed from $\boldsymbol{J}_{\text{sub}} = \boldsymbol{R}_{22}^\top \cdot \boldsymbol{R}_{22} \in \mathbb{R}^{3\times 3}$. The eigensystem of $\boldsymbol{J}$ can then be computed from the efficient techniques presented in Section 4.4 and thus the parameters $\boldsymbol{p} = [c, u_1, u_2, 1]^\top$ estimated.

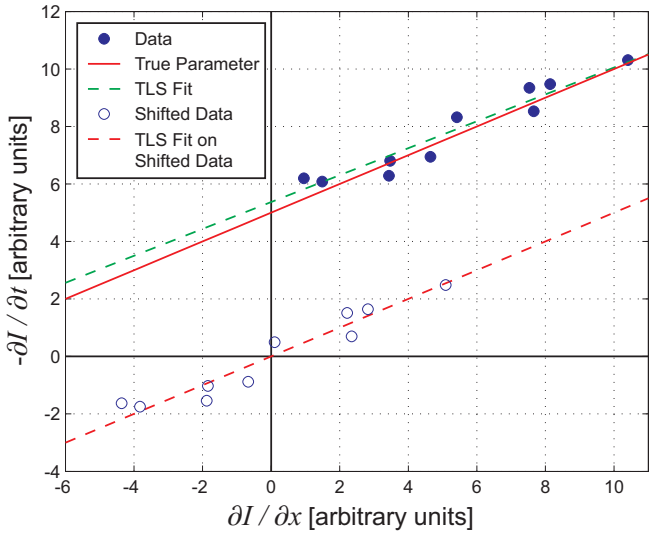

Figure 4.1: *Plot of the model $u \cdot I_x - c = I_t$, where the blue dots indicate data points corrupted by noise. A TLS fit results in a biased estimate (green dotted line). The Mixed TLS-OLS shifts the data to be centered around the origin, where an unbiased TLS fit can be performed. Re-transforming the result gives the true estimate (blue line) which is equivalent to the true model in this case.*

Implementing the algorithm is quite straightforward. Following Equation (4.8) leads to the following expression for the structure tensor $\boldsymbol{J}_{\text{sub}}$ computed from $\boldsymbol{R}_{22}$:

$$\begin{aligned}
\boldsymbol{J}_{\text{sub}} &= \begin{bmatrix} \langle (I_x - \langle I_x \rangle) \cdot (I_x - \langle I_x \rangle) \rangle & \langle (I_x - \langle I_x \rangle) \cdot (I_y - \langle I_y \rangle) \rangle & \langle (I_x - \langle I_x \rangle) \cdot (I_t - \langle I_t \rangle) \rangle \\ \langle (I_x - \langle I_x \rangle) \cdot (I_y - \langle I_y \rangle) \rangle & \langle (I_y - \langle I_y \rangle) \cdot (I_y - \langle I_y \rangle) \rangle & \langle (I_y - \langle I_y \rangle) \cdot (I_t - \langle I_t \rangle) \rangle \\ \langle (I_x - \langle I_x \rangle) \cdot (I_t - \langle I_t \rangle) \rangle & \langle (I_y - \langle I_y \rangle) \cdot (I_t - \langle I_y \rangle) \rangle & \langle (I_t - \langle I_t \rangle) \cdot (I_t - \langle I_t \rangle) \rangle \end{bmatrix} \\
&= \begin{bmatrix} \mathcal{B} * (\overline{I_x} \cdot \overline{I_x}) & \mathcal{B} * (\overline{I_x} \cdot \overline{I_y}) & \mathcal{B} * (\overline{I_x} \cdot \overline{I_t}) \\ \mathcal{B} * (\overline{I_x} \cdot \overline{I_y}) & \mathcal{B} * (\overline{I_y} \cdot \overline{I_y}) & \mathcal{B} * (\overline{I_y} \cdot \overline{I_t}) \\ \mathcal{B} * (\overline{I_x} \cdot \overline{I_t}) & \mathcal{B} * (\overline{I_y} \cdot \overline{I_t}) & \mathcal{B} * (\overline{I_t} \cdot \overline{I_t}) \end{bmatrix},
\end{aligned} \tag{4.10}$$

where $\mathcal{B} \star x$ represents the convolution of x with a binomial filter. $\overline{I_n}$ denotes the gradient of image intensity I reduced by its weighted mean. This can be implemented efficiently as $I_n - (\mathcal{B} \star I_n)$.

The parameter of linear brightness change c can then be solved by substituting the estimated velocities $\tilde{u}_1$ and $\tilde{u}_1$ into the following equation

$$c = \langle I_x \rangle \cdot \tilde{u}_1 + \langle I_y \rangle \cdot \tilde{u}_2 + \langle I_t \rangle \ . \tag{4.11}$$

4.3.2 Geometric Interpretation

Motion from the well known brightness change constraint equation (BCCE) presented in Section 2.2 can be thought of as a plane in the gradient space that passes through the origin. This can readily be seen by setting $I_x = I_y = 0$. Since Equation (2.3) states $u_1 I_x + u_2 I_y + I_t = 0$

it follows immediately that I_t also has to be zero. For this model, all the data terms ($[I_x, I_y, I_t]$) are corrupted by noise and the TLS estimate is the maximum likelihood estimator.

In contrast, a model as presented in Equation (4.1) ($[-1, I_x, I_y, I_t] \cdot [c, u_1, u_2, 1]^\top = 0$), linear brightness change can be thought of as a plane in gradient space that intersects the I_t axis at $c \neq 0$. Again, this can be verified by setting $I_x = I_y$ from which follows $I_t = c$. It is this offset c that leads to the wrong estimates of the standard TLS when computing the model parameters $\boldsymbol{p}$ from the data. This is due to the fact that the constant term -1 appears in the data term. As shown in the previous section, the Housholder reflection leads to subtracting the column mean from the data matrix $\boldsymbol{R}_{22}$ in Equation (4.8). The effect of this transformation is shifting the origin to the center of the data. Thus, for the shifted data the parameters describe a plane through the origin, for which case TLS can be used again. Subsequently, the original offset c has to be computed from the sought parameters and the shifted distance of the data. This interpretation is visualized in Figure 4.1.

4.4 Accelerated Structure Tensor Analysis

4.4.1 Motion from Minors of the Structure Tensor

For the case of $\boldsymbol{J} \in \mathbb{R}^{3\times3}$ it was shown by Barth [2000] that the optical flow field can be obtained from the minors of the structure tensor $\boldsymbol{J}$. The minors $\boldsymbol{M}$ are given by

$$\boldsymbol{M} = \text{Minors}(\boldsymbol{J}). \tag{4.12}$$

The elements $M_{i,j}, (i, j = 1, .., n)$ of $\boldsymbol{M}$ are the determinants of the matrices obtained from $\boldsymbol{J}$ by eliminating the row i and the column j, e.g. for $n = 3$ the one of the resulting minors is $M_{11} = J_{22} \cdot J_{33} - J_{23}^2$.

Assuming that $\boldsymbol{J} \in \mathbb{R}^{n\times n}$ has rank $n-1$ it will now show how the unique eigenvector $\boldsymbol{e}_n \in \mathbb{R}^n$ to the unique vanishing eigenvalue $\lambda_n = 0$ can be computed following [Mota et al., 2001].

The rows of $\boldsymbol{J}$ will be denoted by $\boldsymbol{J}_i$, i.e. $\boldsymbol{J} = [\boldsymbol{J}_1, \boldsymbol{J}_2, \ldots, \boldsymbol{J}_n]^\top$. It is then known that

$$\boldsymbol{J}_i \cdot \boldsymbol{e}_n = 0, \qquad \forall i = 1, \ldots, n\,, \tag{4.13}$$

which means that the rows of $\boldsymbol{J}$ are orthogonal to $\boldsymbol{e}_n$. Since $\boldsymbol{J}$ has rank $n-1$, $\boldsymbol{e}_n$ can be determined by finding a vector $\boldsymbol{v}_k \neq 0$ with the same property of being orthogonal to all $\boldsymbol{J}_i$ and normalizing it.

Because $\boldsymbol{J}_i$ does not have full rank, at least one of the rows, say $\boldsymbol{J}_k$, is a linear combination of the others

$$\boldsymbol{J}_k = \sum_{i\neq k} a_i \boldsymbol{J}_i \qquad a_i \in \mathbb{R}^{\cdot} \tag{4.14}$$

Starting with the single equation

$$0 = \det(\boldsymbol{J}) = \det\left(\left[\boldsymbol{J}_1, \ldots, \boldsymbol{J}_{k-1}, \sum_{i\neq k} a_i \boldsymbol{J}_i, \boldsymbol{J}_{k+1}, \ldots, \boldsymbol{J}_n\right]\right), \tag{4.15}$$

and making use of the fact that the determinant does not change by adding arbitrary multiples of one row to another, one ends up with n equations with $l = 1, \ldots, n$ of the form

$$0 = \det\left([\boldsymbol{J}_1, \ldots, \boldsymbol{J}_{k-1}, \boldsymbol{J}_l, \boldsymbol{J}_{k+1}, \ldots, \boldsymbol{J}_n]\right). \tag{4.16}$$

With the Laplace expansion of the above determinants along the row k one obtains

$$0 = \sum_i (-1)^{i+1} J_{l,i} \cdot M_{k,i} = \boldsymbol{J}_l \cdot \left(\hat{\mathbb{1}}\boldsymbol{M}_k\right), \tag{4.17}$$

where $\mathrm{diag}(\hat{\mathbb{1}}) = [1, -1, 1, \ldots, (-1)^{1+n}]$ and $\boldsymbol{M}_k$ is the k-th row of $\boldsymbol{M}$. As this holds true for all $l = 1, \ldots, n$, the desired vector $\boldsymbol{v}_k$ is found to be orthogonal to all rows of $\boldsymbol{J}$. It is given by

$$\boldsymbol{v}_k = \left(\hat{\mathbb{1}}\boldsymbol{M}_k\right). \tag{4.18}$$

Note, that the above orthogonal relations are true for all k for which $\boldsymbol{J}_k$ is linearly dependent on $\boldsymbol{J}_i, i \neq k$. Thus, there are several alternative ways for constructing the eigenvector $\boldsymbol{e}_n$ from the different $\boldsymbol{v}_k$'s. For the other k's when $\boldsymbol{J}_k$ is linearly independent on the other rows, canceling of the row k in $\boldsymbol{J}$ leaves a rank deficient matrix. This leads to all the minors from $\boldsymbol{M}_k$ being zero and thus $\boldsymbol{v}_k = 0$. The sought eigenvector $\boldsymbol{e}_n$ can obviously not be constructed in this case.

In general it is expensive to find a k such that $\boldsymbol{J}_k$ is linearly dependent on $\boldsymbol{J}_i, i \neq k$, and thus $\boldsymbol{e}_n$ can be constructed from $\boldsymbol{v}_k \neq 0$. But for the motion estimation, where $n = 3$ and the structure tensor $\boldsymbol{J}$ is symmetric, it can simply be afforded to compute all six minors $\{M_{11}, M_{12}, M_{13}, M_{22}, M_{23}, M_{33}\}$, so that it is immediately known for which k the resulting $\boldsymbol{v}_k \neq 0$. In the presence of noise, computations will not result in exact zeros, but the magnitudes of the $\boldsymbol{v}_k$ can be used to determine which are more trustworthy. In the extreme case, when all $\boldsymbol{v}_k$ are almost zero, the rank of the original, unperturbed matrix is probably smaller than $n - 1$. And with the help of the $\mathrm{trace}(\boldsymbol{J}) = \lambda_1 + \lambda_2 + \lambda_3$ it can be determined whether all eigenvalues or only two are small.

As outlined previously, the solution to the TLS problem is the eigenvector $\boldsymbol{e}_n$ to the smallest eigenvalue λ_n normalized to the last component, or

$$\boldsymbol{u} = \begin{bmatrix} u_1 \\ u_2 \\ 1 \end{bmatrix} = \frac{\boldsymbol{e}_3}{e_{3,3}} = \frac{\left(\hat{\mathbb{1}}\boldsymbol{M}_k\right)}{M_{k,3}} = \begin{bmatrix} M_{11}/M_{13} \\ -M_{12}/M_{13} \\ M_{13}/M_{13} \end{bmatrix} = \begin{bmatrix} M_{21}/M_{23} \\ -M_{22}/M_{23} \\ M_{23}/M_{23} \end{bmatrix} = \begin{bmatrix} M_{31}/M_{33} \\ -M_{32}/M_{33} \\ M_{33}/M_{33} \end{bmatrix}. \tag{4.19}$$

For computing a minor of a 3×3 matrix, two multiplications and one summation are required. This means, that for computing the velocity vector $\boldsymbol{u}$ requires 8 multiplications and 3 additions per pixel and frame or 11 floating point operations (FLOP). Computation of all six minors leads to 18 multiplications and 6 additions or 24 FLOP.

4.4.2 Partial Total Least Squares

The estimation of motion with the structure tensor approach is a formulation of the *Total Least Squares Problem* (TLS) by normal equations [Van Huffel and Vandewalle, 1991]. In the

same manner as presented for the structure tensor approach, TLS problems are solved by performing a *Singular Value Decomposition* (SVD) on the data matrix. The sought solution is then the right singular vector to the smallest singular value. In the case of motion estimation, this would correspond to estimating the full flow. In the presence of an aperture problem, the minimum norm solution is computed from a linear combination of eigenvectors to vanishing eigenvalues. The same is true for TLS, where this case is termed *non-generic total least squares* as introduced in Section 3.4.2.

From Section 3.3 it is evident, that under most circumstances it is sufficient to only compute one or two singular values for the task of motion estimation. Hence, significant performance boosts are achievable by not performing a full SVD or eigenvalue analysis, but only compute the eigenvectors actually needed. An algorithm for solving this *Partial Total Least Squares* (PTLS) problem has been presented by Van Huffel and Vandewalle [1991]. The authors perform a detailed performance analysis of the PTLS algorithm and show that the computational cost can be halved by performing PTLS instead of TLS. The accuracy remains the same for both algorithms. An implementation of the PTLS algorithm is made freely available [Van Huffel, 1989]. Due to the exhaustive analysis of the PTLS as compared to TLS, here standard TLS is used. However, it should be noted that a speed-up of 50% in the TLS computation is achievable with PTLS, retaining the same level of accuracy.

4.4.3 Analytical Computation of the Eigensystem

Generally, for finding the eigensystem of matrices $\boldsymbol{J} \in \mathbb{R}^{n\times n}$, with n larger than 2, iterative schemes such as Jacobi rotations [Press et al., 1992] are commonly used. For $\boldsymbol{J} \in \mathbb{R}^{3\times 3}$ Hasan et al. [2001] presented an efficient analytical solution.

Their analytical diagonalization solution is specific to the positive-definite and symmetric tensors. The eigenvalues λ_1, λ_2 and λ_3 of such matrices is given by their characteristic polynomial

$$\det\left(\boldsymbol{J} - \boldsymbol{\Lambda}\boldsymbol{E}_{3\times 3}\right) = \left(\lambda - \lambda_1\right)\left(\lambda - \lambda_2\right)\left(\lambda - \lambda_3\right) = \lambda^3 - \lambda^2 i_1 + \lambda i_2 - i_3 = 0, \tag{4.20}$$

where $\boldsymbol{E}_{3\times 3}$ is the identity matrix. From this equation, three invariants i_n are given:

$$\begin{aligned} i_1 &= \operatorname{trace}\boldsymbol{J} = J_{1,1} + J_{2,2} + J_{3,3} = \lambda_1 + \lambda_2 + \lambda_3 && (4.21)\\ i_2 &= \left(J_{1,1}J_{2,2} + J_{1,1}J_{3,3} + J_{2,2}J_{3,3}\right) - \left(J_{1,2}^2 + J_{1,3}^2 + J_{2,3}^2\right) \\ &= \lambda_1\lambda_2 + \lambda_1\lambda_3 + \lambda_2\lambda_3 && (4.22)\\ i_3 &= \det\boldsymbol{J} = J_{1,1}J_{2,2}J_{3,3} + 2J_{1,2}J_{1,3}J_{2,3} - \left(J_{3,3}J_{1,2}^2 + J_{2,2}J_{1,3}^2 + J_{1,1}J_{2,3}^2\right) \\ &= \lambda_1\lambda_2\lambda_3. && (4.23) \end{aligned}$$

For the analytical solution, the three invariant variables are defined in terms of $i_n, n \in \{1,2,3\}$:

$$v = \left(\frac{i_1}{3}\right)^2 - \frac{i_2}{3} \tag{4.24}$$

$$s = \left(\frac{i_1}{3}\right)^3 - \frac{i_1 i_2}{6} + \frac{i_3}{2} \tag{4.25}$$

$$\phi = \frac{\operatorname{acos}\left(\frac{s}{v}\sqrt{\frac{1}{v}}\right)}{3}. \tag{4.26}$$

The definition of ϕ is valid since $v > 0$ and $s^2 < v^3$ for real eigenvalues λ_n.

The sorted eigenvalues ($\lambda_1 > \lambda_2 > \lambda_3$) are then given by [Hasan et al., 2001]

$$\lambda_3 = \frac{i_1}{3} - 2\sqrt{v}\cos\left(\frac{\pi}{3} - \phi\right) \tag{4.27}$$

$$\lambda_2 = \frac{i_1}{3} - 2\sqrt{v}\cos\left(\frac{\pi}{3} + \phi\right) \tag{4.28}$$

$$\lambda_1 = \frac{i_1}{3} + 2\sqrt{v}\cos(\phi) = i_1 - \lambda_3 - \lambda_2. \tag{4.29}$$

These equations can be rewritten in vector notation, yielding

$$\begin{bmatrix} \lambda_3 \\ \lambda_2 \\ \lambda_1 \end{bmatrix} = \frac{i_1}{3}\left(1 + 2\sqrt{1 - \frac{3i_2}{i_1^2}}\begin{bmatrix} -\cos\left(\frac{\pi}{3} - \phi\right) \\ -\cos\left(\frac{\pi}{3} + \phi\right) \\ \cos\phi \end{bmatrix}\right). \tag{4.30}$$

Generally, for the structure tensor approach one is interested in all three eigenvalues $\lambda_i, i \in \{1,2,3\}$ for computing the rank of the tensor $\boldsymbol{J}$ as well as the confidence and type measures (see Section 5.6.2). Depending on these measures, only the eigenvector $\boldsymbol{e}_3$ to the smallest eigenvalues λ_3 needs to be computed for full flow. Otherwise, if no significant spatio-temporal structure is observed in the data, no eigenvalue needs to be computed, resulting in a significant speedup in the estimation.

From this system of eigenvalues, the corresponding eigenvectors $\boldsymbol{e}_i = (e_{i,x}, e_{i,y}, e_{i,z})^\top$ can be computed by solving the linear system of equations $J\boldsymbol{e}_i = \lambda_i \boldsymbol{e}_i$ for the ratio $e_{i,x} : e_{i,y} : e_{i,z}$.:

$$A_i = J_{1,1} - \lambda_i; \quad B_i = J_{2,2} - \lambda_i; \quad C_i = J_{3,3} - \lambda_i \tag{4.31}$$

$$e_{i,x} = (J_{1,2}J_{2,3} - B_i J_{1,3})(J_{1,3}J_{2,3} - C_i J_{1,2}) \tag{4.32}$$

$$e_{i,y} = (J_{1,3}J_{2,3} - C_i J_{1,2})(J_{1,3}J_{1,2} - A_i J_{2,3}) \tag{4.33}$$

$$e_{i,z} = (J_{1,2}J_{2,3} - B_i J_{1,3})(J_{1,3}J_{1,2} - A_i J_{2,3}) \ . \tag{4.34}$$

The sought parameter vector is given by normalizing the eigenvector $\boldsymbol{e}_3$ to the smallest eigenvalue λ_3, thus

$$\boldsymbol{p} = \frac{\boldsymbol{e}_3}{e_{3,z}}. \tag{4.35}$$

The sought velocity estimate can thus be computed from

$$\boldsymbol{u} = \begin{bmatrix} u_1 \\ u_2 \end{bmatrix} = \begin{bmatrix} \frac{J_{1,3}J_{2,3} - C_3 J_{1,2}}{J_{1,3}J_{1,2} - A_3 J_{2,3}} \\ \frac{J_{1,3}J_{2,3} - C_3 J_{1,2}}{J_{1,2}J_{2,3} - B_3 J_{1,3}} \end{bmatrix}. \tag{4.36}$$

It is emphasized, that the numerator is identical for both u_1 and u_2. Hence, altogether 38 multiplications, 23 additions, two square roots, one cos and one acos are required or roughly 65 floating point operations (FLOP). This technique of computing the velocity $\boldsymbol{u}$ from the structure tensor is thus less efficient than that from the minors by a factor of 3.

4.5 Accuracy and Performance of Results

4.5.1 Test Scenario

In order to test the validity of the novel, real time approaches, performance analyses were performed on several benchmark sequences. Tests were performed both on synthetic sequences as well as on real world sequences with ground truth.

Following Barron et al. [1994], in order to quantify the accuracy of the estimated flow, the following error measures are used. The correct ground truth flow is denoted as $\boldsymbol{u}_c$ and the estimated flow as $\boldsymbol{u}_e$. The first error measure describes the *relative error* in the velocity magnitude:

$$E_r = \left| \frac{|\boldsymbol{u}_c| - |\boldsymbol{u}_e|}{|\boldsymbol{u}_c|} \right| \cdot 100[\%]. \tag{4.37}$$

Because E_r measures only the difference between the estimated and the correct velocity magnitude, no deviation from the correct direction is captured. Therefore the *directional error* is used as a second error measure:

$$E_d = \arccos\left(\frac{\boldsymbol{u}_c \cdot \boldsymbol{u}_e}{|\boldsymbol{u}_c||\boldsymbol{u}_e|} \right) [^\circ]. \tag{4.38}$$

The value of E_d directly gives the angle in 3D between the correct velocity vector and the estimated vector and thus describes how accurately the correct direction has been recovered. Apart from the averaged error values their standard deviation will be reported to determine which range of error values can be expected.

Similar to the test sequence proposed by Barron et al. [1994], the algorithms were tested on a sinusoidal test sequence. The sequence is generated according to

$$g(\boldsymbol{x}, t) = A \cdot (\sin(\boldsymbol{k}_1 \cdot \boldsymbol{x} + \omega_1 t) + \sin(\boldsymbol{k}_2 \cdot \boldsymbol{x} + \omega_2 t)) + B(\boldsymbol{x}, t), \tag{4.39}$$

where $g(\boldsymbol{x}, t)$ is the gray value at pixel location $\boldsymbol{x}$ at time t. A represents a parameter for the dynamic range of the sequence. $B(t)$ indicates the offset of the gray values g and both $\boldsymbol{k}_1$ and $\boldsymbol{k}_2$ represent the wavenumbers of the sinusoidal in the direction of the coordinates x_1 and x_2. ω_1 and ω_2 represent the movement of the pattern in direction of the respective coordinate

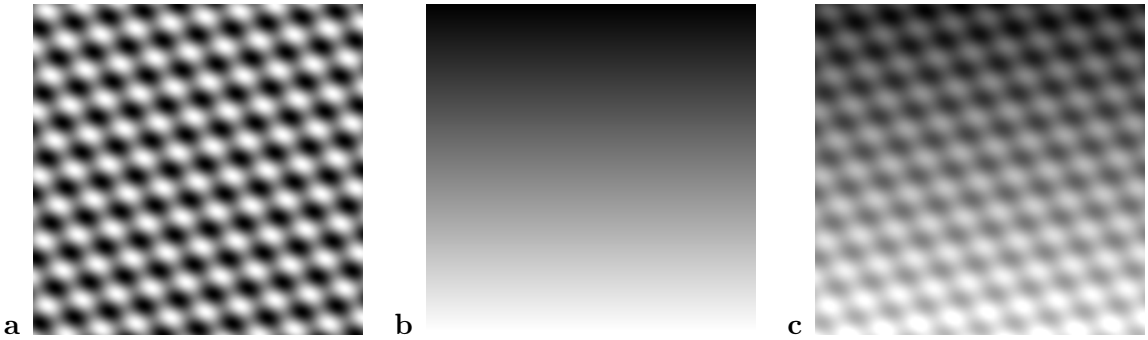

Figure 4.2: *Shown in* **a** *is the basic sinusoidal test sequence, in* **b** *the intensity change which is superimposed with the pattern of* **a**, *resulting in the final test sequence, shown in* **c**.

directions. For the simulation of a linear brightness change, two different image sequences were generated. In the first, the offset B is assumed to be a linear function of time t. The second one is stationary in time but presents a ramp in the y-direction. The wavelength used for the test sequence was chosen to be $\lambda_1 = \lambda_2 = 2\pi/k_1 = 2\pi/k_1 = 15.2$ pixel with an angle between k_1 and the x-axis of $80.5°$ and between k_2 and this axis of $-33.3°$. Two frames of such a test sequence are displayed in Figure 4.2.

For optical flow computation it is interesting to study the dependence of the computed optical flow $\boldsymbol{u} = (u_1, u_2)^\top$ depending on the noise added to the synthetic sequence. In the present context it is of equal importance to know how accurate the intensity change present in the sequence can be detected. To address these issues first a constant intensity change of $B(\boldsymbol{x}, t) = B_0 + a \cdot t$ with $a = 1.5$ gray value / frame was uniformly added to the sequence. In a second step a stationary ramp was added to the sequences, or $B(\boldsymbol{x}, t) = B_0 + a \cdot y$ with $a = 1.5$. With these two test patterns, both local intensity changes as well as global ones could be addressed. The magnitude of the flow was varied from no movement ($|\boldsymbol{u}_c| = 0$ pixel / frame) up to $|\boldsymbol{u}_c| = 10$ pixel / frame in 20 steps, with the direction of the velocity vector along the x axis, or $|\boldsymbol{u}_c| = u_1$.

Although this is not a common situation encountered in real world scenes, most gradient filters possess optimum properties along scan lines with great variations in arbitrary directions in between [Scharr, 2000]. Hence results presented here give a lower bound for movement along other directions, which will not be as accurate due to the gradients computed. Along other directions the actual performance of gradient filters can vary significantly and is subject to filter optimization [Scharr, 2000].

4.5.2 Accuracy of the Plain-, Scaled- and Mixed-TLS

The accuracy of the three alternative techniques was examined on the test sequence, namely the mixed OLS-TLS, the scaled TLS and the plain TLS estimator. Also the accuracy of detecting the optical flow $\boldsymbol{u}_e = [u_e, v_e]^\top$ under different flow magnitudes and different intensity changes was inspected.

Not all the resulting plots are presented in this paper, but some representative ones, as the

results are similar and can readily be extrapolated from the presented cases. In Figure 4.3 the relative errors of the intensity changes are shown. As was found in the previous section, also in this case the OLS-TLS estimator presents the most accurate results, while the scaled TLS estimate is prone to slightly larger errors. The unscaled TLS technique proves to be quite inaccurate, most notably on higher noise levels. Generally all estimators exhibit the highest accuracy on large intensity changes, which were varied for $B(t) = B_0 + a \cdot t$ from $a = 0.0$ to $a = 10.0$ grey value / frame in 20 steps. The accuracy of recovering the flow magnitude proved to be independent of the intensity change in the OLS-TLS estimator and depends linearly on the noise level σ. The TLS estimate is biased toward higher intensity changes.

4.5.3 Accuracy of the Accelerated Tensor Analysis

Also, the accuracy of estimating the motion parameters with the efficient techniques from Section 4.4 were tested and compared to the standard Matlab™ SVD algorithm. The analysis was repeated for thirteen different levels of iid Gaussian white noise added to the sequence. In order to cover a wide range of conditions and to extrapolate sensor noise, the variances of the iid noise chosen were $\sigma^2 \in \{0.0, 0.1, 0.2, 0.3, 0.4, 0.5, 1.0, 1.5, 2.0, 2.5, 3.0, 3.5, 4.0\}$. The noise levels of modern cameras are typically well below $\sigma^2 = 1.0$.

The results of this accuracy test can be seen in Figure 4.4. Here, the angular and relative errors E_d and E_r are pesented for the algorithm based on a singular value decompositon (SVD) implemented in Matlab. The results are identical to those obtained with the analytical solution presented in Section 4.4.3. Variations are of the order of $10^{-8}\%$, which may be neglected. In Figure 4.4, curves are presented at displacements of the sine pattern ranging from 0.01 to 10 pixel/frame in 27 steps. Presented are results for the relative Error E_r computed from the 2D displacement vector $\boldsymbol{u}$, from the constant c of linear brightness change (which is equivalent to U_3 for range flow applications), as well as the full 3D Vector $[u_1, u_2, c]$ (or $[U_1, U_2, U_3]$ for range flow). For the same quantities the angular error E_d is shown, except for c, which is a scalar quantity.
It can be seen that all error measures fluctuate in the absence of noise due to the structure of the sine pattern. The error depends linearly on the noise, which is shown in Figure 4.4**f**for a displacement of 3 pixel/frame, which represents the minimal error for the given sine pattern. The translation of minimal error depends on the wavelength of the translated gray value structure. For longer wavelength (patterns with lower frequencies) the minimum shifts to faster flow velocities, for patterns of higher frequency it shifts towards lower flow magnitudes. Generally, the basic structure of the graphs is always the same, declining slowly from high relative errors at small velocities to a minimum depending on the frequency structure of the signal and then sharply rising at higher velocities. Here, eventually the sampling theorem is violated, leading to completely wrong estimates. It should be noted that the plots presented in Figure 4.4 are drawn on a double logarithmic scale.

It was mentioned that results for the analytical solution and the SVD solution are identical. The results of the estimation based on the minors from Section 4.4.1 were a little different.

Results for the solution based on the minors is shown in Figure 4.5. In this plot, results are compared to that from the SVD computation. In the absence of noise, results are identical. However, with increasing noise the relative error E_r is much higher than that of the SVD, often several orders of magnitude. Also, erratic behavior can be seen in Figure 4.5**a** and **b**. This behavior can be attributed to a few wrong vectors computed. When correct estimates are obtainable, the velocities computed from Equation (4.19) should be identical. However, this must not always be the case. Wrong estimates were segmented by requiring the angular error between the estimates of the velocities form the minors M_{11} to M_{33} to be less than 4°. The results of these segmented velocity estimates are presented in Figure 4.5**c** and **d**. While the errors are much smaller than previously and no erratic behavior is observable, the SVD estimates are still more accurate. It should also be noted that the vector field from the SVD estimates are 100% dense, while the segmented flow from the minors is less than 60% dense. By also segmenting the velocity field from the SVD estimates to the same density as the minor estimates, the accuracy can be even further increased.

4.5.4 Discussion of Results

Concluding it can be stated that the TLS estimator exhibits a strong bias in the case of exactly known data term and thus depends highly on the noise level and intensity change present in the imagery. The mixed OLS-TLS estimator provides much better results and is in fact theoretically the best unbiased estimator under iid Gaussian noise [Van Huffel and Vandewalle, 1989]. Moreover, the reduction of computing the TLS estimate on the submatrix $\boldsymbol{J}_{\text{sub}} \in \mathbb{R}^{3\times3}$ allows more efficient algorithms, which were not possible on the full $\boldsymbol{J} \in \mathbb{R}^{4\times4}$ of the TLS problem. On these smaller 3×3 submatrices, fast techniques for solving the eigensystem problem have been presented. Computing the motion fields from the minors of the structure tensor is the fastest, only requiring 24 floating point operations per pixel. However, it turned out that this technique is not quite as accurate as the standard SVD, particularly in the presence of noise. This behavior can be attributed to the fact that this technique assumes the smallest eigenvalue to vanish. This eigenvalue only vanishes theoretically in the absence of noise and for a perfect fit of model and data. That means that it will only vanish when there is no scatter of data points around the fitted plane. In reality and especially in the presence of noise, this is

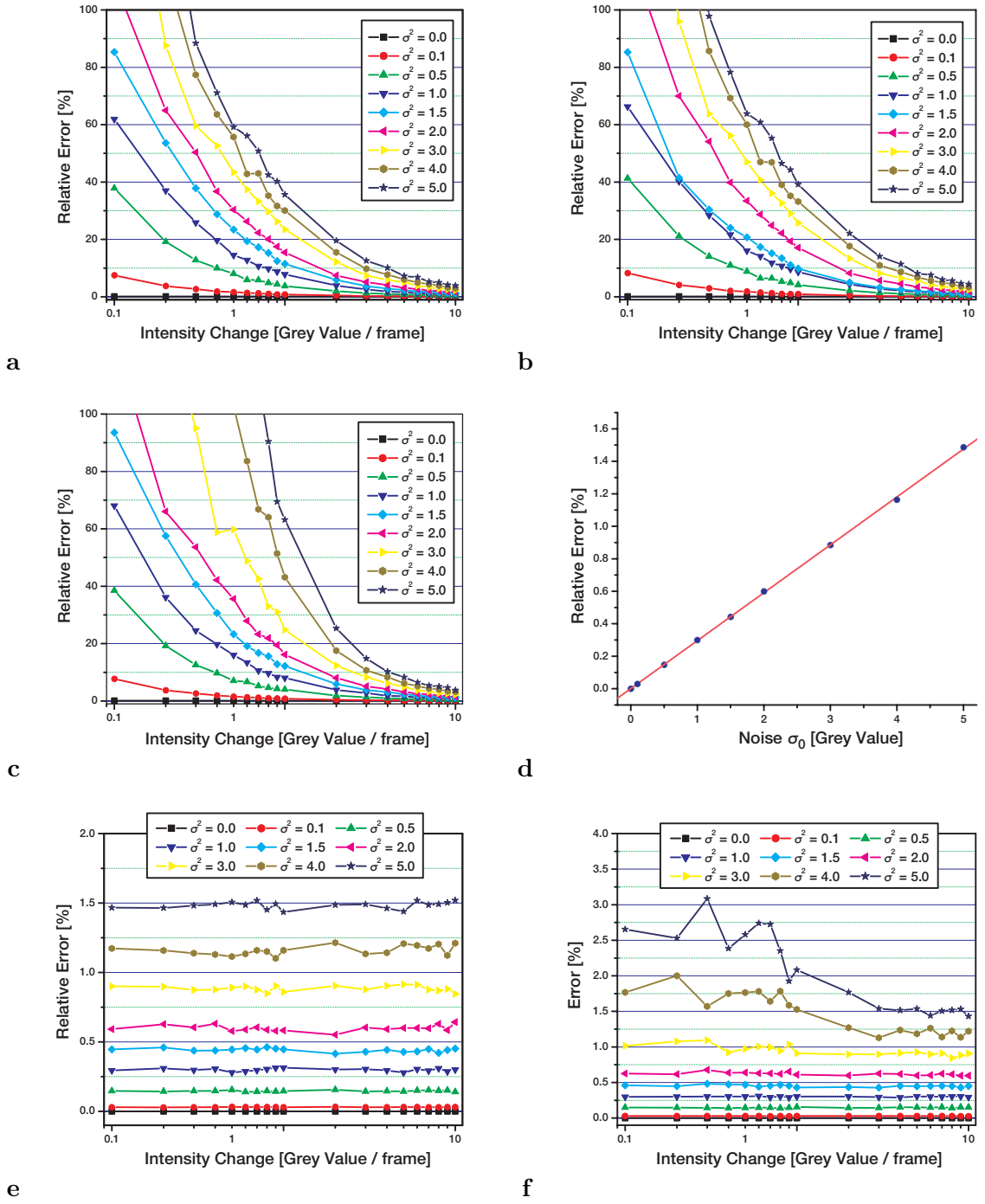

Figure 4.3: *Comparison of the relative errors in estimating an intensity change at fixed flow magnitude. In* **a** *the intensity change is computed from the mixed OLS-TLS estimator and in* **b** *with the scaled TLS estimator, proving that the OLS-TLS produces slightly more accurate results than the scaled TLS analogon. Shown in* **c***and* **d** *are the relative errors in computing the optical flow magnitude* $|\boldsymbol{u}_e|$ *for an increasing level of intensity change. While this accuracy is solemnly a linear function of noise level in the case of OLS-TLS as is shown in* **e**, *the accuracy increases with higher intensity change for TLS. The poor performance of the unscaled TLS is presented in* **f**.

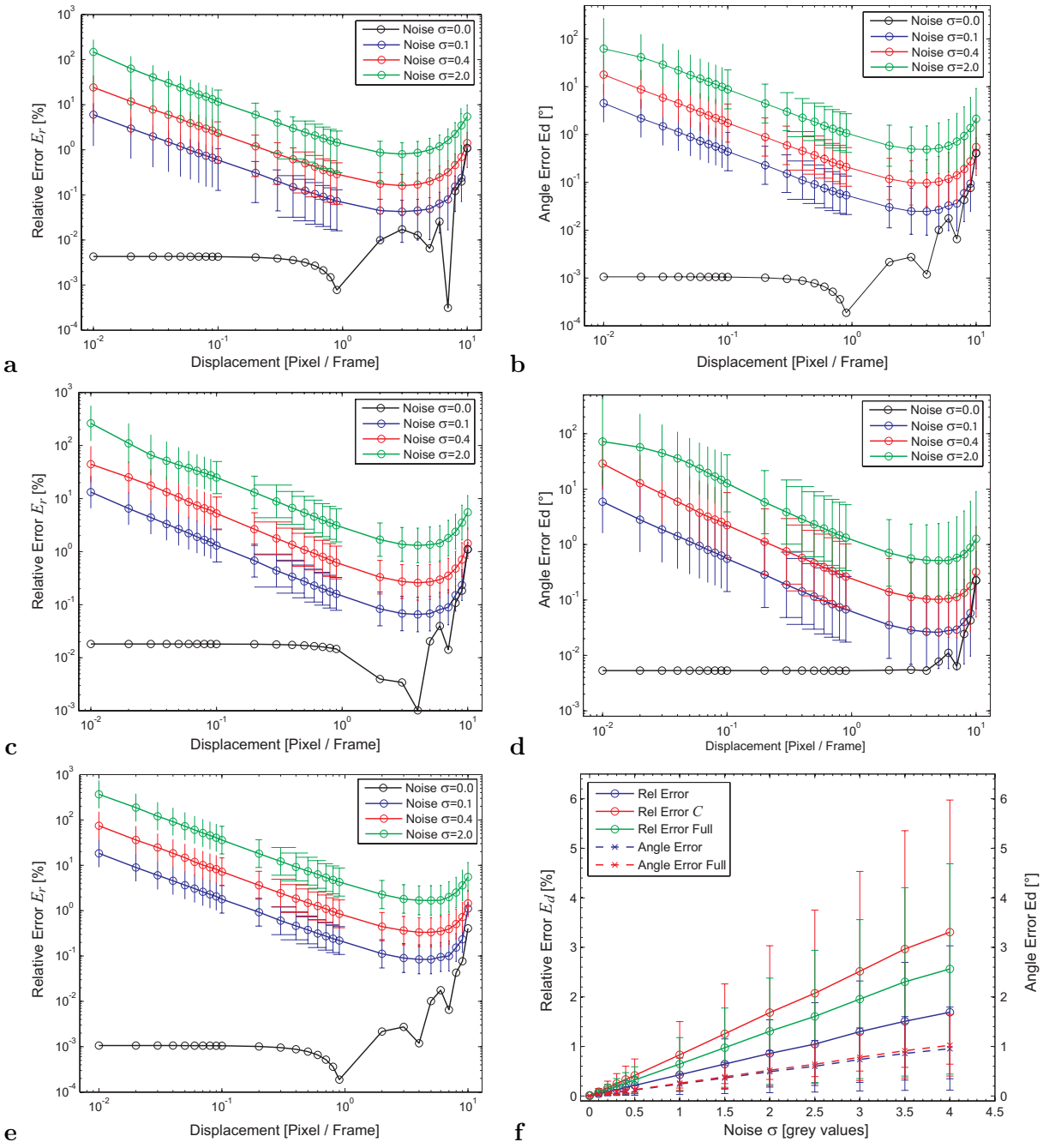

Figure 4.4: ***a*** *relative error of displacement vector,* ***b*** *angular error of displacement vector,* ***c*** *relative error of full parameter vector,* ***d*** *angular error of full parameter vector,* ***e*** *relative error of intensity change,* ***f*** *Noise dependence at displacement of 3 pixel / frame.*

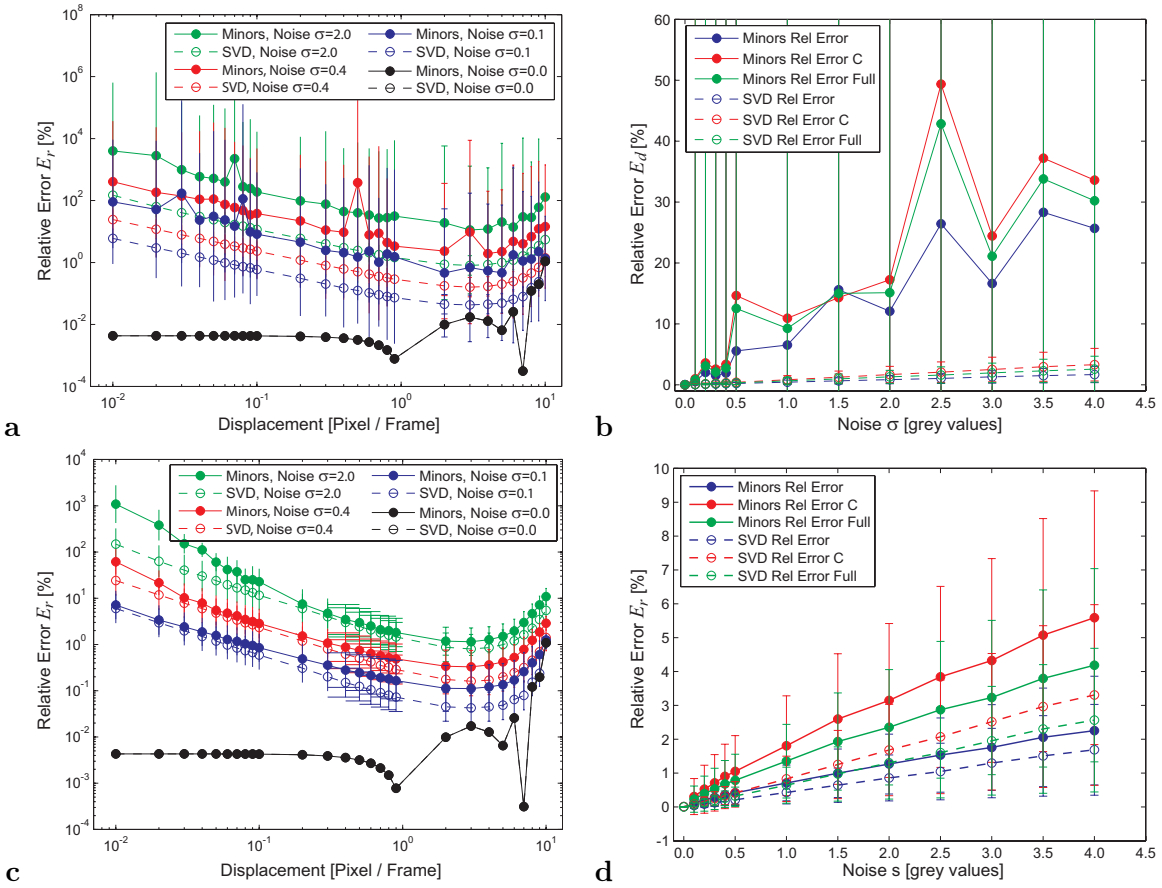

Figure 4.5: *A comparison of estimating motion from the Minors* $\boldsymbol{M}$ *or the SVD of the structure tensor. In* **a** *the relative error* E_r *for both techniques is presented for different displacements and noise levels for 100% dense motion fields. In* **b** *the dependence of* E_r *on the noise level* σ *is shown for a displacement of 3 pixel/frame. Results for the same test are shown in* **c** *and* **d**, *but this time the motion fields computed by the minors are segmented and only 60% dense (see text).*

not the case. Moreover, the magnitude of the smallest eigenvalue will directly depend on the noise level. The assumption of a vanishing eigenvalue thus induces a bias on the estimates of the minors.

A more accurate estimator turned out to be the analytical expression of estimating eigenvalues and eigenvectors of the structure tensor. This technique is not as fast as computing the minors. It requires 65 floating point operations, which is roughly a factor 3 more than for the minors. Keeping in mind that the SVD takes roughly $20 \cdot n^3 = 540$ floating point operations in total [Barlow, 2002], this technique is still faster than the SVD by a factor of 8. In contrast to the approach based on minors, no difference in estimates obtained from the SVD and the analytical solution were detected.

With the efficient techniques of estimating motion from the structure tensor, the highest computational cost has shifted from the eigensystem analysis to actually constructing the structure tensor from derivatives. A significant speed-up of the algorithm is thus achievable by finding faster algorithms in this area. Especially for computing the derivatives of image

intensities, fast implementations on graphics hardware have been presented [Hopf and Ertl, 1999]. Since the computational cost is almost insignificant between the analytical technique and the minor technique in relation to computing the structure tensor, the analytical technique is favored due to its higher accuracy. Also, from this technique all the eigenvalues can be computed without significant additional cost. These eigenvalues are vital for confidence and type measures, as presented in Section 5.

One way of significantly speeding up the estimation of motion from image sequences is implementing the efficient techniques on standard graphics hardware. The rationale is the unrivaled price-performance ratio of this hardware and a comparably easy high level language access to its functionality. The implementation and results will be presented in the following section.

4.6 Implementation on Graphics Hardware

Graphics processors achieve a high throughput for large data volumes by applying a data-stream-based computing paradigm [Hartenstein, 2003]. In particular, it deals much better with the memory gap [Wilkes, 2000], the mismatch of memory and processor performance. Among FPGAs, reconfigurable computing arrays, Processor-in-Memory or stream architectures, graphics processors are neither the most flexible nor powerful devices exploiting data-stream-based processing, but they offer an unrivaled price-performance ratio and a comparably easy high level language access to their functionality. This means that they are the platform of choice for an inexpensive image sequence processing tool. The standard structure tensor solved with Jacobi rotations [Drmac, 1997] was implemented on such hardware. Results were presented in Strzodka and Garbe [2004] and are shown here. Apart from an eigenvalue analysis based on Jacobi rotations, also the fast techniques presented in the previous sections were implemented, leading to a significant speed up. These results will not be presented here, since the speed up is similar to that for Jacobi rotations and results can easily be adapted.

In the following, first the basic algorithm, the visualization, the control of the data-flow and then the configuration of the processing elements in the graphics pipeline will be presented.

4.6.1 Computation

First, the spatial-temporal gradients $\boldsymbol{d} = [g_x, g_y, g_t]$ have to be estimated. A 3 or 5 tab isotropy optimized Sobel filter $\mathcal{D}_q$ is applied in each direction $q \in \{x, y, t\}$: $\boldsymbol{d}_q = \mathcal{D}_q g$ [Jähne et al., 1999]. Then, according to the definition of the stucture tensor from Section 3.3, the elements of the structure tensor $\boldsymbol{J}$ can be computed from the data matrix $\boldsymbol{D}$ as presented in Section 3.3:

$$\boldsymbol{J}_{qr} = \sum_{i=1}^{m} w_i \boldsymbol{D}_{iq} \boldsymbol{D}_{ir} \,. \tag{4.40}$$

Assuming that the weights w_i are chosen to be the binomial coefficients, first the 6 mixed products $(\boldsymbol{d}_q \boldsymbol{d}_r)_{qr}, q \leq r$ are computed and then a binomial filter $\mathcal{B}$ is applied. The weighting

on a 3^2 or 5^2 stencil is computed in the spatial domain. The computational cost can be further reduced by exploiting the separability of the involved filters.

The estimation of the full optical flow field $\boldsymbol{f}$ is only possible if no aperture problem is present [Hildreth, 1984]. This is equivalent to requiring that rank$\boldsymbol{J} = 2$. By analyzing the eigenvalues of $\boldsymbol{J}$ a coherence measure c_e can be computed, indicating regions where full motion can be derived. This coherence measure was introduced by Haußecker and Spies [1999] and is given by

$$c_e = \frac{\lambda_2 - \lambda_3}{\lambda_2 + \lambda_3}, \tag{4.41}$$

where λ_3 and λ_2 are the smallest and second smallest eigenvalues, respectively.

In natural image sequences large areas with negligible spatio-temporal gradients may be present. Since the trace of a matrix is invariant under rotation, trace$\boldsymbol{J}$ presents a good measure for these areas. By only computing the eigensystem of $\boldsymbol{J}$ at locations where the trace is above a certain threshold, unnecessary computational cost is avoided. This approach is refined by treating the diagonal elements of spatial and temporal gradients separately. Thus, it is required:

$$\boldsymbol{J}_{11} + \boldsymbol{J}_{22} > \tau_s \tag{4.42}$$

$$\boldsymbol{J}_{33} > \tau_t\,. \tag{4.43}$$

This condition is not fully rotationally invariant anymore, but allows a much better detection of motion irrelevant regions.

In the application concerned with the real-time presentation of selected motion features rather than ultimate precision in the estimation one can further reduce the computational load without significant loss of accuracy. First, the spatial resolution of the images is reduced with a down-sampling step. This is legitimate since in a real-time display the user is not able to draw any information from a single pixel anyway, and often a smoothing step for the visualization of the motion is applied (Section 4.6.2). After the computation the images are scaled up again for display. The down-sampling is not critical as long as the texture information, which is crucial for the diversification of the structure tensor elements, is not lost. Typically the VGA format (640×480) is scaled to 320×240.

For frame rates higher than 25Hz the temporal resolution of the image sequences is reduced. To avoid temporal aliasing the regularized gradients still use the full temporal resolution and only the time intensive eigenvalue analysis skips intermediate images. Thus, artefacts that would be introduced by a mere sub-sampling are eliminated. At the same time a significant speed up is achieved. This step could be eliminated by employing the fast analytical approach for computing the eigensystem as presented in Section 4.4.3 instead of the Jacobi rotations used here.

4.6.2 Visualization

In this section the visualization process from the raw velocities to the display of motion features in the image sequence will be outlined. Figure 4.6 accompanies the explanation of

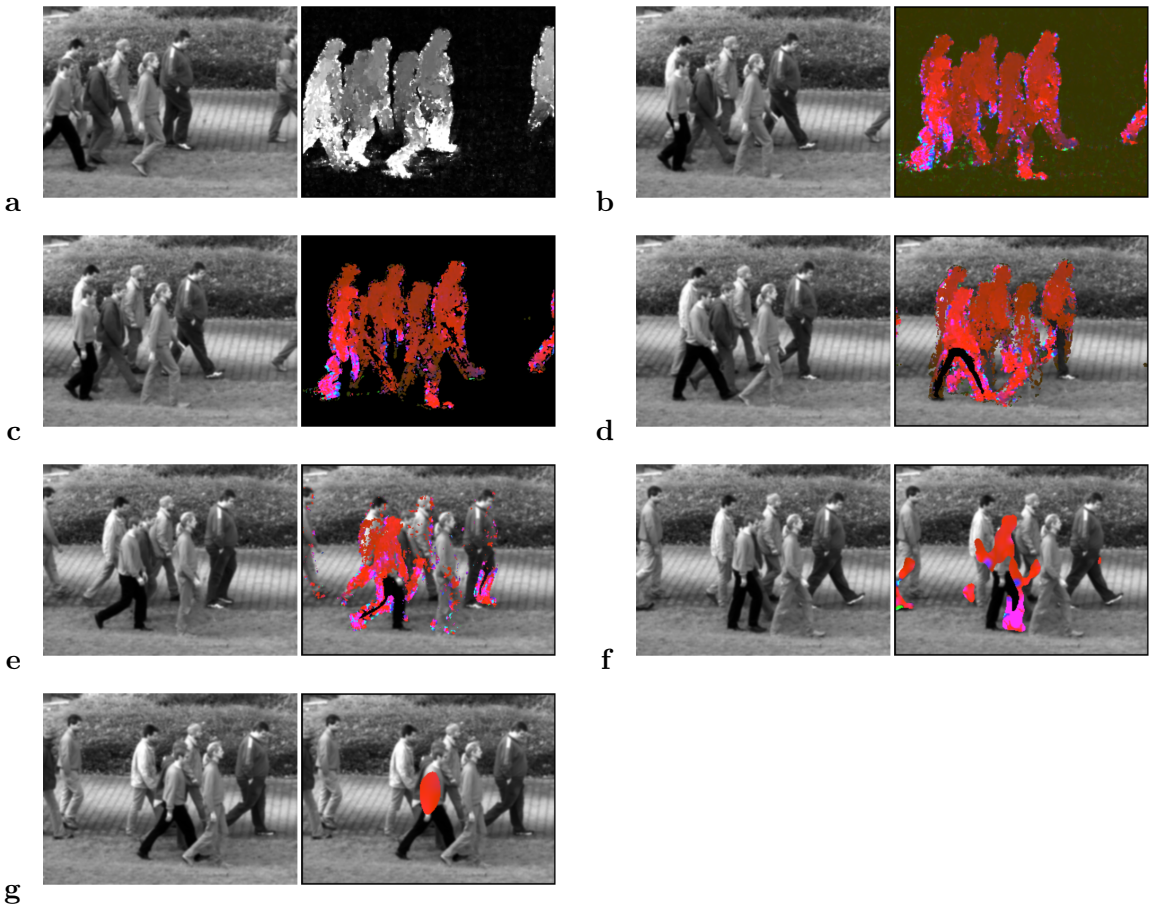

Figure 4.6: *The steps of the visualization pipeline described in Section 4.6.2. Every fifth frame of the sequence is shown.*

the individual steps of this process.

Coloring

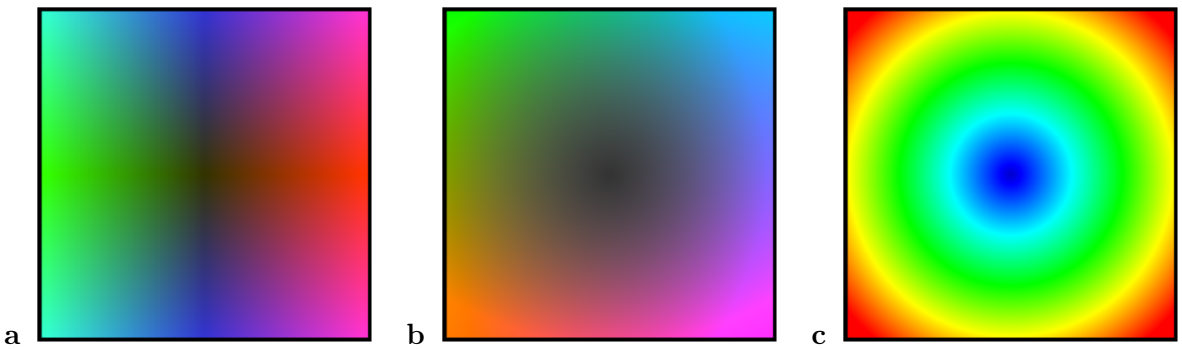

Figure 4.7: *Color maps used for the coloring of the velocities.*

From the motion estimation an image with the estimated x and y velocities $\boldsymbol{u} = [u_1, u_2]$

is obtained. In Figure 4.6**a** the modulus of the velocity can be seen as intensity. Visual representation of vector fields is an extensive topic of its own. However, in real-time image sequences there is little time for computation and the user has only a fraction of a second to perceive and understand the images. A reliable method for conveying a qualitative picture of the motion is to use color. Color is especially useful to catch the eye of the observer in an otherwise gray image [Travis, 1991].

A 2D color map is used to represent the motion field. Theoretically each location in the color map is assigned a different color, such that all directions can be unambiguously distinguished. But it is illusionary to think that this information can correctly be interpreted in real-time. It is more advisable to adapt the color map to the application in mind. For the test sequences of walking people, a map which helps to distinguish the differences in x velocity is used, with the y axis being poorly represented (Figure 4.7**a**). Figure 4.7**b** shows a map which represents all directions equally well. However, this color richness can be often more confusing than helpful and so for the medical data sets, either a rainbow encoding of the velocity modulus (Figure 4.7**c**) or even a single color is applied. Here often the fading explained below is better suited for conveying the motion. From the implementational point of view any texture with a color map could be used. Figure 4.6**b**is an image of the test sequence after the first coloring step.

Blending

The motion estimator works adaptively only on regions which yield sufficiently pronounced spatio temporal structures, which is reflected in the rank of the structure tensor (Equations (4.42) and (4.43)). This saves a lot of computation time in typical sequences as can be seen in Figure 4.6**c**, where the uncomputed area is displayed in black. Despite the air irritations visible in 4.6**b**, most of the background is omitted upon Equation (4.43), while the homogeneous black in the trousers violates Equation (4.42). Areas with a strong aperture problem as computed from Equation (4.41) are also masked out. For visualization purposes this empty area can be used to blend in the original image sequence as shown in Figure 4.6**d**.

Region of Interest

In general the motion field contains velocities of various scales and in a given application. Very often only a small subset of them is of interest. Also at spatial and temporal (very fast motion) discontinuities one can still obtain erroneous results despite the culling based on the quality measure (Equation 4.41). Therefore, the region of interest is identified on the velocity modulus or by other simple measures. In Figure 4.6**e** the faster moving person was highlighted in this fashion.

Smoothing

The previous selector determines the visible value range of the velocities. This produces regions of similar velocity but different size. Here their size and form can be used as a criteria

to differentiate between them. For this purpose, a hierarchical smoothing scheme is applied which smooths the characteristic function of the selected regions on each level. The spatial scale of motion regions are selected by thresholding the obtained values. The preference of this process for regions, expanded in a certain direction, can be influenced by changing the weights of the smoothing mask. The scheme applies the smoothing also to the velocities themselves to obtain a better visual representation. Figures 4.6**f** and **g**show the results after the application of 3 and 5 smoothing steps in the hierarchy respectively.

In the sequence from which Figure 4.6**g**has been extracted only the faster moving person is marked by the display of the motion region. All other motion regions, though similar or even higher in velocity, are masked out. This masking is very general and does not require any knowledge about the objects or type of motion. However, if this knowledge is present it could help to provide even finer feature distinctions. In future, the integration of one of the many motion segmentation techniques, which can incorporate such a-priori information, should be considered. In fact, the test sequence has been chosen to demonstrate that even very similar motion features can be distinguished. Certainly, this result requires a careful setting of the four parameters for the velocity selection and smoothing, but the more pronounced the differences are, the less parameter tuning is needed.

Fading

In some applications one is not only interested in the display of the current motion field, but one wants to visualize the regions already effected by previous motion also. In angiography, for example, the flow of blood marked by a contrast agent is of great interest to the physician. But the motion estimator can only compute velocities at the front of the in- or outflowing agent. Without further processing the visualization of these velocities results in a confusingly fast rush of colors through the image sequence. Such sequences also have a lower temporal resolution, so that the motion estimates at any individual time point are not as reliable as their weighted integration.

During the streaming of the sequence, for each pixel location the point in time at which it represented a non zero velocity is recorded. This information is used to display a fading of the recorded motion. Figure 4.13 shows the benefit of this visualization method.

4.6.3 Data-flow

First it is assumed that the individual images of the image sequence lie in main memory. The images are transported one by one to the graphics card with an asynchronous mechanism (pixel buffer objects), which allows the card to continue the current computation during the transfer. For this several circular buffers are used on the card. Subsequent images load to a buffer position which is not needed in the concurrent computation. Each image is read only once, so that the AGP bus provides sufficient bandwidth in comparison to the number of on-card operations as not to decrease the overall performance. Because all steps of the algorithm are performed on the card, no additional memory transfers are needed. The final result is

displayed directly from the graphics memory onto the screen. Using the graphics card as a "co-processor" for the optical flow computation and transferring the flow estimates back into the main memory was not feasible across the AGP bus due to bandwidth restrictions. Novel architectures such as PCI Express with its higher bandwidth in both directions will abolish this restriction.

On the graphics card the images are represented as pbuffers. These buffers are 2D data arrays which can serve either as a source (texture) or a destination of data streams (see Figure 4.8). The operations of the algorithm are performed by streaming the texture operands through the appropriately configured graphics pipeline (Section 4.6.3) to a target pbuffer. The target pbuffer can then be used as a texture operand in the succeeding operation. Because several such passes are required by the algorithm, mainly floating point pbuffers are employed to retain sufficient precision in intermediate computations.

As long as the same operation is applied to all pixels of the image sequence, the implementation is very fast, as the efficiency of the pipeline grows with the size of the streams. The handling of adaptive exclusion of certain regions from computation requires the use of smaller streams. This process is described in Section 4.6.3.

Currently it is assumed that the image sequence is stored in the main memory. Since each image is transferred only once, the algorithm would work just the same if the images arrived from an external source at a certain memory address one by one. Such a source could be a video camera or any other video stream. In fact, it is possible to decode a video stream in real-time on the CPU, while the graphics processor works on the motion estimation and visualization.

Pipeline Configuration

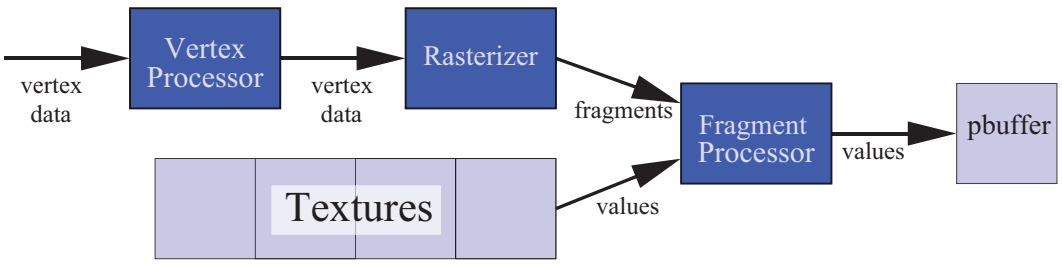

Figure 4.8: *A simple diagram of the DX9 graphics pipeline. Light gray represents data containers, dark gray processing units. In each pass a different texture can serve as the target pbuffer for the output data stream.*

The DX9 graphics pipeline contains two freely programmable parts, the vertex and the fragment processor, as shown in Figure 4.8. The vertex processor mainly manipulates the input vertex and texture coordinates and vertex color. The hard-wired rasterizer interpolates these values for each pixel in the primitive which is currently being drawn, e.g. a triangle. The interpolated values associated with one pixel location are called a fragment. They are manipulated by the fragment processor. The fragment processor combines the fragment data

```
motion estimation {
    start loading of image for next iteration
    sample down current image
    compute optimized gradient with Sobel masks
    assemble the weighted structure tensor
    classify irrelevant regions for culling
    compute motion estimates through
      an eigenvector analysis of the tensor
}
visualization {
    select a range of velocities
    smooth the selected motion regions hierarchically
    record the selected motion areas
    visualize the result: coloring, blending, fading
    display the result
}
```

Figure 4.9: *Overview of one iteration of the main algorithm. Apart from the loading, each line corresponds to the configuration of the fragment processor with the corresponding program and the streaming of the texture operands through the so configured graphics pipeline (see Figure 4.8). Some operations require several passes with slightly different configurations, e.g. smoothing in x and y direction.*

with additional values from up to 16 textures to determine the output value for the current pixel. Each vertex and each fragment is processed independently of the others in the same data stream. Therefore, they can be processed in parallel very quickly. The processing of streams achieves highest performance if the data streams are large and the texture access in the fragment processor uses only neighboring texture values, such that internally bandwidth-efficient memory burst-modes can be used and latency can be hidden with small caches.

The fragment processor bears most of the computational burden in image based problems such as the one presented here. The vertex processor is used only for the generation of texture coordinates to the neighboring values in a texture, whereas each step in the algorithm sketched in Figure 4.9 requires a different configuration of the fragment processor. The design of the configurations was developed in Cg [NVIDIA, 2002], a C-like high level graphics programming language.

The assembly of the structure tensor is implemented according to Equation (3.11) as several passes with configurations for the separable binomial $\mathcal{B}$ and optimized Sobel $\mathcal{D}_q$ filters [Jähne et al., 1999; Scharr, 2000, 2006], and the mixed products $(\boldsymbol{d}_q \boldsymbol{d}_r)_{qr}, q \leq r$. On the other hand, the eigenvector analysis executes in a single pass with a large configuration which performs a constant number of cyclic Jacobi rotations [Drmac, 1997] on $\boldsymbol{J}$. The approximate eigenvectors and eigenvalues are used to estimate the velocities (c.f. Section 3.3) and the coherence measure (Equation (4.41)).

The hierarchical smoother in the visualization pipeline is again a series of filter applications. A multi-grid approach was used to quickly incorporate information from farther regions in the smoothing process. Smaller grids were not generated in that process. This results in the loss of computational savings of smaller grids. The advantage is that on all pixels is operated in the same manner. This results in the advantage of being closer to translation invariance at the added cost of a few extra computations.

The eigenvector analysis of the tensor is by far the longest and thus most demanding fragment program with almost 300 assembly operations for 9 Jacobi rotations and the motion estimation. The main visualization program (coloring, blending, fading) is the next larger with approximately 50 operations. Most configurations have less than 10. Therefore, it makes sense to design an adaptive scheme which skips the eigenvector analysis for irrelevant data. Also, the more efficient techniques of computing the velocity from the minors, as presented in Section 4.4.1, or using the analytical algorithm for computing the eigensystem, as shown in Section 4.4.3, have been implemented. These techniques increase computational efficiency by a factor of 5 or higher.

Adaptivity

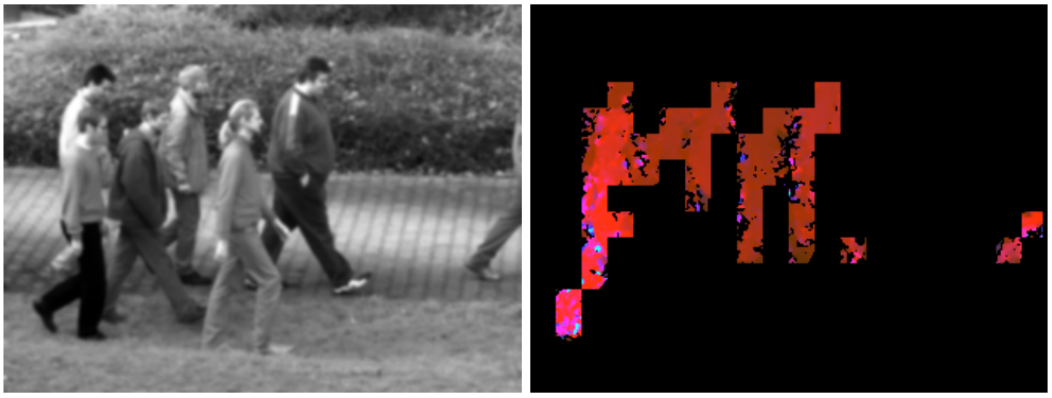

Figure 4.10: *The visible tiling in the adaptive scheme for much too aggressive culling. In Figure 4.6**c** the standard setting is used.*

By analyzing the structure tensor, computation of eigenvectors in areas which do not contribute significantly to the motion field can be skipped (see Equations (4.42) and (4.43)). However, the introduction of efficient dynamic adaptive processing in graphics hardware is not straight forward. There exist per-fragment tests in the graphics pipeline which skip further processing depending on predefined masks and values of the fragments. But these are not very efficient, because they cannot exclude larger areas from processing at once. The fragment processor can also discard fragments, but in such a case the whole fragment program is still executed and only the final result is discarded. Significant speedup can currently be only obtained by culling areas on the vertex level.

The image is divided into tiles, each of which generates a data stream much smaller than the whole image. Smaller streams reduce the efficiency of the pipeline. But this effect is compensated to some extent by the graphics driver. This can efficiently catenate the individual data streams if their defining geometry is given in advance, ideally in a server sided vertex buffer object. A classification step determines which tiles need to be processed further and which can be skipped in the following. The classification step can be performed by combining the data of each tile to a single value and retrieving the values of all tiles with a single read-back to the main memory as in Lefohn et al. [2003], where this technique has been introduced.

A different classification step is used which avoids the read-back by exploiting the occlusion test functionality. The test counts the number of passed fragments at a late stage in the graphics pipeline. The counters can asynchronously be retrieved from the graphics driver, i.e. they do not stall the ongoing computation. By discarding fragments upon the conditions in Equations (4.42) and (4.43), the number of motion relevant pixels in each tile can be obtained. Subsequent processing of this tile can be skipped if the number is below a certain threshold, such as 5%. The transition from Figure 4.6**b** to **c** demonstrates the savings. The tile structure becomes visible if one skips tiles with too many relevant pixels, e.g. 90% in Figure 4.10. For entire images the efficiency of the occlusion test has already been demonstrated in Goodnight et al. [2003]. See also Coombe et al. [2004] for a similar tile based testing.

4.6.4 Results

Two types of image sequences have been shown as examples: the test sequences of walking people to demonstrate the tool's ability to distinguish similar motion features, and an angiography sequences for the enhancement of blood flow. Scientific applications such as those presented in the second part of this thesis will not be addressed here. They will be scrutinized later on and the test sequences of this section are better suited for demonstrating other uses and properties of the implementation.

Motion Features

The sequences with walking people have been recorded in VGA (640×480) format at 100Hz. The computation takes place on reduced 320×240 images. The eigenvector analysis runs on every fourth image resulting in a real-time requirement of 25Hz output frequency. Section 4.6.4 discusses the performance results.

Figure 4.6, discussed in Section 4.6.2, shows the individual steps which made it possible to visually extract the feature of the slightly faster moving person despite smaller regions (arms, legs) of higher velocity. Figure 4.11 shows another sequence of the same kind. In the above examples the parameters must be set carefully to obtain the visual distinction with such clarity. But it is obvious that a higher velocity difference requires only a rough selection of the visualization parameters. For example, for the task of marking persons who move in the wrong direction only the sign of admissible x velocities must be set correctly (Figure 4.12).

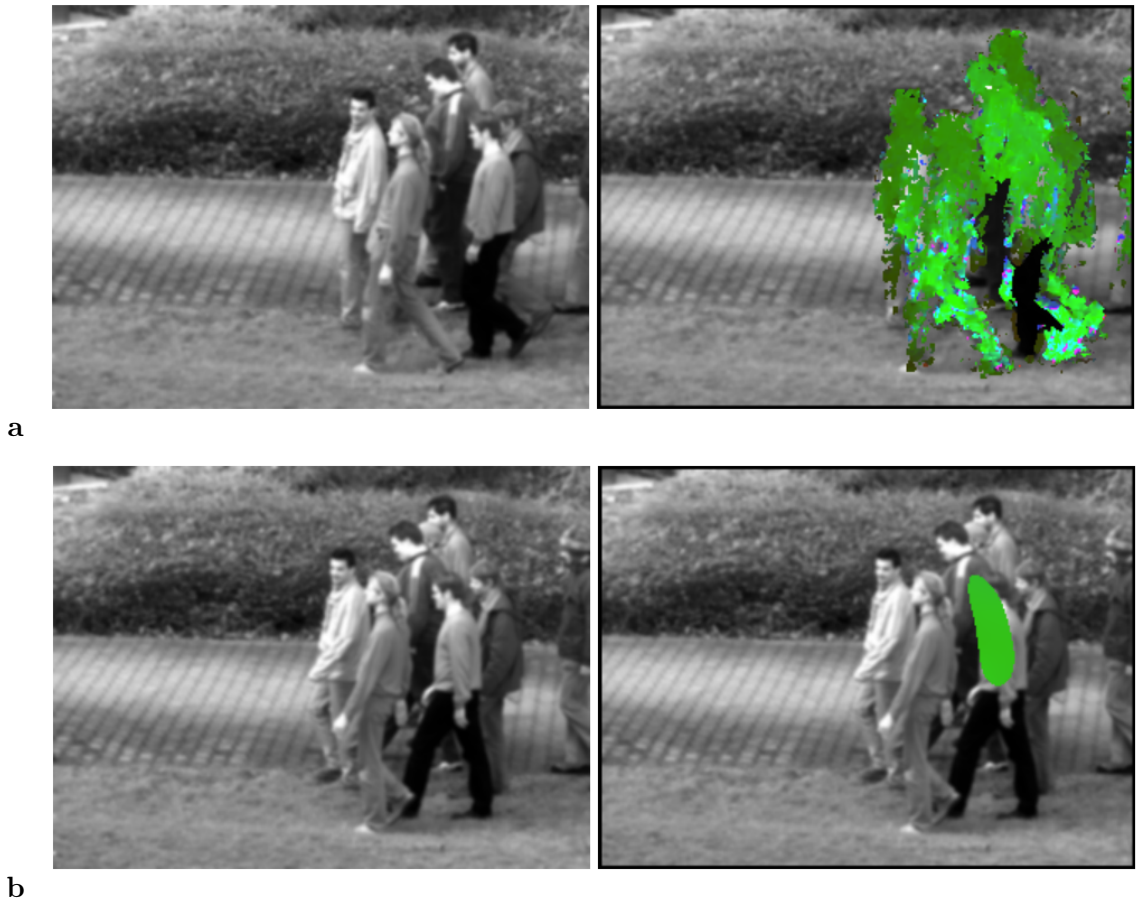

Figure 4.11: *Visual emphasis of faster moving persons. In* **a** *only the slightly brighter green conveys the qualitative velocity difference. The visual mark makes it much clearer in* **b**.

Flow Enhancement

The angiography sequences have a resolution of 1024×1024 at 20Hz. The computation takes place on 256×256 images, without a reduction of the temporal axis.

The first example in Figure 4.13 shows the blood flow in a kidney. It can be seen that the fading of the color helps to understand the distribution of the motion. In the second example shown in Figure 4.14 the motion regions are recorded over a certain spatial scale to help in finding turbulent areas in the vascular system.

Performance

All results were computed with a GeForceFX 5800 Ultra 500MHz graphics processor. Comparisons were conducted on a cache and SSE optimized version of the motion estimator on a Pentium 4 2GHz-FSB400 machine. At the time of these tests, the comparison is still in favor of the micro-processor, since the FX5800 is an old DX9 chip and the performance difference

a

b

c

Figure 4.12: *Marking of people who move in the wrong direction. Despite the occlusion the visual emphasis is very accurate.*

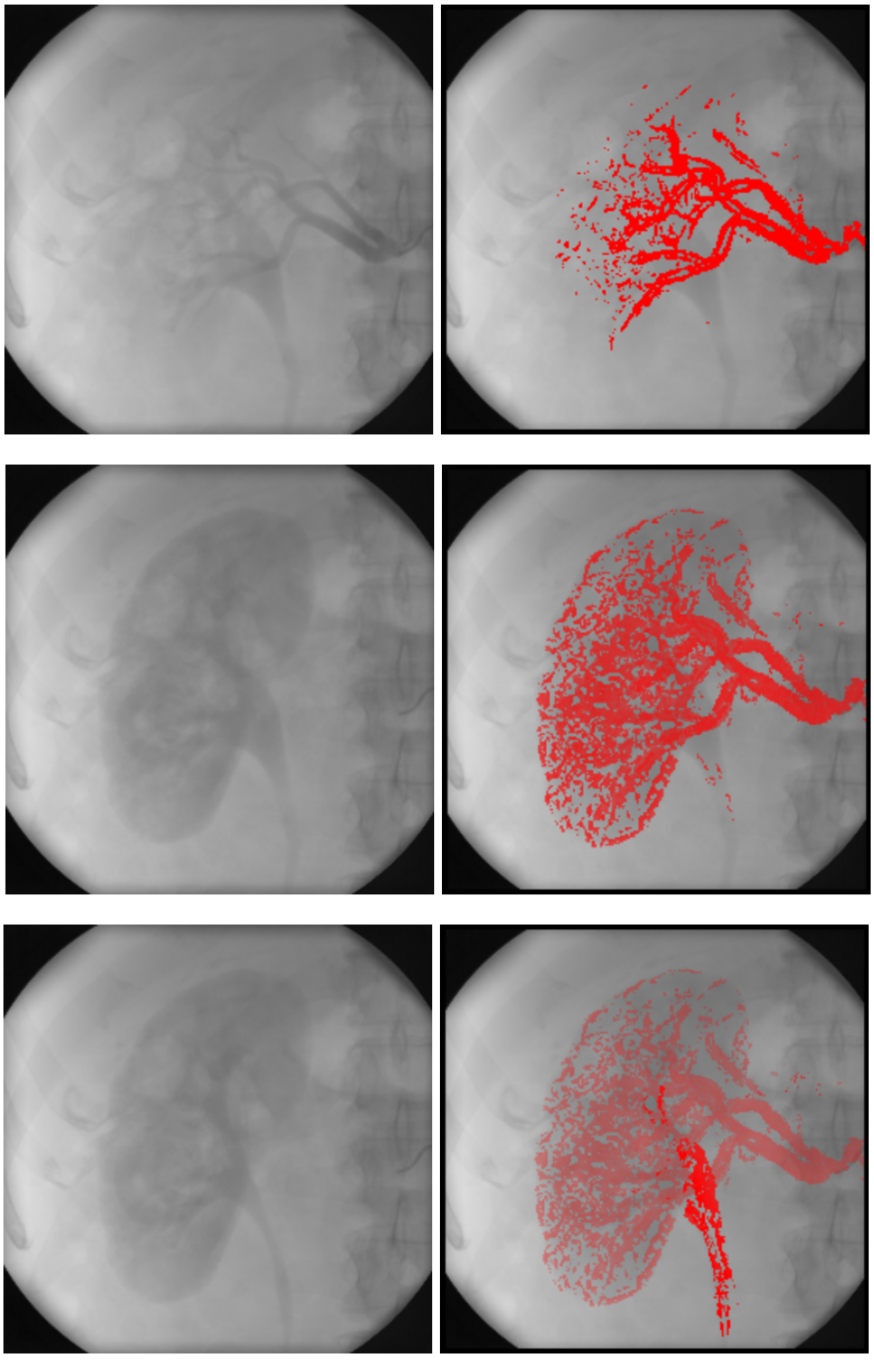

Figure 4.13: *High velocities detected in the blood flow emphasized by a color fading. At the time point of frame* **b** *no velocities can be detected, so that without the fading the frame would not show any color at all.*

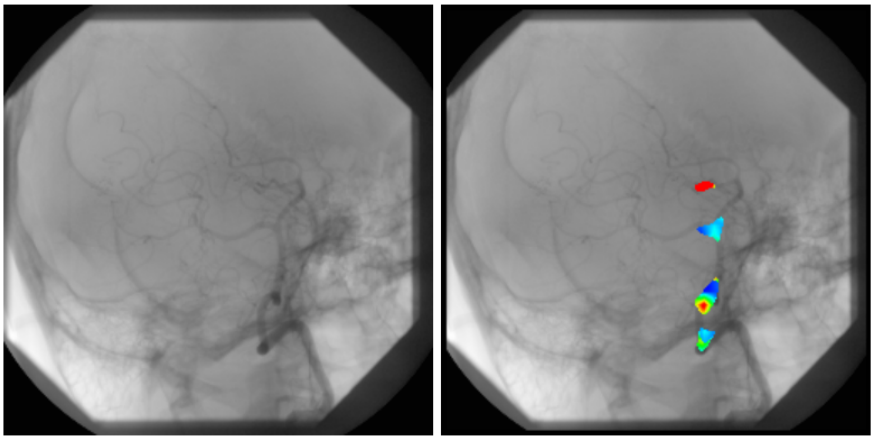

Figure 4.14: *Detected regions of wide-stretched motion in the vascular system. Color indicates the modulus of velocity.*

to the current graphics processors is larger than between the older and more recent Pentium 4 systems [Strzodka and Garbe, 2004].

Sequence	Loops	P4	FX5800	Speedup	Est.+Vis.
Figure 4.6	403	22.4	5.0	4.5	6.0
Figure 4.11	353	19.8	4.3	4.6	5.2
Figure 4.12	303	17.7	3.8	4.7	4.6

The last column shows the graphics hardware timings for the whole process, i.e. motion estimation and visualization. A 4.5 speedup factor was achieved, which is a good value for this computationally intensive problem, in which the micro-processor benefits from its higher internal clock. The algorithm is bound by the fragment processor performance due to the long assembly program for the eigenvector analysis. The program is long despite an hand-optimized vectorization, because 3 consecutive sweeps are computed uniformly on the 3 distinct sub-diagonal elements of the structure tensor. In a software program the choice of sub-diagonal elements within a Jacobi sweep and the overall number of sweeps can be reduced dynamically depending on a user given tolerance. The algorithm would also benefit from the proposed feature of dynamic branching in graphics hardware. However, as of May 2004 a quadrupled speedup is expected simply from the fact that the upcoming generation of graphic cards presumably has four times the number of arithmetic units as the FX5800. In practice this would mean operating in real-time on full VGA image sequences. By employing the fast algorithms presented in Section 4.4, further performance gains up to a factor of 5 or more are conceivable.

4.6.5 Discussion of Results

In this section a tool for the real-time motion estimation and visualization of image sequences has been presented. The precise, dense motion estimation allows to visually distinguish even

very similar features through appropriate post-processing steps. This makes this tool interesting for surveillance applications, as well as for process controll or in observations of scientific measurement. The visualization pipeline contains several stages which can be easily controlled to serve the needs of different applications. Other hardware systems perform even more time consuming motion analysis in real-time but at a much higher price. For the tool presented here, a simple camera and a standard PC with a DX9 graphics card suffice, because efficient use is made of its data-stream-processing capabilities.

The current version implements the basic motion estimation based on the BCCE as well as linear brightness change or range flow as presented in Section 2.5.2 and 2.6 . The tool can also be adapted for other models introduced in Chapter 2 or to multiple transparent motion as presented by Mota et al. [2001].

4.7 Conclusion

In this section different techniques of increasing the efficiency of the structure tensor approach were presented. Fast techniques were presented to decrease the number of floating point operations for the associated eigenvalue analysis. Here computational cost was reduced from 1890 FLOPs for ten sweeps of a Jacoby rotation on a 3×3 tensor to just 24 FLOPs by computing the eigenvector to the vanishing eigenvalue from the minors. For motion models of linear brightness change or range flow, an eigenvalue analysis of a 4×4 matrix is required in standard total least squares approach. Due to the structure of the underlying data matrix, this would result in a bias in the estimates and high computational costs. The bias can be reduced by the mixed OLS-TLS estimator presented in Section 3.4.4. A very efficient way of performing this computation has been presented here, which reduces the eigenvalue analysis of that of a 3×3 submatrix. Hence a significant speedup results for the parameter estimation of these motion models. This is also due to the fact that the aforementioned techniques can be applied to this 3×3 submatrix. The accuracy of these techniques was tested on synthetic sequences, confirming the high level of accuracy of these techniques.

Another significant speedup can be achieved by implementing these algorithms on standard graphics hardware. This is a very appealing concept, since performance increases by a factor of better than 5 is attainable at a modest cost of this hardware. This is due to the highly parallel streaming architecture of these GPUs. Applications of pedestrian detection and a medical visualization were demonstrated. All the processing pipeline from motion estimation to visualization were performed in real time.

Chapter 5

Characterization of Estimates

5.1 Introduction

In Section 3 gradient based techniques have been presented for the estimation of parameter fields from image sequences. This section will be mainly concerned with different methods of characterizing these estimates. An overview of some measures presented in literature will be given which will then be compared to each other on synthetic as well as on real world test sequences. A number of extensions will also be presented along with newly developed measures. These results will be published in Nieuwenhuis et al. [2007].

A confidence measure is defined as a mapping m from the image sequence and the two-dimensional displacement vector field to the interval of confidence [0..1], that is

$$m : \mathbb{R}^3 \times \mathbb{R}^2 \longmapsto [0..1]. \tag{5.1}$$

It can be used as a measure for the correctness of each displacement vector based on information derived from the image sequence and/or the displacement field.

As it turns out two types of measures can be distinguished that are commonly both referred to as confidence measure in literature. These are true *confidence measures* and *situation measures* also referred to as *type measures*. While both of these measures can in principle be used to mark the reliability of a flow field, they are not equally well suited for this task.

Confidence measures derive information from the image sequence and the flow field in order to judge the reliability of a given displacement vector.

Situation measures use the image sequence or filtered information thereof to detect situations for which the calculation of the correct displacement field is impossible. Such situations comprise occlusions and the aperture problem among others.

From this description it follows that situation measures are not able to detect errors in the flow field, since no information from this field is used for computing them. They are not able to distinguish between correct and incorrect displacement vectors, since the underlying

situation might be the same for both. Still, often these measures are used for determining the reliability of a flow filed by interpreting the presence of such situations as a low confidence.

There are numerous important applications for confidence and situation measures. Reliable confidence measures can provide valuable information for the improvement of optical flow methods, for example displacement vectors classified as unreliable can be left out in the result leading to a sparser but more correct displacement field. Another possibility to improve the field could be to let the parameter that controls the smoothness of the field depend on the confidence. Such an approach was presented in Section 3.5.4.

On the other hand, situation measures can be used in image sequence reconstruction where pixels with occlusion need to be found in a first step before the image can be reconstructed in these places. These occluded regions could be identified by a situation measure specialized on occlusion. There are numerous valuable applications for confidence and situation measures. One can go as far as stating that an estimated displacement vector without an associated confidence has no value, especially for scientific applications. For this reason, in this chapter an extensive examination and comparisons of confidence and situation measures for optical flow methods known from literature will be conducted. It succeeds the paper of Barron et al. [1994], where the authors presented different methods and associated confidence measures for the computation of optical flows and compared the performance of these techniques. Concerning confidence measures they qualitatively compared the performance of measures mentioned for each method separately. Here this comparison will be extended to a quantitative analysis over all confidence and situation measures. The results of this analysis will be published in Nieuwenhuis et al. [2007].

Even though confidence measures are of universal importance in the estimation of accurate optical flow fields, this area of research has been neglected in literature. One could even go as far as stating that most confidence measures that were proposed can be categorized as situation measures of sorts. The only attempt to define real confidence measures for optical flows has been made recently by Bruhn and Weickert [2004]. The idea relies on the fact that variational motion estimators define an energy that is minimized during the computation of the displacement field (see Section 3.5 for more details). Therefore Bruhn and Weickert [2004] argue that for variational approaches it always makes sense to use the inverse of the energy of the minimizer at every pixel as confidence measure. This shows exactly how well the motion model is fulfilled at each point in the image sequence. Furthermore they state that any other confidence measure with better performance should be integrated into energy functional. They conclude blatantly that for these reasons the inverse of the energy is the only real confidence measure for optical flows.

Following this rationale, there would be no ground for a comparison of confidence measures but for situation measures at most. Nevertheless two reasons might be put forward why paying a closer look at these measures does indeed make sense:

1. Other motion estimators like the method by Lucas and Kanade [1981] or the approaches from Section 3.3 do not minimize an energy functional explicitly in the estimation process. For these approaches the equivalent would be the inverse of the residual of the fit,

which is proportional to the inverse of the smallest singular value. Also, it could be possible to derive confidence measures that cannot be formulated by an energy functional. Such measures could be based on approaches from machine learning, for example.

2. In practice it is undesirable to formulate estimators with a high complexity functional. This is on the one hand due to computational cost and on the other hand due to the fact that such functionals will no longer be convex any more. Complex energy functionals will thus lead to the increased risk of converging to a local minimum, making the optimization process less reliable.

Generally, in literature it is assumed that confidence measures are innate to the motion estimator framework. Thus measurements of the structure tensor have never been applied to variational approaches or vice versa. In this chapter it will be shown that it is often beneficial to make use of other measures, not inherent to the framework used for the estimation of motion.

In addition to the review of confidence and situation measures from literature, new measures are presented which were found to be missing previously. It is proposed that situation measures do not necessarily have to be based on the image sequence. Instead, they can derive their information only from the flow field. In a way this is similar to image driven of flow driven regularizers in variational estimators as shown by Schnörr and Weickert [2000] and Weickert and Schnörr [2001]. Therefore, smoothness terms of variational techniques [Schnörr and Weickert, 2000; Weickert and Schnörr, 2001; Brox et al., 2004] will be used as situation measures. In this fashion occlusions can well be detected in TLS approaches. Currently, no confidence measures other than the inverse of the energy functional of variational approaches has been proposed in literature. Therefore, the inverse of several fidelity terms typically used in variational approaches are used as confidence measures.

Finally, a possibility is presented to extend any given confidence measure to both a situation measure that is able to detect three different situations at the same time and to an improved confidence measure that takes into account the local surroundings of the displacement vector. These two extensions will be termed *surface situation measures* and *surface confidence measures*, respectively.

5.2 Data and Output Functions

Each situation of confidence measure consists of two parts: 1) a data acquisition method and 2) the output function. The data acquisition method is used to acquire the confidence data, for example a filter response such as the gradient at a pixel location. However, this confidence data by itself cannot be used as a confidence measure, since the value is generally not in the interval between 0 and 1. Also, very often this confidence data is an inverse of what would be defined as a confidence measure. Therefore, monotonous output functions on the data need to be defined that perform the mapping of the confidence data to the interval $[0 \dots 1]$. Assuming that the data values returned by the data acquisition methods are non-negative, the following two output functions were found to be useful for different situations:

1. For data d naturally bounded to a closed interval $[min, max]$:

$$c_{\text{bound}} := \frac{d - min}{max - min}. \tag{5.2}$$

2. For data d which is not bounded to a fixed range:

$$c_{\text{unbound}} := \frac{d^2}{1 + d^2}. \tag{5.3}$$

For cases, in which the data is inversely related to the confidence measure, the corresponding output function are given by

$$c_{\text{bound,inv}} := 1 - c_{\text{bound}}, \quad \text{and} \quad c_{\text{unbound,inv}} := 1 - c_{\text{unbound}}. \tag{5.4}$$

Generally, noise in the image data has a huge effect on the computed confidence values. This can be due to the effect of noise on the actual image data and the associated filter responses thereof, but also due to the errors propagated into the displacement vectors. The output function c_{unbound} and $c_{\text{unbound,inv}}$ are nonlinearly depended on the acquired data d, the effect of this noise is further amplified. Therefore, an adequate scaling of the output functions on the noise is performed as detailed in Nieuwenhuis et al. [2007].

5.2.1 Regularizers as Situation or Confidence Measures

Regularizers can be used as situation or confidence measures to identify locations where the flow field does not correspond to the regularization model. Here we examine four classes of regularizers (image-driven or flow-driven either isotropic or anisotropic) defined by Schnörr and Weickert [2000] and Weickert and Schnörr [2001] plus the homogeneous regularizer used in Horn and Schunk [1981], a temporal regularizer and a space-time regularizer defined in Brox et al. [2004] as well as a total variation (TV) regularizer proposed by Rudin et al. [1992]. The corresponding situation or confidence measure can always be computed using one of the output functions described above, for example

$$c_{unbound,inv} := \frac{1}{1 + reg(x, y, t)^2}. \tag{5.5}$$

All the flow driven regularizers can only be used as situation measures and not as confidence measures. Taking both the flow and the image intensities into account, only the image-driven isotropic and anisotropic regularizers qualify as confidence measures.

5.3 Situation Measures

5.3.1 Problematic Situation to be Detected

In image sequences, due to the structure of the gray value, the full optical flow may not be estimated everywhere. In this section, situation measures are analyzed that try to detect these different location. The measures were estimated from the following four situations :

- Occlusion / Disocclusion
- Aperture Problem
- Homogeneous Regions
- Directed gray value structures

Occlusion/Disocclusion situations pose difficulties for the flow computation method since there are pixels with undefined flow vectors as explained in Section 3.2.2. In the situation of an aperture problem, the flow is not unique as sketched in Section 3.2.1. An example is a long edge of a rectangle moving downwards. Here any flow along the edge could be equally correct. Homogeneous regions pose problems for many flow computation methods since no flow can be detected in these regions due to a lack of gray value structures. Therefore, again from a local point of view, any direction and magnitude of displacement vector could be correct due to the fact that the region looks the same in all directions. Naturally, to be able to estimate full motion, directed gray value structures need to be present in some parts of the image sequence. Also, these areas should be detected by the relevant situation measure. In the following, situations measures, which were used in the analysis, will be presented

5.3.2 Occlusion/Disocclusion Detection

As situation measures for occlusions or disocclusions, exclusively regularizers were used. Here, only the homogeneous regularizer proposed by Horn and Schunk [1981] as well as flow driven isotropic and anisotropic regularizers were used [Rudin et al., 1992; Schnörr and Weickert, 2000; Weickert and Schnörr, 2001; Brox et al., 2004]. Isotropic regularizers are defined as

$$d_{\text{reg,iso}} := \psi\left(|\nabla u_1(\boldsymbol{x},t)|^2 + |\nabla u_2(\boldsymbol{x},t)|^2\right), \tag{5.6}$$

and anisotropic ones according to

$$d_{\text{reg,aniso}} := \operatorname{trace}\left(\psi\left(\nabla u_1(\boldsymbol{u},t)\nabla u_1(\boldsymbol{x},t)^\top + \nabla u_2(\boldsymbol{x},t)\nabla u_2(\boldsymbol{x},t)^\top\right)\right). \tag{5.7}$$

Here $|\cdots|$ indicates the L^2 norm. As output function, Equation (5.4) was used to compute $c_{\text{unbound,inv}}$. The situation measures tested for occlusions are thus:

Name	Reference	Function
`homReg`	[Horn and Schunk, 1981]	$d := \|\nabla u_1(\boldsymbol{x},t)\|^2 + \|\nabla u_2(\boldsymbol{x},t)\|^2$
`isoFlowReg`	[Weickert and Schnörr, 2001]	$\psi(s^2) = \epsilon s^2 + (1-\epsilon)\lambda_2\sqrt{1+\frac{s^2}{\lambda_2}}$
`tvReg`	[Rudin et al., 1992]	$\psi(s^2) = \sqrt{s^2+\epsilon^2}$
`anisoFlowReg`	[Schnörr and Weickert, 2000]	$\psi(J) := \sum_{i=1}^{2}\psi(\lambda_i)v_i v_i^T$
`timeReg`	[Brox et al., 2004]	$d := \|\nabla_t u_1(\boldsymbol{x},t)\|^2 + \|\nabla_t u_2(\boldsymbol{x},t)\|^2$
`spaceTimeReg`	[Brox et al., 2004]	$d := \|\nabla_{\boldsymbol{x},t} u_1(\boldsymbol{x},t)\|^2 + \|\nabla_{\boldsymbol{x},t} u_2(\boldsymbol{x},t)\|^2$

Following Weickert and Schnörr [2001], the weights λ and ϵ in `isoFlowReg` were set to $\lambda = \epsilon = 0.1$. For `anisoFlowReg`, J is a symmetric positive semidefinite matrix with the two orthonormal eigenvectors $\boldsymbol{e}_i, (i \in 1,2)$ with corresponding eigenvalues λ_i.

5.3.3 ApertureProblem

The aperture problem is a localized phenomenon. Therefore, measures based on the structure tensor $\boldsymbol{J}$ can be formulated. In the following the eigenvalues of the structure tensor are assumed to be sorted according to $\lambda_1 \geq \lambda_2 \geq \lambda_3$. According to Haußecker and Spies [1999], the *total coherency measure* c_t, the *spatial coherency measure* c_s and the *corner measure* c_c can be defined according to

$$c_t = \left(\frac{\lambda_1 - \lambda_3}{\lambda_1 + \lambda_3}\right)^2, \quad c_s = \left(\frac{\lambda_1 - \lambda_2}{\lambda_1 + \lambda_2}\right)^2 \quad \text{and} \quad c_c = c_t - c_s. \tag{5.8}$$

As a measure for the aperture problem, both `structCs` and `structCc` are suitable. For `structCs` $d := 1 - c_s$ and for `structCc` $d := c_c$ were chosen with the output functions c_{bound} from Equation (5.2) for both cases.

The measure `structMultipleMotion` has been proposed by Mota et al. [2001] and is based on the assumption that for a reliable motion vector estimate the smallest eigenvalue λ_3 of the structure tensor should be 0. But this measure is neither suited for the recognition of homogeneous regions (here all three eigenvalues are 0 and thus the situation confidence should be low) nor for the recognition of aperture problems (here the the two smallest eigenvalues are close to 0). Therefore the product $K = \prod_i \lambda_i$ of the eigenvalues of J is compared to the average diminished product of the eigenvalues $S = \frac{1}{m}(\lambda_2\lambda_3 + \lambda_1\lambda_3 + \lambda_1\lambda_2)$. In the case of reliable motion ($\lambda_3 = 0$) it follows $K = 0$. Furthermore $S > 0$ if there are two eigenvalues larger than 0. Thus a homogeneous region as well as an aperture problem can be identified by a low value of S. To adjust scales $\sqrt[m]{K}$ will be compared to $\sqrt[m-1]{S}$. Hence the situation confidence should be large if $\sqrt[m]{K} \leq \epsilon \sqrt[m-1]{S}$ and the following situation measure can be derived:

$$d = \frac{\sqrt[m-1]{S}}{\sqrt[m-1]{S} + \sqrt[m]{K}}. \tag{5.9}$$

The output function c_{unbound} from Equation (5.3) is used.

The Hesse matrix $\boldsymbol{H}(I) = \left(\partial^2 I/(\partial x_i \partial x_j)\right)$ is a direct measure for the curvature of gray value structure. Therefore, one can construct the measures `detHessian`, `evHessian`, `condHessian` based on H. The condition number $\kappa(\boldsymbol{H}) = \left|\boldsymbol{H}^{-1}\right| \cdot |\boldsymbol{H}|$ of the Hesse matrix has been proposed by Uras et al. [1988], but Barron et al. [1994] found the determinant of the Hesse matrix $\det(\boldsymbol{H})$ to be reliable. When an aperture problem is present, the curvature along this direction will be zero which means that the smallest eigenvalue of $\boldsymbol{H}$ is also equal to zero, or $\lambda_{\boldsymbol{H},2} = 0$. This also amounts to $\det(\boldsymbol{H}) = 0$. Instead of computing the Hesse matrix directly on the image gray values I, they can also be computed on a smoothed edge map. This is the approach presented by Waxman et al. [1988]. The edge map E is computed by a DOG filter [Jähne, 2005] which is then smoothed with a Gaussian resulting in the activation potential A. The measure `DOGHessian` is then given by $\det(\boldsymbol{H}(A))$. Summing up, the following measures based on the Hesse matrix $\boldsymbol{H}$ can be formulated:

Name	Reference	Function
`condHessian`	[Uras et al., 1988]	$d := \kappa\left(\boldsymbol{H}(\boldsymbol{I})\right)$
`detHessian`	[Barron et al., 1994]	$d := \det\left(\boldsymbol{H}(I)\right)$
`DOGHessian`	[Waxman et al., 1988]	$d := \det\left(\boldsymbol{H}(A)\right)$
`evHessian`		$d := \lambda_{\boldsymbol{H},2}$

For all these measures the output function c_{unbound} from Equation (5.3) was chosen.

Anandan [1989] proposal a measure based on the sum of squared differences (SSD) surface created by varying the flow vector at the current position and for each variation computing the new SSD value. The SSD value of the original location is given by $S_{\min}$. In the presence of an aperture problem, the SSD surface will be elongated in this direction. Therfore the curvature of this surface along the maximum $C_{\max}$ and the minimum $C_{\min}$ principal axis is computed. Along edges the curvature along the maximum principal axis will be high whereas that along the minimum principal axis will be low. This results in the measure `SSDCurve` given by

$$d := \frac{C_{\min} \cdot C_{\max}}{k_1 + k_2 S_{\min} + k_3 C_{\max}}, \tag{5.10}$$

where k_1, k_2, k_3 are constants. k_1 prevents 0 in the denominator, k_2 determines the importance of S_{min} and k_3 bounds the result to the range $[0, 1/k_3]$. Following Anandan [1989], here $k_1 = 150$, $k_2 = 1$ and $k_3 = 0$ were chosen. The output function $c_{\text{unbound,inv}}$ from Equation (5.4) is used for this measure.

5.3.4 Homogeneous Regions

Homogeneous regions can be detected by computing the gradient. Thus the measure `grad` is defined by $d := \nabla I(\boldsymbol{x}, t)$. Another measure closely related it the trace of the structure tensor `structTrace` $d := \mathit{trace}(\boldsymbol{J}) = I_x^2 + I_y^2 + I_t^2$. For both of these measures, $c_{\text{unbound,inv}}$ from Equation (5.4) is used as the output function.

The measures `structMultipleMotion` `detHessian, evHessian, condHessian` `DOGHessian` `SSDCurv` used for detecting the aperture problem from the previous section can also be used to test for homogeneous regions. This highlights a problem with these measures: used by themselves, it can only be detected that the full motion field cannot be computed. Whether this is due to the aperture problem or homogeneous regions, cannot be deduced from these measures. Therefore, a second measure is required to solve this ambiguity, such as `grad` or `structTrace`.

5.3.5 Directed Gray Value Structures

In a local setting, only at directed gray values, such as a corner in an image sequence, is it possible to estimate full motion. Thus it is important to detect these locations where an accurate estimate of motion is potentially possible. Again, some of these measures are based on the structure tensor. The simplest measure is `structLa3` based on Haußecker and Spies

[1999]. Here the underlying assumption is in view of parameter estimation from Section 3.4.2, that the smallest eigenvalue λ_3 should vanish for a perfect estimate, or at least it should be proportional to the noise corrupting the data. A significantly bigger λ_3 is an indication that the model does not describe the data well. Thus, $d = \lambda_3$ can be used as a measure for directed gray value structures, as this is required for the simple motion model. Here the output function $c_{\text{unbound,inv}}$ from Equation (5.4) is used.

Another measure for directed structures is given by the measures from Equation 5.8. It is the total coherence measure `structCc` proposed by Haußecker and Spies [1999]. It measures the normalized difference between the smallest and the biggest eigenvalue leading to $d = ((\lambda_1 - \lambda_3)/(\lambda_1 + \lambda_3))^2$. The relevant output function is c_{bound} from Equation (5.2) is used.

The main shortcoming of using `structLa3` and `structCc` is that they are both a measure for the magnitude of the smallest eigenvalue. However, in other situations such as the aperture problem, this eigenvalue can also be small. Therefore, additional measures would be required.

The third measure was proposed by Barth [2000]. From the minors of the structure tensor three expressions for the velocity can be derived, as shown in Section 4.4.1. Ideally, the velocity estimates should be the same for these expressions. To this end, the cumulated angle difference between these estimates is a measure that indicates, when the assumption of directed structure is not fulfilled in the gray value structure. `structMinors` can be formulated as $d1 = \sum_{i=1}^{4} \sum_{j=1}^{i-1} angleDiff(x_i, x_j)$, which is bounded to $[0, 6\pi]$. The resulting output function is $c_{\text{bound,inv}}$ from Equation (5.4).

5.3.6 Comparison of Situation Measures

The following is a list of the situation measures commonly used in literature as situation measures. They will be compared to each other on test sequences.

Name	Situation	Output Function	Reference
`homReg`	Occlusion	$c_{\text{unbound,inv}}$	[Horn and Schunk, 1981]
`isoFlowReg`	Occlusion	$c_{\text{unbound,inv}}$	[Weickert et al. 2001]
`tvReg`	Occlusion	$c_{\text{unbound,inv}}$	Rudin et al. [1992]
`anisoFlowReg`	Occlusion	$c_{\text{unbound,inv}}$	[Schnörr et al. 2000]
`timeReg`	Occlusion	$c_{\text{unbound,inv}}$	[Brox et al., 2004]
`spaceTimeReg`	Occlusion	$c_{\text{unbound,inv}}$	[Brox et al., 2004]
`structCs`	Aperture	c_{bound}	[Haußecker et al. 1999]
`structCc`	Aperture	c_{bound}	[Haußecker et al. 1999]
`structMultipleMotion`	Aperture	c_{unbound}	[Mota et al., 2001]
`condHessian`	Aperture	c_{unbound}	[Uras et al., 1988]
`detHessian`	Aperture	c_{unbound}	[Barron et al., 1994]
`DOGHessian`	Aperture	c_{unbound}	[Waxman et al., 1988]
`evHessian`	Aperture	c_{unbound}	
`SSDCurve`	Aperture	$c_{\text{unbound,inv}}$	[Anandan, 1989]
`grad`	Homogeneity	$c_{\text{unbound,inv}}$	
`structTrace`	Homogeneity	$c_{\text{unbound,inv}}$	[Haußecker et al. 1999]
`structMultipleMotion`	Homogeneity	c_{unbound}	
`condHessian`	Homogeneity	c_{unbound}	[Uras et al., 1988]
`detHessian`	Homogeneity	c_{unbound}	[Barron et al., 1994]
`DOGHessian`	Homogeneity	c_{unbound}	[Waxman et al., 1988]
`evHessian`	Homogeneity	c_{unbound}	
`SSDCurve`	Homogeneity	$c_{\text{unbound,inv}}$	[Anandan, 1989]
`structLa3`	Directed	$c_{\text{unbound,inv}}$	[Haußecker et al. 1999]
`structCc`	Directed	$c_{\text{unbound,inv}}$	[Haußecker et al. 1999]
`structMinors`	Directed	$c_{\text{bound,inv}}$	[Barth, 2000]

Note: For space considerations, [Haußecker et al. 1999] referrs to [Haußecker and Spies, 1999], [Schnörr et al. 2000] to [Schnörr and Weickert, 2000] and [Weickert et al. 2001] to [Weickert and Schnörr, 2001].

To examine the performance of the situation measures, they were applied to four artificial sequences, one highlighting each situation. For a statement concerning the suitability of a given measure for that situation, the "false positive rate" has also to be computed from examining cases where the relevant situation does not occur. Therefore the ground truth for each sequence was labeled with 0 within the situation, with 1 outside the situation and with 0.5 for invalid pixels. Invalid are pixels at which other situations occur that shall not be examined in the present setting. An example for such invalid pixel are occlusions in the aperture problem sequence. To compare different situation measures, their quality was expressed in two values similar to sensitivity (true positive rate) and specificity (true negative rate).

Since the interest is in the identification of certain situations, the average identification error within the situation E_{inside} and outside the situation E_{outside} are used to describe the performance of the measure. Using $\mathcal{S}$ as the set of pixels within the situation, $\mathcal{T}$ as the set of pixels outside the situation and $c_{\text{truth},i} \in \{0, 1\}$ as the ground truth value at position i, the

following two error measures can be defined:

$$E_{\text{inside}} = \frac{\sum_{i \in \mathcal{S}} |S_i - c_{\text{truth},i}|}{\sum_{i \in \mathcal{S}} |S_i|} \quad \text{and} \quad E_{\text{outside}} = \frac{\sum_{i \in \mathcal{T}} |T_i - c_{\text{truth},i}|}{\sum_{i \in \mathcal{T}} |T_i|} \tag{5.11}$$

$$\text{with} \quad S_i \in [0,1] \quad \text{and} \quad T_i \in [0,1],$$

$c_{\text{truth},i}$ is set to 0 for pixels in S and 1 for pixels in T.

5.4 Confidence Measures

A confidence measure states how well the estimated motion field predicts the change of gray values with respect to time. In order to achieve this, both information concerning the gray values as well as the displacement vector field have to be considered. Without this coupling, the information of only flow field or image intensities can at most be used as a situation measurement. Due to this fact and this definition of a confidence measure, most confidence measures termed as such in literature are in fact situation measures.

In fact, the only real confidence measure proposed previously is the inverse of the energy of variational functionals presented by Bruhn and Weickert [2004]. Here, the idea of Bruhn and Weickert [2004] is taken a step further by demanding of a confidence to possess a direct coupling of image intensities and motion field. Hence, the whole energy functional of variational approaches can be used as such a confidence measure. Moreover, the smoothness term of image driven isotropic or anisotropic regularizer could also be used as such a measure, as here too such a coupling is performed.

The regularizer used in this setting are practically the same as `isoFlowReg` and `anisoFlowReg` from Section 5.3.2, except that for confidence measures they need to be image driven instead of flow driven. Hence `isoImReg` and `anisoImReg` are also the same regularizers as proposed by Schnörr and Weickert [2000] and Weickert and Schnörr [2001]. `isoImReg` is given as

$$d := \psi(|\nabla I(\boldsymbol{x},t)|^2)(|\nabla u_1(\boldsymbol{x},t)|^2 + |\nabla u_2(\boldsymbol{x},t)|^2) \tag{5.12}$$

and `anisoImReg` follows analogously from Section 5.3.2, as the output function, c_{unbound} from Equation (5.3) is used.

Apart from measures based on energy functionals from variational approaches, other measures are conceivable as well. These rely on warping image intensities from frame $I(\boldsymbol{x},t)$ to frame $I_w(\boldsymbol{x},t)$ based on the displacement vector field. The warped frame $I_w(\boldsymbol{x},t)$ is thus given by $I_w = I(\boldsymbol{x}+\boldsymbol{u}, t+1)$ with an appropriate interpolation applied in the subsequent sampling.

Subsequent measures can then be based on a number of different constancy assumptions. It is well known, that higher order differentials of the image intensities I can be formulated as constancy equations of motion, similar to the BCCE introduced in Section 2.2. These are constancy of gray value [Fennema and Thompson, 1979], constancy or gradient [Uras et al., 1988], constancy of the Hessian [Papenberg et al., 2006] and constancy of the Laplacian [Papenberg et al., 2006], as well as constancy of the norm of the gradient, the norm of the

Hessian and the determinant of the Hessian, as summarized by Papenberg et al. [2006]. These constancy equations can always be formulated as

$$\mathcal{D} \circ I_w(\boldsymbol{x}, t) - \mathcal{D} \circ I(\boldsymbol{x}, t) = 0, \tag{5.13}$$

where $\mathcal{D}$ denotes a differential operator operating on I. The residual of this constancy assumption are used as confidence measures in the following. They are denoted as `gradConst`, `gradNormConst`, `hesseConst`, `hesseNormConst`, `hesseDetConst` and `laplaceConst`. The residual of the brightness constancy constraint equation is termed `SSD` or `brithnessConst`, depending on whether the residual is computed in a differential framework ($\boldsymbol{w} \cdot \nabla_{\boldsymbol{x},t} I = 0$, $\boldsymbol{w} = [\boldsymbol{u}, 1]^\top$) or from the sum of squared differences (SSD). To this end, the residual of the cross correlation can also be used as a measure, termed `CrossCorr`. All of these measures use the output function c_{unbound} from Equation (5.3), except `CrossCorr`, which is bounded by $[-1, 1]$ resulting in $c_{\text{bound,inv}}$ from Equation (5.4).

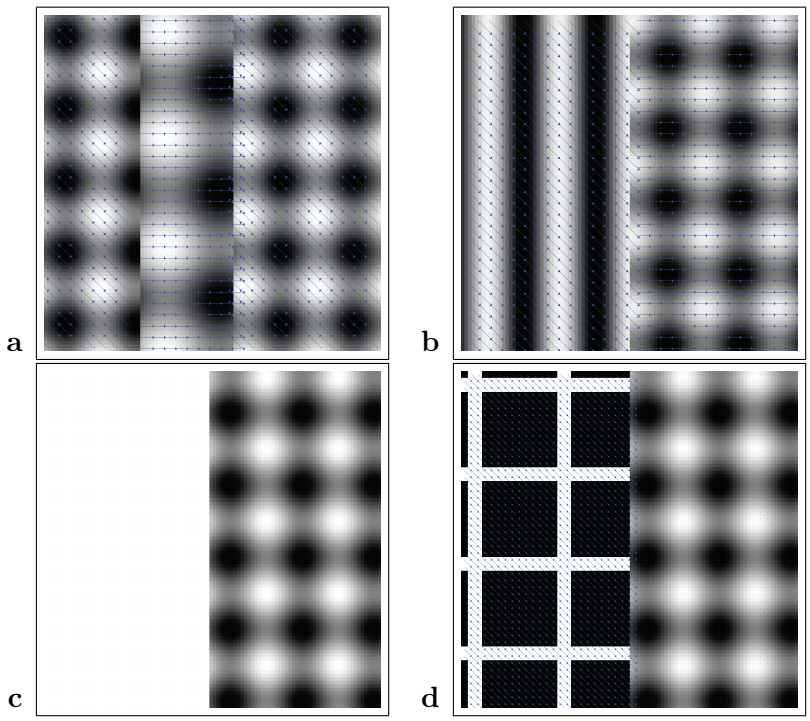

Figure 5.1: *Single frames of the four synthetic sequences to test the situation measures:* ***a*** *occlusion,* ***b*** *aperture problem* ***c*** *homogeneous regions and* ***d*** *directed structures.*

5.5 Surface Measures

Generally, in all previous measures, be it confidence or situation measure, no spatial information of these measures is used for increasing their accuracy. Moreover, additional information can be extracted from confidence measures by analyzing their spatial structure. For example, in the presence of the aperture problem, a similar geometry is expected in the local map

of confidence measures. Occlusions, on the other hand, will lead to a significant lowering of the local neighborhood of the confidence map. The accuracy of confidence measures can also be improved by analyzing these measures in a local neighborhood. This has lead to the formulation of two such measures: *surface situation measures* and *surface confidence measures*.

5.5.1 Surface Situation Measures

By considering spatial changes of a confidence measure, situations such as occlusions/disocclusions, the aperture problem and homogeneous regions can be detected at the same time. A local confidence surface is created by changing the displacement vector $\boldsymbol{u}_0$ at a certain location $\boldsymbol{x}_0$ both in x_1 and x_2 direction. These changes could be in an interval of [-0.9,0.9] in steps of 0.3. In this way a surface of size 7×7 is obtained. Depending on the application, a different configuration could be chosen. By analyzing this 7×7, the following situation measures can be detected:

Occlusion: No correct flow vector exists at $\boldsymbol{x}_0$ and in its neighborhood. This will lead to very low values for all confidences of the surface.

Homogeneity: Similar to the gray value structure, the confidence surface will also be flat and exhibit low curvature in all directions.

Aperture Problem: Here, along the edge representing the aperture program, the confidence measure will have similar values. This leads to a low curvature in the confidence surface. As opposed to homogeneous regions, the curvature along the other direction will be high.

The principal curvatures can be computed from the eigenvalues of the Hessian, estimated on this confidence surface. Also, different shape operators from differential geometry might be used [Burke, 1985; Spivak, 1999]. The eigenvalues of the Hessian is denoted by $\lambda_{\text{surf},1}$ and $\lambda_{\text{surf},2}$ with $\lambda_{\text{surf},1} \geq \lambda_{\text{surf},2}$. Together with the maximum confidence $c_{\max}$ located at $\boldsymbol{x}$, this leads to the following three surface measures s for occlusion (s_{occ}), for the aperture problem (s_{aper}) and for the detection of homogeneous regions s_{hom}:

$$s_{\text{occ}} = \frac{\lambda_{\text{surf},2} \cdot c_{\max}}{1 + \lambda_{\text{surf},2}}, \quad s_{\text{aper}} = \left(\frac{\lambda_{\text{surf},1} - \lambda_{\text{surf},2}}{\lambda_{\text{surf},1} + \lambda_{\text{surf},2}} \right)^2, \quad s_{\text{hom}} = (1 - s_{\text{apperture}}). \tag{5.14}$$

5.5.2 Surface Confidence Measures

Apart from analyzing the shape of the surface of local confidence, it is also possible to refine the original confidence measure c_0 at the point $\boldsymbol{x}_0$. This is done by normalizing the local confidence surface to 1. It can then be thought of as a probability density function $p(\boldsymbol{x})$. In a next step, the error e_i is computed between any of the displacement vectors $\boldsymbol{u}_i$ in the support of the surface Ω and the original vector $\boldsymbol{u}(\boldsymbol{x}_0)$. The weighted sum of these errors $e(\boldsymbol{x}_i)$ is then a measure for the accuracy of the estimated vector. This confidence is thus estimated according to

$$c_{\text{surf}} = \sum_{i \in \Omega} p(\boldsymbol{x}_i) \cdot e(\boldsymbol{x}_i). \tag{5.15}$$

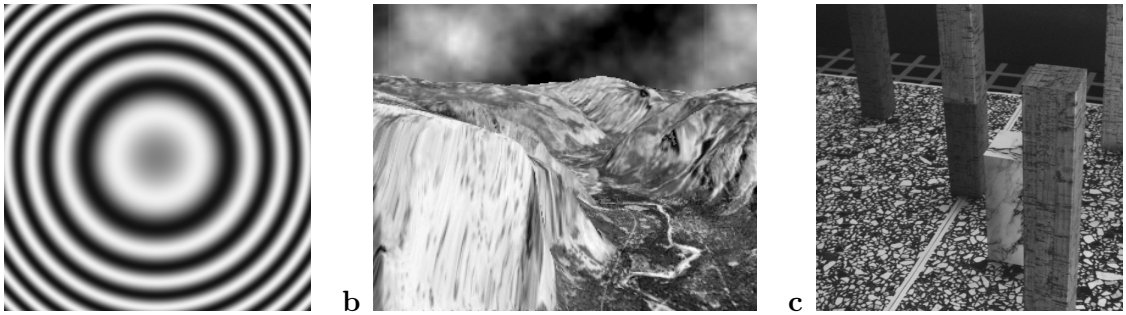

Figure 5.2: *The Sequence for testing noise is shown in* **a***, a frame from the Yosemite sequence is shown in* **b** *and that for the Marble sequence in* **c***.*

5.6 Results

The different presented measures were analyzed on a number of synthetic test sequences as well as on the well known Marble sequence [Otte and Nagel, 1994, 1995]. First the situation measures were tested. To this end, synthetic sequences were generated, that focus on one situation each. Individual frames of the four test sequences are shown in Figure 5.1. The confidence measures were tested on Lynn Quam's Yosemite [Heeger, 1987] and the Marble sequence [Otte and Nagel, 1994, 1995]. Also, the dependence of the measures on noise was tested by corrupting a test sequence with noise of varying intensity. Frames of these test sequences are shown in Figure 5.2**a**.

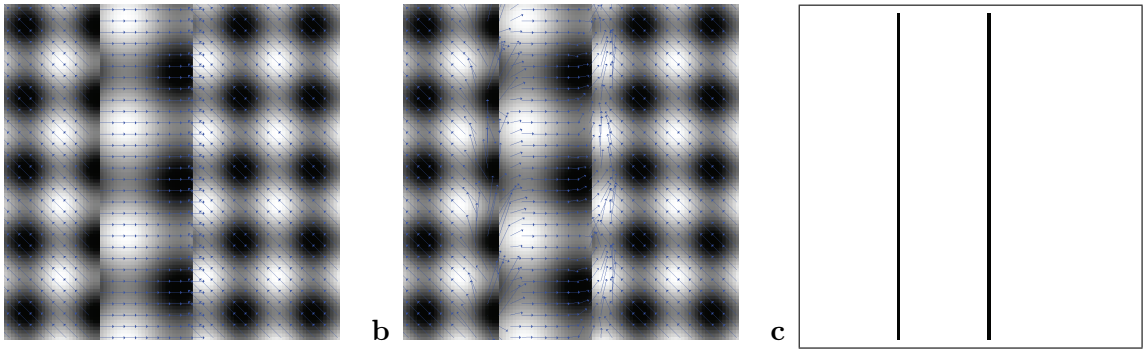

Figure 5.3: **a** *artificial sequence containing occlusion/disocclusion for testing of situation measures. The ground truth flow is shown as overlay.* **b** *calculated flow field,* **c** *Ground truth (0 within situation, 1 outside).*

In order to compare the performance of different confidence and situation measures quantitatively, the following methodology is used:

- For the situation measures, different synthetic sequences are used that highlight a range of different situations that should be detected. For pixels within the given situation, an index is set to 0. The index is set to 1 for pixels outside that region and pixel are excluded from the analysis by setting the index to 0.5. Subsequently two values are calculate: 1) the average deviation from 0 for pixels in the situation and 2) the average

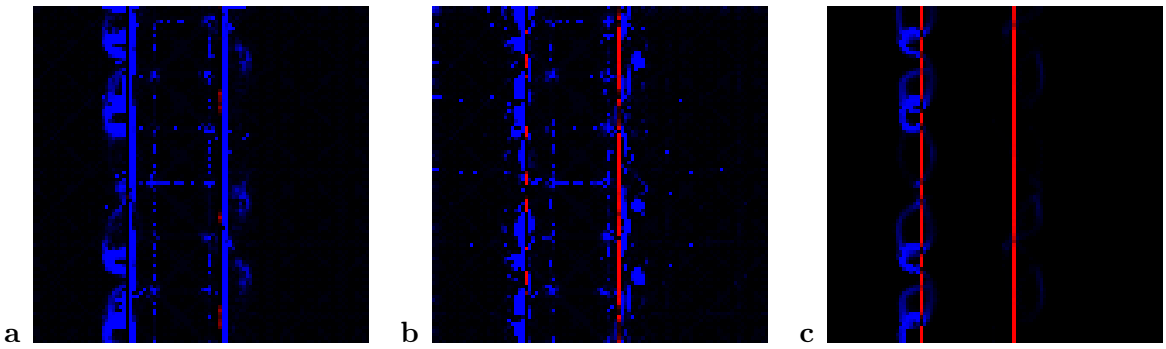

Figure 5.4: *Classification result for the* `SSM-hessConst` *measure in* ***a****, for* `SSM-ssd` *and for* `SSM-crossCorr` *in* ***c****. Red: within situation, blue: outside situation. The lower the value the more correct the result.*

deviation from 1 for pixels outside the situation.

- For the confidence measures, an optimal confidence is computed from a given test sequence I, a given displacement field $\boldsymbol{u}$ and the associated ground truth flow field $\boldsymbol{u}_c$. Computed confidence measures are then compared to this optimal confidence.

As it turns out, noise in the image sequence has important effects on confidence measures. Therefore these effects will be analyzed by computing the measures on sequence with different levels of artificial noise.

5.6.1 Situation Measures

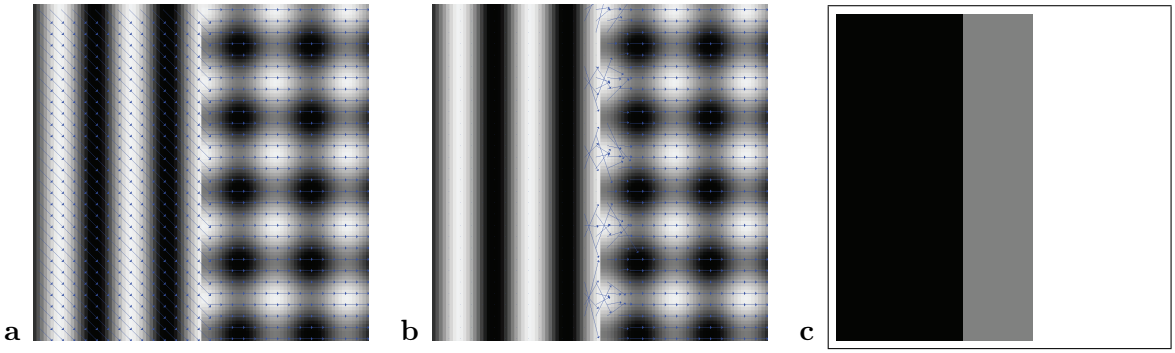

Figure 5.5: ***a*** *artificial sequence (containing the aperture problem for the examination of situation measures) with ground truth flow,* ***b*** *calculated flow field,* ***c*** *ground truth (0 within situation, 1 outside, 0.5 for invalid pixels).*

The displacement fields have been calculated using the structure tensor method described in Bigün et al. [1991]. On these vector fields, the situation measures were computed. For each sequence, three examples of the relevant situation measures are presented, one for the best measure, one for an intermediate measure and one for a measure of low quality.

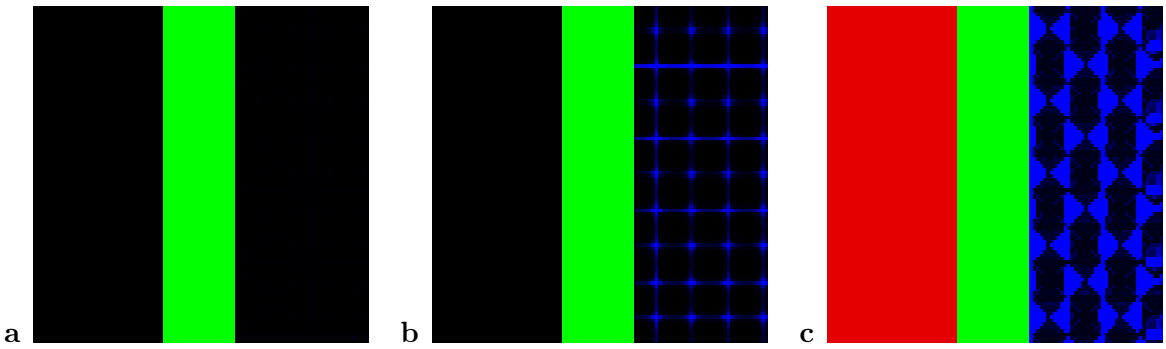

Figure 5.6: *Result from the aperture sequence for the* `SSM-laplaceConst` *measure in* ***a****, the* `detHess` *measure in* ***b*** *and the* `ssdSurface` *in* ***c****. The coloring scheme is the same as in Figure 5.4, plus green which indicates excluded regions.*

To show these results we will display the difference of the calculated classification result and the ground truth for the current situation. In order to be able to discern pixels within the situation from pixels outside the situation we use different color channels. The red channel contains only pixels within the situation, the blue channel all pixels outside the situation and the green channel all pixels that have been masked out. Thus the darker the red and blue color the more correct the classification result.

Finally we will show a table demonstrating the E_{inside} and the E_{outside} error. The table is sorted by the sum of these error measures. To indicate surface situation measures we use the abbreviation "SSM" in front of such measures.

Noteworthy are the good results of this new concept of the surface measures for all four situations, namely occlusion, aperture problem, homogeneous regions and directed gray value structures.

Method	E_{inside}	E_{outside}
`SSM-hessConst`	0.032	0.099
`SSM-laplaceConst`	0.077	0.091
`SSM-hessNormConst`	0.160	0.108
`SSM-ssd`	0.464	0.087
`spaceTimeReg`	0.506	0.094
`SSM-brightnessConst`	0.540	0.130
`timeReg`	0.610	0.082
`homReg`	0.800	0.044
`SSM-crossCorr`	0.076	0.990

Table 5.1: *Results of situation measures for occlusion sequence.*

Occlusion / Disocclusion

The occlusion sequence in Figure 5.3 shows a sine pattern moving in the up-left direction which is blocked by a bar moving in the down-right direction. Hence on both sides of the bar

Method	E_{inside}	E_{outside}
`SSM-laplaceConst`	0.000	0.009
`SSM-hessConst`	0.000	0.009
`SSM-ssd`	0.000	0.020
`SSM-hessNormConst`	0.000	0.028
`structCs`	0.000	0.063
`SSM-brightnessConst`	0.000	0.097
`detHessian`	0.000	0.097
`logHessian`	0.056	0.077
`singhSurface`	0.0157	0.188
`evHessian`	0.000	0.278
`structMultipleMotion`	0.013	0.290
`structCc`	0.006	0.309
`SSM-crossCorr`	0.000	0.929
`ssdSurface`	0.000	1.000

Table 5.2: *Results of the situation measure for the aperture problem.*

either occlusion or disocclusion occurs.

The measurement yielding the best results for the occlusion sequence using the sum of the error definitions E_{inside} and E_{outside} is the surface situation measure applied to the `hessConst` measure, closely followed by `SSM-laplaceConst`. The results of this `SSM-hessConst` id presented in Figure 5.4**a**. The surface measure applied to the `SSD` measure yielded intermediate results, which can be seen in Figure 5.4**b**. The worst results were found for the measure `SSM-crossCorr` based on the surface measure applied to the cross correlation measure. These results are shown in Figure 5.4**c**. The results of all applicable situation measures is given in Table 5.1.

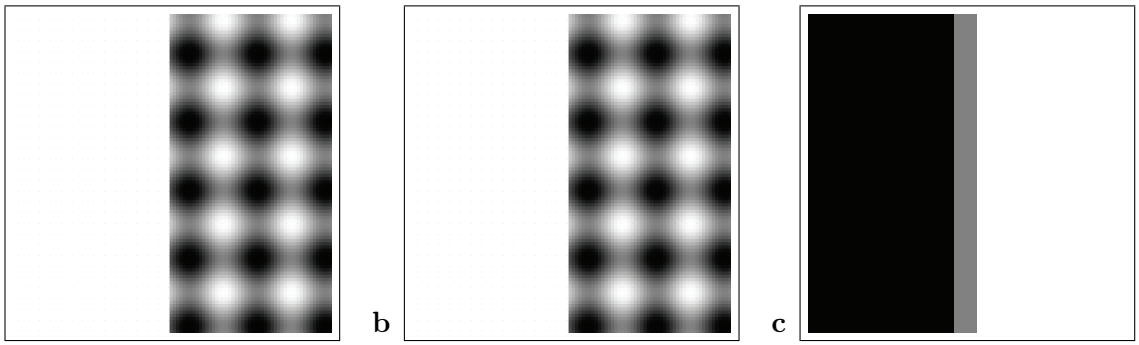

Figure 5.7: *The artificial sequence for testing homogeneous regions is shown in* ***a****. The calculated flow field can be seen in* ***b****. The ground truth of the situation measure is given in* ***c*** *(0 within situation, 1 outside, 0.5 for invalid pixels).*

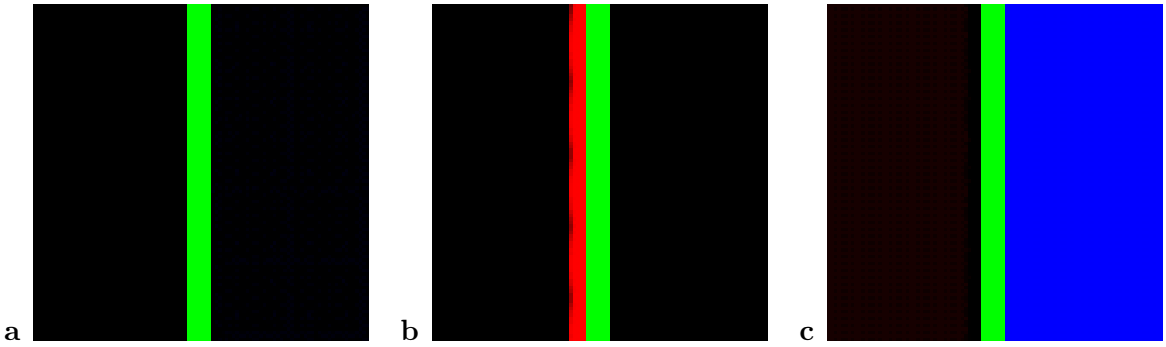

Figure 5.8: *The results for* `SSM-laplaceConst` *in* ***a****, for* `structTrace` *in* ***b*** *and for* `structMultipleMotion` *in* ***c****. The color scheme is the same as in Figure 5.6.*

Aperture Problem

The test sequence for the aperture problem is shown in Figure 5.5. It consists of a plane sine wave pattern translated to the right in horizontal direction only. On the right side a 2D sine pattern which is moving in the down-right direction. Therefore, the left part of the sequence can be used to detect the aperture problem, the right part to check the false positive rate of the measure. The noise level of this sequence was 0.235.

The measurement yielding the best results for the aperture problem sequence is again the surface situation measure applied to the laplace constancy measure (`laplaceConst`). This measure resulted in almost identical results to the surface measure applied to the `hessConst` measure. The result of `SSM-laplaceConst` is presented in Figure 5.6**a**. A measure with intermediate results is the determinant of the Hessian (`detHess`), the results of which can be seen in Figure 5.6**b**. The worst results were achieved with the surface situation measure applied to the `crossCorr` measure. This is shown in Figure 5.6**c**. The results for all measures are given in Table 5.2.

Homogeneous Regions

The measures for detecting homogeneous regions are tested on the stationary sequence shown in Figure 5.7. The left part is of a constant intensity (white). The right part contains a two-dimensional sine pattern.

The measurement yielding the best results for the homogeneous regions sequence is again the `SSM-laplaceConst` measure as seen in Figure 5.8**a**. A measure with intermediate results is the trace of the structure tensor (`structTrace`) presented in Figure 5.8**b**. A low quality measure for this sequence is the multiple motion measure (`structMultipleMotion`) in Figure 5.8**c**. The results for all measures are summarized in Table 5.3.

Directed gray value structures

The last situation to be analyzed is that of directed structures. The relevant sequence is shown in Figure 5.9. It contains a pattern of white lines on black background on the left which is

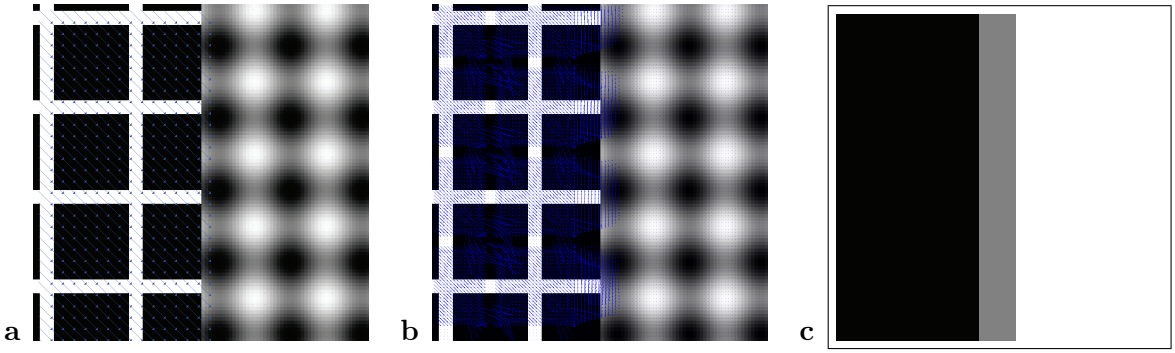

Figure 5.9: *The synthetic sequence for testing directed structures is shown in* **a** *with ground truth vector field overlain. The computed vector field is displayed in* **b** *and the ground truth situation measure is presented in* **c** *(0 within situation, 1 outside, 0.5 for invalid pixels).*

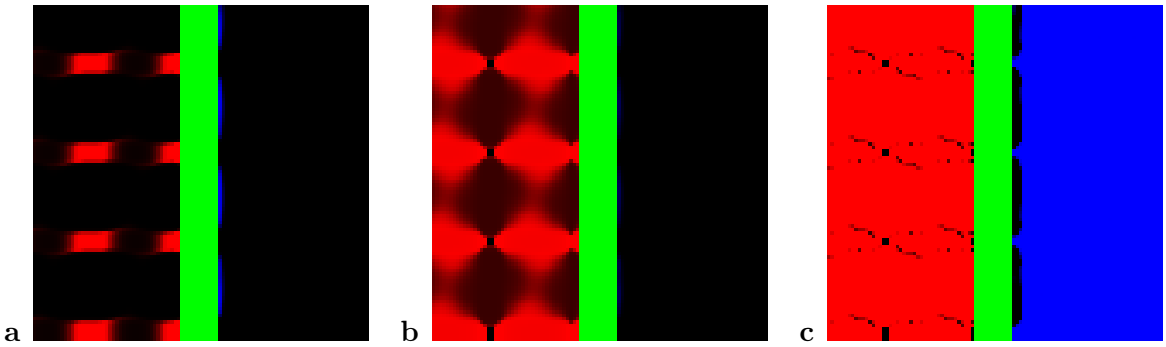

Figure 5.10: *Classification result for the* `structEv3` *measure in* **a**, *for* `structCt` *in* **b** *and for* `structMinorsAmplitude` *in* **c**. *The coloring scheme is the same as in Figure 5.4.*

moving in the down-right direction. On the right side a static 2D sine pattern is used. In this way we can examine whether the measure is able to recognize directed gray value structures, as well as the aperture problem and homogeneous regions. The noise level of this sequence has been estimated as 0.0535.

The measurement, yielding the best results is the `structEv3`, measures the smallest eigenvalue of the structure tensor. This measure is presented in Figure 5.10**a**. A measure with intermediate results is the total coherency measure `structCt`, which can be seen in Figure 5.10**b**. The worst results were computed with the minors amplitude measure, `structMinorsAmptlitude`. The results of this measure are shown in Figure 5.10**c**. Table 5.4 presents the results for all situation measures.

5.6.2 Confidence Measures

The confidence and situation measures were tested on a number of different sequences with ground truth available. To be able to compare different confidence measures for a given image sequence I, a computed flow field $\boldsymbol{u}$ and a ground truth flow field $\boldsymbol{u}_c$ are used to compute an optimal confidence measure. This optimal confidence measure is derived from the angular

Method	E_{inside}	E_{outside}
`SSM-laplaceConst`	0.000	0.002
`SSM-hessConst`	0.000	0.002
`SSM-hessNormConst`	0.000	0.002
`SSM-ssd`	0.000	0.003
`grad`	0.000	0.008
`SSM-brightnessConst`	0	0.041
`structTrace`	0.106	0.001
`detHessian`	0.000	0.129
`logHessian`	0.016	0.118
`evHessian`	0.000	0.262
`SSM-crossCorr`	0.000	0.870
`ssdSurface`	0.000	1.000
`singhSurface`	0.487	0.527
`structMultipleMotion`	0.812	1.000

Table 5.3: *Results for sequence of homogeneous regions.*

`Method`	E_{inside}	E_{outside}
`structEv3`	0.113	0.013
`structMinorsAngular`	0.500	0.015
`structMinorsAngle`	0.533	0.015
`structCt`	0.578	0.005
`structMinorsAmplitude`	0.979	0.946

Table 5.4: *Situation Measure Results for Directed Structures Sequence.*

error, normalized to the range $[0, 1]$. This angular error was introduced in Barron et al. [1994] and is given by

$$\alpha = \operatorname{acos}\left(\frac{(u_1, u_2, 1)^\top (u_{c,1}, u_{c,2}, 1)}{\|(u_1, u_2, 1)^\top\| |[u_{c,1}, u_{c,2}, 1]^\top|}\right) \quad \text{and} \quad err_{\text{angular}} = \frac{\alpha}{\pi}. \tag{5.16}$$

The advantage of the angular error is, that errors in the angle as well as in the amplitude are taken into account.

The optimal confidence measure c_{opt} is then the inverted normalized angular error, since a low confidences should be given for high errors. This leads to

$$c_{\text{opt}} = 1 - err_{\text{angular}}. \tag{5.17}$$

Influence of Noise

It is important to analyze the influence of noise on the presented measures. To this end, different noise levels of iid Gaussian noise were added to the relevant sequences and the measures computed. In Figure 5.11 is a plot of the effect of noise on the translating ring pattern. This pattern is show in Figure 5.2**a**.

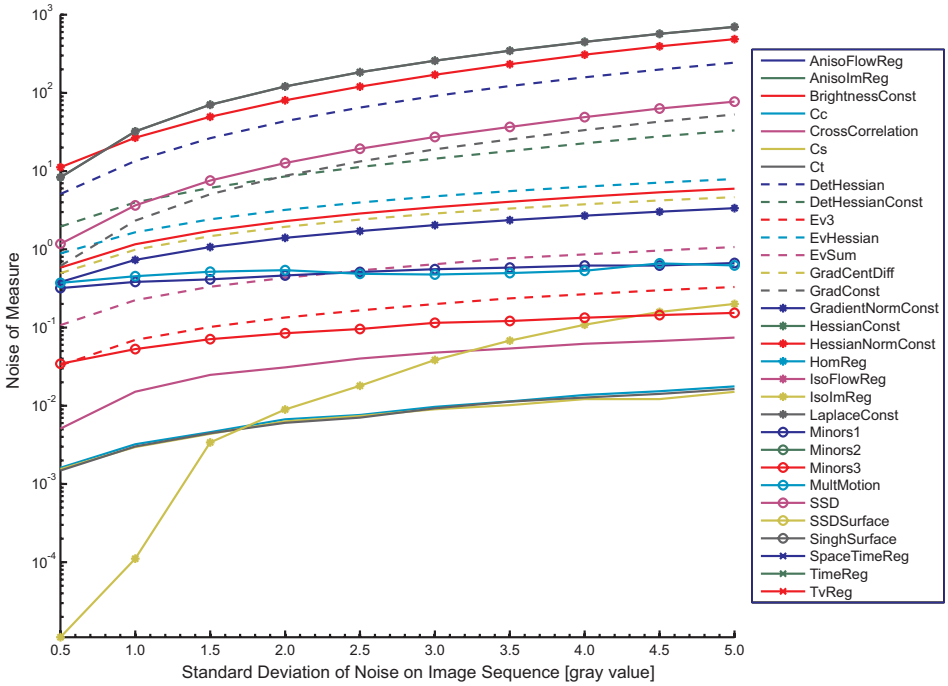

Figure 5.11: *The influence of noise on confidence and situation measures. Plotted is the noise in the measure against the standard deviation of the additive noise in the image sequence.*

It is readily observed the measurements using higher derivatives such as the confidence measures based on the Hessian are more susceptible to noise. Furthermore, the higher the order of the involved derivatives, the stronger is this influence. This is a result that is to be expected. It can also be seen that the situation measures based on the structure tensor are much less sensitive to noise. This can be attributed to the integration area of the structure tensor which can be thought of as an additional smoothing.

Results on Test Sequences

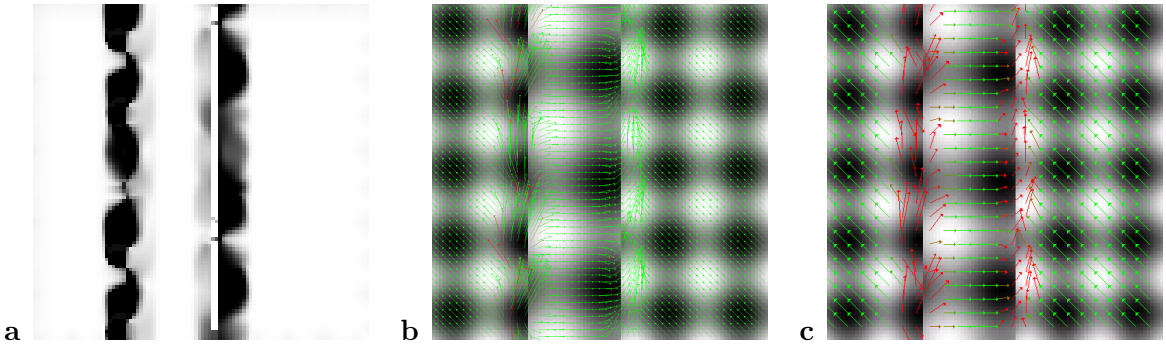

Figure 5.12: *Optimal confidence for the calculated displacement field of the occlusion sequence in* ***a****, the result for* `isoImReg` *in* ***b*** *that for* `timeReg` *in* ***c****. A high confidence is denoted by green, a low confidence by red.*

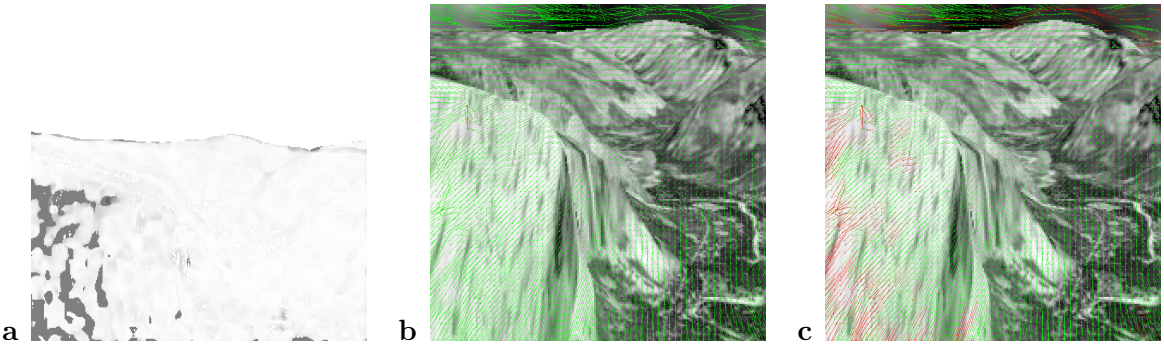

Figure 5.13: *The optimal confidence map can be seen in* **a** *(white: high confidence, black: low confidence). In* **b** *the results for the* `structMinorsAngular` *is shown and in* **c** *the same for* `anisoFlowReg` *(green high confidence, red low confidence).*

As an example of the output of the confidence measure, results are shown for the occlusion sequence in Figure 5.12. In Figure 5.12**a** the optimal confidence measure c_{opt} is shown. This optimal confidence measure was computed from Equation (5.17). As can be seen in Figure 5.12**b**, the measure does not compute a low confidence measure to a number of vectors that are clearly wrong as compared to the ground truth sequence. The result of `timeReg` shown in Figure 5.12**c** are far better. Vectors, pointing in the wrong direction, are marked dark red, which denotes a low confidence value. All presented confidence measures were tested on this synthetic sequence as well as on all the other situation measures. Due to space limitations not all results will be presented here. Apart from the "real" confidence measures, those used in literature as such measures, were also tested on these sequences. It has been shown before that those measures are in reality situation measures and ill suited as confidence measures. This proposition was supported by the measurements. All the situation measures performed worse than the real confidence measures.

A more realistic synthetic sequence than the very simple situation sequences is the well known Yosemite sequence. Results for this sequence are shown in Figure 5.13. In Figure 5.13**a** the optimal confidence is shown. It can clearly be seen that the motion estimator had problems in estimating the true velocity in the lower left region, where the optimal confidence is low. The measure shown in Figure 5.13**b** was not very well suited for computing the correct confidence. A high confidence is computed even for wrong vectors. The measure from Figure 5.13**c** resulted in much better estimates. It can clearly be seen that wrong vectors are color red, as would be expected from a good confidence measure. `anisoFlowReg` performed best on the Yosemite sequence, while `structMinorsAngular` performed worst.

The measurements were repeated on the well known Marble sequence. Results can be seen in Figure 5.14. The optimal confidence measure is presented in Figure 5.14**a**. The results of two measures are shown in Figure 5.14**b** and **c** respectively. Again, the measure in **b** is not well suited as a confidence measure. A number of wrong vectors are marked in green, indicating a high confidence measure. The measure shown in **c** is much better suited as a confidence measure. Wrong vectors are clearly marked red, indicating a low confidence. Such vectors could be segmented out and excluded from further processing steps. The `anisoFlowReg`

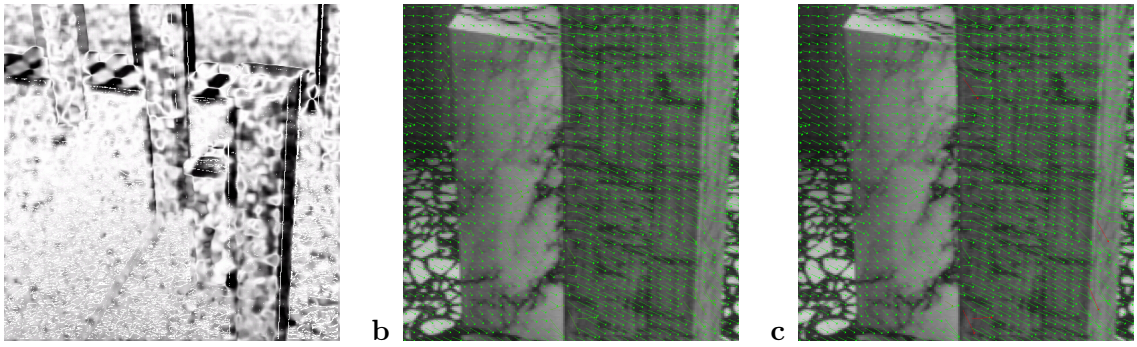

Figure 5.14: *The optimal confidence map can be seen in* **a** *(white: high confidence, black: low confidence). In* **b** *the results for the* `SSM-crossCorr` *is shown and in* **c** *the same for* `anisoFlowReg`.

measure performed best, while the `SSM-crossCorr` performed worse. Altogether it can be seen that there exist a much bigger scatter in results of the Marble sequence as compared to the much simpler synthetic sequences. This is probably due to the more complex flow field and more variance in the underlying image intensities. This indicates the difficulty of finding a perfect confidence measure for arbitrary real world scenes.

More detailed analysis of these results with a complete list of the resulting measures can can be found in Nieuwenhuis et al. [2007].

5.7 Conclusion

For the accurate estimation of motion, it is important to be able to detect problematic locations in image sequences. Such locations could be areas with the aperture problems or occlusions. Here, an estimation is not possible. This leads either to wrong estimates or to diffusion of information from other locations. On the other hand, it is also important to know how well the motion was estimated, which can be expressed as a confidence measure. In this chapter, a survey was conducted of of techniques presented previously in literature. The measures were classified either as situation measures or confidence measures. Situation measures are able to detect problematic locations in image sequences. Synthetic test sequences were generated that focus on individual of such problematic areas. The relevant measures were then tested on these sequences.

Extending current techniques, new measures were also developed. These were termed surface measures. On confidence measures, they construct a "confidence surface" by varying the estimated vectors locally and compute the confidence measure. The curvatures of this surface is then computed and analyzed for problematic situations. For example, in the presence of an aperture problem, the confidence surface also exhibits similar properties, which can be detected by analyzing the Hessian of this surface. The advantage of performing these analysis on the confidence surface as opposed to the image data directly is, that more information is accumulated in the confidence measure. This additional information can be used to achieve better results than can be obtained from computing these measures on the image data.

From the presented confidence and situation measures, a valuable tool is available for segmenting inaccurate estimates and thus increasing the accuracy of the parameter estimator.

Chapter 6

A Phase Field Method for Joint Denoising, Edge Detection and Motion Estimation

6.1 Introduction

In Section 3 a number of different techniques have been introduced that allow to estimate the parameters of the motion models from Section 2. This task of motion estimation is a fundamental problem in computer vision. In particular, global variational approaches initiated by the work of Horn and Schunk [1981] are increasingly popular. Initial problems such as the smoothing over discontinuities or the high computational cost have been resolved successfully [Nagel and Enkelmann, 1986; Weickert and Schnörr, 2001; Bruhn et al., 2003]. Motion also poses an important cue for object detection and recognition. This is relevant in applications such as pedestrian detection for intelligent vehicles. Also a number of scientific applications exist where such a segmentation of objects based on their motion is relevant. Regions of different fluid motion might be detected based on their flow patterns, leading to the detection of different processes taking place. Also, corrupted image data such as reflections could be detected based on their motion, leading to the exclusion in subsequent analysis [Garbe and Jähne, 2001]. While a number of techniques first estimate the motion field and segment objects later in a second phase [Wang and Adelson, 1994], an approach of both computing motion as well as segmenting objects at the same time is much more appealing. First advances in this direction were investigated by Schnörr [1994], Odobez and Bouthemy [1995], Odobez and Bouthemy [1998], Caselles and Coll [1996], Mémin and Pérez [1998] and Paragios and Deriche [2000]. Recently, Papenberg et al. [2006] considered a TV regularization of motion fields, which allows for jumps in those fields and optical flow constraints involving higher order gradients.

The idea of combining different image processing tasks into a single model in order to cope with interdependencies has drawn attention in several different fields. In image registration, for instance, a joint discontinuity approach for simultaneous registration, segmentation and image restoration has been proposed by Droske et al. [2005]. This approach was extended by

Droske et al. [2005] incorporating phase field approximations. Kapur et al. [2001] and Unal et al. [2004] have combined segmentation and registration applying geodesic active contours described by level sets in both images. Feron and Mohammad-Djafari [2004] proposed a Bayesian approach for the joint segmentation and fusion of images via a coupling of suitable hidden Markov Models for multi–modal images. Vemuri et al. [2003] have also used a level set technique to exploit a reference segmentation in an atlas. The interested reader is referred to Davatzikos et al. [1996] for further references.

Recently, Keeling and Ring [2005] investigated the relation between optimization and optical flow extraction. A first approach which relates optical flow estimation to Mumford–Shah image segmentation was presented by Nesi [1993]. Recently, Rathi et al. [2005] investigated active contours for joint segmentation and optical flow extraction. Cremers and Schnörr [2002] and Cremers and Soatto [2004] presented an approach for joint motion estimation and motion segmentation with one functional. Incorporating results from Bayesian inference, they derived an energy functional, which can be seen as an extension to the well known Mumford and Shah [1989] approach. Their functional involves the length of boundaries separating regions of different motion, as well as a "fidelity-term" for the optical-flow assumption. [Amiaz and Kiryati, 2005, 2006] extended motion estimation [Brox et al., 2004] to contour-based segmentation, following the well known segmentation scheme presented by Vese and Chan [2002]. The authors demonstrated that extending the motion estimator to edge detection in a variational framework leads to an increase in accuracy. However, as opposed to the framework in this chapter, the authors do not include image denoising in their framework. Including a denoising functional together with motion estimation in a variational framework has been achieved by Nir et al. [2005]. They report significant increases in the accuracy of motion estimation, particularly with respect to noisy image sequences. However, edges are not detected, but errors of smoothing over discontinuities are lessened by formulating the smoothness constraint in a L_1 metric. Brox et al. [2006] presented a Vese and Chan [2002] type model for piecewise smooth motion extraction. Here, the decomposition of image sequences into regions of homogeneous motion is encoded in a set of level set functions, and the regularity of the motion field is controlled by a total variation functional. The approach presented in this chapter is inspired by these investigations.

In this chapter an algorithm will be presented that combines denoising and edge detection with the estimation of motion. This results in an energy functional incorporating fidelity- and smoothness-terms for both the image sequence and the flow field. Moreover, an anisotropic enhancement of the flow along the edges of the image in the sense of Nagel and Enkelmann [1986] is incorporated. The model is implemented using the phase-field approximation in the spirit of Ambrosio and Tortorelli [1992] approach for the original Mumford–Shah functional. The identification of edges is phrased in terms of a phase field function, no *a-priori* knowledge of objects is required, as opposed to formulations of explicit contours. A particular focus is on optical flow constraints which are not only continuously distributed over shaded or textured regions, but might be concentrated on edges, such as in the case of moving objects without texture and shading. In contrast to a level set approach, the built-in multi-scale of the phase field model enables a natural cascadic energy relaxation approach and thus an efficient

computation. Indeed, no initial guess for the edge set and the motion field will be required. The algorithm is a truly $d+1$ dimensional algorithm, considering time as an additional dimension to the d-dimensional image data. This fully demonstrates the conceptual advantages of the joint approach. Nevertheless, a transfer of the method for only two consecutive time frames is possible but not investigated here. The characteristics of the novel approach are:

- The distinction of smooth motion fields and optical flow discontinuities is directly linked to edge detection, improving the reliability of the motion estimation.
- The denoising and segmentation task will profit from the explicit coupling of the sequence via the brightness constancy assumption.
- The phase field approximation is expected to converge to a limit problem for vanishing scale parameter, with a strict notion of edges and motion field discontinuities not involving any additional filtering parameter.
- In each step a set of three relatively simple linear systems have to be solved for the image intensity, the edge description via the phase field, and the motion field, respectively. Only a small number of iterations are required.

This approach has been presented in Telea et al. [2006] with details and a more rigorous mathematical proof given in Preusser et al. [2007].

This chapter is organized as follows: In Section 6.2 Mumford–Shah type image denoising and edge detection is reviewed, in Section 6.3 a generalized optical flow equation is discussed, and in Section 6.4 the minimization problem is presented. Section 6.5 shows how to approximate the segmentation in terms of a variational phase field model. Furthermore, the proof of the existence of solutions of this model is sketched and the limit behavior is discussed. Section 6.6 propounds the corresponding Euler-Lagrange equations, which are discretized applying the usual finite element procedure in Section 6.7. The results of the presented approach both on synthetic and real world scenes are presented in Section 6.8. This chapter concludes with a summary in Section 6.9.

6.2 The Mumford–Shah Functional

In their pioneering paper, Mumford and Shah [1989] proposed the minimization of the following energy functional:

$$E_{MS}[I,S] = \lambda \int_{\Omega} (I-I_0)^2 \,\mathrm{d}\mathcal{L} + \frac{\mu}{2} \int_{\Omega\setminus S} |\nabla I|^2 \,\mathrm{d}\mathcal{L} + \nu \mathcal{H}^{d-1}(S)\,, \tag{6.1}$$

where I_0 is the initial image defined on an image domain $\Omega \subset \mathbb{R}^d$ and λ, μ, ν are positive weights. Here, one asks for a piecewise smooth representation I of I_0 and an edge set S, such that I approximates I_0 in the least-squares sense. I ought to be smooth apart from the free discontinuity S and, in addition, S should be smooth and thus small with respect to the

$(d-1)$-dimensional Hausdorff-measure $\mathcal{H}^{d-1}$. Mathematically, this problem has been treated in the space of functions of bounded variation BV, more precisely in the specific subset SBV [Ambrosio et al., 2000]. In this chapter, a phase field approximation for the Mumford–Shah functional (6.1) will be used, such as that proposed by Ambrosio and Tortorelli [1992]. They describe the edge set S by a phase field ζ which is supposed to be small on S and close to 1 apart from edges. Thus, one asks for minimizers of the energy functional

$$E_\epsilon[I,\zeta] = \int_\Omega \lambda(I-I_0)^2 + \frac{\mu}{2}(\zeta^2+k_\epsilon)\,|\nabla I|^2 + \nu\epsilon\,|\nabla\zeta|^2 + \frac{\nu}{4\epsilon}(1-\zeta)^2\,\mathrm{d}\mathcal{L}\,, \tag{6.2}$$

where ϵ is a scale parameter and $k_\epsilon = o(\epsilon) \ll 1$ a small positive regularizing parameter, that mathematically ensures strict coercivity with respect to I. On edges the weight ζ^2 is expected to vanish. Hence, the second term measures smoothness of I but only apart from edges. The last two terms in the integral encode the approximation of the $d-1$ dimensional area of the edge set and the strong preference for a phase field value $\zeta \approx 1$ apart from edges, respectively. For larger ϵ one obtains coarse, blurred representations of the edge sets and corresponding smoother images I. With decreasing ϵ the representation of the edges is successively refined and more image details are included.

6.3 Generalized Optical Flow Equation

In image sequences different types of motion fields can be observed: locally smooth motion visible via variations of object shading and texture in time, or jumps in the motion velocity apparent at edges of objects moving in front of a background. The goal of this chapter is an identification of corresponding piecewise smooth optical flow fields in piecewise smooth image sequences

$$I : [0,T]\times\Omega \mapsto \mathbb{R}\,; \quad (t,x) \to I(t,x)$$

for a finite time interval $[0,T]$ and a spatial domain $\Omega \subset \mathbb{R}^d$ with $d = 1,2,3$. In what follows, $\partial\Omega$ is assumed to be Lipschitz. The flow fields are allowed to jump on edges in the image sequence. Hence, the derivative DI splits into a singular and a regular part. The regular part is a classical gradient $\nabla_{(t,x)}I$ in space and time, whereas the singular part lives on the singularity set S, that is the set of edge surfaces in space–time. Time slices of S are the actual image edges S with respect to space–time. The singular part represents the jump of the image intensity on S, i. e., one observes that $D^sI = (I^+ - I^-)n_s$. Here, I^+ and I^- are the upper and lower intensity values on both sides of S, respectively. Now, suppose that the image sequence I reflects an underlying motion with a piecewise smooth flow field v, which is allowed to jump only on S. Thus, S represents object boundaries moving in front of a background, which might as well be in motion. In strict mathematical terms, it is supposed that I, $v \in SBV$ (the set of functions of bounded variation and vanishing Cantor part in the gradient) [Evans and Gariepy, 1992; Ambrosio et al., 2000]. In this general setting without any smoothness assumption on I and v, the optical flow equations introduced in Chapter 2

have to be generalized. In the context of this chapter it is assumed that the simple BCCE motion model from Section 2.2 holds. More complex models could also be used.

Apart from moving object edges, this brightness constancy assumption $I(t+s, x+s\,v) = const$ holds for motion trajectories $\{(t+s, x+s\,v) \,:\, s \in [0,T]\}$, that is

$$\nabla_{(t,x)} I \cdot w = 0\,, \tag{6.3}$$

where $w = (1, v)$ is the space–time motion velocity. On edges, the situation is more complex and in general requires prior knowledge. For instance, a white circular disk moving in front of a black background is visually identical to a black mask with a circular hole moving with the same speed on a white background. Hence, it is ambiguous on which $\pm$ side of the edge $w^{\pm}$ vanishes and on which side a non–trivial optical flow equation $n_s \cdot w^{\pm} = 0$ holds. This ambiguity is not resolved via semantic assumptions. In what follows, it is instead assumed that locally only one object – in the example either the circle or the mask – is moving on a stationary remaining background. Hence, it is ruled out that foreground and background are in motion. In other words, the background is defined as that image part which is not moving, and the foregound correspondingly. Then, one of the two values of w on both sides of the edge vanishes by assumption and the optical–flow–constraint can be rewritten on the edge without identifying foreground or background by

$$n_s \cdot (w^+ + w^-) = 0. \tag{6.4}$$

This in particular includes the case of a sliding motion without any modification of the object overlap, where $n_s \cdot w^+ = n_s \cdot w^- = 0$.

6.4 Mumford–Shah Approach to Optical Flow

In this chapter a simultaneous denoising, segmentation and flow extraction on image sequences is sought. Hence, the motion field generating an image sequence will be incorporated into a variational method. This is achieved by formulating a corresponding minimization problem in the spirit of the Mumford and Shah [1989] model:

Definition 8 (Mumford–Shah type optical flow approach) *Given a noisy initial image sequence $I_0 : D \mapsto \mathbb{R}$ on the space time domain $D = [0,T] \times \Omega$, we define the following energy*

$$\begin{aligned} E_{\mathrm{MSopt}}[I, w, S] \;=\; & \int_D \frac{\lambda_I}{2} (I - I_0)^2 \, d\mathcal{L} + \int_{D\setminus S} \frac{\lambda_w}{2} \left(w \cdot \nabla_{(t,x)} I\right)^2 \, d\mathcal{L} \\ & + \int_{D\setminus S} \frac{\mu_I}{2} \left|\nabla_{(t,x)} I\right|^2 \, d\mathcal{L} + \int_{D\setminus S} \frac{\mu_w}{q} \left|\nabla_{(t,x)} w\right|^q \, d\mathcal{L} + \nu \mathcal{H}^d(S) \end{aligned} \tag{6.5}$$

for a piecewise smooth image sequence I and a piecewise smooth motion field $w = (1, v)$ with a joint jumps set S. Furthermore, on S the optical flow constraint $n_s \cdot (w^+ + w^-) = 0$ from Equation (6.4) is required. A minimizer (I, w, S) of the corresponding constraint minimization problem is sought.

The first and second term of the energy are fidelity terms with respect to the image intensity and the regular part of the optical flow constraint, respectively. The third and fourth term encode the smoothness requirement of the image intensities I and the flow field w. Finally, the last terms represents the area of the edge surfaces S. The fidelity weights λ_I, λ_w, the regularity weights μ_I, μ_w and the weight ν controlling the phase field are supposed to be positive and $q \geq 2$. It is emphasized that, without any guidance from the local time–modulation of shading or texture on both sides of an edge, there is still an undecidable ambiguity with respect to foreground and background.

6.5 Phase field approximation

Similar to the original model for denoising and edge detection, the above Mumford–Shah approach with its explicit dependence on the geometry of the edge set is difficult to implement. Usually, additional strong assumptions either on the image sequence I or on the motion field v are needed. For a corresponding parametric approach the interested reader is referred to the recent results by Cremers and Soatto [2004] and Cremers and Schnörr [2002]. The level set approach proposed by Brox et al. [2006] does not explicitly encode motion concentrated on edges. In the approach presented in this chapter, the aim is not to impose any additional assumption neither on the image sequence I nor on the motion field v. Therefore a suitable approximation of the above model is sought.

To gain more flexibility and, in addition, to incorporate a simple multi-scale approach into the model, a phase-field formulation (6.2) in the spirit of Ambrosio and Tortorelli [1992] is proposed here. Let the phase field ζ be an auxiliary variable that describes the edge set S. Outside of S the phase filed should be $\zeta \approx 1$ and on S it should vanish. As in the original Ambrosio–Tortorelli model, a scale parameter ϵ controls the thickness of the region with small phase field values. Thus, the following energy functionals are formulated:

$$E^{\epsilon}_{\text{fid}}[I, w] = \int_D \frac{\lambda_I}{2}(I - I_0)^2 + \frac{\lambda_w}{2}\left(w \cdot \nabla_{(t,x)} I\right)^2 \, \mathrm{d}\mathcal{L}\,, \tag{6.6}$$

$$E^{\epsilon}_{\text{reg},u}[I, \zeta] = \int_D \frac{\mu_I}{2}(\zeta^2 + k_\epsilon)\left|\nabla_{(t,x)} I\right|^2 \, \mathrm{d}\mathcal{L}\,, \tag{6.7}$$

$$E^{\epsilon}_{\text{reg},w}[w, \zeta] = \int_D \frac{\mu_w}{q}\left|P[\zeta]\nabla_{(t,x)} w\right|^q \, \mathrm{d}\mathcal{L}\,, \tag{6.8}$$

$$E^{\epsilon}_{\text{phase}}[\zeta] = \int_D \left(\nu\epsilon\left|\nabla_{(t,x)}\zeta\right|^2 + \frac{\nu}{4\epsilon}(1-\zeta)^2\right) \mathrm{d}\mathcal{L}\,. \tag{6.9}$$

These energy contributions control the approximation of the initial image I_0 and the optical–flow–constraint in (6.6), the regularity of I in (6.7) and w in (6.8). The regularity of the shape of the phase field ζ is enforced through (6.9). Here, as in the original model $k_\epsilon = o(\epsilon) > 0$ is a "safety" coefficient, which is later on needed to establish existence of solutions of the approximate problem. The energy $E^{\epsilon}_{\text{reg},w}$ ensures piecewise smooth motion fields and an extension

of motion velocities first concentrated on edges. If one would consider in a straightforward way the integral $\int_D \frac{\mu_w}{q} \left|P[\zeta]\nabla_{(t,x)}w\right|^q \mathrm{d}\mathcal{L}$ the motion field would form approximate jumps on S. But without any coupling of a concentrated motion constraint on S and the motion field in homogeneous regions on the image sequence, the velocity in these regions would converge to zero. One way to resolve this shortcoming is to introduce different phase field scales for the image intensity I and the motion field w. However, this is not very practical concerning a suitable discretization on digital images with limited pixel resolution. A better alternative is to encode the desired properties in the operator $P[\zeta]$:

- Close to the edges, where $\zeta \leq \theta^-$, for some θ^- with $0 < \theta^- < 1$, $P[\zeta]$ should behave like the original edge indicator ζ^2, as was proposed by Ambrosio and Tortorelli [1992].
- Except for the edges, where $\zeta \geq \theta^+$ for $\theta^- < \theta^+ < 1$, $P[\zeta]$ is expected to be the identity matrix, which enforces an isotropic smoothness modulus for the motion field w.
- In the spirit of the classical approach by Nagel and Enkelmann [1986] , $P[\zeta]$ will be an approximate projection onto level sets of the phase field function in the intermediate region. These level sets are surfaces approximately parallel to the edge set in space time. Thus, information on the optical flow is mediated along the edge set, without a coupling across edge surfaces.

An explicit definition for $P[\zeta]$ fulfilling these properties is the following:

$$P[\zeta] = \alpha(\zeta^2)\left(\mathbb{I} + k_\epsilon - \beta(\zeta^2)\frac{\nabla_{(t,x)}\zeta}{\left|\nabla_{(t,x)}\zeta\right|_\delta} \otimes \frac{\nabla_{(t,x)}\zeta}{\left|\nabla_{(t,x)}\zeta\right|_\delta}\right),$$

where $|z|_\delta = (|z|^2 + \delta^2)^{\frac{1}{2}}$ represents a regularized normal. Furthermore, $\alpha : \mathbb{R} \to \mathbb{R}_0^+$ and $\beta : \mathbb{R} \to \mathbb{R}_0^+$ are continuous blending functions, with $\alpha(s) = \max\left(0, \min\left(1, \frac{s}{\theta^-}\right)\right) + k_\epsilon$ and $\beta(s) = \max\left(0, \min\left(1, \frac{1-s}{1-\theta^+}\right)\right)$. Concerning algebraic notation, $\nabla_{(t,x)}w(t,x)$ is a $(d+1)^2$ matrix and thus $P[\zeta]\nabla_{(t,x)}w$ represents the matrix product. As the norm of matrices, the Frobenius norm is assumed given by $|A| = \sqrt{\mathrm{tr}(A^T A)}$. Suitable choices for the parameters are $\theta^+ = 0.8$ and $\theta^- = 0.0025$. For vanishing ϵ and a corresponding steepening of the slope of I, this operator basically leads to a "separated diffusion" on both sides of S in the relaxation of the energy.

The energies $E^\epsilon_{\mathrm{reg},u}$, $E^\epsilon_{\mathrm{phase}}$, and the first term of E_{fid} are identical to those in the original Ambrosio–Tortorelli approach as outlined above. In addition, an optical flow field w is sought that fulfills the optical flow constraint encoded in the second term of $E^\epsilon_{\mathrm{fid}}$ (care for Figure 6.1 for a first test case). At the same time, this term implies a strong coupling of the image intensities along motion trajectories – which turns into a flow-aligned diffusion in the corresponding Euler–Lagrange equations – for the benefit of a more robust denoising and edge detection. Figure 6.2 shows an example where a completely destroyed time step in the image sequence is recovered by this enhanced diffusion along motion trajectories. Due to the regularity energy $E^\epsilon_{\mathrm{reg},w}$ this motion field is isotropically smooth apart of the approximate jump set of I. The smoothness modulus is characterized by a successively stronger anisotropy

along level sets of I while approaching the approximate jump set. The energy term $E^{\epsilon}_{\mathrm{reg},w}$ (6.8) is very similar to the corresponding smoothness term in the classical approach by Nagel and Enkelmann [1986], where tangential diffusion steered by the local structure tensor, is considered for the regularization of the motion field. In the above multi–scale approach no additional pre-computation of the structure tensor is required.

The projection operator $P[\zeta]$ couples the smoothness of the motion field w to the image geometry, which is in fact very beneficial for the purpose of piecewise smooth motion extraction. The reverse coupling, which would try to align tangent spaces of level sets of I to the motion field, is not required and might even be misleading. The optical flow term in the fidelity energy $E^{\epsilon}_{\mathrm{fid}}$ already couples image sequence gradients to the motion field in a direct way. Hence, the solution is not found by computing global minimizers of the sum of all energies. Moreover, the phase field approximation problem is formulated as follows:

Definition 9 (Solution of the phase field model) *For a given noisy space time image $I_0 : D \mapsto \mathbb{R}$ and boundary data $v_\delta \in W^{1,q}(D, \mathbb{R}^d)$ for the velocity field, a space time image $I \in W^{1,2}(D, \mathbb{R})$, a motion field $w = (1, v + v_\delta)$, with $v \in W^{1,q}_0(D, \mathbb{R}^d)$, and a phase field $\zeta \in W^{1,2}(D, \mathbb{R})$ denote a solution of the phase field model, if I and ζ minimizes the restricted energy*

$$E^{\epsilon}_{\mathrm{fid}}[I, w] + E^{\epsilon}_{\mathrm{reg},u}[I, \zeta] + E^{\epsilon}_{\mathrm{phase}}[\zeta], \tag{6.10}$$

for fixed w in $W^{1,2}(D, \mathbb{R}^{d+1})$. For fixed $I, \zeta \in W^{1,2}(D, \mathbb{R})$, the motion field w minimizes the global energy

$$E^{\epsilon}_{\mathrm{global}}[I, w, \zeta] = E^{\epsilon}_{\mathrm{fid}}[I, w] + E^{\epsilon}_{\mathrm{reg},u}[I, \zeta] + E^{\epsilon}_{\mathrm{reg},w}[w, \zeta] + E^{\epsilon}_{\mathrm{phase}}[\zeta]\,. \tag{6.11}$$

Remark: The definition of I and ζ as the minimizer of a restricted functional is not only sound with respect to applications. Indeed, a simultaneous relaxation of the global energy with respect to all unknowns is theoretically questionable. $E^{\epsilon}_{\mathrm{reg},w}$ is not convex in ζ and it cannot be expected that this energy contribution is lower semi–continuous on a suitable set of admissible functions. With the above notion of solutions, the direct method in the calculus of variations can be applied. In particular, one observes compactness of the sequence of the phase fields associated with a minimizing sequence of image sequences I and motion fields w.

Theorem 2 (Existence of solutions) *Suppose $d + 1 < q < \infty$, $\lambda_I, \lambda_w, \mu_I, \mu_w, \nu, \epsilon > 0$ and let $k_\epsilon > 0$. Then there exists a solution (I, w, ζ) of the phase field problem introduced in Definition 9.*

This theorem can be proven by rewriting the phase field approach as an energy minimization problem, which allows to apply the direct method from the calculus of variations. For fixed w the energy functional

$$E_w[I, \zeta] := E^{\epsilon}_{\mathrm{fid}}[I, w] + E^{\epsilon}_{\mathrm{reg},u}[I, \zeta] + E^{\epsilon}_{\mathrm{phase}}[\zeta] \tag{6.12}$$

is strictly convex and by the direct method a unique minimizer is obtained. The minimizing phase field is given as the weak solution of the corresponding Euler Lagrange equation

$$-\epsilon\Delta\zeta + \frac{1}{4\epsilon}\zeta = f[I,\zeta] := \frac{1}{4\epsilon} - \frac{\mu_I}{2\nu}\left|\nabla_{(t,x)}I\right|^2\zeta\,. \tag{6.13}$$

Applying the weak maximum principle it is observe that $\overline{\zeta} \equiv 1$ is a super solution and $\underline{\zeta} \equiv 0$ a sub solution. Thus, $\zeta[w]$ is uniformly bounded, i. e. $0 \le \zeta[w] \le 1$.

Given $(I[w], \zeta[w])$ the global energy $E^\epsilon_{\text{global}}$ is considered solely as a functional of the motion field $w = (1, v)$:

$$E[w] = E^\epsilon_{\text{global}}[I[w], w, \zeta[w]]$$

on the admissible set

$$\mathbf{a} := \left\{ w \,:\, w = (1, v + v_\delta)\,,\; v \in W_0^{1,q}(D, \mathbb{R}^{d+1}) \right\}.$$

This leads to the definition of $\underline{E} := \inf_{w\in\mathbf{a}} E[w]$.

Finally, taking into account convexity properties of the integrands, Fatou's lemma and the modulus of continuity of E_{fid} and $E_{\text{reg},w}$ with respect to w and $P[\zeta]$, respectively, it can be shown that (using Einstein's summation convention):

$$\begin{aligned}
E[w] &= E_{\text{global}}[I[w], w, \zeta[w]] = E_{\text{global}}[I, w, \zeta] \\
&= \int_D \frac{\lambda_I}{2}\left(\liminf_{k\to\infty}\lambda_i^k I^i - I_0\right)^2 + \frac{\lambda_w}{2}\left|\liminf_{k\to\infty} w\cdot\left(\lambda_i^k\nabla_{(t,x)}I^i\right)\right|^q \mathrm{d}\mathcal{L} \\
&\quad + \int_D \frac{\mu_I}{2}(\zeta^2 + k_\epsilon)\left|\liminf_{k\to\infty}\lambda_i^k\nabla_{(t,x)}I^i\right|^2 + \frac{\mu_w}{q}\left|\liminf_{k\to\infty} P[\zeta]\lambda_i^k\nabla_{(t,x)}w^i\right|^q \mathrm{d}\mathcal{L} \\
&\quad + \int_D \left(\nu\epsilon\left|\liminf_{k\to\infty}\lambda_i^k\nabla\zeta^i\right|^2 + \frac{\nu}{4\epsilon}(1 - \liminf_{k\to\infty}\lambda_i^k\zeta^i)^2\right)\mathrm{d}\mathcal{L} \\
&\le \underline{E} + \rho + \lambda_w C_w C_I^2\rho + \mu_w C_w^q\rho,
\end{aligned}$$

where the constants C_I and C_w are defined as $C_w = \sup_{k=1,\cdots,\infty}\max\left\{\left|w^k\right|_{L^\infty}, \left|\nabla_{(t,x)}w^k\right|_{L^q}\right\}$ and $C_I = \sup_{k=1,\cdots,\infty}\left|\nabla_{(t,x)}I^k\right|_{L^2}$.

This estimate holds for any $\rho \ge 0$. Thus, one obtains $E[w] \le \underline{E}$, which implies that w is a minimizer of the energy E and hence (I, w, ζ) a solution of our phase field problem. The complete proof is detailed in Preusser et al. [2007].

Remark: The above problem formulation is not only sound with respect to the actual modeling, but it will allow a simple relaxation approach (see below). Indeed, experimentally one observes convergence in $3-5$ iterations. Concerning the analytical treatment, the above formulation makes no differentiation of the operator $P[\zeta]$ with respect to ζ necessary. Furthermore, based on the direct methods in the calculus of variations, existence of solutions for the approximate problems can be established on a suitable set of admissible functions for the image intensity, the phase field and the motion field for $q \ge 3$. A rigorous treatment of the limit behavior for $\epsilon \to 0$ is still open.

Applying formal asymptotics, one verifies that the phase field approach proposed here indeed converges to the above Mumford–Shah model. For small ϵ one expects a steeping of the gradient I on a strip of thickness ϵ around the edge set. The phase field ϕ will approximate 1 apart from a decreasing neighborhood of the edge surface. For $\epsilon \to 0$ convergence of $E_{\mathrm{reg},u}$ and $E_{\mathrm{reg},w}$ to $\int_{D\setminus S} \frac{\mu_I}{2} \left|\nabla_{(t,x)} I\right|^2 + \frac{\mu_w}{q} \left|\nabla_{(t,x)} I\right|^q \,\mathrm{d}\mathcal{L}$ and of $E^\epsilon_{\mathrm{phase}}$ to $\mathcal{H}^d(S)$ is expected. Under these assumptions on the qualitative behavior $\int_D (w \cdot \nabla_{(t,x)} I)^2 \,\mathrm{d}\mathcal{L}$ converges to the second term of E_{MSopt}, whereas on the edge surface one observes a concentration of energy on the jump set scaling like $O(\epsilon^{-1})$. Furthermore, it can be observed that in the limit the optical–flow–constraint $n_S \cdot (w^+ + w^-) = 0$ is reproduced from the sharp interface Mumford–Shah approach. A rigorous validation of this limit behavior is still open.

6.6 Variations of the Energy and the Algorithm

In what follows, the Euler–Lagrange equations of the above energies are considered. Thus, the variations of the energy contributions with respect to the involved unknowns I, w, ζ need to be computed. The variation of an energy E in direction ζ with respect to a parameter function z will be denoted by $\langle \delta_z E, \zeta \rangle$. For the ease of implementation in the following the variations and the algorithm will be confined to the case $q = 2$. Obviously, higher order problems with $q < 2$ can be formulated accordingly. Using straightforward differentiation for sufficiently smooth I, w, ζ and initial data I_0 one obtains

$$\begin{aligned}
\langle \delta_I E^\epsilon_{\mathrm{fid}}[I,w], \vartheta \rangle &= \lambda_w \int_D (\nabla_{(t,x)} I \cdot w)(\nabla_{(t,x)} \vartheta \cdot w) + \lambda_I \int_D (I - I_0)\vartheta \,, && (6.14)\\
\langle \delta_w E^\epsilon_{\mathrm{fid}}[I,w], \psi \rangle &= \int_D \lambda_w \,(\nabla_{(t,x)} I \cdot w)(\nabla_{(t,x)} I \cdot \psi) \,, && (6.15)\\
\langle \delta_I E^\epsilon_{\mathrm{reg},u}[I,\zeta], \vartheta \rangle &= \int_D \mu_I (\zeta^2 + k_\epsilon) \nabla_{(t,x)} I \cdot \nabla_{(t,x)} \vartheta \,, && (6.16)\\
\langle \delta_\zeta E^\epsilon_{\mathrm{reg},u}[I,\zeta], \xi \rangle &= \int_D \mu_I \zeta \left|\nabla_{(t,x)} I\right|^2 \xi \,, && (6.17)\\
\langle \delta_w E^\epsilon_{\mathrm{reg},w}[w,\zeta], \psi \rangle &= \int_D \mu_w P[\zeta] \nabla_{(t,x)} w : \nabla_{(t,x)} \psi \,, && (6.18)\\
\langle \delta_\zeta E^\epsilon_{\mathrm{phase}}[\zeta], \xi \rangle &= \int_D 2\nu\epsilon \nabla_{(t,x)} \zeta \cdot \nabla_{(t,x)} \xi + \int_D \frac{\nu}{2\epsilon} (\zeta - 1)\xi \,, && (6.19)
\end{aligned}$$

for scalar test functions ξ, ϑ and velocities $\psi = (0, \pi)$. Here, for ease of notation $A : B := \mathrm{tr}(B^T A)$ is used. Now, summing up the different terms as in (6.10) and integrating by parts results in the following system of partial differential equations (PDEs):

$$\begin{aligned}
-\mathrm{div}_{(t,x)} \left(\frac{\mu_I}{\lambda_I} (\zeta^2 + k_\epsilon) \nabla_{(t,x)} I + \frac{\lambda_w}{\lambda_I} w (\nabla_{(t,x)} I \cdot w) \right) + I &= I_0 && (6.20)\\
-\epsilon \Delta_{(t,x)} \zeta + \left(\frac{1}{4\epsilon} + \frac{\mu_I}{2\nu} \left|\nabla_{(t,x)} I\right|^2 \right) \zeta &= \frac{1}{4\epsilon} && (6.21)\\
-\frac{\mu_w}{\lambda_w} \mathrm{div}_{(t,x)} \left(P[\zeta] \nabla_{(t,x)} v \right) + (\nabla_{(t,x)} I \cdot w) \nabla_x I &= 0, && (6.22)
\end{aligned}$$

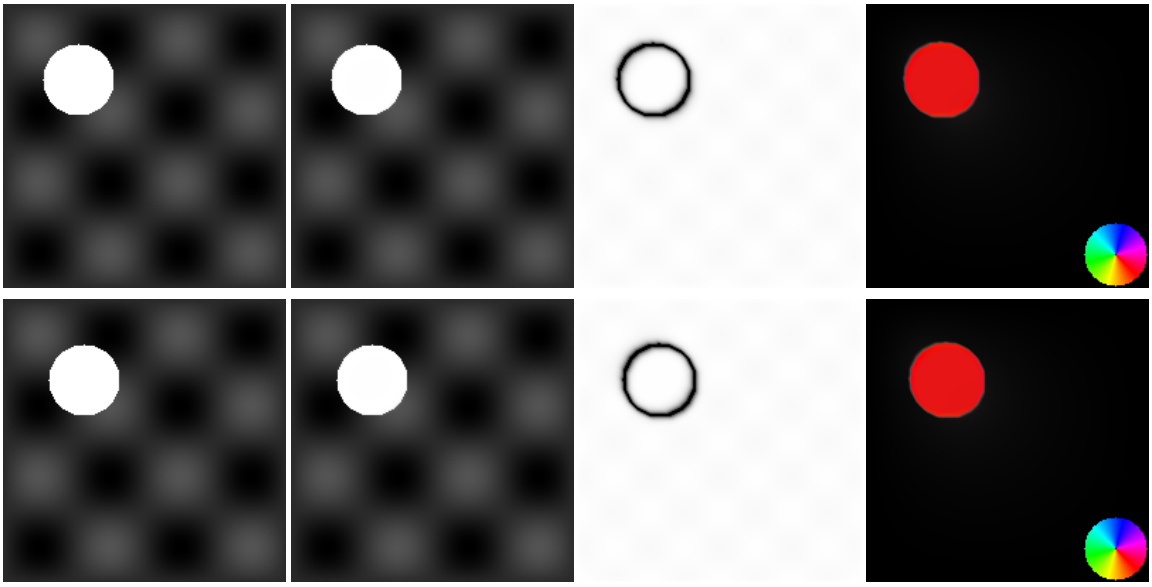

a **b** **c** **d**

Figure 6.1: *Top to bottom: The 3rd and 7th frames of the test sequence are shown in* **a** *and the corresponding smoothed image in* **b**. *The phase field and the color coded optical flow field can be seen in* **c** *and* **d**.

as the Euler–Lagrange equations characterizes the necessary conditions for a solution (I, w, ζ) of the above stated phase field approach.

It should be noted that the full Euler–Lagrange equations, characterizing a global minimizer of the energy, would involve additional variations of $E_{\text{reg},w}$ with respect to ζ.

Following Ambrosio and Tortorelli [1992], the following iterative algorithm is proposed for the solution of the phase field problem with $q = 2$:

Step 0. Initialize $I = I_0$, $\zeta \equiv 1$, and $w \equiv (1, 0)$.
Step 1. Solve (6.20) for fixed w, ζ.
Step 2. Solve (6.21) for fixed I, w.
Step 3. Solve (6.22) for fixed I, ζ, return to **Step 1.**

The algorithm consists of a consecutive solution of linear partial differential equations. Alternative, one might iterate Step 1 and 2 first until convergence is reached and then, in an outer iteration, the identification of the motion field w could be considered. Even though, this second variation seems to be closer to the definition of solutions of the phase field problem, the above algorithm converges to the same solution. It does so much faster in the applications considered.

6.7 Finite Element Discretization

The Finite Element method (FEM) used for approximating the functional presented in this chapter is similarly to the Finite Element method proposed by Bourdin [1999] and Bourdin

and Chambolle [2000] for the phase field approximation of the Mumford–Shah functional. To solve the above system of PDEs $[0,T] \times \Omega$ is overlaid by a regular hexahedral grid. In the following, the spatial and temporal grid width are denoted by h and τ respectively. Hence, image frames are at a distance of τ and pixels of each frame are placed on a regular mesh with grid size h. To avoid tri-linear interpolation problems each hexahedron is subdivided into 6 tetrahedra. On this tetrahedral grid the space of piecewise affine, continuous functions $\mathbb{V}$ is considered. One seeks discrete functions $U, \Phi \in \mathbb{V}$ and $V \in \mathbb{V}^2$, such that the discrete and weak counterparts of the Euler Lagrange equations (6.20), (6.21) and (6.22) are fulfilled. This leads to the solution of systems of linear equations for the vectors of the nodal values of the unknowns U, Φ, V. The interested reader is referred to Preusser et al. [2007] for a detailed description of the matrices and the resulting systems of equations. A careful implementation is required to ensure an efficient method. For a time-space volume of K time steps and images of $N * M$ pixels, the finite element matrices for I and ζ have $N\,M\,K\,C$ entries, where $C = 15$ is the number of nonzero entries per row, equal to the number of couplings of a node. The finite element matrix for V has four times more elements, as V is a two-dimensional vector. Using an efficient custom-designed compressed row sparse matrix storage, presently datasets of up to $K = 10$ frames of $N = 500, M = 320$ pixels can be handled in less than 1GB memory. The linear systems of equations are solved applying a classical conjugate gradient method. For the pedestrian sequence (Fig. 6.6), one such iteration takes 47 seconds on a Pentium IV PC at 1.8 GHz running Linux. The complete method converges after 2 or 3 such iterations. Large video sequences are computed by shifting a window of $K = 6$ frames successively in time. Thus, temporal boundary effects are avoided.

6.8 Results and Discussion

In this section several results of the proposed method for two dimensional image sequences are presented. In the considered examples, the parameter setting $\epsilon = h/4$, $\mu_I = h^{-2}$, $\mu_w = \lambda_I = 1$, $\lambda_w = 10^5 h^{-2}$ and $C(\epsilon) = \epsilon$, $\delta = \epsilon$ has proven to give good results.

First, a simple example of a white disk moving with constant speed $v = (1,1)$ on a black background as shown in Figure 6.1. A small amount of smoothing results from the regularization energy $E_{\text{reg}} I^\epsilon$ (Fig. 6.1**b**), which is desirable to ensure robustness in the resulting optical flow term $\nabla_{(t,x)} I \cdot w$ and removes noisy artifacts in real-world videos, e.g. Figure 6.5 and Figure 6.6. The phase field clearly captures the moving object's contour. The optical flow is depicted in Figure 6.1**c** by color coding the vector directions as shown by the lower-right color wheel. Clearly, the method is able to extract the uniform motion of the disc. The optical flow information, available only on the motion edges (black in Figure 6.1**c**), is propagated into the information-less area inside the moving disk, yielding the final result.

In the next example, the simple moving circle sequence is revisited, but this time noise is added to it. Moreover, the information of frame 10 in the sequence is completely destroyed as can be seen in Figure 6.2. The results for frames 3 and $9-11$ are shown Figure 6.2. The phase field detects the missing circle in the destroyed frame as a temporal edge surface in the sequence. Thus ϕ drops to zero in the temporal vicinity of the destroyed frame. This is still

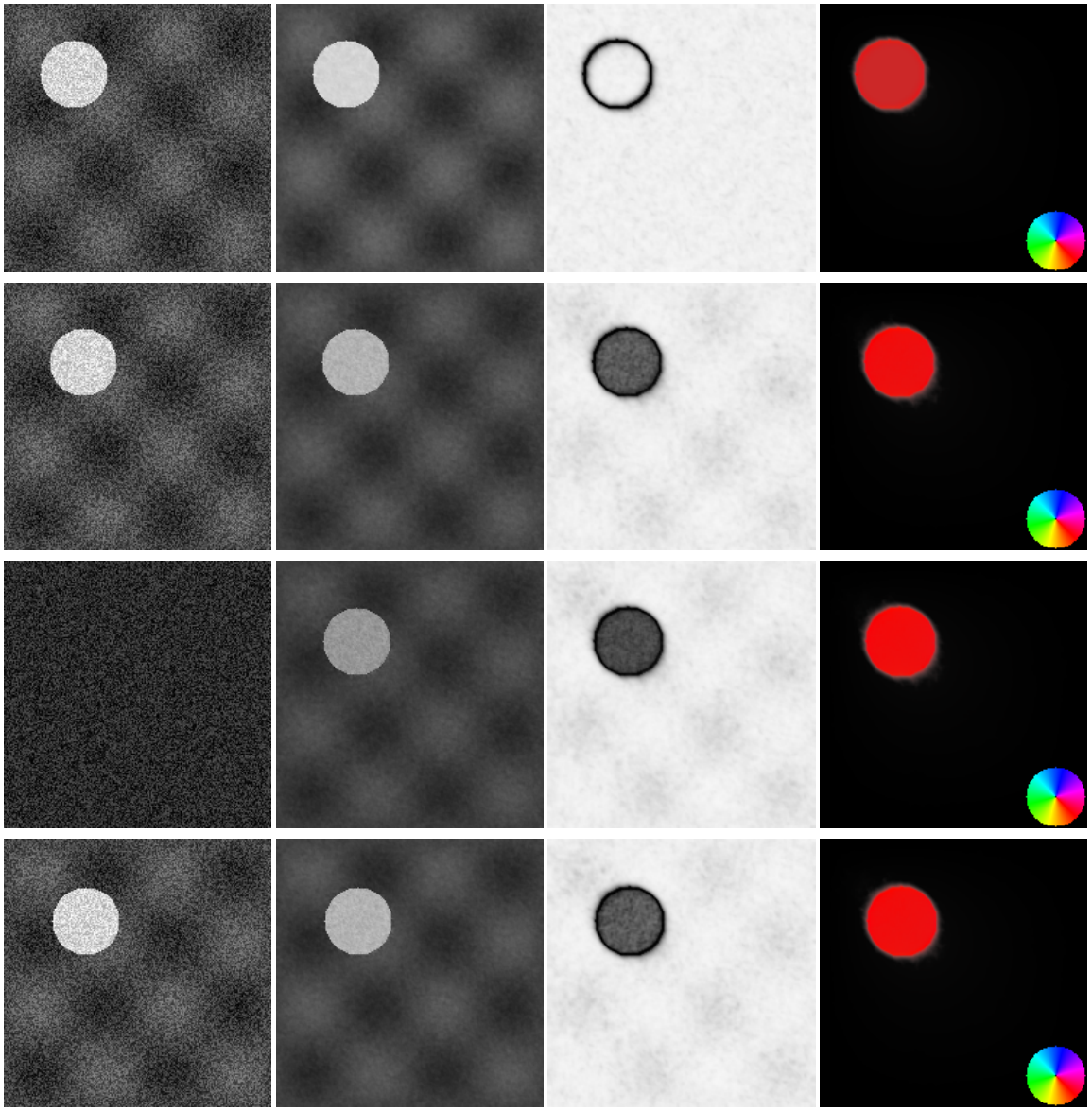

Figure 6.2: *Noisy circle sequence: From top to bottom, frames* 3 *and* $9-11$ *are shown. (**a**) original image sequence, (**b**) smoothed images, (**c**) phase field, (**d**) estimated motion (color coded).*

visible in the previous and next frames, shown in the second and third row. However, this does not hamper the restoration of the correct optical flow field, shown in the fourth column. This result is due to the anisotropic smoothing of information from the frames close to the destroyed frame. For this example, the parameter $\epsilon = 0.4h$ was used.

Next, in Figure 6.3, a real video is analyzed: The camera translates and rotates while looking at some blocks on a noisy background. Both, this and the next example come from the publicly available dataset collection used in McCane et al. [2001]. Despite the low resolution and contrast of the input and the quick camera motion, both visible in the phase field presented

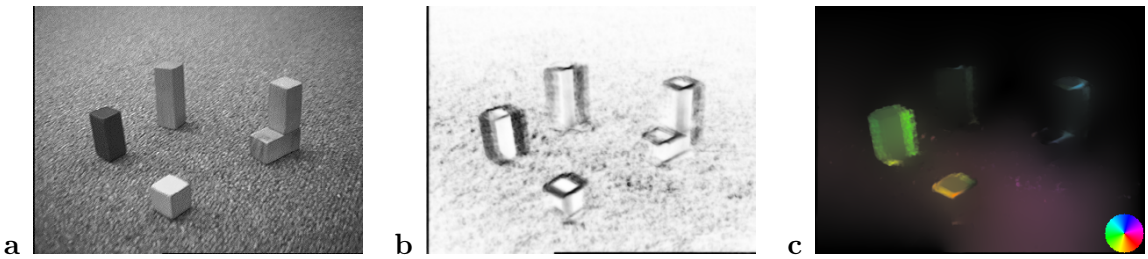

Figure 6.3: *Results for the blocks sequence: Frame 5 of the sequence in* **a**, *the phase field in* **b** *and the color coded optical flow field in* **c**.

in Figure 6.3**b**, the novel method is able to extract the apparent motion of the blocks, in this case a counterclockwise spin, from the noisy background. A close inspection of the phase field allows to recover the contours of the blocks. The noisy background poses no problem and no erroneous segmentation is performed as would be the case in a purely gray-valued segmentation. At the same time the estimated motion field is very smooth inside the individual blocks, without significant smearing across the motion discontinuities. Segmenting multiple objects within the scene poses no problem to the algorithm. This is due to the fact that no implicit shapes or number of objects are assumed.

A second synthetic example is shown in Figure 6.4, using data from the same collection used by McCane et al. [2001]. Here, a textured sphere spins on a textured background as displayed in Figure 6.4**a**. Again, the new technique is able to clearly segment the moving object from the background, even though the object does not change position. For the computation a phase field parameter $\epsilon = 0.15h$ was used. The extracted optical flow field clearly shows the spinning motion and the discontinuous motion field, as can be seen in Figure 6.4**d**.

Next, the results of a well known real video sequence, the so-called Hamburg taxi sequence, is visualized. Figure 6.5 shows the smoothed image I, phase field ϕ and color-coded optical flow field v as well as an original frame of that sequence. The new technique detects the image edges well, as can be seen in Figure 6.5**c**. Also, the upper-left rotating motion of the central car is extracted accurately as displayed in Figure 6.5**c**. As it should be, the edges of the stationary objects, clearly visible in the phase field, do not contribute to the optical flow. Moreover, the moving car is segmented as one single object in the optical flow field. It can be seen that the motion information is extended from the moving edges to the whole moving shape.

Finally, the algorithm is used to analyze a complex video sequence, taken under outdoor conditions by a monochrome video camera. The sequence shows a group of walking pedestrians in Figure 6.6 (top). The human silhouettes are well extracted and captured by the phase field (Figure 6.6 (middle)). A vector plot of the optical flow field is not presented, as it is hard to interpret it visually at the video sequence resolution of 640 by 480 pixels. However, the color-coded plot of the optical flow filed (Figure 6.6 (bottom)) clearly reproduces the moving limbs of the pedestrians. The overall red and blue color corresponds to the walking directions. The estimated motion is smooth inside the areas of the individual pedestrians and not smeared across the motion boundaries. In addition, the algorithm nicely segments the different moving

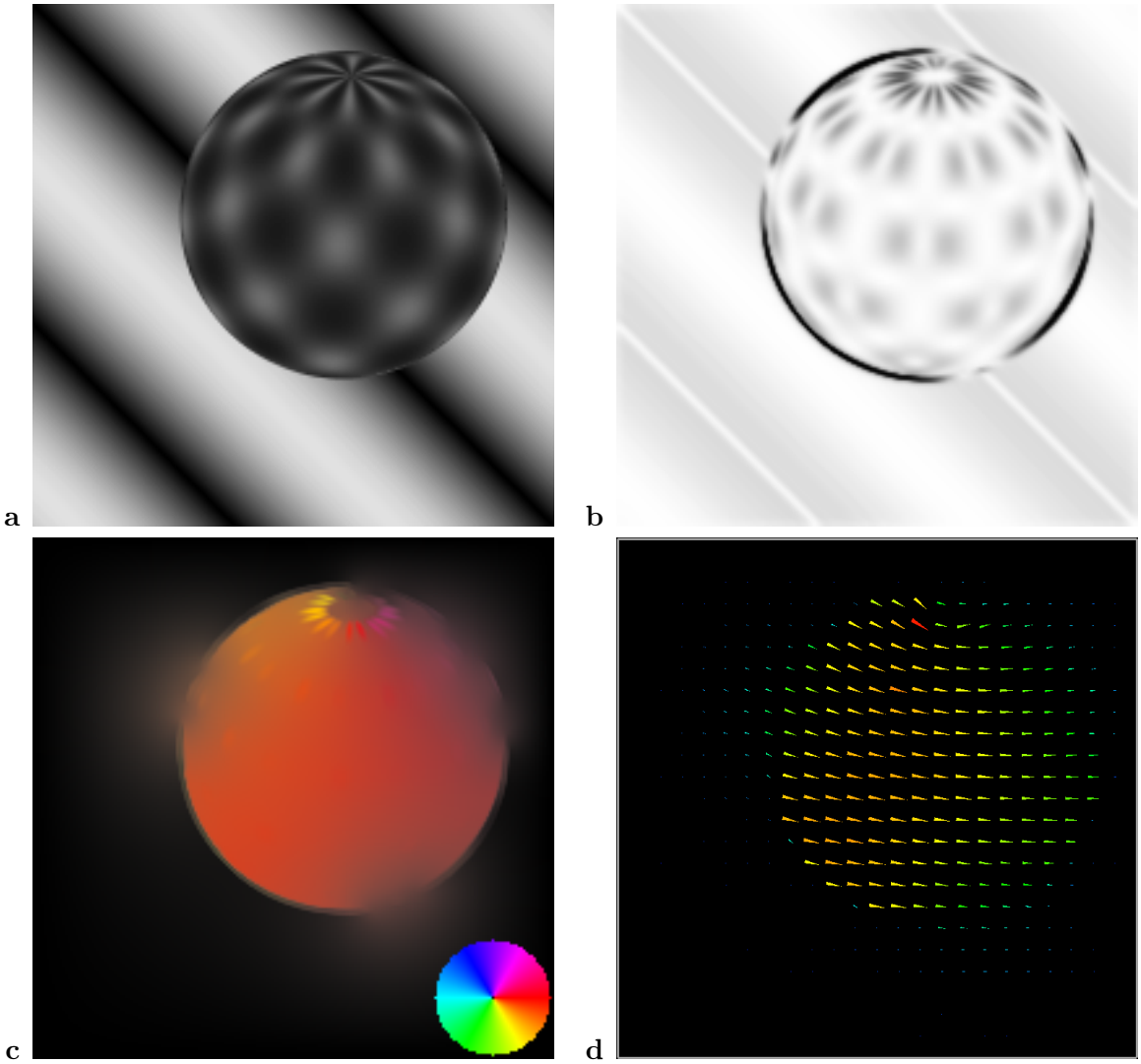

Figure 6.4: *Rotating sphere: The smoothed image is shown in* **a**, *the phase field in* **b**, *and the color coded optical flow in* **c**. *In* **d** *a vector plot of the optical flow with color coded flow magnitude is displayed.*

persons. The cluttered background poses no big problem to the segmentation, nor are the edges of occluding and overlapping pedestrians, who are moving at almost the same speed.

6.9 Conclusion

In this chapter an algorithm has been presented that incorporates the phase-field approach presented by Ambrosio and Tortorelli [1992] into a Mumford and Shah [1989] type functional. Smoothness and fidelity terms for both the image sequence and the flow field are incorporated in this functional. This has lead to an algorithm that combines denoising of image sequences and edge detection with the estimation of motion. Piecewise smoothness is assumed for

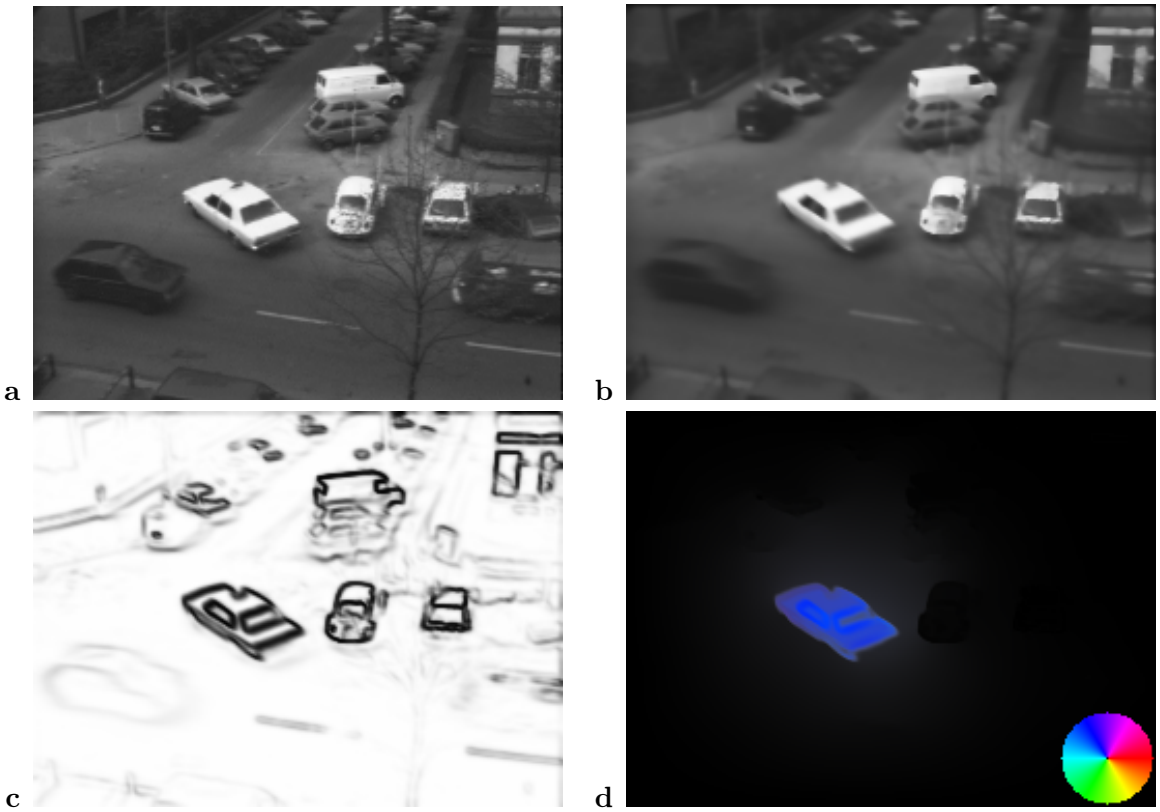

Figure 6.5: *Taxi sequence: The 11th original frame in* ***a****, the smoothed image in* ***b****, the phase field in* ***c*** *and the color coded flow field in* ***d****.*

the motion field. Thus, no smoothing across motion boundaries takes place. Moreover, an anisotropic enhancement of the flow along the edges of the image in the sense of Nagel and Enkelmann [1986] is incorporated. This formulation of object boundaries by a phase-field requires not a prior knowledge of the number or shapes of objects in the scene. This makes this algorithm well suited for a number of applications. The solver of the functional can be implemented very efficiently, due to its inherent multi-scale approach.

The algorithm has been tested on a number of synthetic sequences. It was clearly demonstrated that the algorithm is even capable of performing a very simple image inpainting. On a synthetic sequence, an object diapered for one frame. Due to the smoothness term of image intensities along trajectories, the object reappeared in the smoothed image. The object edges were also reproduced by the phase field very well. This leads to a appropriate smoothing of the optical flow field and the image intensities inside objects. However, no smoothing occurs across object boundaries. This results in very sharp denoised images.

Apart from synthetic test sequences, the algorithm was also tested on real world sequences. To this end, the well known Hamburg taxi sequence was used as well as a higher resolved scene of pedestrians. The algorithm also performed quite well on these real world sequences. On the taxi sequence, motion information, which can only be obtained on edges, propagates into homogeneous areas such as the windscreens. Yet, this information does not diffuse to areas

outside the car. The edges of limbs of pedestrians were also clearly found, even in areas of low contrast. Again, neither initial values for the edges of the objects nor their shape has to be used for this technique.

This makes it feasible to use this algorithm on scientific data to recover information lost due to artifacts. For this type of application it is very important that no a priori information regarding the objects is required. In thermographic image sequences, for example, artifacts from reflections might be corrected in the data. These reflections appear in all possible shapes, depending both on the reflected object as well as the shape of the reflecting medium. In air-sea interactions, reflections on the water surface are very complex due to the strongly and irregularly curved wavy water surface.

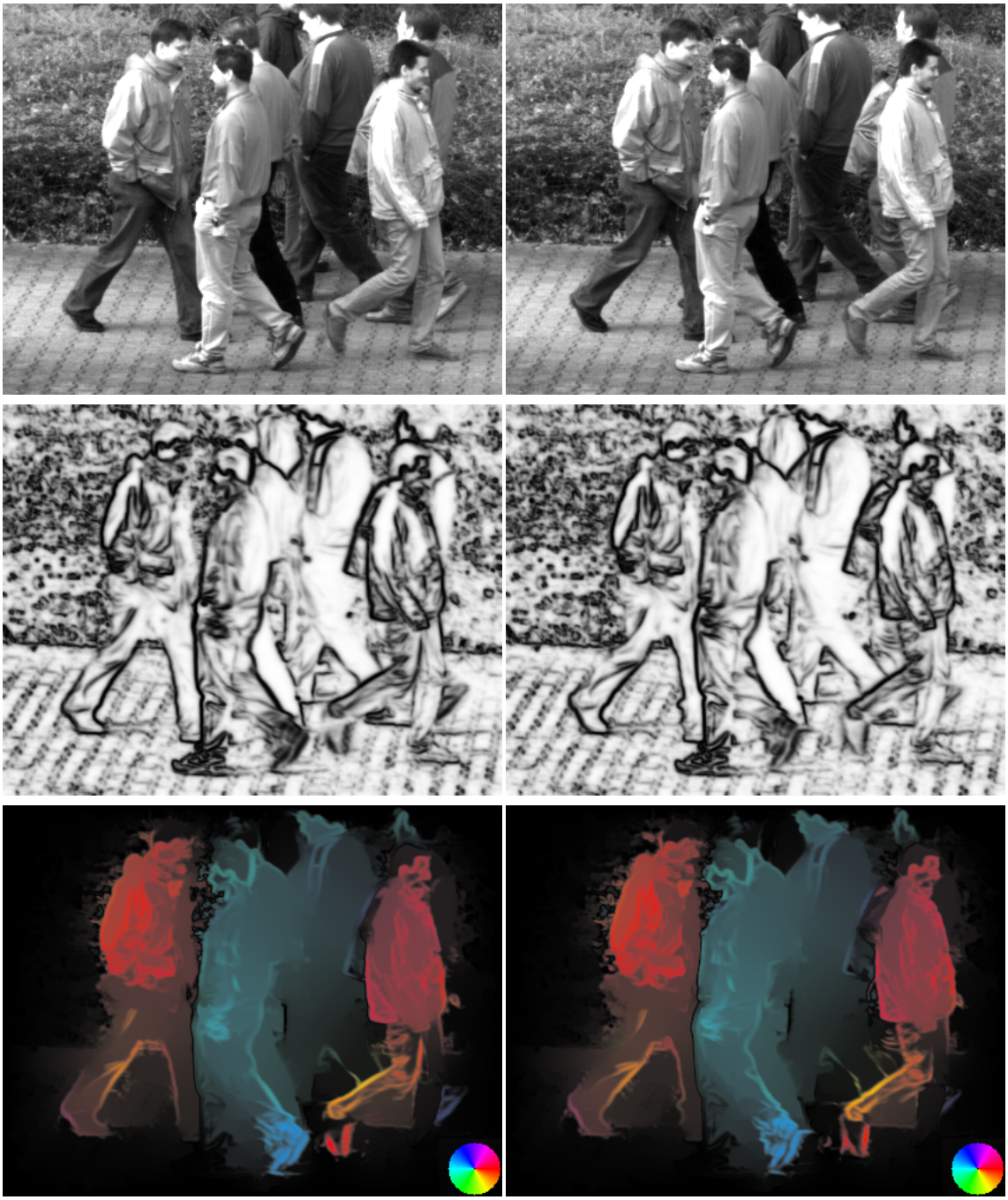

Figure 6.6: *Pedestrian video: Frames from original sequence (top); phase field (middle); optical flow, color coded (bottom).*

Part II

Fluid Dynamic Problems

Chapter 7

Air-Water Interactions

7.1 Introduction

Current state of the art techniques for measuring the transfer velocities of gases are based on *mass balance methods* where tracer concentrations in the water are artificially modified and changes are measured over time. The effect of changes in concentration caused by diffusion due to currents in the ocean can be accounted for by introducing a second tracer with a different diffusivity, a technique known as the *dual tracer method* [Geernaert, 1999; Fairall et al., 2000]. These methods yield point measurements with integration times as long as days. Recently direct *eddy correlation techniques* have been introduced [McGillis et al., 2001a]. Here the integration times are shortened somewhat to make measurements on time scales of less than an hour feasible. Still these measurements present point measurements with integration times too long to predict and link the transfer velocities to small scale interactions, often taking place on time scales of less than seconds. The same problems hold true for measurements of the transport of heat. While the different techniques may help in relating the mean transfer velocities to other mean quantities such as wind speed, roughness of the sea surface or whitecap coverage and thus help in finding semi-empirical parameterizations, they are not adequate for gaining a deeper understanding of the transport processes involved.

The use of an infrared camera with its spatially resolved temperature measurement opens up new possibilities for studying air-water heat transfer. Spatial structures of the upper most ten micrometers are observable, which allows to draw conclusions concerning the transport processes involved [Haußecker, 1996]. An analysis of the predominant scales of turbulence has also been conducted [Schimpf, 2000]. The use of infrared cameras for measurements at the sea surface have found wider acceptance, as other parameters important to transport processes such as Langmuir circulations [Veron and Melville, 2001], wave-breaking dynamics [Jessup et al., 1997a] and micro scale wave breaking [Jessup et al., 1997b] can be detected with such devices as well. Still, the unsolved issue of estimating heat fluxes directly at the air-water interface at high temporal and spatial resolution prevails. Only by measuring the heat flux and the small scale processes influencing the transfer of heat on the same spatial and temporal scales simultaneously, a deeper understanding of the transport phenomena involved

can be attained.

A temperature difference ΔT or concentration difference ΔC will lead to the transport of heat or mass, expressed by the heat flux j_{heat} or mass flux j_g. Due to the linearity of both Fourier's and Fick's laws for the transport of heat and mass respectively, this transport can be expressed by the transfer velocity k independent of the concentration difference. For the transport of heat this velocity is defined by

$$k_{\text{heat}} = \frac{j_{\text{heat}}}{\rho c_p \Delta T}, \tag{7.1}$$

with the density ρ and the specific heat c_p of sea water.

Techniques for estimating the net heat flux k_{heat} as well as the transfer velocity k_{heat} from thermography will be presented in this chapter. Apart from this transport, the transport of mass and momentum is of great interest. The transport of mass can be deduced from the transport of energy. This is due to the fact that a number of transport processes are similar for both the transport of heat and that of masses, such as gas tracers. Strong experimental evidence exists, backing up this assumption ([Jähne et al., 1989] and [Jähne et al., 1998]). Therefore, from measurements of the transport of heat, the relevant quantities can be scaled to the transport of mass. The relation of the heat transfer velocity k_h and the mass transfer velocity of a certain gas k_g is given by

$$\frac{k_g}{k_h} = \left(\frac{\text{Sc}_h}{\text{Sc}_g}\right)^n, \tag{7.2}$$

where Sc_h and Sc_g are the Schmidt numbers of heat and gas respectively and n is the Schmidt number exponent [Jähne et al., 1998]. From this equation the gas transfer velocity k_g can be deduced from the heat transfer velocity k_h since the Schmidt numbers are known.

Apart from the transport of energy and mass, the transport of momentum is the third quantity transported across the air-water interface. Momentum is transported from the atmosphere to the ocean by friction at the sea surface. This leads to the flux of momentum to be split in two compartments: Momentum can be transferred due to viscous shear in the water sided viscous boundary layer (this is called viscous stress τ_μ) or due to pressure difference on the upwind and downwind faces of waves (this part is termed form drag). As will be shown in this chapter, a novel technique has been developed that makes it possible to measure the viscous stress directly at the air water interface from active thermography. Therefore, in this chapter it will be demonstrated that the transport of both heat and momentum can be measured directly from infrared thermography. The momentum of mass can then be dueduced from the transport of heat, making infrared themography a valuable tool for research in air-water interactions.

This section is organized as follows: In Section 7.2 two models of transport at the air-water interface will be presented, on which subsequent estimations are based. The well known model of surface renewal is sketched in Section 7.2.1. A novel model, the eddy renewal model, is developed in Section 7.2.2. In Section 7.3 both models will be used for estimating the temperature difference ΔT across the water sided thermal boundary layer. This is a very

important quantity for remote sensing [Schlüssel et al., 1990] as it is for subsequent techniques for estimating the net heat flux from thermography. In Section 7.4 a technique will be outlined for estimating surface flows as well as the material derivative dT/dt directly at the interface from passive thermography. It will also be shown that divergences and convergences can readily be obtained. In Section 7.5 techniques will be presented for measuring the time of residence of water parcels at the water surface. This is the first time that this important parameter of the surface renewal model can be measured directly at the interface. From this parameter, together with ΔT, the transfer velocity of heat can be measured from infrared thermography, which will also be demonstrated in the same section. In Section 7.6 the probability density function of the surface renewal time scale will be measured. Three techniques of measuring the net heat flux directly at the air-water interface will be presented in Section 7.7. Two of these are based on the surface renewal model, one is based on the eddy renewal model. The technique of measuring viscous shear stress at the air-water interface will be detailed in Section 7.8. This technique is based on active thermography and advanced motion models, taking heat absorption in water into account. The experimental set-up both for active and for passive thermography will be shown in Section 7.9. Results of measurements conducted in the laboratory as well as in the field will be presented in Sections 7.10 and 7.11, respectively. This chapter concludes with a brief summary in Section 7.12.

Parts of this chapter have been published in Garbe et al. [2004], Schimpf et al. [2004] and Hara et al. [2006].

7.2 Transport Models

When studying transport phenomena at the sea surface it is important to have an understanding of the basic physical processes involved. A detailed introduction to a number of commonly used transport models at the air-sea interface is presented in Garbe [2001]. In the following, use is made only of the surface renewal model and the eddy renewal model. They will be shortly described in Section 7.2.1 and Section 7.2.2 respectively. A comparison of the two model will be given in Section 7.2.3.

7.2.1 Surface Renewal Model

Considerable success has been obtained with a simple model which allows small parcels of water adjacent to the interface to be replaced randomly by water from the well mixed turbulent layers from the bulk of the water. This so called *surface renewal model* has been introduced in chemical engineering by Higbie [1935] who assumed periodic renewal of the water parcels. The model was then extended in chemical engineering to include statistically distributed random events by Danckwerts [1951], Hariott [1962] and Rao et al. [1971]. It was later applied to the air-sea interface by Brutsaert [1975b], Brutsaert [1975a], Liu and Businger [1975], Liu et al. [1979], Jähne [1980] and Soloviev and Schlüssel [1994].

In this model the motion of the molecular sublayer can be expected to remain locally laminar and parallel to the interface. As such the sea water at the sea surface cannot be easily

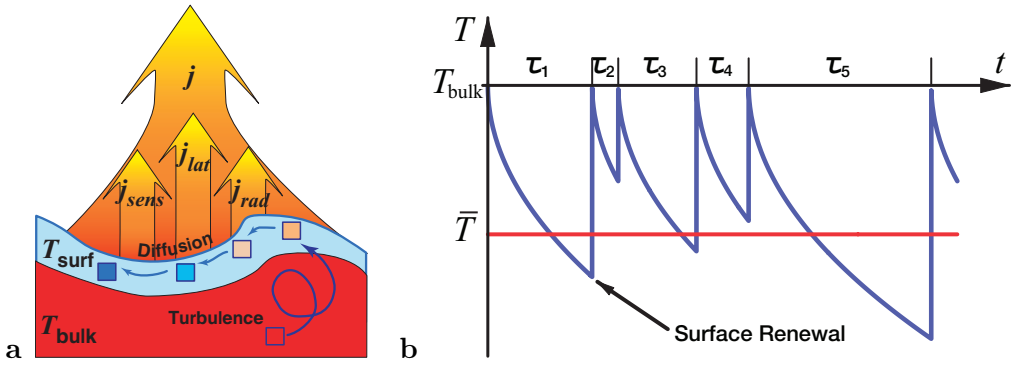

Figure 7.1: ***a*** *Schematic drawing of the thermal boundary layer and the surface renewal model.* ***b*** *Illustration of the sea surface temperature T with respect to time t.*

replaced by the water from the bulk, although it can come very close to it. It is instructive to consider an individual fluid parcel in the mixing layer. Because of the very high efficiency of turbulent transport it will be at the same temperature T_{bulk} as the bulk. Due to a stochastic renewal process it will be moved very close to the interface. The sea surface is subject to the net heat flux j, composed of the sensible heat flux j_{sens} due to conduction, the latent heat flux j_{lat} resulting from evaporative cooling and the long-wave radiative heat flux j_{rad}. A sketch of this model can be observed in Figure 7.1 **a**. During daytime, short-wave fluxes owing to solar irradiation will also be present. These are of no concern here as only measurements during night time are under consideration. As opposed to short-wave solar irradiation, which is a volumetric source of heat, the fluxes present during the night are only effective directly at the sea surface. Once injected into the boundary layer by the renewal process, the water parcels equilibrate with the surface. This equilibration takes places by thermal conduction as formulated in Fourier's law. This process is similar to that of mass transport, where Fick's laws of diffusion are applicable. The relevant three-dimensional diffusion equation is given by

$$\frac{dT}{dt} = \frac{\partial T}{\partial t} + u\frac{\partial T}{\partial x} + v\frac{\partial T}{\partial y} + w\frac{\partial T}{\partial z} = \kappa\Delta T = \kappa\left(\frac{\partial^2}{\partial x^2} + \frac{\partial^2}{\partial y^2} + \frac{\partial^2}{\partial z^2}\right)T, \tag{7.3}$$

where $(u,\, v,\, w)$ are water velocities in $(x,\, y,\, z)$ directions, and κ is the molecular diffusivity. The coordinate system is defined such that x and y are in horizontal and z is in vertical (upward) from the mean water surface.

From this diffusion equation, the following governing equation can be found by assuming that horizontal gradients are negligible in comparison to vertical gradients and further employing a constant flux boundary condition at the interface:

$$\frac{\partial T}{\partial t} = \kappa\frac{\partial^2 T}{\partial z^2}, \qquad 0 \le t \le \alpha\tau, \tag{7.4}$$

where τ is the renewal time scale and $\alpha\tau$ is the actual interval between the renewal events (the coefficient α is determined later). The boundary conditions are given by

$$j_{\text{heat}} = -k\frac{\partial T}{\partial z} = -\kappa\rho c_p\frac{\partial T}{\partial z}, \quad \text{at} \quad z = 0, \tag{7.5}$$

and

$$T = T_{\text{bulk}}, \quad \text{at} \quad z = -\infty. \tag{7.6}$$

The initial condition at $t = 0$ is set to

$$T = T_{\text{bulk}}, \qquad \text{for all} \;\; z. \tag{7.7}$$

The model can be solved universally by introducing the following non-dimensional variables

$$\tilde{t} = \frac{t}{\tau}, \qquad \tilde{z} = \frac{z}{\delta}, \qquad \widetilde{T} = \frac{(T - T_{\text{bulk}})k}{\delta j_{\text{heat}}} \quad \text{with} \quad \delta^2 = \kappa\tau. \tag{7.8}$$

This leads to the following governing equation

$$\frac{\partial \widetilde{T}}{\partial \tilde{t}} = \frac{\partial^2 \widetilde{T}}{\partial \tilde{z}^2}, \qquad 0 \leq \tilde{t} \leq \alpha, \tag{7.9}$$

with the non-dimensional boundary conditions

$$\frac{\partial \widetilde{T}}{\partial \tilde{z}} = -1, \quad \text{at} \quad \tilde{z} = 0, \tag{7.10}$$

$$\widetilde{T} = 0, \quad \text{at} \quad \tilde{z} = -\infty. \tag{7.11}$$

In the non-dimensinoal form, the initial condition reduces to

$$\tilde{T} = 0, \qquad \text{for all} \;\; \tilde{z}. \tag{7.12}$$

It should be noted that for the surface renewal model, the temperature field is determined by a single governing equation together with appropriate boundary and initial conditions. The solution of (7.9) to (7.12) can be obtained analytically as

$$\widetilde{T} = 2\sqrt{\tilde{t}}\left[\frac{-\tilde{z}}{2\sqrt{\tilde{t}}}\text{erfc}\left(\frac{-\tilde{z}}{2\sqrt{\tilde{t}}}\right) - \frac{1}{\sqrt{\pi}}\text{e}^{-\left(\frac{-\tilde{z}}{2\sqrt{\tilde{t}}}\right)^2}\right]. \tag{7.13}$$

Here erfc represents the complementary error function. It is defined as $\text{erfc}(z) = 1 - \text{erf}(z)$. The error function is given by the integral of the Gaussian distribution $\text{erf}(z) = 2/\sqrt{\pi}\int_0^z \exp(-\eta^2)\text{d}\eta$.

At the surface ($\tilde{z} = 0$) Equation (7.13) reduces to

$$\widetilde{T}_{\text{surf}} = -2\sqrt{\frac{\tilde{t}}{\pi}}. \tag{7.14}$$

This can be scaled back to dimensional form from Equation (7.8), resulting in [Soloviev and Schlüssel, 1996]:

$$\begin{aligned} T_{\text{surf}}(t) &= \alpha j_{\text{heat}}\sqrt{t - t_0} + T_{\text{bulk}}, \quad t \geq t_0, \\ &\text{with} \quad \alpha = \frac{2}{\sqrt{\pi\kappa}c_p\rho}, \end{aligned} \tag{7.15}$$

where j_{heat} is the net heat flux just below the water surface and t_0 the time at which a surface renewal event occurred. The thermal diffusivity is indicated by κ, the specific heat by c_p and the density of sea water by ρ. Under conditions found frequently over the open ocean, the temperature difference across the thermal boundary layer $\Delta T = T_{\text{bulk}} - T_{\text{surf}}$ is of the order of $0.1 - 0.3$ K [Wick et al., 1996].

Affixed to the surface renewal model is the probability density function $p(\tau)$ of times between consecutive surface renewal events. Following Kraus and Businger [1994], a probability density function (pdf) $p(\tau)$ is defined which represents the fractional area of the surface fluid elements that have been in contact with the interface for a time τ. From Taylor's theorem [Taylor, 1938], $p(\tau)$ is equivalent to the probability of finding a surface renewal event taking place after the passing of time $\tau = t - t_0$.

It is assumed that the turbulence in the interior of the fluid governs the mechanism for replacing the surface elements. This represents a random process and it is argued that each fluid element has the same probability of being replaced. From this assumption, Kolmogorov [1962] and Soloviev and Schlüssel [1994] deduce a logarithmic normal distribution of the form

$$p(\tau) = \frac{1}{\sqrt{\pi}\sigma\tau/t'} e^{-\frac{(\ln \tau/t' - m)^2}{\sigma^2}}, \quad t > 0, \tag{7.16}$$

where m is the mean value of $\ln \tau/t'$ and σ^2 the variance for the logarithm of the scaled random variable τ. t' is a unit scaling factor. The mean time between burst t_* is the expectation value of this distribution, given by

$$t_* = \langle p(\tau) \rangle = \int_0^\infty p(\tau)\, \tau/t'\, d\tau = t' \cdot e^{\frac{\sigma^2}{4} + m}. \tag{7.17}$$

The function of the sea surface temperature with respect to time for the logarithmic normal pdf is illustrated in Figure 7.1.

This type of model pdf was shown experimentally by Rao et al. [1971] and more recently by Garbe [2001], Garbe et al. [2002a] and Garbe et al. [2004]. For this reason a surface renewal model with a logarithmic normal pdf is assumed in deriving the techniques presented in this thesis.

The surface renewal model is in principle a one dimensional model parameterizing the transport with the time water parcels stay in contact with the interface. The renewal event itself is considered instantaneous. It does not allow heat conduction during upwelling. This means, that this type of model presents a close approximation of processes in medium to strong winds. Under these conditions upwelling velocities are very high. However, in low wind conditions other models might be better suited for describing the transport processes. In the next section such a model will be introduced, which explicitly describes the transport of water parcels in eddies. In this *eddy renewal* model, heat conduction takes place during the upwelling process.

7.2.2 Eddy Renewal Model

In the previous section the surface renewal model was described. This model is one dimensional and makes statistical assumptions on the time in between renewal events. The model

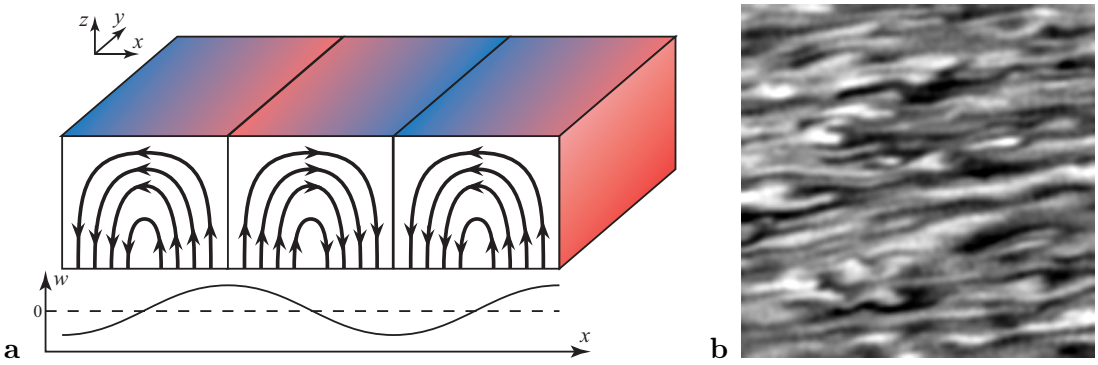

Figure 7.2: ***a*** *Schematic drawing of near surface turbulence as approximated by eddy renewal model. The wind direction is along the z direction.* ***b*** *An IR image for comparison.*

proposed by Danckwerts [1951] is an approximation of turbulent upwelling. It is assumed that a renewal event takes place instantly. Water parcels in the interface are replaced immediately with water from the bulk. These water parcels are not allowed to exchange heat during their upwelling process. This is a very simplistic model which is not completely realistic hydrodynamically. However, in the presence of strong shear induced turbulence as well as microscale wave breaking processes, the upwelling velocities can be quite substantial, making Danckwerts' [Danckwerts, 1951] model quite appropriate. Experimental evidence thus seems to agree quite well with this type of model in medium to high wind speeds [Schimpf et al., 2004; Garbe et al., 2004; Münsterer and Jähne, 1998]. The same holds true for parameterizations derived from this model [Soloviev and Schlüssel, 1994]. However, deviations are conceivable in low wind regimes. Under these conditions, turbulence is driven by convection. Here, vertical velocities are found to be lower, leading to more significant heat exchange during upwelling. Also, it appears that distinct turbulence patterns exist with the characteristics of Langmuir turbulence. The images often show elongated patches of warm water alternating with cold water streaks, with their long axes aligned with the predominant wind direction (see Figure 7.2**b**). Under these conditions, an eddy model based on Lamont and Scott [1970] or Fortescue and Pearson [1967] is hydrodynamically more appealing. This model assumes that turbulent velocity fluctuations predominate over any mean relative velocity. It is assumed that turbulent eddies exist which are very much smaller than waves. The surface can thus be considered as flat. Both the models of Lamont and Scott [1970] and Fortescue and Pearson [1967] are very similar, the difference in between them being the eddy sizes dominant in the transfer process. While Fortescue and Pearson [1967] favors large eddies, Lamont and Scott [1970] argues that smaller eddies in the inertial subrange are the dominant ones. A comparison of the two models can be found in Brtko and Kabel [1976].

In the following the surface turbulence is visualized as Langmuir-type eddies whose cross section looks like Figure 7.2**a**. This gives the general physical description of long "rollers" spinning next to each other but in alternating directions, creating alternating regions of upwelling and downwelling, as first described by Fortescue and Pearson [1967]. When temperature is

added to the model, this equates to regions of warm water upwelling, cooled water downwelling and regions of fairly constant temperature between. While Lamont and Scott [1970] studied such a model with eddies bounded by both top and bottom boundaries, here it is assumed that eddies are bounded by the top free surface boundary only, in order to simulate Langmuir type turbulence interacting with the air-sea interface. In the following this model is called the "eddy renewal model" in contrast to the existing "surface renewal model". This is also to distinguish it from the "eddy cell" [Lamont and Scott, 1970] or "large eddy" [Fortescue and Pearson, 1967] models, in which the boundary conditions are different. The eddy renewal model was first proposed in Hara et al. [2006].

As in the surface renewal model, the coordinate system is defined such that x and y are in horizontal and z is in vertical (upward) from the mean water surface, as shown in Figure 7.2**a**. The mean wind and wave direction is set to be in positive y. The equation governing the temperature field T is given by the same three-dimensional diffusion equation presented in Equation (7.3). Also, the boundary conditions and inital condition introduced in Equations (7.5)- (7.7) are identical to the surface renewal model. However, contrasting this model it is not assumed that the horizontal gradients of the temperature age negligible. In the eddy renewal model it is assumed that the process is stationary in time and uniform in the wind direction y. This is a valid assumption for the elongated streaks observes in the infrared imagery. If the turbulent eddies are assumed to be uniform in y and stationary in t, Equation (7.3) simplifies to

$$u\frac{\partial T}{\partial x} + w\frac{\partial T}{\partial z} = \kappa\left(\frac{\partial^2}{\partial x^2} + \frac{\partial^2}{\partial z^2}\right)T. \tag{7.18}$$

It is further assumed that the water velocity at the surface is periodic with a wavenumber $\tilde{k}$ such that

$$u = u_0 \sin(\tilde{k}x), \quad \text{at} \quad z = 0. \tag{7.19}$$

Then, the Taylor expansion in the vertical direction around $z = 0$ yields

$$u = u_0 \sin(\tilde{k}x) + \left[\frac{\partial u}{\partial z}\right]_{z=0} z + \dots. \tag{7.20}$$

The continuity equation requires from $\partial v/\partial y = 0$ that

$$\frac{\partial w}{\partial z} = -\frac{\partial u}{\partial x} = -\tilde{k}u_0 \cos(\tilde{k}x) - \left[\frac{\partial^2 u}{\partial z \partial x}\right]_{z=0} z + \dots, \tag{7.21}$$

hence,

$$w = -z\tilde{k}u_0 \cos(\tilde{k}x) - \left[\frac{\partial^2 u}{\partial z \partial x}\right]_{z=0} \frac{z^2}{2} + \dots. \tag{7.22}$$

Again, similar non-dimensional variables to the Equations (7.8) for the surface renewal model are introduced:

$$\tilde{x} = \tilde{k}x, \qquad \tilde{z} = \frac{z}{\delta}, \qquad \widetilde{T} = \frac{(T - T_{\text{bulk}})k}{\delta j_{\text{heat}}}, \tag{7.23}$$

with

$$\delta^2 = \frac{\kappa}{\tilde{k}u_0}, \tag{7.24}$$

where δ is the depth scale of the diffusive sublayer and is determined by the diffusivity κ and the surface divergence scale $\tilde{k}u_0$. Then, the normalized governing equation and boundary conditions become

$$\sin\tilde{x}\frac{\partial\widetilde{T}}{\partial\tilde{x}} - \tilde{z}\cos\tilde{x}\frac{\partial\widetilde{T}}{\partial\tilde{z}} = \frac{\partial^2\widetilde{T}}{\partial\tilde{z}^2} + \mathcal{O}(\tilde{k}\delta), \tag{7.25}$$

$$\frac{\partial\widetilde{T}}{\partial\tilde{z}} = -1, \quad \text{at} \quad \tilde{z} = 0, \tag{7.26}$$

$$\widetilde{T} = 0, \quad \text{at} \quad \tilde{z} = -\infty. \tag{7.27}$$

Therefore, provided the diffusive sublayer depth is much smaller than the wavelength of the eddies ($\tilde{k}\delta \ll 1$), heat diffusion is governed by a single set of governing equation and boundary conditions, regardless of the size and intensity of the turbulent eddies.

7.2.3 Comparison of Eddy Renewal and Surface Renewal Model

Both the surface renewal and the eddy renewal model are distinctly different. The surface renewal model uses a characteristic time scale τ for parameterizing exchange processes. Due to the one dimensionality of the model, no spatial information enters the model. On the other hand, the eddy renewal model assumes temporal stationarity. No temporal information is used in the model which purely relies on spatial temperature distributions. Both models can therefore be thought of as complementary to each other. This makes it important to look closely at the implications of both.

By comparing (7.8) and (7.24), it is clear that the renewal time scale τ in the surface renewal model is equivalent to the inverse of the surface divergence $\tilde{k}u_0$ in the eddy renewal model. In fact, the inverse of the surface divergence can be interpreted as a time scale over which a water parcel travels from the upwelling region to the downwelling region.

In Figure 7.3 the solution of the eddy renewal model (7.25) to (7.27) is compared with the solution of the surface renewal model (7.9) to (7.12). In order to make the results better comparable, the coefficient α is set 5.54 so that both the mean surface temperature and the surface heat flux are identical between the two models. (That is, the actual (dimensional) interval between the renewal events in the surface renewal model is 5.54 times the inverse of the surface divergence $\tilde{k}u_0$ in the eddy renewal model if the two eddies yield the same heat transfer velocity.) In addition, the temperature scale is adjusted so that the normalized mean surface temperature is equal to -1.

The result of the eddy renewal model clearly shows that warm water is advected up to the surface, across the surface, and is then transported downwards. Rather than the motion of the water being described by an event, the motion is described as a continuous flow from

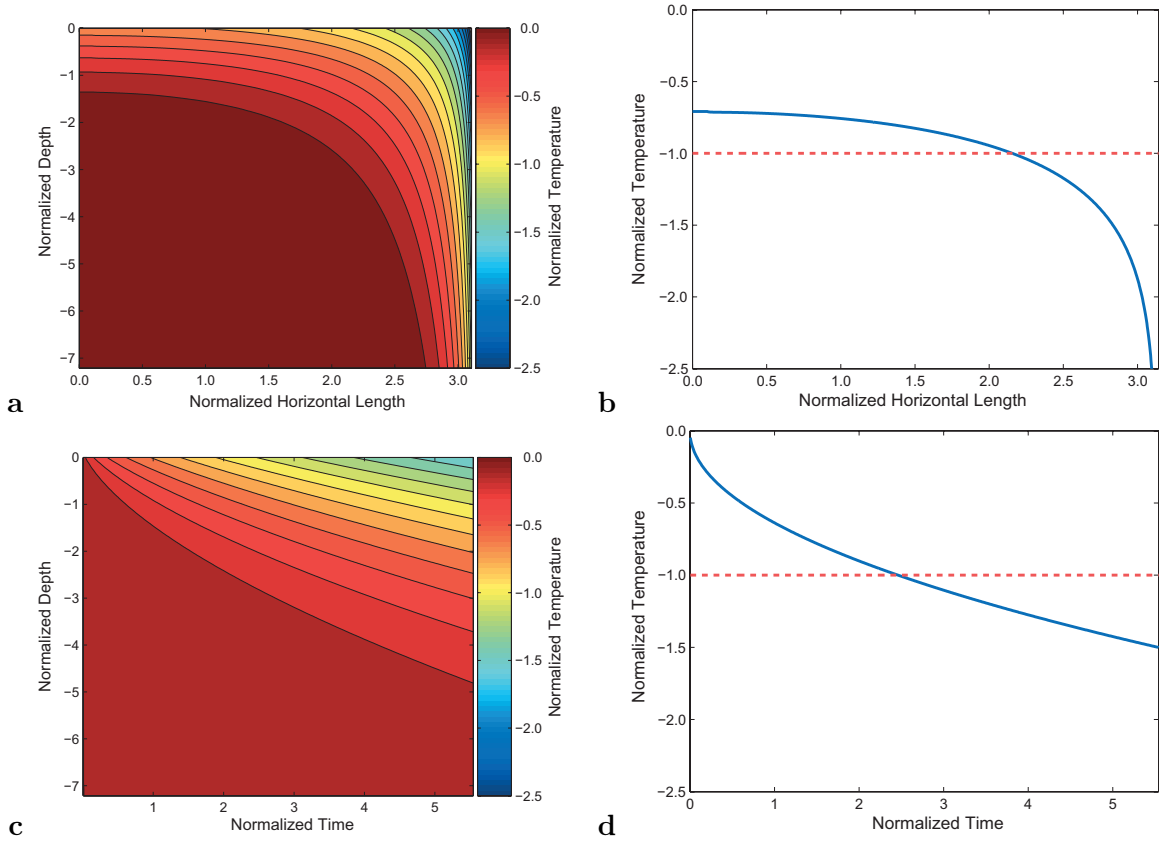

Figure 7.3: ***a*** *Normalized temperature distribution (indicated by color scales) based on eddy renewal model.* ***b*** *Normalized surface temperature distribution (solid line) and its mean (dashed line) based on eddy renewal model.* ***c*** *Normalized temperature distribution (indicated by color scales) based on surface renewal model.* ***d****Normalized surface temperature distribution (solid line) and its mean (dashed line) based on surface renewal model.*

upwelling to downwelling. Once the water has moved down sufficiently far from the surface, it is assumed that the turbulent motions of the mixed layer will blend the downwelled water with the existing mixed layer.

One obvious difference between the eddy renewal model and the surface renewal model is the observability of the bulk temperature T_{bulk} at the surface. While T_{bulk} is the temperature, which is just not observable in the surface renewal model, the difference in between observable temperatures and T_{bulk} can be quite substantial in the eddy renewal model. This difference between the models can be easily explained. In the surface renewal model, the process that transfers water to the surface is assumed to be instantaneous. That is, no time is given for the bulk water advected to the surface to exchange temperature due to conduction. The eddy renewal model allows for the bulk water to change temperature as it is advected closer to the surface. The strength of the temperature change is based on the strength of the vertical motions of the eddy.

Another way to interpret the difference between the models is to compare histograms of

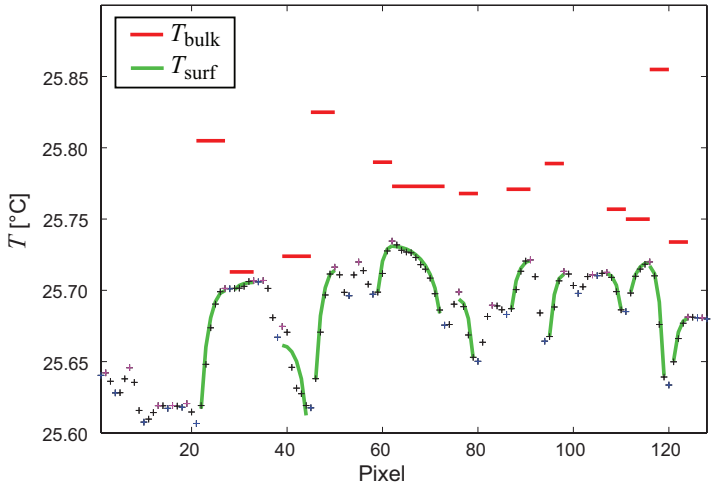

Figure 7.4: *The fit of the eddy renewal model to a column of an infrared image orthogonal to the wind direction. The relation in between T_{bulk} and T_{surf} can be seen for the eddy renewal model. The difference in between both temperatures can be substantial.*

the surface temperatures. Once again, the differences between the two models is striking. In the surface renewal model, it is clear that the water reaches colder temperatures more quickly than it does in the eddy renewal model. However, the maximum value of the bulk temperature is never observed at the surface in the eddy renewal model. This leads to two very different histograms. With the eddy renewal model, the histogram increases with temperature up to the maximum temperature, which is still lower than the bulk temperature, and then suddenly decreases to zero. The histogram of the surface renewal model, on the other hand, decreases with temperature but remains non zero all the way to the bulk temperature. These two different histograms are observable in Figure 7.4.

7.3 The Cool Skin Temperature Difference

7.3.1 ΔT from Surface Renewal

Measuring the temperature difference across the thermal boundary layer invasively is a difficult undertaking due to thin layer extending less than 1 mm beneath the wavy interface. Combining model assumptions with a statistical analysis of the infrared imagery, this important parameter can be retrieved to an accuracy of less than 1% from modern IR cameras. The statistical analysis is based on fitting an analytical function to the temperature distribution at the sea surface. The analytical function can be derived from the surface renewal model, as is outlined in Garbe et al. [2004]. Here use is made of ΔT given by Equation (7.15) and the log-normal distribution of $p(\tau)$ for surface renewal events. The temperature distribution at the sea surface

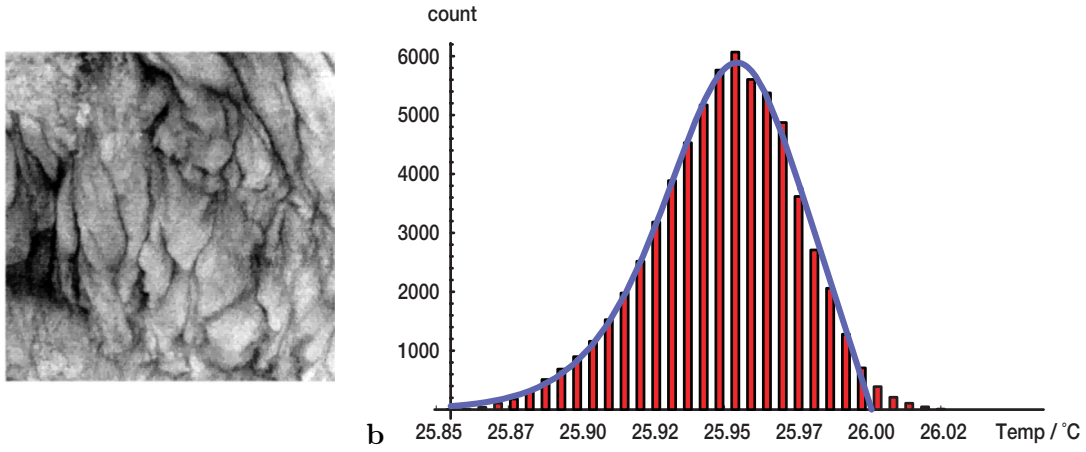

Figure 7.5: *The analytical function describes the temperature distribution of the IR image shown in* ***a*** *quite well, as can easily be verified from the fit in* ***b****.*

$p(T_{\text{surf}})$ is then given by

$$p(T_{\text{surf}}) = \mathfrak{S}(\text{sign}(j)\cdot\Delta T)\frac{|T_{\text{surf}}-T_{\text{bulk}}|}{(\alpha j)^2}\exp\left[\frac{\sigma^2}{4}-m\right] \cdot\text{erfc}\left[\frac{\sigma}{2}-\frac{m}{\sigma}+\frac{1}{\sigma}\ln\left(\frac{T_{\text{surf}}-T_{\text{bulk}}}{\alpha j_{\text{heat}}}\right)^2\right], \quad \text{with} \quad \alpha=\frac{2}{\sqrt{\pi\kappa}\rho c_p}, \tag{7.28}$$

for $j_{\text{heat}} \neq 0$ and $p(T_{\text{surf}}) = \delta(\Delta T)$ for $j_{\text{heat}} = 0$ [Haußecker et al., 2001; Garbe et al., 2004]. Here $\Delta T = T_{\text{surf}} - T_{\text{bulk}}$ denotes the temperature difference, erfc is the complementary error function, $\delta(x)$ denotes Dirac's delta distribution, sign(x) the sign function and $\mathfrak{S}(x)$ the Heaviside unit step function

$$\text{sign}(x) = \begin{cases} 1, & x \geq 0 \\ -1, & x < 0 \end{cases} \quad \text{and} \quad \mathfrak{S}(x) = \begin{cases} 1, & x \geq 0 \\ 0, & x < 0 \end{cases}. \tag{7.29}$$

The complementary error function is defined as $\text{erfc}(z) = 1 - \text{erf}(z)$ and the error function given by the integral of the Gaussian distribution $\text{erf}(z) = 2/\sqrt{\pi}\int_0^z \exp(-\eta^2)\text{d}\eta$.

From Taylors hypothesis the analytical function for the probability density function $p(T_{\text{surf}})$ can be fitted to the frequency density function of the temperature distribution from an individual image, as can be seen in Figure 7.5. This makes it possible to estimate the temperature of the bulk T_{bulk} with the frame rate of the IR camera. The mean temperature $\overline{T_{\text{surf}}}$ at the sea surface is given as the expectancy value of the temperature distribution

$$\overline{T_{\text{surf}}} = \int_{-\infty}^{\infty} T_{\text{surf}}\cdot p(T_{\text{surf}})\,\text{d}T_{\text{surf}}. \tag{7.30}$$

This integration can be solved numerically, resulting in a value for $\overline{T_{\text{surf}}}$ that is much less prone to errors in the data than calculating $\overline{T_{\text{surf}}}$ by just summing over the image intensities and

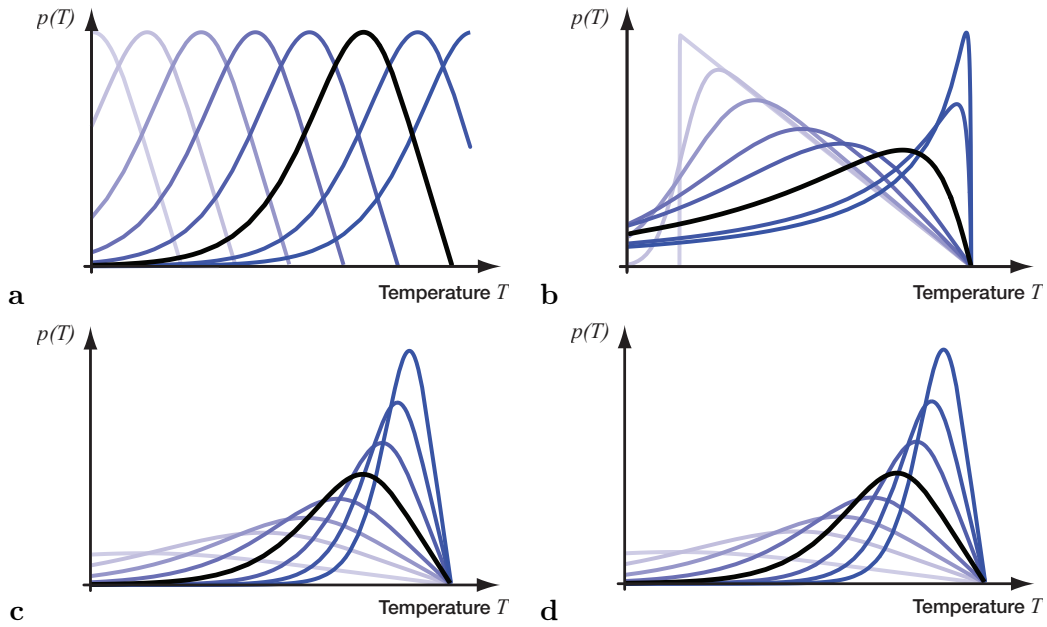

Figure 7.6: *Plot of the probability density function $p(\tau)$. Both T_{bulk} and σ can be estimated independently from the fit, as is evident from the plots of different T_{bulk} in* ***a*** *and the same for different values of σ in* ***b****. The values for j_{heat} and m cannot be computed independently, as is apparent from the same plots for different m in* ***c*** *and different values of j_{heat} in* ***d****.*

dividing by the number of pixels. From the knowledge of both T_{surf} and T_{bulk} the temperature difference $\Delta T = T_{\text{surf}} - T_{\text{bulk}}$ can be computed.

Even though the temperature of the bulk water T_{bulk} can be estimated from a statistical analysis of the temperature distribution of the sea surface, this frequency data does not hold enough information to independently estimate all parameters of the analytical function in Equation (7.28). An illustration of the interdependence of the parameter m and the heat flux j_{heat} is presented in Figure 7.6.

The interdependence of the parameters m and j_{heat} is expressed in the fact that the same analytical curve can be fitted for different values of m and j_{heat}. This can easily be verified by analyzing Equation (7.28). The terms in this equation can be divided into two groups, namely into terms that normalize the function and terms that are responsible for the general shape of $p(T_{\text{surf}})$. Equating both the shape and normalization terms for two values of m and j_{heat} leads to a condition under which the same curve results for different values of j_{heat} and m. This condition is given by

$$\left(\frac{j_2}{j_1}\right)^2 = e^{m_1 - m_2}. \tag{7.31}$$

It can in fact be shown by the same procedure, that the same histogram only results from different combinations of m and j_{heat}, but not from other combinations of the parameters. Due to this dependence of the two parameters j_{heat} and m, it is possible to eliminate them from Equation (7.28). From Equation (7.31) it can be seen that $j_{\text{heat}} \cdot \exp(m) \equiv \beta^2$, where β^2

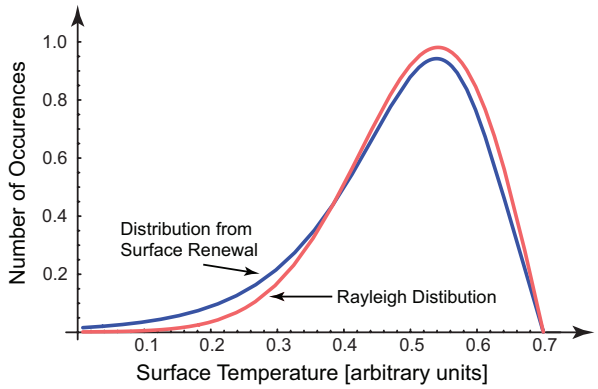

Figure 7.7: *A comparision of the Rayleight distribution presented by Zhang and Harrison [2004] to the distribution deriuved from the surface renewal model in Equation (7.32).*

is an arbitrary constant. Introducing this expression in (7.28) leads to

$$p(T_{\text{surf}}) = \mathfrak{S}(\text{sign}(j)\Delta T)\frac{|T_{\text{surf}} - T_{\text{bulk}}|}{(\alpha\beta)^2}\exp\left[\frac{\sigma^2}{4}\right]\cdot\text{erfc}\left[\frac{\sigma}{2} + \frac{1}{\sigma}\ln\left(\frac{T_{\text{surf}} - T_{\text{bulk}}}{\alpha\beta}\right)^2\right],$$
$$\text{with} \quad \alpha = \frac{2}{\sqrt{\pi\kappa}\rho c_p} \quad \text{and} \quad \beta^2 = e^m \cdot {j_{\text{heat}}}^2. \qquad (7.32)$$

This expression depends on the parameter T_{bulk}, σ and β only. From analyzing Figure 7.6 it becomes apparent that T_{bulk} shifts the distribution, σ is a measure for the general shape and β represents the width of the distribution. In that figure, the plot for different β looks the same as that for different j_{heat} or m.

In a laboratory study at a wind speed range from 4 m/s to 11 m/s, Zhang and Harrison [2004] reported no significant change in the shape of the distribution of surface temperatures. They found the distribution to be approximated by a Rayleigh distribution. The authors did not motivate their choice for this distribution. As it turns out, the Rayleigh distribution shares prominent features with the analytical distribution presented in Equation (7.32). This can be seen from Figure 7.7. The measurements of Zhang and Harrison [2004] indicate that the shape of temperature distributions is not altered under a range of different heat fluxes j_{heat}. This becomes apparent from Equation 7.32, where j_{heat} is not a direct parameter in the surface temperature distribution. Moreover, different values of j_{heat} can be compensated by corresponding values of m.

Accuracy of Parameter Estimation

In order to test the validity of results gained from the statistical analysis proposed in Section 7.3, the effect of noise in the input data on the estimated parameters was examined on synthetic data in a Monta-Carlo type analysis. The synthetic data was generated, presenting the same distribution of gray values as a thermal image of the sea surface. The relative errors in the fit parameters were analyzed under varying noise level of the input data. The results of this analysis is presented in Figure 7.8.

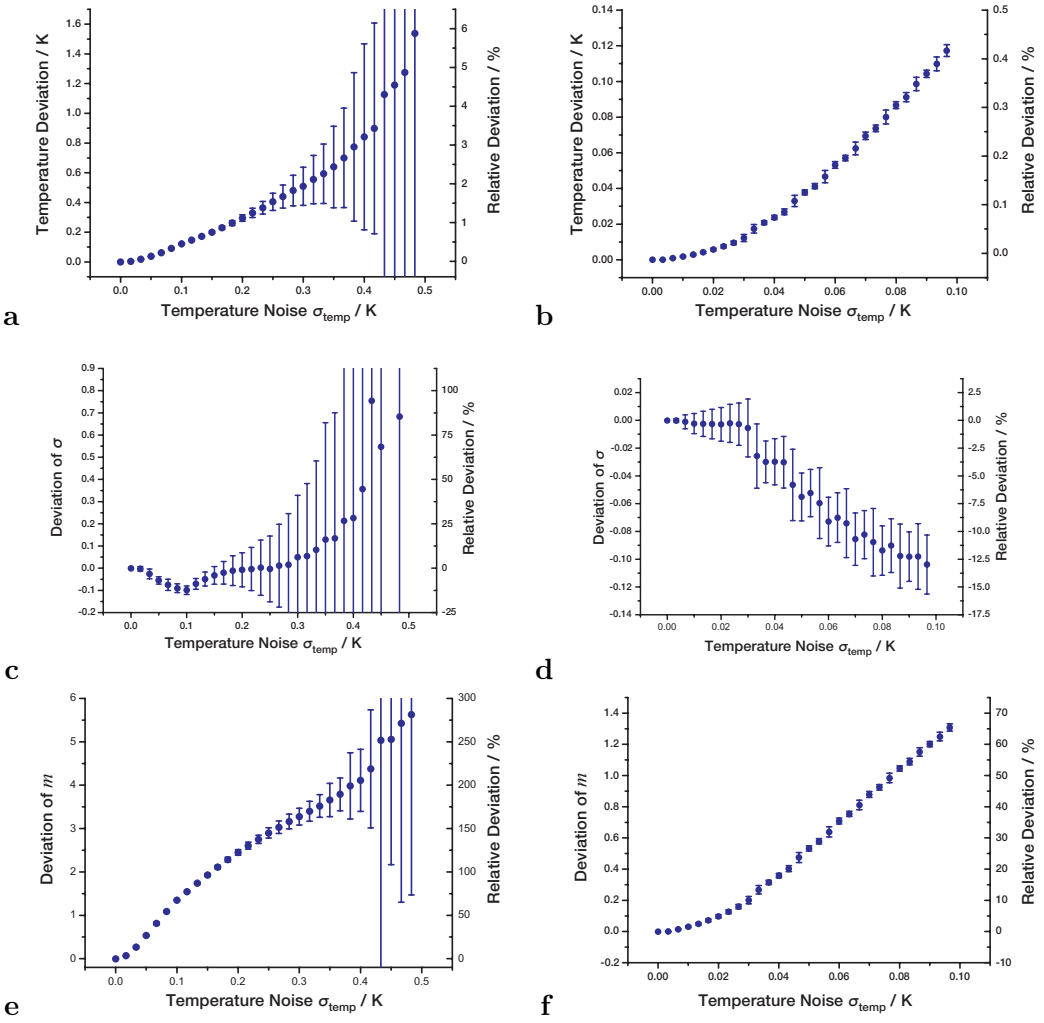

Figure 7.8: *The dependence of the extracted parameters from the statistical analysis on the noise. In* ***a*** *the dependence of the error of* T_{bulk} *on the noise ranging from 0.0 to 0.5 K is shown. In* ***b*** *the same for lower noise levels from 0.0 to 0.1 can be seen. In* ***c****,* ***d****,* ***e*** *and* ***f*** *the analogue for the error of the other parameters* σ *and* m *is given.*

By comparing the results it becomes apparent that the bulk temperature T_{bulk} can be estimated with a relative accuracy of below 1% for noise levels of 0.2 K. For the noise level of the infrared camera, typically 25 mK, the error in T_{bulk} was found to be well below 5 mK. This is in good agreement with previous findings on real data [Schimpf et al., 2004].

7.3.2 ΔT from Eddy Renewal

In the previous section a statistical analysis of the temperature distribution for estimating ΔT has been presented. By assuming the surface renewal model, it is possible to estimate ΔT by fitting an analytical function to this data. In low wind speed regimes, the eddy renewal model presented in Section 7.2.2 might be a better description of the transport processes at the air-sea interface. In this section, another technique for estimating ΔT from the eddy renewal

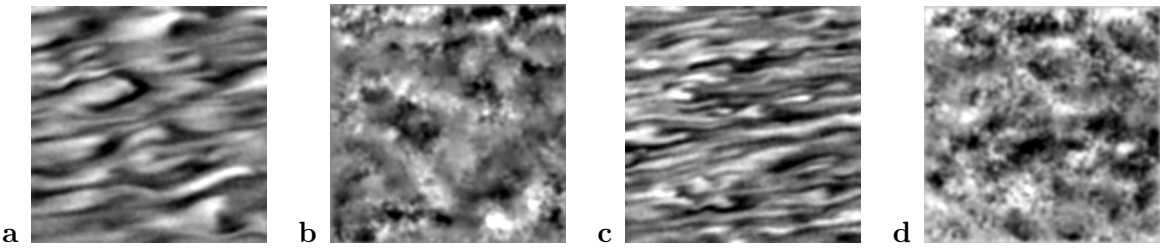

Figure 7.9: *The divergence estimated for the infrared sequences. In* **a** *an image recorded in the experiment with a wind speed of* 2 *m/s can be seen with the corresponding divergence in* **b**. *The same is shown in* **c** *and* **d** *for a sequence acquired during an experiment at a wind speed of* 4.2 *m/s. Regions of larger positive divergence are bright and appear to be cumulating in warmer regions of the infrared images, also indicated by a higher gray value.*

model will be outlined. It should be more suited to the low wind regime. This technique has been published by Hara et al. [2006].

Estimating T_{bulk} and hence ΔT from the eddy renewal model is quite straight forward. The minima and maxima are detected along columns of individual frames of the thermographic image sequence. These columns are oriented orthogonal to the dominant wind direction. This can be achieved either through the orientation of the IR camera in the set-up or, if this is not possible, through transforming the image sequence afterwards. The temperature of these extrema as well as their separation is used to fit the non-dimensional solution of the normalized governing equation (7.25) and the boundary conditions (7.26)-(7.27) to the data. Through this fit, the non-dimensional solution is scaled to dimensional form. This leads directly to the sought value for T_{bulk} and hence ΔT. In Section 7.10.2 and 7.11.1 results of this estimation will be presented on laboratory and field data respectively.

7.4 Estimating Surface Flows and the Material Derivative from Passive Thermography

Techniques that estimate the net heat flux, the probability density function (pdf) of surface renewal events and the transfer velocity of heat from passive infrared image sequences will be presented. All these techniques rely on the material derivative $dT/dt = dT_{\text{surf}}/dt$ as one important parameter [Garbe et al., 2004]. This is true for both the surface renewal model as well as for the eddy renewal model.

For a number of observation, it is also important to quantify surface flows directly at the air-water interface. For example, surface divergence models parameterize the heat flux and transfer velocity from surface divergence [Banerjee et al., 2004; Turney et al., 2005]. A standard approach is to seed the water surface with particles and perform particle imaging velocimetry (PIV) measurements on them [McKenna and McGillis, 2004]. This approach has the disadvantage that for particles floating at the interface, in upwelling regions a void of such particles exists. This problem can be circumvented by particles of neutral buoyancy floating in the water body. However, here defining the surface and not measuring particles below is

a challenging problem. An approach was developed by Jehle [2007], where this effect in conjunction with a dye in the water body is used for recovering a full 3D flow volume. At a wind sheared interface, particles "sticking out" of the water body might be subject to an additional forcing by the wind and cannot be used.

These problems can be avoided by using a thermopgraphic technique for estimating surface flows [Garbe et al., 2003b]. Due to the small penetration depth of IR radiation into water ($\approx 10\mu$m), measurements are conducted right at the surface. Turbulences are not effected in any way for passive thermography and only very mildly from active thermography, where patches of water are heated up by a couple of tenths of a Kelvin. Motion is estimated from the techniques introduced in Chapter 3. Different parametric motion models can be used as those presented in Chapter 2.3.1. This makes it possible to estimate divergences and convergences directly in the motion estimation process [Garbe et al., 2003c,b]. An example of those results is shown in Figure 7.9.

Similar to estimating surface divergence and flow fields, the algorithm for computing the material derivative dT/dt relies on estimating motion with the gradient based approach presented in Chapter 3. This has been presented in Garbe et al. [2003b]. Accuracy improvements were introduced in Garbe and Jähne [2001] and Garbe et al. [2002e]. Therefore, only a brief overview of the technique shall be presented here.

The material derivative is given by $\mathrm{d}T/\mathrm{d}t = \partial T/\partial t + \boldsymbol{u} \cdot \boldsymbol{\nabla} T$, where T is the sea surface temperature and $\boldsymbol{u} = [u_1, u_2]^\top$ the surface flow. This derivative can be formulated in vector notation, yielding

$$\boldsymbol{d}^\top \cdot \boldsymbol{p} = [-1, T_x, T_y, T_t] \cdot [c, \delta x, \delta y, \delta t]^\top = 0, \tag{7.33}$$

where the subscripts A_B denote partial derivatives of the variable A along the coordinate B. c is the parameter of linear temperature change. The transpose of a vector $\boldsymbol{a}$ is indicated by $\boldsymbol{a}^\top$. The total derivative dT/dt is then given by $dT/dt = c/\delta t$ and the velocities by $u = \delta x/\delta t$ and $v = \delta y/\delta t$.

Equation (7.33) is identical to Equation (2.25) in Section 2.5.2, where the linear brightness change model was introduced. Thus, applying this model at the sea surface yields the material derivative from the constant c in Equation (7.33). The model parameters can then be computed using the framework introduced in Chapter 3, in which the gradient based motion estimation framework was presented.

When dealing with thermal images from the sea surface, especially with field data, reflections from the surroundings are impossible to eliminate. Such reflections cannot be eliminated by a global threshold because their apparent temperature is very close to that of the thermal structures of the sea surface. However, they can be detected as outliers and segmented by a robust estimation of dT/dt [Garbe and Jähne, 2001], as is shown in Figure 7.11. Only through this step an accurate estimation of dT/dt is possible, as is the computation of T_{bulk} from the algorithm introduced in Section 7.3. This technique has been explained in detail in Garbe [2001] and will not be elaborated here any further.

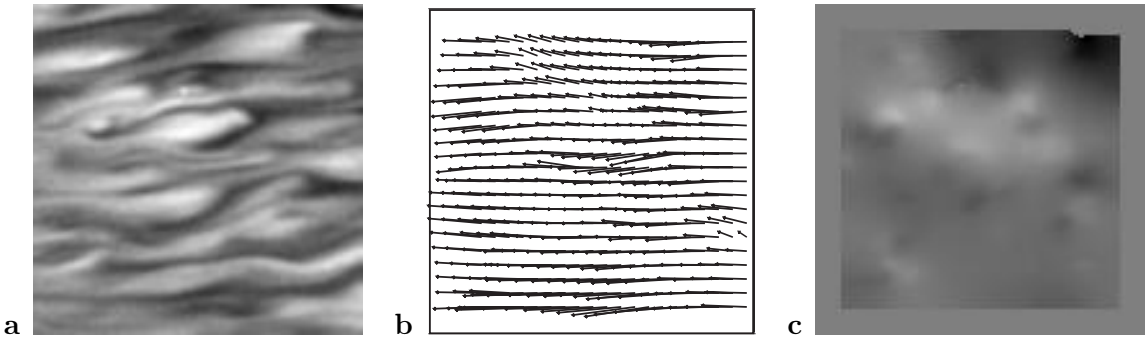

Figure 7.10: *In* **a** *an IR image is shown with the corresponding 2D optical flow in* **b** *and the total derivative of the temperature in* **c** *([-0.6, 0.4]K/frame).*

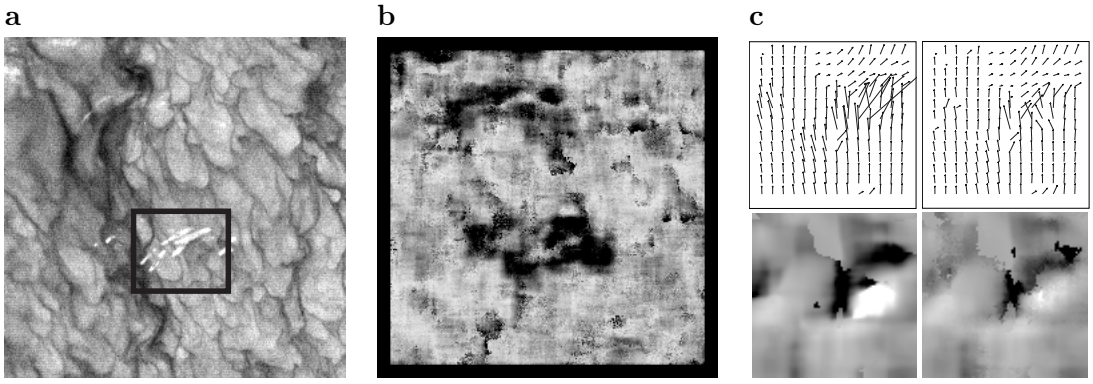

Figure 7.11: **a** *An IR image,* **b** *the number of weights as computed by LMSOD. Black areas indicate fewer weights which corresponds to reflections.* **c** *The flow field and the total derivative* dT_{surf}/dt *inside the box in* **a**. *Black regions indicate where no parameters could be estimated.*

7.5 Surface Renewal Time Constant and Transfer Velocity of Heat

As was pointed out in Section 7.2.1 the time of residence of a water parcel at the sea surface $\tau = t - t_0$ is an important parameter in the model of surface renewal. From the definition of the transfer velocity in Equation (7.1) it becomes apparent that τ is equivalent to k_{heat}. This can be verified by inserting Equation (7.15) into Equation (7.1), leading to

$$k_{\mathrm{heat}} = \frac{1}{\rho c_p \alpha \sqrt{\tau}} = \frac{1}{2}\sqrt{\frac{\pi\kappa}{\tau}}. \tag{7.34}$$

As it turns out, τ can be measured directly using thermography. From the assumption that k_{heat} is a well behaved function in space and time, Equation (7.34) states that the same holds true for τ. This implies that τ can be measured regardless of a slowly changing heat flux, since this would lead to a change in ΔT and hence a constant k_{heat} and τ.

Reformulating Equation (7.15) leads to an expression for τ:

$$\tau = t - t_0 = \left(\frac{T_{\mathrm{surf}}(t) - T_{\mathrm{bulk}}}{\alpha j_{\mathrm{heat}}}\right)^2, \quad \text{with} \quad \alpha = \frac{2}{\sqrt{\pi\kappa} c_p \rho}. \tag{7.35}$$

In this equation the surface temperature T_{surf} is given directly by the temperature calibrated infrared images. The bulk temperature T_{bulk} can either be measured with thermometers or from thermography as has been outlined in Section 7.3. Measuring T_{bulk} from thermometers is an extremely difficult undertaking, as ΔT is usually of the magnitude of 0.1K and the boundary layer extends less than a one millimeter beneath the surface. Also, a thermal stratification may be present very close to the interface making the measurement of T_{bulk} dependent on the chosen depth and may thus lead to wrong results.

Another problem in Equation (7.35) is the measurement of the net heat flux j_{heat}. This can be circumvented by differentiating Equation (7.15) with respect to time and solving it for j_{heat}. This leads to

$$j_{\mathrm{heat}} = \frac{2\sqrt{\tau}}{\alpha}\frac{d}{dt}T_{\mathrm{surf}}(t). \tag{7.36}$$

By substituting Equation (7.36) into Equation (7.35) the following expression for τ can be derived:

$$\tau = t - t_0 = \frac{1}{2}\frac{T_{\mathrm{surf}}(t) - T_{\mathrm{bulk}}}{\frac{d}{dt}T_{\mathrm{surf}}(t)} = \frac{1}{2}\frac{\Delta T(t)}{\dot{T}_{\mathrm{surf}}(t)}, \tag{7.37}$$

where in the dotted notation $\dot{x}$ indicates the total derivative with respect to time.

In this reformulation of the problem, only ΔT and the total derivative $d/dt\ T_{\mathrm{surf}} = \dot{T}_{\mathrm{surf}}$ have to be estimated for measuring τ. ΔT can be computed with the technique described in Section 7.3.1. Likewise, $\dot{T}_{\mathrm{surf}}$ can be estimated from thermography employing the motion estimation approach presented in Section 7.4. It should be noted that ΔT is computed for every pixel of the thermal image sequence as is $\dot{T}_{\mathrm{surf}}$. Likewise τ is estimated at every pixel, leading to a temporally and spatially highly resolved measurement limited only by the thermal imager.

Once τ is known from Equation (7.37) for every pixel of the IR image sequence the transfer velocity k_{heat} follows from Equation (7.34). This leads to

$$k_{\mathrm{heat}} = \sqrt{\frac{\pi\kappa}{2}} \cdot \sqrt{\frac{\dot{T}_{\mathrm{surf}}}{\Delta T}}. \tag{7.38}$$

It is of course important to analyze possible errors in the estimation of both τ and k_{heat} by the proposed technique. Assuming the errors in the estimation to be distributed according to Gaussian statistics, the deviation in the estimate can be derived by error propagation. This leads to the relative error given by

$$\frac{\sigma_{k_{\mathrm{heat}}}}{k_{\mathrm{heat}}} = \frac{1}{2}\frac{\sigma_\tau}{\tau} = \frac{1}{2}\sqrt{\left(\frac{\sigma_{\Delta T}}{\Delta T}\right)^2 + \left(\frac{\sigma_{\dot{T}_{\mathrm{surf}}}}{\dot{T}_{\mathrm{surf}}}\right)^2}. \tag{7.39}$$

In conditions typical for air-sea gas exchange the relative errors of ΔT and $\dot{T}_{\mathrm{surf}}$ can both be approximated by $\sigma_{\Delta T}/\Delta T \approx \sigma_{\dot{T}_{\mathrm{surf}}}/\dot{T}_{\mathrm{surf}} \approx 5\%$. This leads to a relative error of about $\sigma_\tau/\tau \approx 7.1\%$ and $\sigma_{k_{\mathrm{heat}}}/k_{\mathrm{heat}} \approx 3.6\%$.

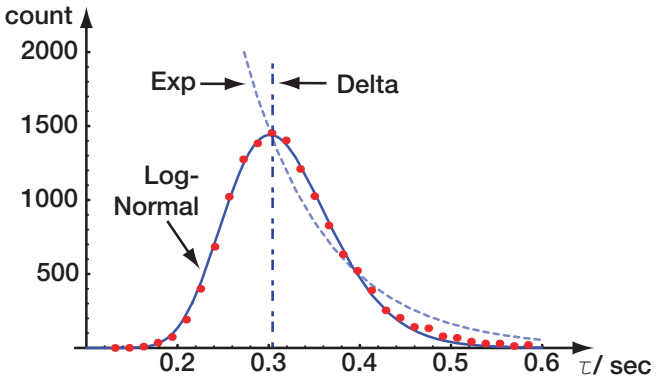

Figure 7.12: *The frequency data of the time of residence τ of a water parcel at the sea surface. The fitted log-normal distribution approximates the data quite well. Fitted are also exponential and delta distribution. The data points were computed from one sequence of the GasEx II data.*

7.6 The PDF of Surface Renewal from Thermography

The pdf of surface renewal gives rise to speculations regarding the exact processes involved in the renewal events and justifies the statistical analysis of the sea surface temperature described in Section 7.3 as well as some of the techniques in estimating the heat flux described later on.

In order to be able to make a quantitative statement on this pdf, a statistical analysis on the time of residence τ of water parcels at the water surface is performed. From Equation (7.37) a value for τ can be computed at every pixel. Given the theoretical log-normal $p(\tau)$ from Equation (7.16), the values for σ and m can be computed together with error estimates for the individual parameters. This is achieved by fitting $p(\tau)$ to the histogram of τ by means of least squares as can be seen in Figure 7.12. From the parameters σ and m the characteristic mean time between surface renewals t_* can be computed from Equation (7.17). This presents a powerful means of verifying the pdf of surface renewal.

7.7 Heat Flux Estimates

In previous sections different techniques for estimating ΔT, τ and k_{heat} non-invasively have been presented. Another important parameter for air-water heat exchange is the net heat flux j_{heat}. The heat flux j_{heat} for a substance of mass M is defined as the rate of change of heat Q across the surface area A, or

$$j_{\text{heat}} = \frac{dQ/dt}{A} = \frac{Mc_p}{A}\frac{dT}{dt}. \tag{7.40}$$

In the following two distinct methods based on the surface renewal model one based on the eddy renewal model for estimating the net heat flux from thermal image sequences will be presented. Both the pdf- and the square root method method are based on the surface renewal model and were introduced in Garbe et al. [2004].

7.7.1 PDF Method

This method may be used to compute the mean heat flux over part of the sequence. It is termed *pdf-method* since it is based on the assumption of a log-normal pdf of the characteristic time of surface renewal. It was presented in [Garbe et al., 2002a]. Evidently some assumptions have to be made in order to derive the net heat flux from this analysis. The first one is of course that the surface renewal model as introduced in Section 7.2.1 describes the transport processes sufficiently well. The other is that the pdf of the times of residence of the water parcels at the sea surface can be described by a log-normal distribution. As indicated in Section 7.6, strong experimental evidence exist to make this a valid assumption. In Section 7.7.2 another technique will be introduced which does not rely on any assumptions concerning the pdf of surface renewal. Comparing results of these two techniques can be seen as an indirect verification of the assumption concerning the pdf of surface renewal made by the *pdf method*.

The average temperature difference across the cool skin of the ocean can be computed according to [Garbe et al., 2002a]:

$$\overline{\Delta T} = \int_0^\infty p(\tau)\tau^{-1} \left(\int_0^t \Delta T(t')dt' \right) d\tau. \tag{7.41}$$

The integration of this equation with the log-normal pdf from Equation (7.16) and the expression for ΔT from Equation (7.15) yields

$$\overline{\Delta T} = \frac{2}{3}\alpha j \sqrt{t_*} \exp(-\sigma^2/16) \quad \text{with} \quad \alpha = \frac{2}{\sqrt{\pi\kappa}c_p\rho}. \tag{7.42}$$

This expression can be solved for the heat flux j_{heat}, which together with Equation (7.17) for t_* leads to

$$j_{\text{heat}} = \frac{3}{2}\frac{\overline{\Delta T}}{\alpha} \cdot \exp\left[-\left(\frac{\sigma^2}{16} + \frac{m}{2} \right) \right]. \tag{7.43}$$

Both parameters σ and m can be computed from the pdf of surface renewal as outlined in Section 7.6.

7.7.2 Square Root Method

As opposed to the pdf method outlined in the previous section this technique does not rely on assumptions concerning the pdf of times between consecutive surface renewal events $p(\tau)$. Use is made only of the surface renewal model introduced in Section 7.2.1 for deriving this method. This makes the square root method very well suited for estimating the net heat flux j_{heat}. In Garbe et al. [2004] this technique was derived from plugging the expression for τ from Equation (7.35) into Equation (7.15) and solving for j_{heat}. Here it is derived from the non-dimensional form from Section 7.2.1. This will make the similarity and differences to the expression derived from the eddy renewal model in the next section more apparent.

The solution of the surface renewal model directly at the surface ($z = 0$) was found to be $\widetilde{T}_{\text{surf}} = -2\sqrt{\tilde{t}}/\sqrt{\pi}$ in Equation (7.14). The rate of change of this surface temperature is thus

given by

$$\frac{d\widetilde{T}_{\mathrm{surf}}}{d\tilde{t}} = \frac{\partial\widetilde{T}_{\mathrm{surf}}}{\partial\tilde{t}} = -\frac{1}{\sqrt{\pi\tilde{t}}}. \tag{7.44}$$

Computing the product of $\widetilde{T}_{\mathrm{surf}}$ and $d\widetilde{T}_{\mathrm{surf}}/d\tilde{t}$ results in

$$\widetilde{T}_{\mathrm{surf}}\frac{d\widetilde{T}_{\mathrm{surf}}}{d\tilde{t}} = \frac{2}{\pi}, \tag{7.45}$$

or

$$\frac{k^2}{\kappa {j_{\mathrm{heat}}}^2}(T_{\mathrm{surf}} - T_{\mathrm{bulk}})\frac{dT_{\mathrm{surf}}}{dt} = \frac{2}{\pi} \tag{7.46}$$

in a dimensional form. Therefore, if simultaneous measurements are made of both $\Delta T = T_{\mathrm{surf}} - T_{\mathrm{bulk}}$ and dT_{surf}/dt for any pixel in an infrared image, it is possible to estimate the heat flux at this pixel as

$$\frac{j_{\mathrm{heat}}}{k} = \sqrt{\frac{\pi}{2}}\sqrt{\frac{1}{\kappa}(T_{\mathrm{surf}} - T_b)\frac{dT_{\mathrm{surf}}}{dt}} \quad \text{or} \tag{7.47}$$

$$j_{\mathrm{heat}} = \frac{\sqrt{2}}{\alpha}\sqrt{\Delta T \cdot \frac{\mathrm{d}}{\mathrm{d}t}T_{\mathrm{surf}}(t)} \quad \text{with} \quad \alpha = \frac{2}{\sqrt{\pi\kappa}c_p\rho}, \tag{7.48}$$

as presented in Garbe [2001] and Garbe et al. [2004].

The sign of the heat flux j_{heat} in Equation (7.48) is affixed to a heating-up or cooling-down of water parcels at the sea surface. Therefore, it can be deduced from the sign of the total derivative dT_{surf}/dt, or $\mathrm{sign}(j) = \mathrm{sign}(dT_{\mathrm{surf}}/dt)$.

For specifying the error bounds of the square root method, errors can be assumed to be Gaussian distributed. Error propagation then leads to the relative error given by

$$\frac{\sigma_{j_{\mathrm{heat}}}}{j_{\mathrm{heat}}} = \frac{1}{2}\sqrt{\left(\frac{\sigma_{\Delta T}}{\Delta T}\right)^2 + \left(\frac{\sigma_{\dot{T}_{\mathrm{surf}}}}{\dot{T}_{\mathrm{surf}}}\right)^2}. \tag{7.49}$$

The relative error of both ΔT and $\dot{T}_{\mathrm{surf}}$ are typically of the order of $\sigma_{\Delta T}/\Delta T \approx \sigma_{\dot{T}_{\mathrm{surf}}}/\dot{T}_{\mathrm{surf}} \approx 5\%$. Thus $\sigma_{j_{\mathrm{heat}}}/j_{\mathrm{heat}} \approx 3.6\%$ should be achievable for j_{heat}.

In general conditions of interest for air-sea gas exchange, net heat fluxes during the night will be of around $j \approx 200$ W/m^2. With a relative error of 4% the absolute error would be $\sigma_{j_{\mathrm{heat}}} = 8$ W/m^2. This is within the bounds of errors the TOGA CORE experiment tried to achieve [Fairall et al., 1996b].

7.7.3 Net Heat Flux from the Eddy Renewal Model

For the eddy renewal model, the rate of change of non-dimensional surface temperature $\widetilde{T}_{\mathrm{surf}}$ following a fluid parcel is given by

$$\frac{d\widetilde{T}_{\mathrm{surf}}}{d\tilde{t}} = \sin\tilde{x}\frac{\partial\widetilde{T}_{\mathrm{surf}}}{\partial\tilde{x}}, \tag{7.50}$$

which follows from Equation (7.25) for $\tilde{z} = 0$. By the same approach as in the previous section, the heat flux can be expressed as

$$\frac{j_{\text{heat}}}{k} = \sqrt{\frac{1}{\widetilde{T}_{\text{surf}} \sin\tilde{x} \frac{\partial \widetilde{T}_{\text{surf}}}{\partial \tilde{x}}}} \sqrt{\frac{1}{\kappa}(T_{\text{surf}} - T_{\text{bulk}}) \frac{dT_{\text{surf}}}{dt}}. \tag{7.51}$$

Unlike in Equation (7.47) for the surface renewal model, the product $(T_{\text{surf}} - T_{\text{bulk}})(dT_{\text{surf}}/dt)$ is not uniquely related to the heat flux but the relationship depends on $\tilde{x}$. That is, it depends on where the pixel is located relative to the eddy below. However, if the estimates of $\sqrt{(T_{\text{surf}} - T_{\text{bulk}})(dT_{\text{surf}}/dt)}$ are averaged over many pixels, the results can be related to the averaged heat flux as

$$\left\langle \frac{j_{\text{heat}}}{k} \right\rangle = \left(\left\langle \sqrt{\widetilde{T}_{\text{surf}} \sin\tilde{x} \frac{\partial \widetilde{T}_{\text{surf}}}{\partial \tilde{x}}} \right\rangle \right)^{-1} \left\langle \sqrt{\frac{1}{\kappa}(T_{\text{surf}} - T_{\text{bulk}}) \frac{dT_{\text{surf}}}{dt}} \right\rangle, \tag{7.52}$$

provided the distribution of j_{heat} is uncorrelated with the eddy distribution. Here, $\langle \cdot \rangle$ denote averages over many pixels. The coefficient $\left(\left\langle \sqrt{\tilde{T} \sin\tilde{x} (\partial \widetilde{T}_{\text{surf}}/\partial \tilde{x})} \right\rangle \right)^{-1}$ is calculated to be 1.33, while $\sqrt{\pi/2} = 1.25$ in the surface renewal model. Therefore, the mean heat flux estimates are only 6% higher with the eddy renewal model compared to those with the surface renewal model. This can be considered to be close to the noise level of estimates. Therefore, in the following no specific results for the net heat flux estimates based on the eddy renewal model will be presented. They can always be considered to be higher by 6% as compared to the results presented based on the surface renewal model.

7.8 Viscous Stress from Active Thermography

The transport of energy, momentum and mass across the air-sea interface are central questions in the study of air-sea interaction and ocean atmosphere modeling. In previous sections the transport of energy, or heat, was analyzed closely and techniques were presented of estimating the net heat flux as well as the transfer velocity from thermography [Garbe et al., 2003b, 2004]. The transport of mass, or different gases, is not subject of this thesis. A long standing effort has been put into measuring the transfer of mass across the air water interface [Liss and Slater, 1974; Broecker and Peng, 1974, 1982; Jähne et al., 1987; Watson et al., 1991] as well as parameterizing this transfer [Liss and Merlivat, 1986; Wanninkhof, 1992; Wanninkhof et al., 1993; Wanninkhof and McGillis, 1999]. Due to the advantages of using heat as a proxy for mass transfer, research has been undertaken to scale from the transfer velocity of heat to that of gas [Jähne et al., 1989; Haußecker et al., 1995, 2001; Schimpf et al., 2004; Atmane et al., 2004]. A review on the subject of air-water mass transfer can be found in Jähne and Haußecker [1998].

Apart from the transport of energy and mass, the transport of momentum is of great importance for ocean-atmosphere modeling as well as for understanding the processes at the air-sea interface. The transport of momentum from atmosphere to ocean is the driving force in

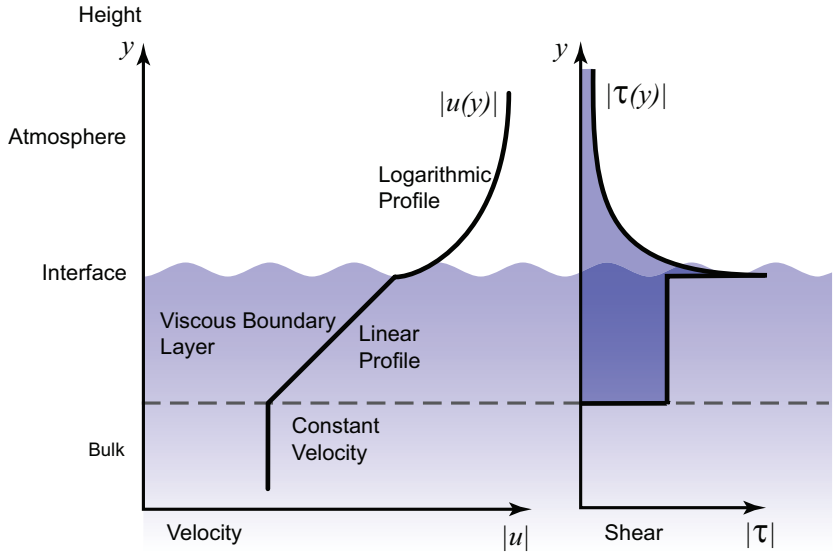

Figure 7.13: *Sketch of the velocity profile $u(z)$ and the shear τ at the sea surface. In the bulk, the velocity is considered constant with vanishing shear τ. In the viscous boundary layer, the velocity changes linearly as seen in plane Couette flow, leading to a constant shear. Above the sea surface, the wind profile is logarithmic and the resulting shear $\tau \sim 1/z$.*

a number of interfacial processes. Generally, the momentum flux τ is partitioned into viscous stress τ_μ and wave-induced stress τ_w. The wave induced stress, also known as form stress, is due to pressure force acting on the slope of waves. This stress τ_w is strongly connected to the wave age β, which is defined as the momentum transfer rate from wind to waves per unit wave momentum. A recent analysis of this quantity in the air-sea momentum flux budget analysis can be found in [Kukulka and Hara, 2005]. Banner and Peirson [1998] conducted experiments and tried to measure the partition of the total momentum transfer into the viscous and the wave-induced stress. Contrary to Okuda et al. [1977] they found a large partition of more than 50% of the total momentum transfer to be made up by the wave-induced stress. More recently Uz et al. [2002] found the partition of total momentum flux to wave induced stress to be 64% for typical conditions. This figure is in close agreement to the results published by Banner and Peirson [1998].

While Okuda et al. [1977] measured the viscous stress τ_μ from hydrogen bubbles, Banner and Peirson [1998] performed their tangential stress measurements with a PIV technique using particles of diameters ranging from 20-60 µm. The discrepancy in the results between Okuda et al. [1977] and Banner and Peirson [1998] can be attributed to a large part in uncertainties in the use of hydrogen bubbles for the flow visualization. The resulting bubbles in measurements by Okuda et al. [1977] and McLeish and Putland [1975] before them are quite large leading to a number of difficulties, as detailed by Banner and Peirson [1998].

While Banner and Peirson [1998] produced some excellent results to the extend of measuring viscous stress in relation to wave phase, their technique relying on PIV measurements is not applicable to the field. This represents a significant drawback and opens room for further

investigations. In this section a novel technique will be presented that relies on active thermography for measuring the viscous stress τ_μ [Garbe et al., 2007a]. Currently, only laboratory measurements have been conducted. They will be presented in Section 7.10.4. Due to the simple experimental set-up, which is presented in Section 7.9, this technique should be well adapted to field use.

Underlying to this technique is the assumption of plane Couette flow in the viscous boundary layer. The resulting linear velocity profile is sketched in Figure 7.13. Information concerning the velocity structure with depth cannot be recovered from passive thermography. Therefore, active thermography is necessary, as shall be described in the next section.

7.8.1 Motion Estimation for Active Thermography

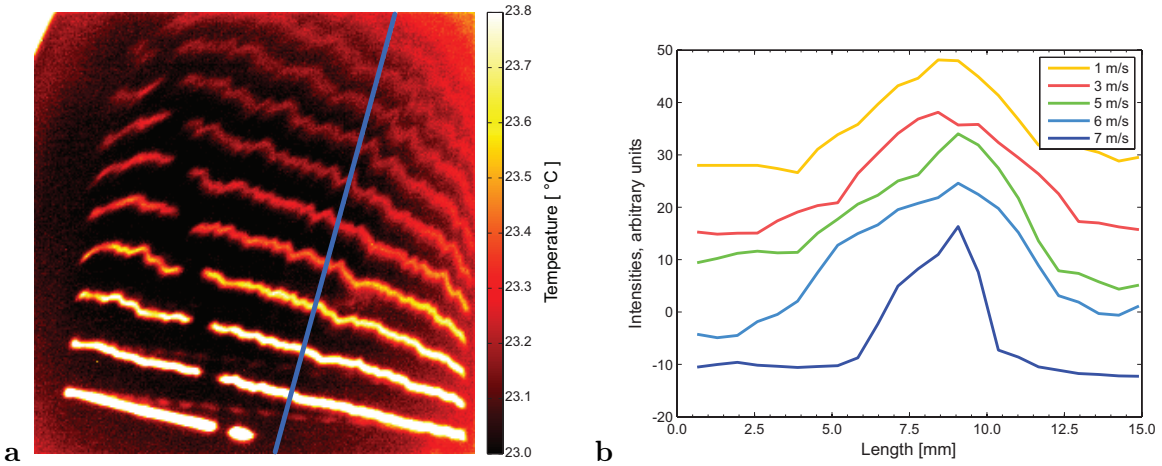

Figure 7.14: *In* **a** *a thermal image at 5.0 m/s wind speed directed from bottom to top is shown. Straight lines are written with a CO_2 laser at the bottom of the frame. Indicated by the blue circle is a section of the profile of the blue line for different wind speeds, which are presented in* **b**. *The profiles are shifted for better visualization and thus presented in arbitrary units of image intensities.*

For measuring motion accurately from active thermography, it is important to derive a motion model that takes into account the underlying fundamental processes. In Figure 7.14**a** an image from active thermography is shown. Here, a line pattern is written onto the interface which is advected downstream from the heated location downwind. Principally any conceivable pattern can be written to the interface. Here a line pattern was chosen for illustration purposes. For applications in the field a simple line pattern is disadvantageous, since velocities tangential to the lines cannot be estimated due to the aperture problem as explained in Section 3.2.1.

As can be seen from Figure 7.14**a**, the appearance of the structures written with the laser are distorted as they are advected downstream. The leading edge appears to remain sharp, while the trailing edge blurs increasingly with time. This change of shape of the written temperature structure becomes increasingly more pronounced at stronger wind-speeds, associated with a higher shear at the interface. This can be seen in Figure 7.14**b** where profiles

of the temperature structure are shown for different wind speeds. In these experiments a surface film was present, effectively suppressing waves. The whole wind induced shear stress is thus transferred to viscous stress.

These blurring effects have to be incorporated into the motion model. Otherwise inaccurate motion fields will be estimated. First the equations of motion will be derived not taking decay of infrared radiation with depth due to absorption in water into account. This is of course a very crude approximation, as the penetration depth in water is only a few µm. Hence in a second step this absorption will be modeled explicitly. Only from this motion model can the viscous shear stress τ_μ be estimated from the data.

Motion Model without Infrared Absorption in Water

In velocity profile in the viscous boundary layer is considered to decrease linearly with depth. This type of flow can thus be approximated by plane Couette flow. In this configuration, the flow in between two plates is driven by the relative velocity of the boundary plates. In active thermography a laser is used for heating up patches of water. Due to its penetration depth, the laser heats up a three dimensional structure inside the viscous boundary layer. This structure gets sheared due to the velocity profile. In thermography an infrared camera is used for imaging these heated patches of water. In the imaging process the three dimensional structure is projected onto the sensor. This leads to an integration over depth in the boundary layer. The shearing of the thermal structure and the subsequent integration leads to an apparent smearing of the structure with an accompanying decrease in intensity. This process was sketched in Figure 2.10. Results of a computer simulation of this process are shown in Figure 7.15 **a** and **b**.

The equation of motion for such an process was derived in Section 2.7.1. Here the applicable model is that of the two plates in motion, where the upper plate translates with the velocity U_δ, the lower one with U_0. At the air-sea interface, U_δ can be considered as the velocity of the water surface, while U_0 is not accessible. Estimating the velocity of the intensity structures subject to shear and integration over the viscous boundary layer can be achieved by solving the differential equation $dT/dt = -(t)^{-1}T$, which is the same as Equation (2.63). Also taking into account isotropic conduction of the heat pattern, this differential equation can be expanded to

$$\frac{dT}{dt} = u\frac{\partial T}{\partial x} + v\frac{\partial T}{\partial y} + \frac{\partial T}{\partial t} = \kappa\Delta T - \frac{1}{t}T, \tag{7.53}$$

where κ is the thermal diffusivity and t is the time since the thermal structures were written. Rewriting this equation in vector notation leads to

$$\frac{dT}{dt} = d^\top \cdot p = \begin{bmatrix} \frac{\partial^2 T}{\partial x^2} + \frac{\partial^2 T}{\partial y^2} & \frac{1}{t}T & \frac{\partial T}{\partial x} & \frac{\partial T}{\partial y} & \frac{\partial T}{\partial t} \end{bmatrix} \cdot \begin{bmatrix} -\kappa & 1 & u & v & 1 \end{bmatrix}^\top = 0\ . \tag{7.54}$$

This type of equation can be solved straight forward with the local gradient based approach presented in Section 3. If the exact time t is not available since the thermal structures were written, one might also estimate this parameter. This will reduce the accuracy a little bit,

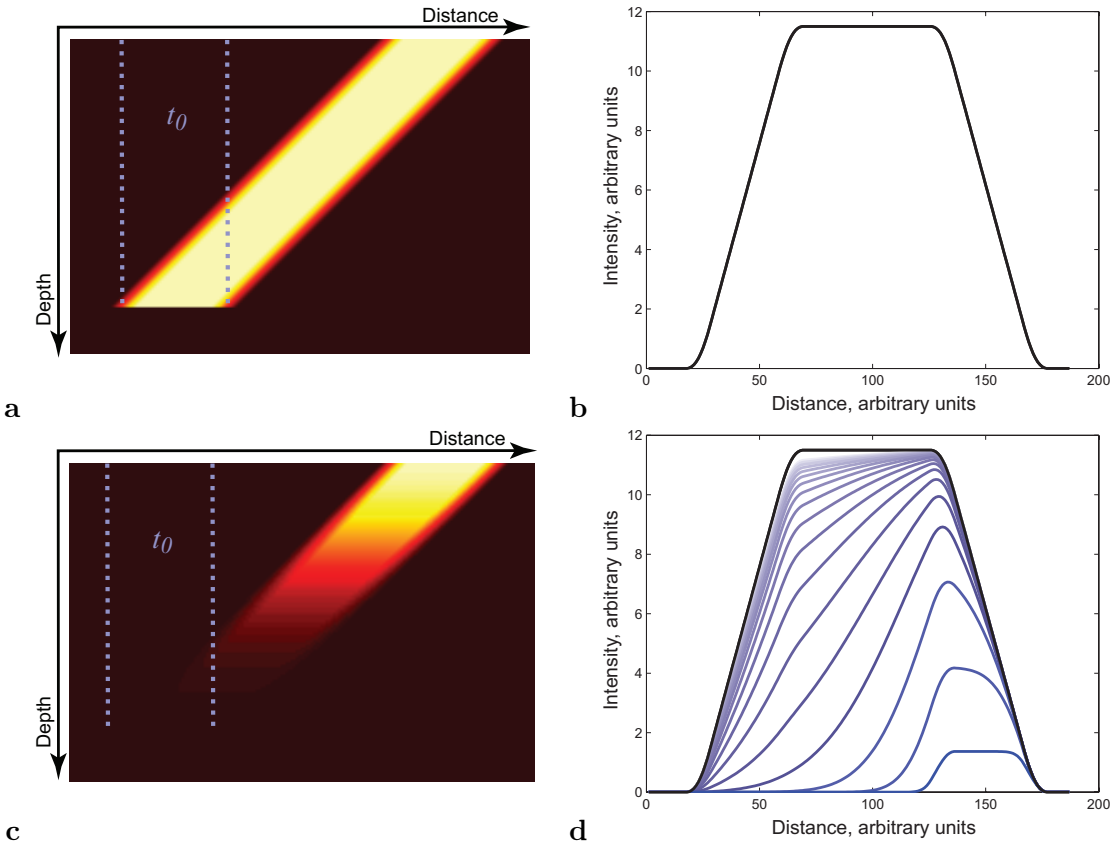

Figure 7.15: *Simulation of the viscous boundary layer heated up locally by a CO_2 laser at time t_0 (indicated by blue lines in* ***a*** *and* ***c****. Shown is the shearing of the temperature structure due to the velocity gradient. In* ***b*** *and* ***d*** *the depth integrated intensities are shown. In* ***a*** *and* ***b*** *the intensities remain constant with depth, in* ***c*** *and* ***d*** *the intensities are attenuated due to the Lambert-Beer law. In* ***d*** *plots are presented for different penetration depths. In all plots the wind direction is from left to right.*

but an estimation of the velocities u and v shoul still be more accurate than not taking this term into account. The motion constraint equation for this case is given by

$$\frac{dT}{dt} = d^\top \cdot p = \left[\begin{array}{ccccccc} \frac{\partial^2 T}{\partial x^2} + \frac{\partial^2 T}{\partial y^2} & T & \frac{\partial T}{\partial x} & \frac{\partial T}{\partial y} & \frac{\partial T}{\partial t} \end{array} \right] \cdot \left[\begin{array}{ccccc} -\kappa & \frac{1}{t} & u & v & 1 \end{array} \right]^\top = 0. \qquad (7.55)$$

7.8.2 Absorption with Depth

In the previous section, the motion constraint equation for heat structures was derived without taking absorption in the water body into account. For active thermography, a CO_2 laser is used for heating up water parcels. These parcels are visualized with an IR camera sensible in the range from 3-5µm. In this spectral range, the penetration depth or radiation is only approximately 10 µm. Equally, the penetration depth of the CO_2 laser is $\lambda 11.5 \mu m$. This strong absorption needs to be considered in order to gain accurate estimates of velocity from the motion estimation framework presented in this thesis.

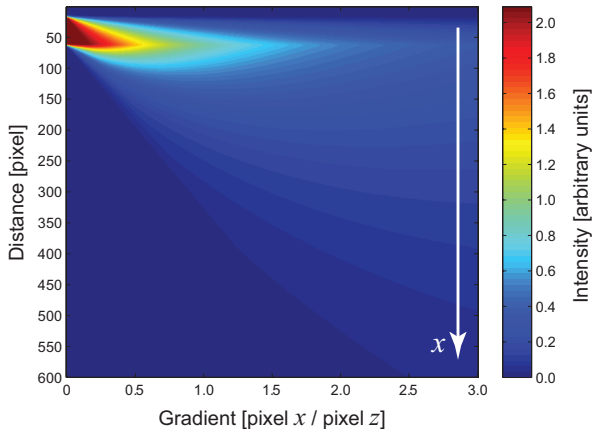

Figure 7.16: *A simulation of the intensities recorded by the IR camera a fixed time t after the pattern has been written to the surface. Wind induces a shear along the x-axis (from top to bottom). From left to right, the velocity gradient dx/dz increases. It can clearly be seen that the image intensity is smeared over a wide area for strong velocity gradients. Also, it should be noted that the intensity maximum remains at a fixed location at the trailing edge of the written structure. For this simulation $U_0 = 0$.*

In Section 2.7.1 the equation of motion for plane Couette Flow was derived. The displacement $x(z,t)$ from the velocity profile $v(z)$ is given in Equation (2.59) to

$$x_{U_0}(z,t) = \frac{z}{\delta}(U_\delta - U_0) \cdot t + U_0 \cdot t = \frac{z}{\mu}\tau \cdot t + U_0 \cdot t. \tag{7.56}$$

Here δ is the separation of the two "plates" and U_δ the velocity of the upper plate. U_0 is the velocity of the lower plate μ is the viscosity of water, τ the shear stress and t the time since the thermal structure was written with the laser.

The absorption of radiation with depth is modeled by Lambert-Beer's law. Integration with depth thus results in

$$T(x,t) = \int_{\frac{\mu(x-c-U_0 t)}{t\tau}}^{\frac{\mu(x-U_0 t)}{t\tau}} e^{-\kappa z}\, \mathrm{d}z = \frac{1}{\kappa} e^{\frac{\kappa\mu(tU_0 - x)}{t\tau}} \cdot \left(e^{\frac{c\kappa\mu}{t\tau}} - 1\right). \tag{7.57}$$

Differentiating this equation with respect to times yields the following differential equation:

$$\frac{dT}{dt} = \left(\frac{\kappa \cdot \mu \cdot x}{t^2 \cdot \tau} + \frac{\kappa \cdot \mu \cdot c}{t^2 \cdot \tau}\left(\frac{1}{e^{-\frac{\kappa\mu c}{t\tau}} - 1}\right)\right) T. \tag{7.58}$$

When not considering absorption, the motion constraint equation was derived to $dT/dt = t^{-1}T$ in Section 2.7.1. By noting that

$$\lim_{x \to 0} \quad \frac{x}{e^{-\alpha x} - 1} = -\frac{1}{\alpha}. \tag{7.59}$$

Equation (7.58) reduces to $dT/dt = -t^{-1}T$, which is exactly the constraint equation that was found in the setting without absorption. This formulation is thus consistent to previous findings.

While it is possible to use Equation (7.58) to solve the motion problem, it is generally preferred to approximate this solution. The measurement is conducted by heating up water parcels with a CO_2 laser. The width c of the structure is small compared to the distance x the water parcels traverses during the measurement. Therefore, Equation (7.58) can be approximated by requiring $\lim c \to 0$. This results in

$$\overset{\lim}{c \to 0} \quad \frac{dT}{dt} = \left(\frac{\kappa\mu x}{t^2\tau} - \frac{1}{t}\right) T = \left(\frac{\alpha x}{t^2} - \frac{1}{t}\right) T \quad \text{with} \quad \alpha = \frac{\kappa\mu}{\tau}, \tag{7.60}$$

which can also be written as

$$\frac{dT}{dt} = u_1 \frac{\partial T}{\partial x} + u_2 \frac{\partial T}{\partial y} + \frac{\partial T}{\partial t} = \frac{T}{t}\left(\frac{\alpha x}{t} - 1\right) = \frac{T}{t}\left(\alpha\sqrt{u_1^2 + u_2^2} - 1\right). \tag{7.61}$$

The parameters of this constraint equation can again be estimated by writing it in vector notation, leading to

$$\begin{bmatrix} \frac{T}{t} & \frac{\partial T}{\partial x} & \frac{\partial T}{\partial y} & \frac{\partial T}{\partial t} \end{bmatrix} \cdot \begin{bmatrix} \xi_{c\to 0} & u_1 & u_2 & 1 \end{bmatrix}^\top = \boldsymbol{d}^\top \cdot \boldsymbol{p} = 0, \tag{7.62}$$
$$\text{with} \quad \xi_{c\to 0} = 1 - \alpha\sqrt{u_1^2 + u_2^2}.$$

The parameter vector $\boldsymbol{p}$ can now be estimated from the data with the algorithm presented in Section 3. From the parameters $\xi_{c\to 0}$ and $\boldsymbol{u} = [u_1, u_2]^\top$ the surface stress $\tau_{c\to 0}$ and thus the friction velocity $u_\star = \sqrt{\tau/\rho}$ can be computed from

$$\tau_{c\to 0}(\xi_{c\to 0}, ||\boldsymbol{u}||_2) = \frac{\kappa \cdot \mu}{1 - \xi_{c\to 0}}\sqrt{u_1^2 + u_2^2} = \frac{\kappa \cdot \mu}{1 - \xi_{c\to 0}}||\boldsymbol{u}||_2 \tag{7.63}$$

$$u_{\star;c\to 0}(\xi_{c\to 0}, ||\boldsymbol{u}||_2) = \sqrt{\frac{\tau}{\rho}} = \sqrt{\frac{\kappa \cdot \mu}{\rho(1 - \xi_{c\to 0})}||\boldsymbol{u}||_2}, \tag{7.64}$$

where $||\cdot||_2$ is the L-2 norm. The subscript $c \to 0$ indicates that this solution only holds for the limit case $\lim c \to 0$.

It is evident that τ and hence $u_\star$ can be computed from digital image processing. However, it should be noted that one of the assumptions leading to expression (7.61) was that c is extremely small, actually $\lim c \to 0$. Naturally, in real world applications the width c of the patterns written on the sea surface will have a finite extend. It is thus important to quantify the error introduced by this assumption. Therefore, the difference in between the accurate and the approximated solution is analyzed next. This difference is given by

$$\frac{dT}{dt} - \left(\frac{dT}{dt}\right)_{\substack{\lim \\ c\to 0}} = \left(\frac{\alpha \cdot c}{t^2}\left(\frac{1}{e^{-\frac{\alpha\cdot c}{t}} - 1}\right) + \frac{1}{t}\right) \cdot T = \gamma T, \tag{7.65}$$
$$\text{with} \quad \gamma = \frac{\alpha \cdot c}{t^2}\left(\frac{1}{e^{-\frac{\alpha\cdot c}{t}} - 1}\right) + \frac{1}{t} \quad \text{and} \quad \alpha = \frac{\kappa \cdot \mu}{\tau}.$$

It was shown in Equation (7.61) that an expression for the limit case $c \to 0$ can be found. It is instructive to examine the opposite case of $c \to \infty$. It can be shown that

$$\overset{\lim}{c \to \infty} \quad \gamma = -\frac{1}{t} \quad \text{or} \tag{7.66}$$

$$\overset{\lim}{c \to \infty} \frac{dT}{dt} - \left(\frac{dT}{dt}\right)_{\substack{\lim \\ c\to 0}} = -\frac{T}{t}. \tag{7.67}$$

Therefore, the initial expression can by corrected by subtracting $1/t$ from it. This results in

$$\frac{dT}{dt} = \frac{T}{t}\left(\frac{\alpha x}{t} - 2\right) = \frac{T}{t}\left(\alpha\sqrt{u_1^2 + u_2^2} - 2\right). \tag{7.68}$$

Writing this expression in vector notation leads to

$$\begin{aligned}\left[\begin{array}{cccc} \frac{T}{t} & \frac{\partial T}{\partial x} & \frac{\partial T}{\partial y} & \frac{\partial T}{\partial t} \end{array}\right] \cdot \left[\begin{array}{cccc} \xi_{c\to\infty} & u_1 & u_2 & 1 \end{array}\right]^\top = \boldsymbol{d}^\top \cdot \boldsymbol{p} = 0, \\ \text{with} \quad \xi_{c\to\infty} = 2 - \alpha\sqrt{u_1^2 + u_2^2}.\end{aligned} \tag{7.69}$$

Analogous to Equations (7.63) and (7.64), $u_\star$ and τ for the limit case $c \to \infty$ can be estimated from

$$\tau_{c\to\infty}(\xi_{c\to\infty}, ||\boldsymbol{u}||_2) = \frac{\kappa\cdot\mu}{2-\xi_{c\to\infty}}\sqrt{u_1^2+u_2^2} = \frac{\kappa\cdot\mu}{2-\xi_{c\to\infty}}||\boldsymbol{u}||_2 \tag{7.70}$$

$$u_{\star;c\to\infty}(\xi_{c\to\infty}, ||\boldsymbol{u}||_2) = \sqrt{\frac{\tau}{\rho}} = \sqrt{\frac{\kappa\cdot\mu}{\rho(2-\xi_{c\to\infty})}||\boldsymbol{u}||_2}, \tag{7.71}$$

where this time the subscript $c \to \infty$ emphasizes the fact that this solution is only accurate for the limit case of $\lim c \to \infty$.

For some structures written with the laser, both limit cases presented so far might be too inaccurate. A better approximation can be found by developing the factor γ from Equation (7.65) into a Taylor Series Expansion around $c \to 0$. This leads to

$$\gamma = -\frac{\alpha\cdot c}{2\cdot t^2} - \frac{\alpha^2\cdot c^2}{12\cdot t^3} + \frac{\alpha^4\cdot c^4}{720\cdot t^5} + \mathcal{O}(c^6). \tag{7.72}$$

Similar to the previous approximations of $\lim c \to 0$ and $\lim c \to \infty$, this expression for γ can be inserted into the equation $dT/dt = T/t(\alpha u - 1 + \gamma)$, which yields

$$\tau_c = \frac{\kappa\cdot\mu\,(2\cdot t\cdot||u||_2 - c)}{2\cdot t\cdot(1-\xi)} = \frac{\kappa\cdot\mu}{1-\xi}||u||_2 - \frac{\kappa\cdot\mu\cdot c}{2\cdot t\cdot(1-\xi)} \tag{7.73}$$

$$\begin{aligned}\tau_{c^2} = \frac{\kappa\cdot\mu}{4\cdot t\cdot(1-\xi)}\Bigg(&2\cdot t\cdot||u||_2 - c \\ &+ \sqrt{4\cdot t\cdot||u||_2\cdot(t\cdot||u||_2 - c) - \frac{c^2}{3}(1-4\cdot\xi)}\Bigg).\end{aligned} \tag{7.74}$$

The friction velocity $u_\star$ can then be estimated from the shear stress τ according to $u_\star = \sqrt{\tau/\rho}$. Here, for τ_c and τ_{c^2} linear and second order terms in c are used from Equation (7.72) respectively.

In this section a few motion constraint equations were developed that make it possible to estimate the viscous shear stress τ from active thermography. At the same time, accurate estimates of surface flow are also achieved from the same technique. This is due to the fact that both τ and the parameters of motion u and v are estimated as parameters of the motion model.

7.8.3 Error Analysis

Prior to using this new technique for measuring the viscous shear stress in laboratory settings or in the field, it is important to quantify the error in the estimates. This error will depend on many factors such as noise of the imager and specific set-up. Assuming Gaussian errors, the error σ_τ can be anticipated from error propagation. This leads to

$$\sigma_\tau = \frac{\kappa \cdot \mu}{(1-\xi)^2} \sqrt{\frac{\left(u_1^2+u_2^2\right)\sigma_\xi^2 + (\xi-1)^2 \cdot u_1^2\sigma_{u_1}^2 + (\xi-1)^2 \cdot u_2^2\sigma_{u_2}^2}{u_1^2+u_2^2}} \tag{7.75}$$

$$\frac{\sigma_\tau}{\tau} = \sqrt{\frac{\sigma_\xi^2}{(\xi-1)^2} + \frac{u_1^2 \cdot \sigma_{u_1}^2 + u_2^2 \cdot \sigma_{u_2}^2}{\left(u_1^2+u_2^2\right)^2}}. \tag{7.76}$$

Usually, the error in computing u_1 and u_2 is the same. Therefore it can be assumed that $\sigma_u \overset{!}{=} \sigma_{u_1} = \sigma_{u_2}$. This leads to

$$\sigma_\tau = \frac{\kappa \cdot \mu}{(1-\xi)^2} \sqrt{\sigma_\xi^2 + (\xi-1)^2\,\sigma_u^2} \tag{7.77}$$

$$\frac{\sigma_\tau}{\tau} = \sqrt{\frac{\sigma_\xi^2}{(\xi-1)^2} + \frac{\sigma_u^2}{u_1^2+u_2^2}}. \tag{7.78}$$

The error for $u_\star$ as well as relative errors are given by

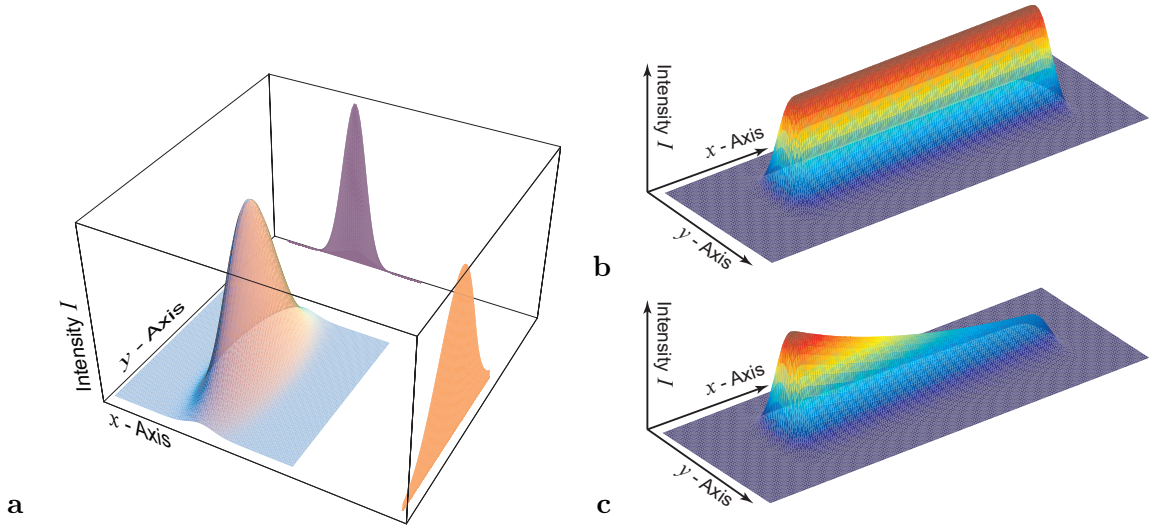

Figure 7.17: *In* **a** *the Gaussian profile of the incident radiative heat flux is shown, in* **b** *frame 124 of the intensity of the simulated IR image sequence is shown without Lambert Beer's law and in* **c** *with decay as model by Lambert Beer's law.*

$$\sigma_{u_\star} = \frac{1}{2}\sqrt{\frac{\kappa \cdot \mu \cdot \left\{\left(u_1^2+u_2^2\right)^2\sigma_\xi^2 + (\xi-1)^2\left(u_1^2\sigma_{u_1}^2 + u_2^2\sigma_{u_2}^2\right)\right\}}{\rho\,(1-\xi)^3\left(u_1^2+u_2^2\right)^{3/2}}} \tag{7.79}$$

$$\frac{\sigma_{u_\star}}{u_\star} = \frac{1}{2}\sqrt{\frac{\sigma_\xi^2}{(1-\xi)^2} + \frac{u_1^2\sigma_{u_1}^2 + u_2^2\sigma_{u_2}^2}{(1-\xi)\left(u_1^2+u_2^2\right)^2}}. \tag{7.80}$$

Again, these expressions can be simplified by assuming that $\sigma_u \stackrel{!}{=} \sigma_{u_1} = \sigma_{u_2}$. This results in

$$\sigma_{u_\star} = \frac{1}{2}\sqrt{\frac{\kappa\cdot\mu}{\rho\,(1-\xi)}\left(\frac{\sqrt{u_1^2+u_2^2}\cdot\sigma_\xi^2}{(1-\xi)^2}+\frac{\sigma_u^2}{\sqrt{u_1^2+u_2^2}}\right)} \tag{7.81}$$

$$\frac{\sigma_{u_\star}}{u_\star} = \frac{1}{2}\sqrt{\frac{\sigma_\xi^2}{(1-\xi)^2}+\frac{\sigma_u^2}{(1-\xi)\left(u_1^2+u_2^2\right)}}. \tag{7.82}$$

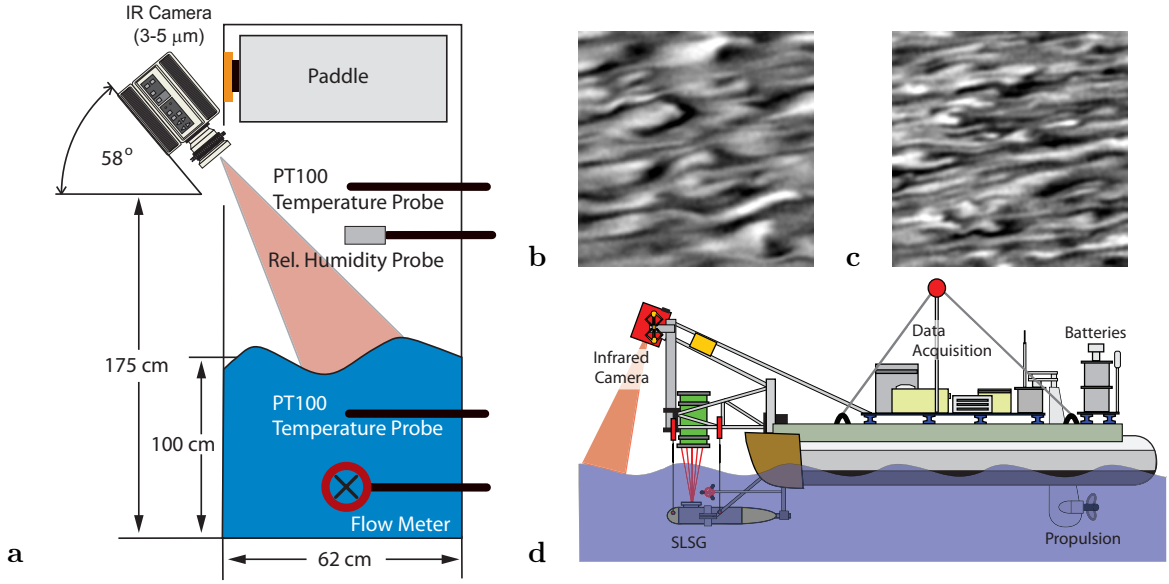

Figure 7.18: *In* **a** *a schematic cross section of the Heidelberg Aeolotron can be seen. An infrared camera images a* (40×40) cm^2 *area of the water surface, with an angle of incidence of about 30°. Presented in* **b** *is a drawing of the LADAS catamaran as was used during the GasExII experiment.*

In order to assess the relative accuracy of this new technique, the motion of water parcels can be assumed to be directed along a scanline of the imager ($u = u_1$ and $u_2 = 0$). Hence

$$\frac{\sigma_\tau}{\tau} = \frac{1}{2}\sqrt{\frac{\sigma_\xi^2}{\left(\frac{\kappa\mu}{\tau}u\right)^2}+\frac{\sigma_u^2}{u^2}} \tag{7.83}$$

$$\frac{\sigma_{u_\star}}{u_\star} = \frac{1}{2}\sqrt{\frac{\sigma_\xi^2}{\left(\frac{\kappa\mu}{\tau}u^2\right)^2}+\frac{\sigma_u^2}{\frac{\kappa\mu}{\tau}u^3}}. \tag{7.84}$$

The penetration depth for IR radiation in the spectral range of 3-5 µm is roughly 10µm, that of the CO_2 laser ($\lambda = 10.8\mu m$) is 11.5µm. Hence $\kappa = 4.57\cdot10^4 m^{-1}$. The viscosity of water at 20°C is $\mu = 1.002\cdot10^{-3}$ kg $m^{-1}s^{-1}$. From these quantities, one can estimate that the relative accuracy of the shear stress should easily be better than 5%.

7.8.4 Synthetic Data

In order to analyze the validity of the proposed technique it was tested on simulated data. Also, by varying the level of noise, the robustness of the algorithm to sensor noise was tested.

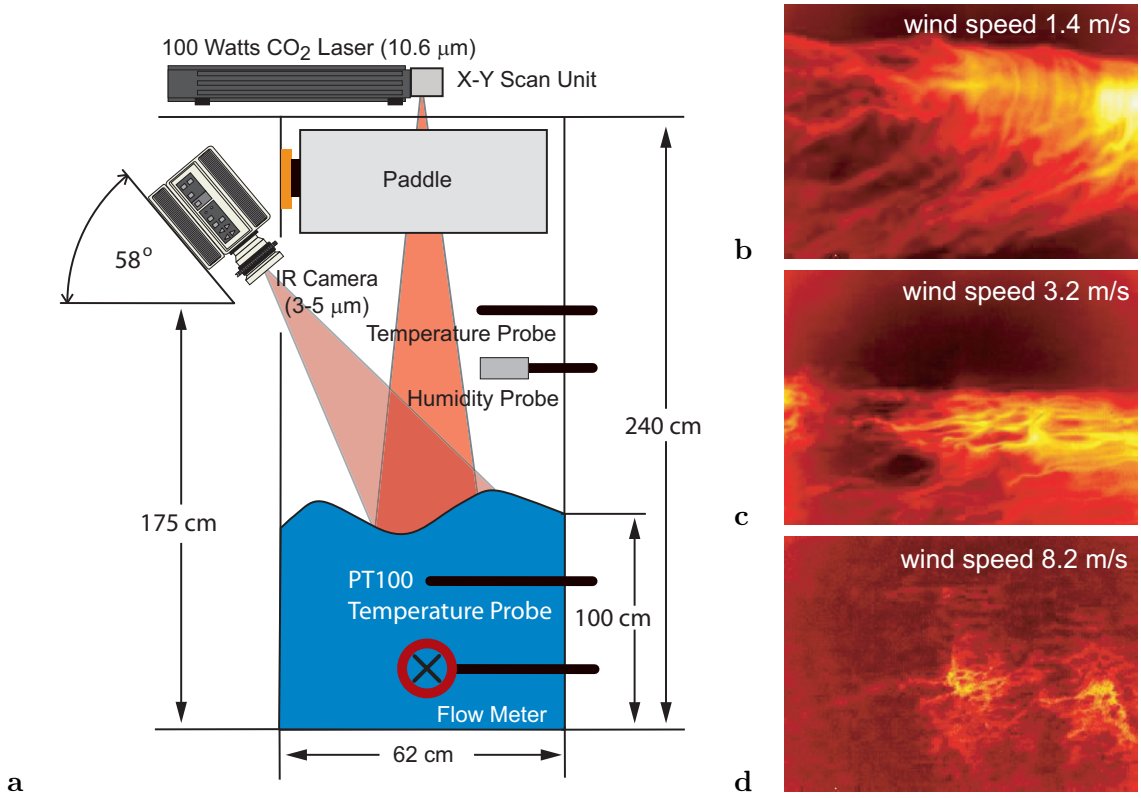

Figure 7.19: *Images of typical thermal structures as seen with the active IR technique. The wind velocities are 1.4 m/s, 3.2 m/s and 8.2 m/s in* ***a****,* ***b*** *and* ***c*** *respectively. In all cases, the direction of the wind is from right to left.*

The laser was simulated to be a 2D Gaussian with different widths in the x_1 and x_2 direction. An image of the simulated laser profile is shown in Figure 7.17**a**. The shearing of the heated structure due to the velocity profile was then simulated. Two simulations were run, one taking absorption of radiation in water into account, one without absorption. These two simulations are presented in Figure 7.17**b** and 7.17**c**. This transport equation was discretized on a $[x, y, z] = 256 \times 64 \times 480$ grid in 125 time steps. Different noise levels were added to this sequence. The parameter estimation was performed on this sequence. The result of the velocity vector field was very accurate. The relative error was well below 1% for noise levels equivalent to the IR camera. Detailed information regarding this simularion and results are presented in Garbe et al. [2007a].

7.9 Experimental Set-Up

Infrared thermography represents an excellent tool for measuring boundary layer processes directly at the air water interface. This is due to the high temperature resolution of modern IR cameras as well as to the high absorption of water in the two spectral windows where midwave (3-5µm) and longwave (8-10µm) IR cameras are sensitive. This leads to a very shal-

low penetration depth of around 10 µm into the boundary layer. Added to this is an easy geometric and radiometric calibration of these cameras. More in-depth information about the IR properties of water and calibration of IR cameras can be found in Garbe [2001].

In this thesis two classes of thermographic techniques are presented. The first class relies on imaging temperature fluctuations at the air-water interface due to a "natural" net heat flux at the interface. From this technique the temperature difference ΔT, the flow velocity directly at the interface, the net heat flux j_{heat}, as well as the transfer velocity k and parameter of the underlying transport model and their statistics can be estimated. This class is termed *passive* thermography, since no external sources of heat are used for conducting these measurements. The downside of this technique is that it can only be used for conditions with sufficiently strong heat fluxes present. Otherwise the surface temperature will be homogeneous and no patterns are visible. Under these circumstances, an external heat source such as a CO_2 laser can be used for applying an external heat flux to the topmost surface layer. If this heat flux is spatially homogeneous, turbulences will become visible, as is shown in Figure 7.19. Alternatively, patterns can be written to the interface, marking individual patches of water. This class of techniques, relying on an external heat flux are called *active* thermography. A subclass of this technique is also termed *controlled flux technique* (CFT), since this external heat flux can be controlled precisely. This allows to analyze the response of the sea surface to this controlled heat flux in a linear system theoretical approach [Jähne et al., 1989, 2007].

For *passive* thermography, no active elements such as lasers are needed for heating up patches of water. The experimental set-up is thus much simpler than that of active techniques [Haußecker, 1996]. Due to the presence of a net heat flux between water and air, the interface will be at a different temperature than the water bulk. Under most conditions, the net heat flux will be directed from the water to the airside. This leads to a cooling of the interface. This effect is also known as the *cool skin of the ocean* [Merz, 1920; Woodcock and Stommel, 1947; Wu, 1985; Fairall et al., 1996a]. Turbulence advects bulk water of a different temperature into the interface, which is detected with the infrared camera. Typical images of these turbulences can be seen in Figure 7.18. The magnitude of these structures varies generally from less than 0.1K to 0.2-0.3K, depending on the forcing. Because the temperature structures at the air-water interface are quite minute, great experimental care has to be taken not to obscure the investigated processes. Central to the experimental set-up is an infrared camera. In recent years commercial camera systems have become readily available. They provide high frame rates and low noise levels. However, in the present context the temperature differences to be analyzed are in the range of $0.01 - 0.3$ K and thus close to the noise level of modern cameras, which is typically 25 mK. The same holds true for the frame rate, as surface drift and wave motion is significant at higher wind speeds, calling for higher sampling rates to circumvent motion blurring or problems due to Shannon's sampling theorem [Shannon, 1949]. In this respect the techniques presented here would improve immensely from imaging devices with even lower noise levels and higher frame rates.

In experiments conducted at the Heidelberg wind-wave facility (the Aeolotron), an Amber

Radiance 1 camera was used. For field experiments during the GasExII cruise thermographic image sequences were acquired with an Amber Galileo MWIR camera. Both cameras are based around a Stirling cooled InSb detector made up of a square 256×256 focal plane array. The sensor is sensitive in a wavelength window of $3 - 5$ µm. The frame rate of the cameras is 60 Hz and 100 Hz for the Radiance and Galileo camera, respectively. The integration times were chosen between 1.3 and 1.9 ms, depending on the temperature of the water body. Longer integration times tend to exhibit a better signal to noise ratio while increasing the danger of overflows occurring in the image. To avoid strong reflections at the sea surface, the cameras in both field and laboratory experiments are mounted at an angle of about 60° to the mean sea surface. Illustrations of the set-up for laboratory and field measurements are presented in Figure 7.18.

For *active* thermography, a heat source is needed in addition to the set-up for passive thermography. For the active techniques presented in this thesis, this laser needs to be synchronized with the infrared imager. This synchronization is achieved by triggering the laser with an integral reduction of the frame rate of the camera. Depending on the needed output power, one of these three different CO_2 lasers were used for this thesis: 25W Synrad 48-2 laser, a 100W Synrad Evolution and 200W Synrad Firestar f-series. High power lasers are needed, when spatially homogeneously areas are heating up at the water surface. Generally, the water is heated by less than one Kelvin. Stronger heating of the water is not necessary due to the high sensitivity of the IR cameras. This is important, since a strong heating would lead to a stable stratification and an associated change in turbulent structures close to the interface. The set-up for active thermography is shown in Figure 7.19.

7.10 Laboratory Experiments

Channel Height	Channel Width	Inner Radius	Outer Radius	Mean Circumference	Volume of Channel
2.407m	0.616m	4.241m	4.958m	29.217m	44.68m^3

Water Surface Area	Nominal Water Depth	Nominal Water Volume	Maximal Wind Speed
18.00m^2	1.15m	20.70m^3	15m/s

Table 7.1: *Key technical data of the Heidelberg Aeolotron.*

Laboratory measurements were conducted at the Heidelberg Aeolotron, a dedicated circular wind wave facility. Wind speeds of up to 15 m/s can be attained by a rotating fibre glass enforced paddle ring. To allow precise heat flux measurements the walls of the Aeolotron are insulated by a 9 cm thick layer of Styrodur™ and are coated with a highly reflective aluminium foil in the air space. This ensures that the heat is transported predominantly through the water surface and not through the walls of the facility.

In order to vary the heat flux, the temperature of the water body can be increased by a 15.2 kW heating system. The air space is controlled by a closed loop air conditioning system

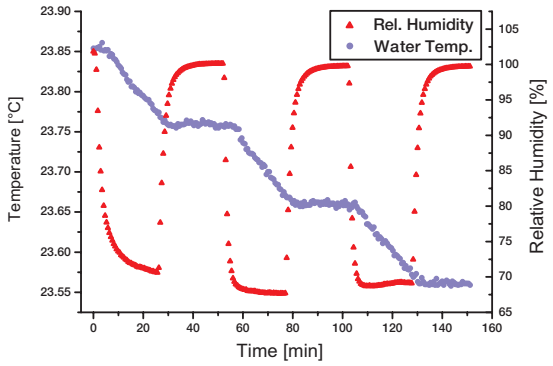

Figure 7.20: *The water temperature and the relative humidity of the experiment conducted at a wind speed of 4.2 m/s.*

with independent control of humidity and air temperature. High positive and negative heat fluxes at the water interface of more than 1 kW/m^2 are achievable by 64.1 kW cooling and 15.6 kW heating capacity of the gas space. The specifications of the Aeolotron are given in Table 7.1.

7.10.1 Measurements of ΔT with Surface Renewal Model

The temperature difference ΔT can be measured in the Aeolotron in two ways. In the context of this work the most important technique is obviously computing ΔT from the statistical analysis of the infrared imagery as outlined in Section 7.3.1. The reason is that only this analysis is equally applicable to the sea surface in field measurements. Also, ΔT is estimated with the same device as the other parameters of heat exchange, resolving cross calibration issues.

Another way of measuring ΔT can be conducted by intermittently switching the net heat flux j_{heat} on and off. In the experiments the net flux is given by the latent heat flux, since the sensible heat flux is zero due to the same air and water temperatures as is the radiative heat flux due to the reflective coating of the walls of the Aeolotron. A typical plot of water temperatures and relative humidity for such an experiment is presented in Figure 7.20. In the absence of a net heat flux the cool skin equilibrates and the surface temperature T_{surf} is equivalent to the bulk temperature T_{bulk}. This leads to a homogeneous image in the infrared camera of the bulk temperature T_{bulk}. In the presence of a net heat flux j_{heat} the thermal boundary layer develops and the surface temperature T_{surf} is different from that of the bulk T_{bulk}. The temperature difference $\Delta T = T_{\mathrm{surf}} - T_{\mathrm{bulk}}$ can be computed from the images acquired during flux and no flux conditions, taking a steady decline of T_{bulk} due to j_{heat} into account. These measurements are shown in Figure 7.21. An extensive analysis of this method and a comparison to the results of the statistical approach of Section 7.3.1 has been performed by Schimpf et al. [2004] for different wind speeds with and without a surfactant. The results of this analysis are presented in Table 7.2. Both methods are in excellent agreement at all

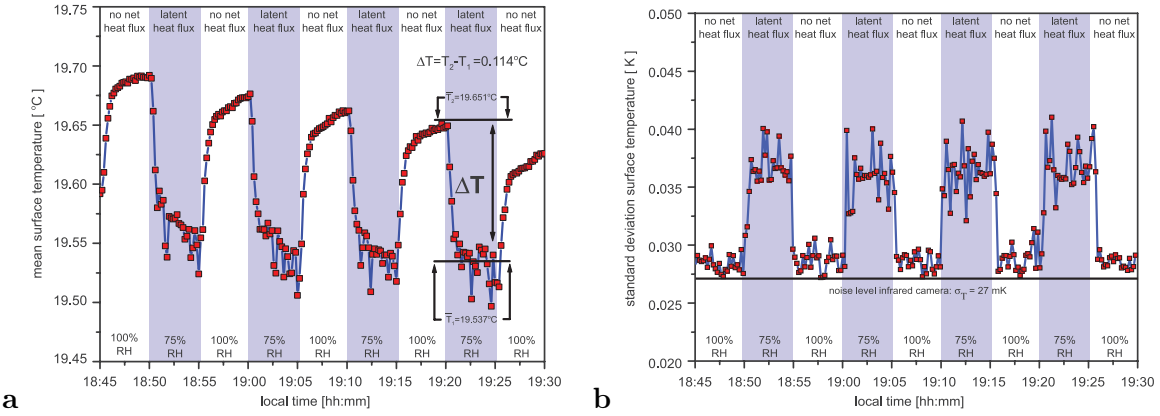

Figure 7.21: ***a*** *The mean surface temperature* T_{surf} *and* ***b*** *standard deviation for periodically varying latent heat flux (wind speed 4.5 m/s, slick-covered surface). If no net heat flux density at the water surface is present (relative humidity* $\approx 100\%$*, surface temperature fluctuations at noise level), the infrared imager measures* T_{bulk}*. In the presence of a heat flux, the surface temperature immediately cools down, and temperature fluctuations at the water surface occur.* ΔT *is calculated from the difference of the mean bulk and the mean surface temperature.*

series	wind speed $[m/s]$	$u_{\star w}$ $[cm/s]$	ΔT (DMT) $[K]$	ΔT (fit) $[K]$
A	1.2	0.16	0.044±0.003	0.041±0.004
C	2.2	0.39	0.026±0.004	0.032±0.003
B	4.6	1.09	0.032±0.004	0.038±0.003
D	5.8	1.51	0.028±0.003	0.034±0.003
I	1.3	0.11	0.230±0.024	0.071±0.007
K	2.2	0.20	0.177±0.012	0.111±0.016
J	4.5	0.51	0.103±0.007	0.115±0.015
L	6.1	0.74	0.054±0.003	0.052±0.004

Table 7.2: *Results of the measurements in the wind-wave facility. Series A-D: clean interface, series I-L: surfactant present (Triton-X-100, bulk concentration 3 ppm). Comparison of* ΔT *estimates of the fitted temperature distribution and of the difference of the measured mean temperatures (DMT) [Schimpf et al., 2004].*

wind speeds examined, ranging from 1.2 m/s up to 6.1 m/s. It was shown that the statistical analysis presents a strong bias towards lower estimates at low wind speeds in the presence of surface slicks. This can be attested to a damping of turbulence due to the surface film [Schimpf et al., 2004].

An error analysis of this method for calculating the temperature difference on synthetic data has been presented in Section 7.3.1. It was shown that an accuracy of less than 3 mK can be expected, a value well in agreement with the empirical findings presented in Table 7.2.

7.10.2 Measurements of ΔT with the Eddy Renewal Model

In this section the technique for estimating ΔT from the eddy renewal model will be analyzed. This technique was presented in Section 7.3.2. In order to assess the applicability of this model to passive thermography, this technique was applied to laboratory data. Measurements were conducted in the Heidelberg Aeolotron and the results were compared to the estimates derived from the statistical approach which was presented in Section 7.3.1. An example of the infrared image and the results of the analysis are presented in Figure 7.22**a** to 7.22**f**.

The mean wind direction in Figure 7.22**a** is from right to left. The pronounced streaks of cold water in the direction of the wind can clearly be seen. As has been outlined in Section 7.3.2, the model is fitted to the infrared data and thus scale the dimensionless variables from Equation (7.23)-(7.24). The first step of the analysis is to examine the temperature variation along a vertical column of pixels (perpendicular to the wind) as shown by the + symbols in Figure 7.22**b**. Next, local temperature maxima (red + symbols) and minima (blue + symbols) are identified, and each interval between a maximum point and a neighboring minimum point is defined as one eddy. For each eddy, the theoretical temperature variation curve of the eddy renewal model (green lines) is fitted in a least squares sense to estimate the bulk temperature below the eddy (red lines). Eddies consisting of 4 pixels or less tend to yield less accurate estimates of the bulk temperature and are excluded from this analysis.

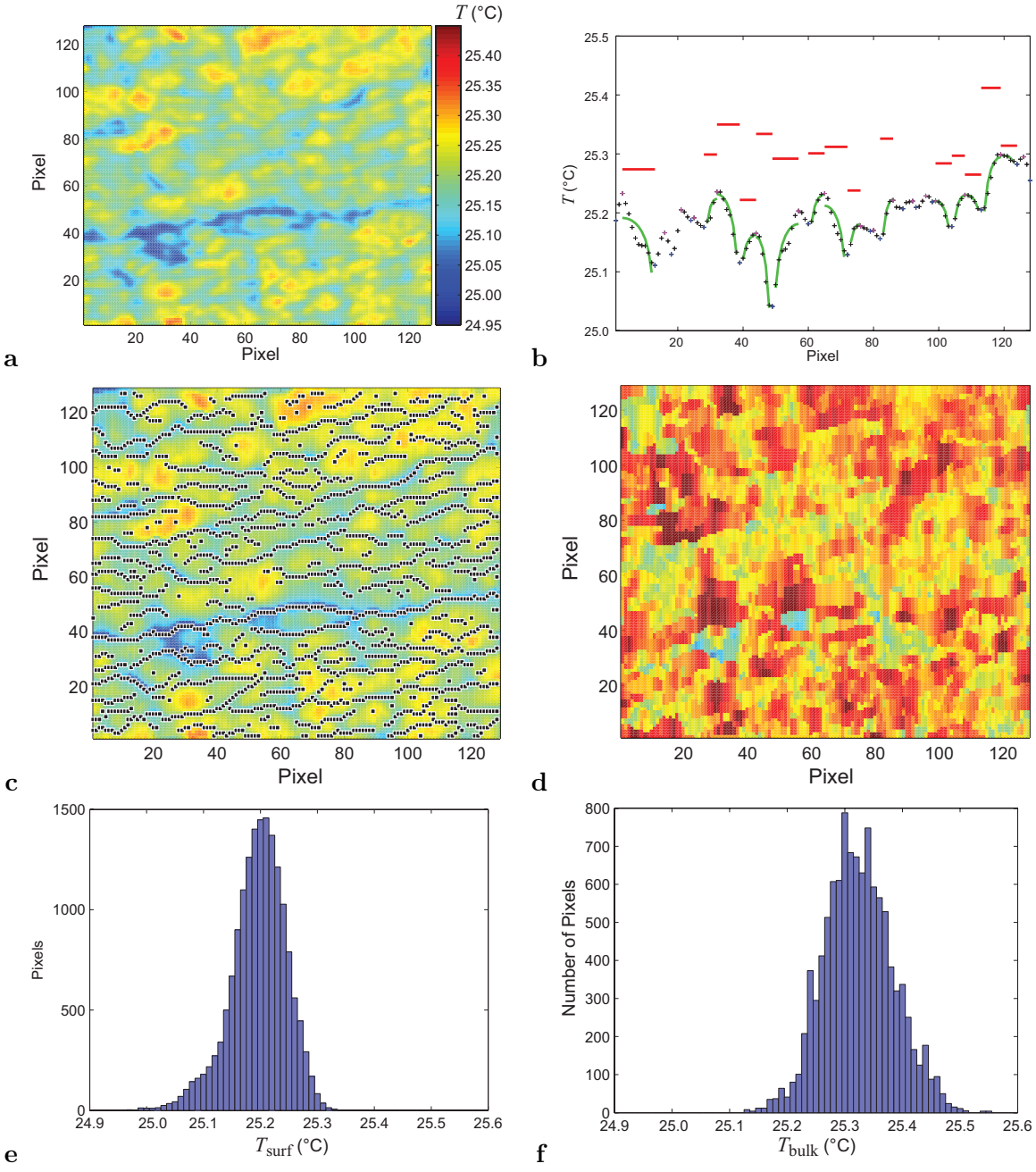

Figure 7.22: *Analysis of infrared image from AEOLOTRON wind wave tank.* ***a*** *Observed surface temperature distribution.* ***b*** *Observed surface temperature along a single column (+), local maxima (red +), local minima (blue +), fit to eddy renewal model (green line), and estimated bulk temperature (red line).* ***c*** *Modeled surface temperature distribution. Black pixels indicate local temperature minima corresponding to downwelling zones.* ***d*** *Estimated bulk temperature distribution.* ***e*** *Histogram of observed temperature.* ***f*** *Histogram of estimated bulk temperature.*

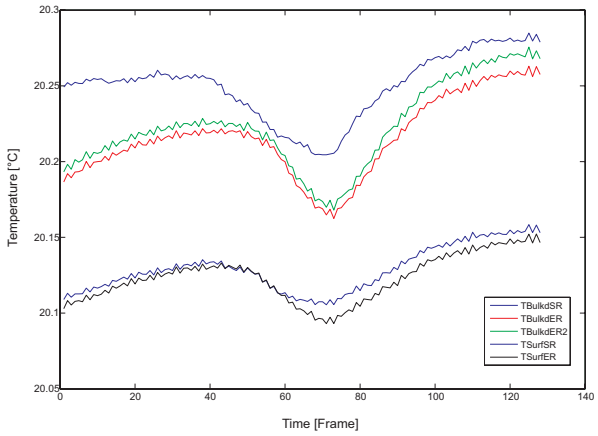

Figure 7.23: *A comparison of the eddy renewal model against the surface renewal model. The measurements of T_{bulk} and thus ΔT agree strikingly well between the two models.*

Since the eddy renewal model solution is not strictly valid at the downwelling location, the minimum temperature point within each eddy is not used in the fit. Figure 7.22**b** clearly shows that the local theoretical fit is generally consistent with the observed temperature profile, that is, both profiles show slow temperature variation near the maxima and rapid decrease towards the minima. The local estimate of the bulk temperature fluctuates, but it is consistently above the observed maximum temperature of each eddy.

After the same analysis is performed along all columns, the resulting fitted temperature field is shown in Figure 7.22**c**, in which the local minima are identified by black pixels. This method is able to identify cold streaks clearly because the locations of the temperature minima tend to vary slowly in the wind direction. This suggests that the near surface eddies are indeed elongated in the mean wind direction. The model also reproduces the observed temperature field very well. This can readily be seen by comparing Figure 7.22**a** and Figure 7.22**c**. The corresponding eddy by eddy estimates of the bulk temperature are presented in Figure 7.22**d**. Again, the variation from one column to the next is relatively small. The histogram of the observed temperature distribution and the histogram of the estimated bulk temperature exhibit similar overall variability as seen in Figure 7.22**e**and 7.22**f**. The mean of the observed bulk temperature is 25.32°C and the mean observed temperature is 25.23°C. If the surface renewal model is applied and the bulk temperature of this image is estimated from the distribution of the observed temperature using the method proposed in Garbe et al. [2004], the bulk temperature is estimated to be 25.33°C. This is almost identical to the estimate based on the eddy by eddy analysis with the eddy renewal model.

These results, based on Figure 7.22 were computed just from one frame. A long time series of these measurements is shown in Figure 7.23. It can be seen that the results of both the eddy renewal and surface renewal agree quite well. This is quite astonishing, since both are based on different assumptions. The surface renewal model is parameterized with the time τ since the instantaneous renewal event. This 1D model implies spatial homogeneity. Also, it

does not allow heat exchange during upwelling of water parcels. On the other hand, the eddy renewal model assumes that near surface eddies are stationary, uniform in the mean wind direction, and periodic in the cross wind direction, being consistent with the characteristics of the Langmuir turbulence. The model predicts surface temperature patterns with warm elongated patches bounded by cold streaks, both being parallel to the wind direction.

7.10.3 Measurements of Net Heat Flux and Transfer Velocity

The main purpose of the measurements conducted in the Heidelberg Aeolotron was to test the validity of proposed algorithms of estimating the net heat flux j_{heat} at the sea surface. In that respect the different techniques of estimating j_{heat} had to be compared to each other, as well as to a ground truth measure of the flux. Only through this analysis can the confidence bounds for the techniques be established as well as the limitations revealed. The results of these measurements were presented in Garbe et al. [2004].

Ground Truth of Net Heat Flux

The Heidelberg Aeolotron is equipped with a Prema™ 3040 high precision thermometer collecting data from eight calibrated PT100 sensors in the water body. The precision of this thermometer is specified to 0.001 K with an accuracy of measurements with the PT100 elements of 0.004 K [Prema, 2000]. Thus the temperature change of the bulk water can be measured, which is directly related to the net heat flux. The ground truth data for the heat flux j_{true} can be computed from Equation (7.40) and compared to the results estimated by the proposed algorithms.

From error propagation the accuracy of the ground truth is found to be

$$\frac{\sigma_{j_{\text{heat}}}}{j_{\text{heat}}} = \sqrt{\left(\frac{\sigma_h}{h}\right)^2 + \left(\frac{\sigma_{dT/dt}}{dT/dt}\right)^2}. \tag{7.85}$$

The temperature decline dT/dt is estimated from linear regression by fitting a line with intersect ($y = ax + b$) to the part of the data, where a constant heat flux is present. The fit can be performed to a relative accuracy of less than 1% and the measurement of the water height in the Aeolotron is performed with an acoustic measuring device, with a relative accuracy much better than that. The total relative accuracy of the net heat flux measured this way is thus equally better than 1%.

For an accuracy evaluation of the proposed algorithms only the net heat flux through the air-water boundary is of interest. The residual transport of heat through the walls of the facility are computed from Equation (7.40) during times devoid of an air-water interfacial heat flux. The flux measured this way was found to be below 0.48 Wm^{-2} during all experiments conducted. Fluxes of this magnitude are of the order of accuracy for the ground truth measurement and thus negligible. The values of j_{true} estimated from the technique introduced in this section are presented in Table 7.4.

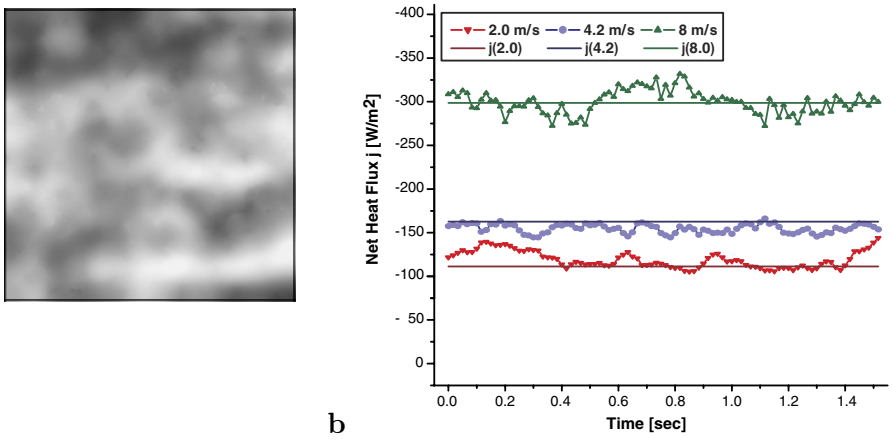

Figure 7.24: ***a*** *An image of the estimated net heat flux. Bright areas indicate strong fluxes [-130,-100] W/m^2.* ***b*** *The mean of the net heat flux computed from every frame for one sequence.*

Thermographic Measurements

Wind Speed	σ	m	t_* [s]
2.0 m/s	0.62 ± 0.02	1.65 ± 0.003	5.81 ± 0.05
4.2 m/s	0.61 ± 0.02	0.50 ± 0.02	1.82 ± 0.03
8.0 m/s	0.37 ± 0.02	-1.10 ± 0.09	0.34 ± 0.04

Table 7.3: *Results of the statistical analysis.*

Both the pdf method introduced in Section 7.7.1 and the square root method presented in Section 7.7.2 were used for computing the net heat flux in the experiments. As stated earlier the square root method is the preferred technique for it is not statistical in nature. Apart from making fewer assumptions on the nature of the heat transfer process, only this approach makes both spatially and temporal highly resolved estimates possible.

The pdf of times between surface renewal events was computed following Section 7.6. Under all conditions analyzed the estimated data followed the logarithmic normal distribution from Equation (7.16) very well. The parameters σ and m computed from the fit of the distribution to the data is presented in Table 7.3. Also shown in this table is t_* which can be computed from σ and m as presented in Equation (7.17).

The good agreement of the data with a log-normal distribution makes the approach of the pdf technique for estimating the net heat flux seem valid. The results obtained from the pdf method as compared to the ground truth net heat flux is thus another verification of this assumption. It is of course much more indirect than fitting the distribution to the data of τ as shown in Section 7.6.

Results of the square root technique are presented in Figure 7.24 for one image sequence and in Figure 7.25 for a measurement of 20 minutes. Shown is the high spatial resolution for j_{root} of less than 3 mm^2. The accuracy of the technique can also be seen in a sequence in which the mean heat flux estimated from individual images is shown and compared to the

ground truth heat flux j_{truth}. It should be noted that the temporal resolution is the frame rate of the infrared camera, which was 60 Hz in the measurements conducted in the Aeolotron. The fluctuations in the estimate are not due to errors but seem to be undulated due to waves passing through the imaged area.

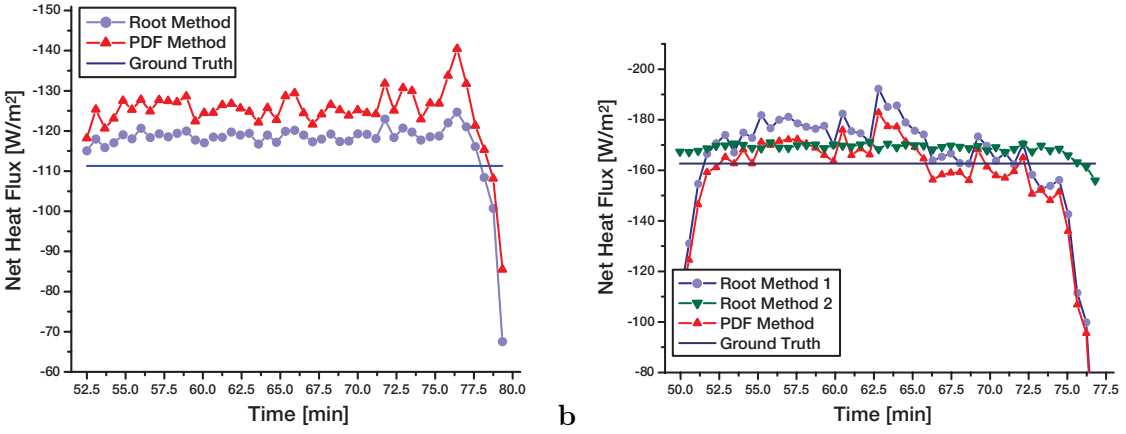

Figure 7.25: *Heat flux estimate for wind of 2 m/s in* **a** *and 4.2 m/s in* **b**. *Shown are the results from the pdf method* j_{pdf} *and the square root method* j_{root}, *as well as the ground truth value* j_{true}. *In* **b** j_{root} *was computed with the value of* ΔT *estimates from the corresponding sequence (method 1) and also with the same mean value* $\overline{\Delta T}$ *from all the sequences (method 2).*

Presented in Figure 7.25 is the resulting heat flux estimate during the time of low relative humidity in the Aeolotron. Shown are the heat fluxes computed from both the square root method and the pdf method, as well as the ground truth value. The values shown are means derived from 90 images. The sudden decrease in the heat flux at the end of the measurements is due to the air conditioning system being turned off, leading to a sharp rise in relative humidity, which in turn causes the heat flux to terminate.

Deviations in the estimate are largely due to fluctuations in the estimation of the temperature difference ΔT. This is evident from Figure 7.25 **b** where the heat flux was computed using the square root method with the estimated value for ΔT from every single sequence and with the mean value for ΔT from all the sequences. The estimate with the same value for ΔT hardly fluctuates at all.

In Table 7.4 the mean estimates of the net heat fluxes j_{root} and j_{pdf} for experiments at different wind speeds are presented. It is evident that both the estimates j_{root} and j_{pdf} are very close in accuracy. However, there seems to be a bias for the pdf method at low wind speeds towards higher values, whereas it seems to be closer to the ground truth j_{true} at higher wind speeds as compared to j_{root}. Overall both estimates seem to be closer to the true value in stronger winds than in the low wind speed case of 2 m/s. An explanation for this wind speed dependence is the applicability of the surface renewal model. In low wind speeds, the transport is driven by buoyancy while it is driven by shear in higher wind speed. Since the surface renewal model describes the shear driven transport better, the results are more accurate in this regime. This is even more true for the pdf method which not only assumes the surface renewal model but also a log-normal pdf. Hence the stronger bias of j_{pdf} in lower

wind speeds. Also, the effect of adventitious surface films in the Aeolotron become more dominant for low wind speeds. Again, these films lead to changes in the transport processes of heat, which are not modeled accurately by surface renewal. This influence of surface films and inaccuracies regarding the surface renewal model were also shown for the measurement of ΔT in Section 7.10.1.

Wind Speed	u_* [m/s]	ΔT [K]	j_{true} [Wm^{-2}]	j_{pdf} [Wm^{-2}]	j_{sqrt} [Wm^{-2}]	t_* [s]
2.0 m/s	0.23	0.140 ± 0.003	-111 ± 3	-124 ± 11	-118 ± 7	5.81 ± 0.05
4.2 m/s	0.66	0.100 ± 0.004	-163 ± 2	-162 ± 11	-165 ± 14	1.82 ± 0.03
8.0 m/s	1.45	0.053 ± 0.003	-304 ± 3	-273 ± 23	-280 ± 22	0.34 ± 0.04

Table 7.4: *Results of the heat flux measurements. Standard deviations of j_{root} and j_{pdf} were computed from fluctuations in the data while j_{true} was derived from the fit.*

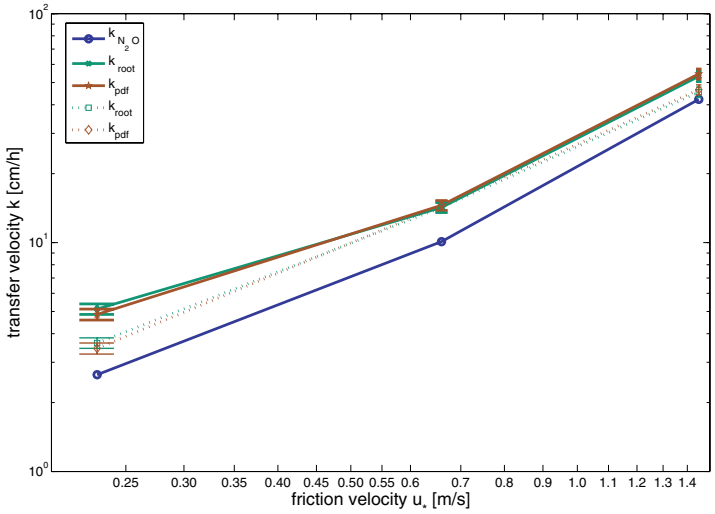

Figure 7.26: *The laboratory measurements of the heat transfer velocity k_{600} computed from k_{heat} and $k_{\text{N}_2\text{O}}$. The velocities are plotted against u_* in a log-log scale graph.*

Wind Speed	u_* [m/s]	k_{pdf} [cm/h]	k_{root} [cm/h]	$k_{600,\text{pdf}}$ [cm/h]	$k_{600,\text{root}}$ [cm/h]	$k_{600,\text{N}_2\text{O}}$ [cm/h]
2.0 m/s	0.23	76 ± 7	72 ± 4	3.64 ± 0.34	3.45 ± 0.19	2.65
4.2 m/s	0.66	139 ± 9	142 ± 12	14.24 ± 0.92	14.55 ± 1.23	10.09
8.0 m/s	1.45	443 ± 37	454 ± 36	45.38 ± 3.79	46.50 ± 3.69	42.23

Table 7.5: *Results of the heat transfer velocity k measurements. The Prandl number $Pr = 6.295$ and Schmidt number exponent $n = 0.5$ were used, except for the measurement of 2.0 m/s wind speed where $n = 2/3$ was employed.*

The heat transfer velocity was computed according to Equation (7.38). Thus, it is computed both spatially and temporally highly resolved. For comparison the transfer velocity for N_2O was measured from mass balance techniques [Nielsen, 2004]. For comparison the transfer velocities were scaled to a Schmidt number of $Sc = 600$ following Equation (7.2). The values

of the transfer velocities estimated for the different experiments are presented in Table 7.5. These estimated values are plotted against the friction velocity u_* in Figure 7.26.

It becomes apparent that the transfer velocities of heat are higher than the measurements for N_2O by a factor of roughly 30%. This discrepancy is higher than what is expected from the error analysis of the technique. In order to resolve this discrepancy, further measurements under a range of different wind and surfactant conditions are required and will be conducted in the future.

7.10.4 Laboratory Measurements of Viscous Stress from Active Thermography

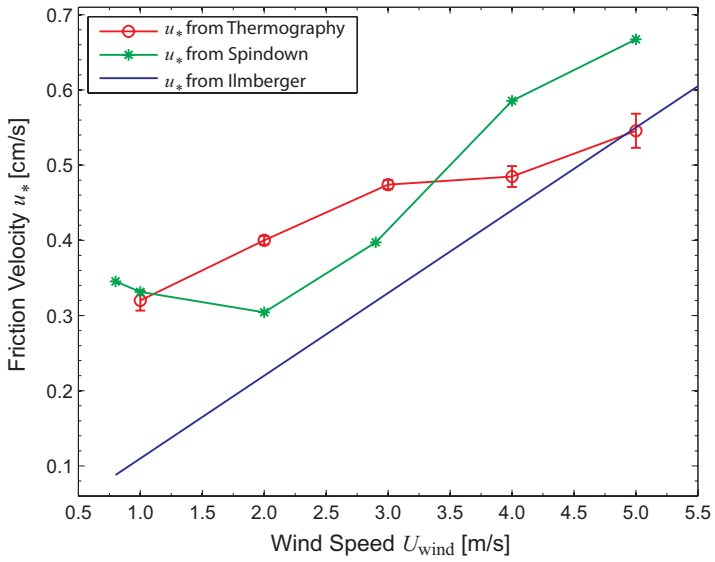

Figure 7.27: *Results for measurements conducted at the small wind wave facility in Heidelberg.*

The novel technique for estimating the viscous shear stress τ_μ from active thermography was also tested in a laboratory setting. In the small Heidelberg angular wind wave facility measurements were conducted on surfactant covered water. As a surfactant, stearic acid (octadecanoic acid, or $CH_3(CH_2)_{16}COOH$) was used. This insoluble surfactant was applied . Waves were suppressed due to the surfactant coverage. The reason for this setting is, that the form drag cannot be resolved with this technique. Comparison with independent measurements of τ are thus difficult to achieve in the presence of waves, because it is not known exactly how much of the shear stress is due to form drag. This uncertainty can thus be resolved by measuring on flat water surfaces. The wind speed range covered was from 1.0 m/s up to 5.0 m/s. At higher wind speeds, the surfactant would break up in certain areas and sporadic waves growth was visible. Measurements in this regime would thus have lead to bigger uncertainties in the independent measurement of τ.

Ground truth measurements of τ were achieved with the "spin down" technique. For this technique, flow velocity of the bulk is measured and at a known point in time the wind

generating force is turned off. From the following exponential decay of the bulk velocity, the drag of the walls can be computed. In the presence of wind, this drag is in equilibrium with the drag of the wind on the water body and hence the shear stress τ. More details concerning this technique can be found in Ilmberger [1980].

From the measurement of τ_μ the friction velocity $u_\star = \sqrt{\tau/\rho}$ can be computed. The results of these measurements is presented in Figure 7.27. Shown are the results of $u_\star$ from the novel technique based on active thermography, the results from the spin down technique and the results from a parameterization that was found by Ilmberger [1980]. It can clearly be seen that both the results from the spin down technique and from thermography are very close to each other. At low wind speed of 1 m/s both measurements agree within the error bars. The maximum discrepancy can be seen at 5 m/s where the measurements differ by as much as 10-15%. This is a bigger discrepancy than would be expected based on the error analysis in Section 7.8.3 or the measurements on synthetic data in Section 7.8.4. More measurements in different facilities are needed in order to better assess the accuracy of this technique. For this reason, currently a linear wind wave facility is being constructed. In such a facility, the shear stress can also be computed from determining the wind profile close to the boundary. This would thus present an alternative measurement of τ. Also, it should be noted that both measurements of $u_\star$ are both larger than the results of the parameterization. It should be noted that the parameterization was derived in a different wind wave facility. Therefore, it is not unlikely that the parameterization does not hold accurately in the facility in which the measurements were conducted.

7.11 In-Situ Measurements

The techniques presented in this work have been successfully employed in laboratory conditions. As shown in the previous section, in the Heidelberg Aeolotron a precise comparison of the estimated values for the net heat flux and other parameters to the actual fluxes was possible. In this section the applicability of the techniques for field use will be shown and some results of measurements conducted during the GasExII experiment will be presented. The data has been presented previously in Garbe et al. [2004].

7.11.1 Measurements of ΔT

ΔT from the surface renewal model

The statistical analysis introduced in Section 7.3 was used to estimate the temperature difference ΔT during the GasExII cruise. The values computed for T_{surf}, T_{bulk} and the corresponding ΔT can be seen in Figure 7.28 for one individual sequence. Also shown are the results of the estimation ΔT for a typical deployment. The results for the deployments on year day 52, 54, 58 and 59 are shown in Figure 7.29. The temperature difference estimated from meteorological data is also presented for the same deployment. It is a striking feature that the method of estimating ΔT from the infrared images is lower than the estimate from

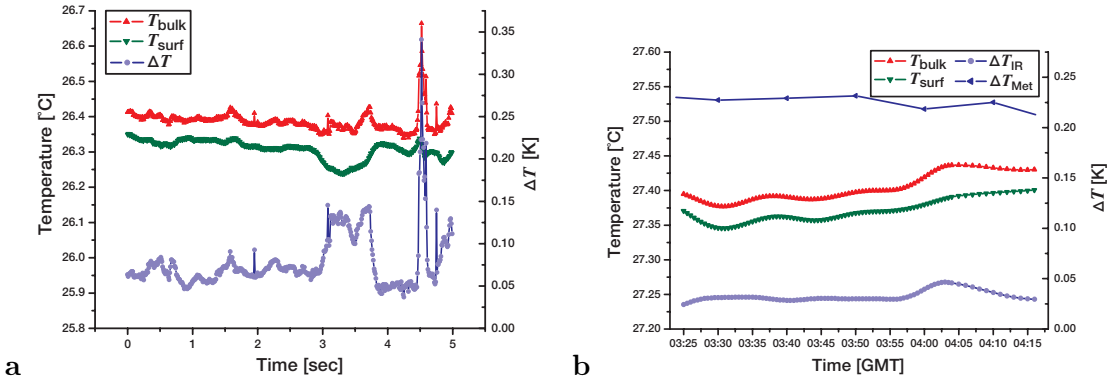

Figure 7.28: *The temperature of both the bulk T_{bulk} and surface T_{surf} as well as the temperature difference ΔT for typical deployment. In* ***a*** *the estimated values for one sequence is shown (year day 58, 2001). The whole data set for the whole deployment of year day 54, 2001 is shown in* ***b*** *where the values are compared to the ones derived from micro-meteorological measurements.*

the meteorological data by 0.1-0.2 K. This is of course a significant difference in the estimates.

It should be noted that the value for ΔT estimated from meteorological measurements has not been assessed directly from temperature measurements. Moreover it has been computed from bulk parameterization of Fairall et al. [1996a]. In a recent experiment Ward and Redfern [1999] measured ΔT directly and compared their findings to the predictions of different bulk parameterizations. They found discrepancies in the order of $0.05 - 0.2$ K with a standard deviation in between $0.079 - 0.098$ K and a bias ranging from $0.003 - 0.037$ K between prediction and measurement, depending on the parametrization.

The values for ΔT could not be compared to other measurements. The model is only applicable to nocturnal measurements meaning that LADAS was deployed shortly after sunset. Due to day time solar irradiation it is to be expected that a temperature stratification in the bulk of the water was present. Due to the diffusion process it will take the stratification in the bulk much longer to clear away than the processes in the thermal boundary layer. A comparison will need to be much better than 0.05K, which can hardly be achieved under stratified conditions, not even taking instrument cross calibration issues into account. In order to the analyze the discrepancy between the IR technique and current invasive measurements, further experiments are necessary.

ΔT from the eddy renewal model

In this section the eddy renewal model is applied to infrared images of acquired during the GasEx 2001 experiment. An example of the surface image (128×128 pixels corresponding to roughly 0.5 m by 0.5 m) is shown in Figure 7.31**a**. The mean wind goes from right to left and the image shows cold streaks that tend to be parallel to the wind. The first step of the analysis is to examine the temperature variation along a vertical column of pixels (perpendicular to the wind) as shown by the + symbols in Figure 7.31**b**. Next, local temperature maxima (red + symbols) and minima (blue + symbols) are identified, and each interval between a maximum

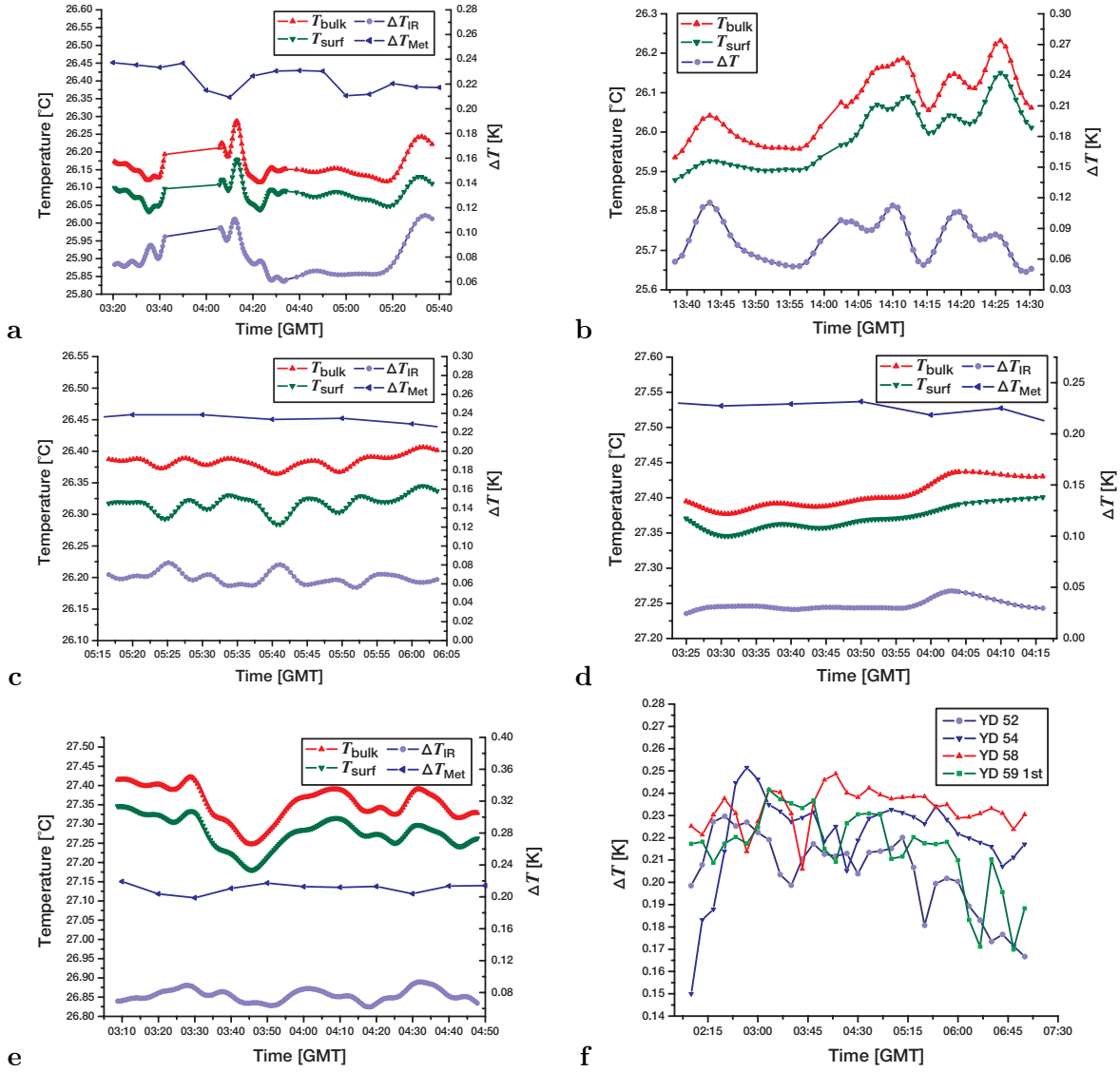

Figure 7.29: *The temperature of both the bulk T_{bulk} and surface T_{surf} as well as the temperature depression ΔT. From the deployments on on year day 59 in* ***a*** *and* ***b*** *respectively and from the deployments on year day 58, 54 and 52 in* ***c****,* ***d*** *and* ***e****, as well as the equivalent data obtained from Hare [2001] for the corresponding deployments in* ***f****.*

point and a neighboring minimum point is defined as one eddy. For each eddy, the theoretical temperature variation curve of the eddy renewal model (green lines) is fitted (with the least square error method) to estimate the bulk temperature below the eddy (red lines). Eddies consisting of 4 pixels or less tend to yield less accurate estimates of the bulk temperature and are excluded from this analysis. This represents the same analysis as the one conducted on laboratory data in Section 7.10.2.

Again, the minimum temperature point within each eddy is not used in the best fit analysis, since the solution from the eddy renewal model is not strictly valid at the downwelling location.

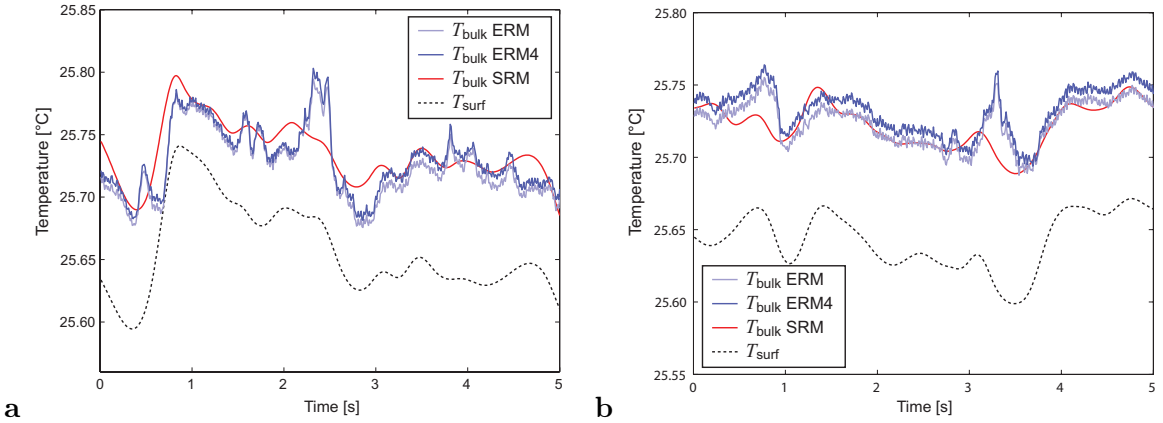

Figure 7.30: *Two different time series of measurements from the GasEx 2001 field data in* ***a*** *and* ***b****. The bulk temperature is computed with the surface renewal model (T_{bulk} SRM) and for the eddy renewal model (T_{bulk} ERM). (T_{bulk} ERM4) indicated that estimates with eddy sizes bigger than 4 pixel were considered.*

Figure 7.31**b** clearly shows that the local theoretical fit is generally consistent with the observed temperature profile, that is, both profiles show slow temperature variation near the maxima and rapid decrease towards the minima. The local estimate of the bulk temperature fluctuates but is consistently above the observed maximum temperature of each eddy.

The fitted temperature field for all columns is shown in Figure 7.31c, in which the local minima are identified by black pixels. As shown for laboratory data, the model reproduces the observed temperature field very well (compare Figure 7.31**a** and Figure 7.31**c**). The corresponding (eddy by eddy) estimates of the bulk temperature are presented in Figure 7.31**d**. Again, the variation from one column to the next is relatively small. The mean of the computed bulk temperature is 25.75°C and the mean observed temperature is 25.67°C. Using the surface renewal model, the bulk temperature can also be estimated from the method presented in Section 7.3.1. Here the bulk temperature is computed to be 25.74°C, which is almost identical to the estimate based on the eddy by eddy analysis with the eddy renewal model.

When the analysis based on the eddy renewal model is applied to a sequence of images, the variations of the mean surface temperature and the bulk temperature may be investigated as shown in Figure 7.30. Overall, the variation of the bulk temperature is very small (less than 0.05°C over 500 images corresponding to about 5 seconds). The bulk temperature estimates with the eddy renewal model (average of the estimates from eddy by eddy fit to the theoretical curve) are surprisingly close to the estimates with the surface renewal model using the method outlined in Section 7.3.1. Shown in Figure 7.30 are two time series as example. Virtually all sequences analyzed resulted in a similar picture that estimates from the surface renewal model and the eddy renewal model are almost identical. The estimates from the surface renewal model appear much smoother than the eddy renewal model. This is due to the fact that results were integrated for 5 frames in time. This leads to an smoothing of the results.

If smaller eddies (4 pixels or less) are included in the analysis, the eddy by eddy bulk temperature estimates show more scatter but the mean estimate per image remains very

similar to the estimate without smaller eddies, suggesting that this technique is not sensitive to filtering of small scale eddies.

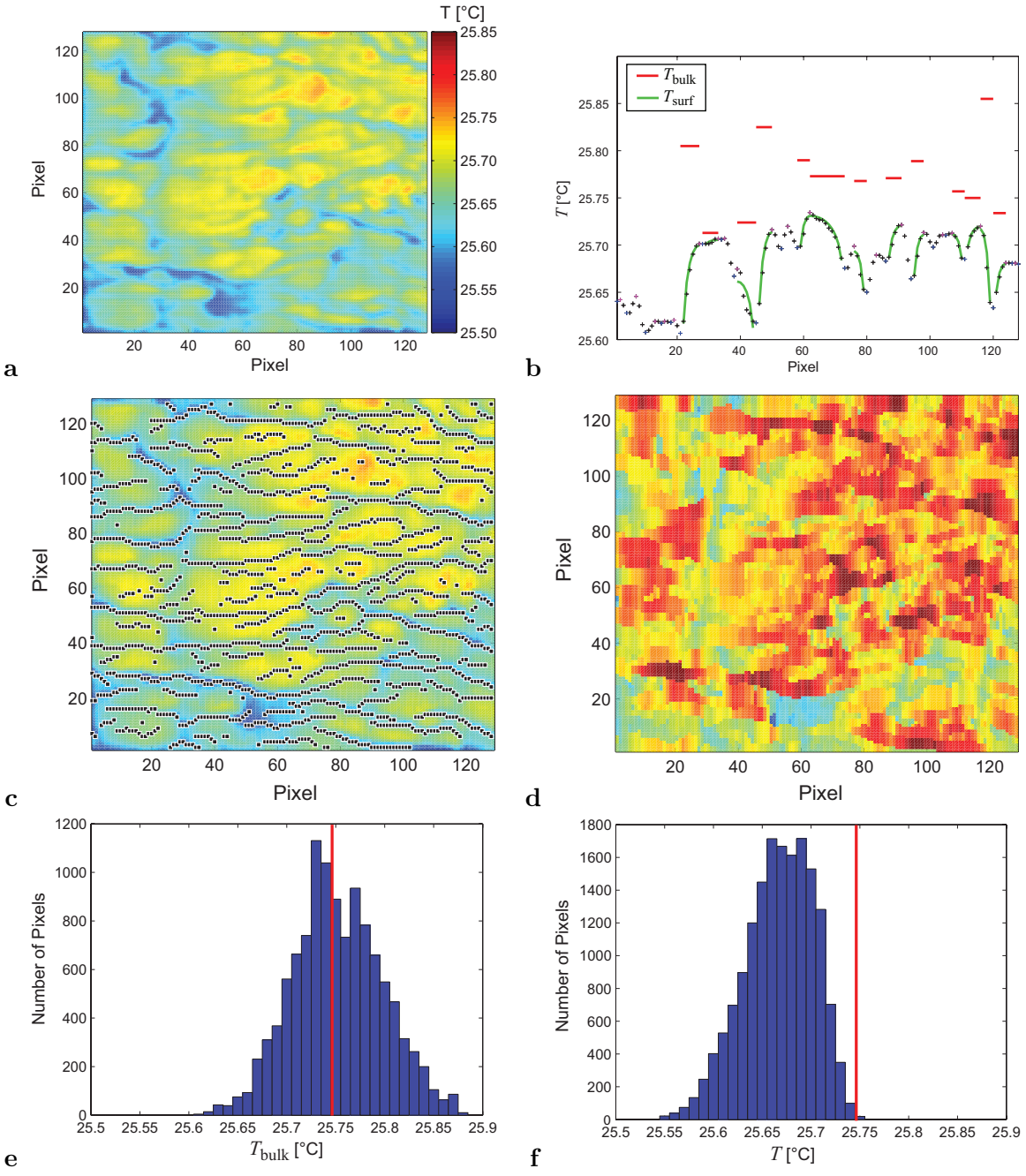

Figure 7.31: *Analysis of infrared image from GasEx 2001.* ***a*** *Observed surface temperature distribution.* ***b*** *Observed surface temperature along a single column (+), local maxima (red +), local minima (blue +), fit to eddy renewal model (green line), and estimated bulk temperature (red line).* ***c*** *Modeled surface temperature distribution. Black pixels indicate local temperature minima corresponding to downwelling zones.* ***d*** *Estimated bulk temperature distribution.* ***e*** *Histogram of observed temperature.* ***f*** *Histogram of estimated bulk temperature.*

7.11.2 Measurements of Net Heat Flux and Transfer Velocity

An important parameter for the model of surface renewal is the probability density function of times between consecutive surface renewal events. As has been presented in the previous section, the assumption of a log-normal pdf was supported in the laboratory measurements conducted. The findings were consistent with the field measurements, were no deviations from the log-normal pdf were detected. Minor deviations from this distribution were caused by images corrupted from reflections. The results for the parameters σ and m of the logarithmic normal distribution can be seen in Table 7.6.

The net heat flux was estimated from the techniques presented in Sections 7.7.1 and 7.7.2. The results for the heat flux at this high temporal resolution are presented in Figure 7.32. Here j_{root} for one image sequence is presented as well as for a whole deployment. Results for four deployments are presented in Table 7.7.

The main difference between the estimate based on j_{root} or j_{pdf} can thus be stated as the higher resolution of j_{root} as it is not statistically based. Also, since fewer assumptions are needed for its derivation, this method is clearly favored. Nevertheless it is interesting to compare the performance of both techniques under a variety of conditions. This represents another verification of the assumptions made in estimating j_{pdf}. If both techniques estimate the same value for the net heat flux it can be inferred indirectly that the probability density function $p(\tau)$ accurately models the statistical properties of the surface renewal process.

Meteorological measurements of heat fluxes from the eddy correlation technique were conducted on board the R/V Ronald H. Brown [Hare, 2001]. Apart from verifying consistent results of both estimates j_{root} and j_{pdf} to one another, the results were also compared to the estimates based on those meteorological techniques j_{met}. A typical deployment is shown in Figure 7.32. It can generally be stated that there exists a good agreement between the estimates. Within the margin of error, the agreement with the meteorologically derived heat flux estimates j_{met} seems to be quite good. Also there seems to be a slight correlation to the wind speed, as can be seen in Figure 7.32 **a**, where peaks in the heat flux are followed by peaks in the wind velocity. However, it should be noted that measurements of the meteorological data were conducted on the bow tower of the research vessel, whereas the techniques based on thermography were conducted on LADAS. Both were separated by about 100 m during the measurements.

From the measurements of the net heat flux the transfer velocities of heat can be computed according to Equation (7.1). In order to compare these results to those of different trace gases these transfer velocities of heat can be scaled to that of CO_2 at a temperature of 20°C (k_{600}). Here use is made of Equation (7.2). The results of these heat transfer measurements are presented in Table 7.8.

In Figure 7.33 estimates of the heat transfer velocity k_{heat} and the equivalent transfer velocity for CO_2 scaled to $Sc = 600$ are shown. The results were obtained during the CoOP 1995, CoOP 1997, GasEx 2001 experiments, and the from in the Heidelberg wind-wave facility are plotted versus water side friction velocity. These results have been published in Schimpf et al. [2004]. The results of the laboratory experiments are consistent with earlier measurements of

Year Day	Wind Speed	u_* [m/s]	σ	m	t_* [s]
52	5.23 m/s	0.199	0.51 ± 0.02	0.06 ± 0.06	1.08 ± 0.05
54	4.18 m/s	0.154	0.46 ± 0.02	-0.77 ± 0.02	0.49 ± 0.03
58	5.05 m/s	0.184	0.48 ± 0.02	-0.28 ± 0.02	0.83 ± 0.05
59	4.76 m/s	0.179	0.56 ± 0.02	0.67 ± 0.03	2.13 ± 0.04

Table 7.6: *Results of the statistical analysis of the renewal process.*

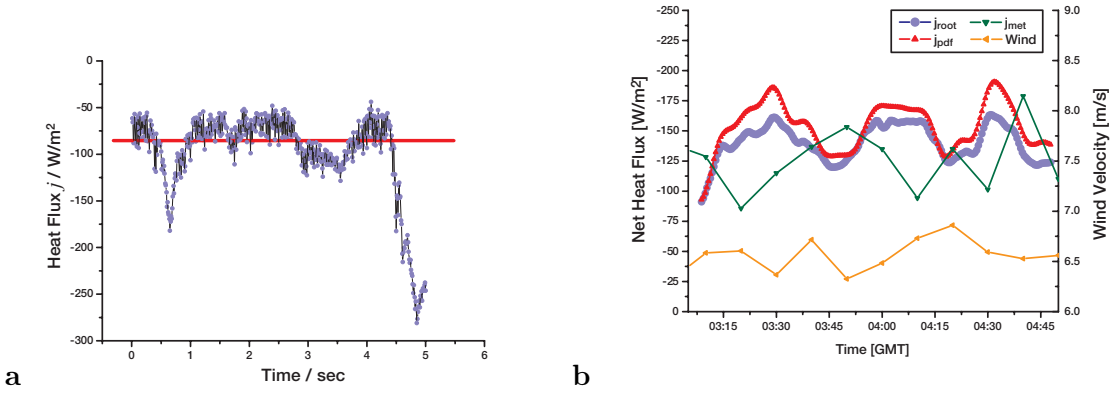

Figure 7.32: ***a*** *The estimated net heat flux for one sequence of year day 58, 2001.* ***b****The Flux estimate for the whole deployment of year day 52, 2001. Plotted are the estimates of* j_{root}, j_{pdf} *and the one derived from meteorological techniques,* j_{met}, *as well as the wind velocity.*

Jähne et al. [1987] utilizing classical mass balance methods (He, CH4, CO2 and Xe) and a laser induced fluorescence technique [Münsterer and Jähne, 1998] employed in the same facility. At a slick-covered interface, near-surface turbulence is suppressed and thus the transport process across the interface is not as effective as in case of a clean interface. The presence of a surface film reduces the heat transfer velocity at constant wind stress roughly by a factor of five in comparison to a clean interface. Gas exchange experiments performed in the same wind-wave tank utilizing systematic variations of wind stress and surfactant concentration showed also a strong inverse relationship between gas transfer velocity and enhanced wave damping caused by a surface film [Frew et al., 1995].

In Figure 7.34 the scaled transfer velocities ($Sc = 600$), obtained during the different field campaigns and in the wind-wave facility are plotted versus wind speed and compared with the

Year Day	Wind Speed	u_*	j_{met} [W/m^2]	j_{root} [W/m^2]	j_{pdf} [W/m^2]
52	5.23 m/s	0.199	-129.06	-141 ± 7	-145 ± 7
54	4.18 m/s	0.154	-116.60	-124 ± 6	-91 ± 5
58	5.05 m/s	0.184	-142.47	-143 ± 7	-154 ± 8
59	4.76 m/s	0.170	-119.65	-121 ± 6	-113 ± 6

Table 7.7: *Results of the GasExII net heat flux measurements. The errors of the meteorological estimates are not known.*

Year Day	Wind Speed	u_* [m/s]	$k_{600,\mathrm{root}}$ [cm/h]	$k_{600,\mathrm{pdf}}$ [cm/h]
52	5.23 m/s	0.199	18.08 ± 0.92	18.56 ± 0.95
54	4.18 m/s	0.154	38.28 ± 1.95	28.33 ± 1.45
58	5.05 m/s	0.184	20.18 ± 1.03	21.63 ± 1.10
59	4.76 m/s	0.170	14.03 ± 0.72	13.08 ± 0.67

Table 7.8: *The transfer velocities of heat, scaled to a Schmidt number of $Sc = 600$. Due to the interface conditions the Schmidt number exponent $n = 1/2$ was used.*

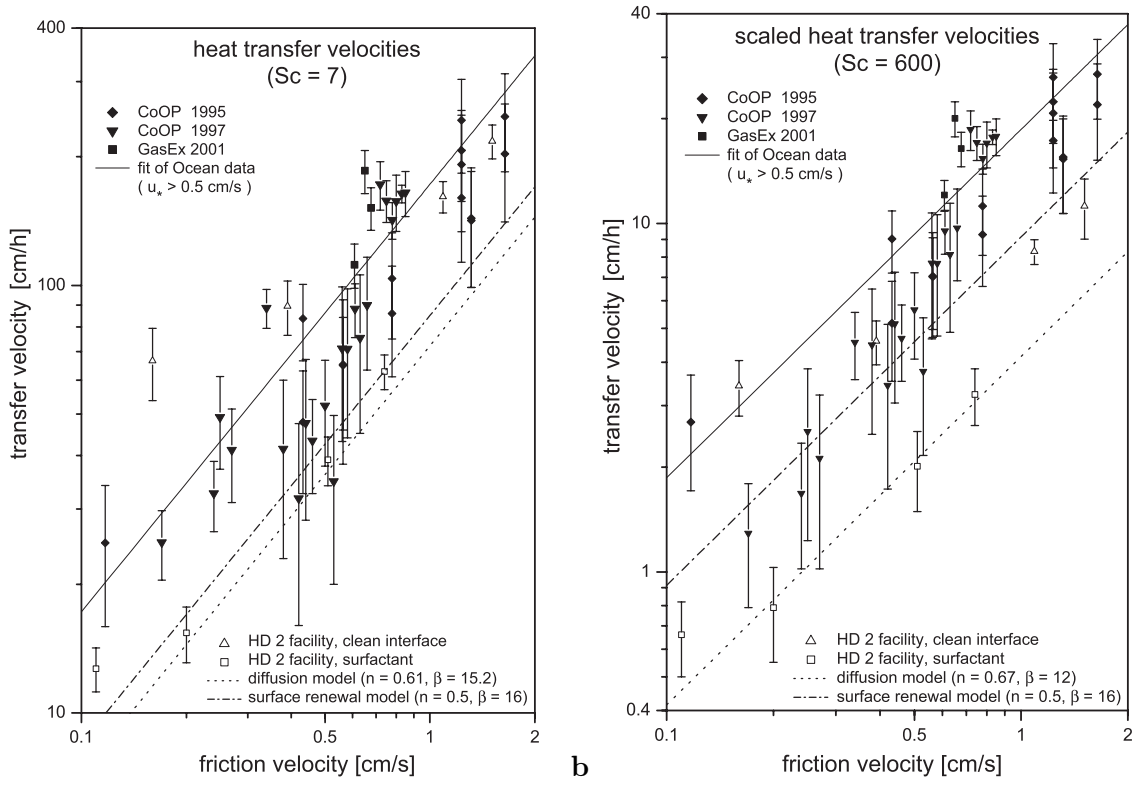

Figure 7.33: *Heat transfer and scaled transfer velocities during the CoOP 1995, CoOP 1997, and GasEx 2001 experiments and in the wind-wave facility plotted versus water side friction velocity. For comparison the theoretical approaches of Deacon [1977], Münnich and Flothmann [1975], and a fit of the field data for $u_\star > 0.5$ cm/s are shown [Schimpf et al., 2004].*

empirical relationships of Liss and Merlivat [1986], Wanninkhof [1992] and Wanninkhof and McGillis [1999]. For a clean interface, the increase of the scaled transfer velocities with wind speed is nonlinear and the values for low wind speeds (1.2 and 2.2 m/s) are outside the area defined by the above mentioned relationships between wind speed and gas transfer rate. This discrepancy might be due to a bias in the parameterizations. Recently, a modification was proposed by Zhang and Cai [2006]. They argue that at zero wind speed, the transfer velocity should not go to zero for a number of reasons. They assume a transfer velocity of about 5 cm/h in the absence of wind, based on the findings of McGillis et al. [2001b] and McGillis et al. [2004]. For a more detailed discussion, the reader is referred to Schimpf et al. [2004].

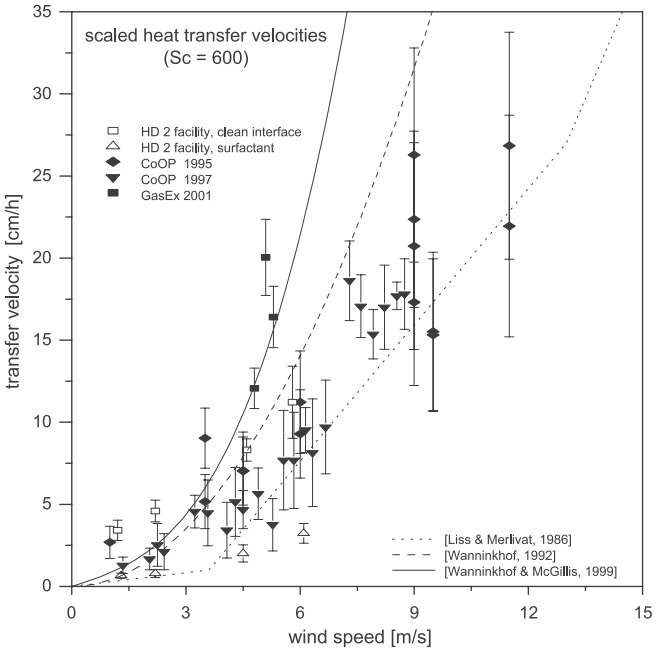

Figure 7.34: *Transfer velocities scaled to k600. Measurements conducted during the CoOP 1995, CoOP 1997, and GasEx 2001 experiments and in the Heidelberg wind-wave facility plotted versus wind speed. For comparison the empirical relationships of Liss and Merlivat [1986], Wanninkhof [1992], and Wanninkhof and McGillis [1999] are shown [Schimpf et al., 2004].*

7.12 Conclusions

In this chapter the application of using infrared thermography for research in air-sea interactions has been presented. One technique was shown to estimate the viscous shear stress τ_μ from active thermography. This technique extends the motion model of plane Couette flow from Chapter 2.7.1 to take Lambert Beer's law of absorption with depth into account. This leads to an accurate estimation of surface flows and an estimate of the sought shear stress. The technique was tested in the laboratory on a slick covered surface so that waves were suppressed. The difference to ground truth measurements was close to 10% for extreme cases. A modern, temporally higher resolved IR camera would certainly improve accuracy.

Apart from the viscous shear, two models of transport across the air-water interface were used to measure δT, the net heat flux j_{heat} and the transfer velocity of heat k_{heat}. These models were the well known surface renewal model and a newly developed eddy renewal model. Both models make complementary assumptions as far as temporal stationarity of spatial homogeneity are concerned. Surprisingly, the estimates of ΔT were almost identical under all conditions analyzed, both for laboratory measurements and for field data. For the net heat fluxes, estimates from the eddy renewal model were found to be higher by 6% as opposed to the surface renewal model.

An important quantity of the surface renewal model is the probability of surface renewals taking place. This probability is expressed by the probability density function of times in

between consecutive surface renewal events $p(\tau)$. Assuming this pdf to be log-normally distributed, an analytical function for the frequency data of the surface temperature at the sea surface T_{surf} was derived. Parameters of this analytical function are the bulk temperature T_{bulk} and the net heat flux j_{heat}, apart from the parameters describing the log-normal distribution. The excellent agreement of this analytical function fitted to the frequency data of T_{surf} can be seen as an indirect verification of the assumption made in deriving this function. This assumption is the surface renewal model with the probability of surface renewal events to be distributed log-normally. Apart from verifying this assumption through the fit, the bulk temperature T_{bulk} can be gained from the distribution of the sea surface temperatures. This technique was examined on synthetic data and perform an error analysis of estimating T_{bulk} under varying noise levels of the input data. For the noise levels of current IR cameras the accuracy of retrieving the bulk temperature is found to be 3mK. Schimpf et al. [2004] verified these findings in laboratory measurements.

From modern digital image sequence analysis, the total derivative of the sea surface temperature with respect to time can be estimated. From this total derivative the time of residence of a water parcel at the sea surface τ is computed at every pixel of the infrared image sequence. Analyzing the frequency data of τ gives a direct verification of the pdf. It can be shown that a log-normal distribution describes this frequency data very well. From a fit of the log-normal distribution to the frequency data, its parameters σ and m can be gained. Assuming the proposed surface renewal model with the log-normal pdf, an expression of the net heat flux j_{pdf} is derived. With this formulation j_{pdf} can be computed from the parameters σ an m. This net heat flux j_{heat} is compared to the accurately known net heat flux under laboratory conditions. The excellent agreement of the measured flux poses another indirect verification of the surface renewal model together with its log-normally distributed pdf. Making no assumption concerning the pdf of surface renewal, another expression for the net heat flux j_{root} is derived, based on the model of surface renewal alone. From this expression the net heat flux can be estimated from thermal infrared image sequences at the frame rate of the IR imager at pixel resolution. This allows for accurate, both temporally and spatially highly resolved heat flux measurements. Results of measurements with a spatial resolution of 1.5×1.5 mm^2 and a temporal resolution of 10ms at a relative error of 5% are presented. Measurements both under laboratory and field conditions are shown. Results of the transfer velocity are compared to those of N_2O under laboratory conditions. A discrepancy of 30% was detected, the reason for which has to be addressed in future experiments.

All of this demonstrates that the presented surface renewal model with a log-normal pdf is a good approximation of the transport of heat through the sea surface interface. The model produces consistent results for the estimation of different parameters of ocean-atmosphere heat transfer. The results are also applicable for the transfer of gas. This is due to Schmidt number scaling, from which the transfer velocity of mass can be deduced from the transfer velocity of heat. The presented model together with its application to infrared thermography is an interesting tool for analyzing the effect of waves, bubbles, rain and surfactants on the transfer of heat and mass.

A new model of the near surface turbulence and resulting air-water heat transfer has been

developed to explain infrared images of air-water interfaces under low to moderate winds. The model (called an eddy renewal model) assumes that near surface eddies are stationary, uniform in the mean wind direction, and periodic in the cross wind direction, being consistent with the characteristics of the Langmuir turbulence. The model predicts surface temperature patterns with warm elongated patches bounded by cold streaks, both being parallel to the wind direction. When the model is applied to real infrared images from field and laboratory experiments, it identifies cold streaks and reproduces surface temperature distribution very well. The model yields bulk temperature estimates over each eddy. The bulk temperature estimates averaged over individual infrared images are very close to the estimates based on the surface renewal model using the method of Garbe et al. [2004].

Chapter 8

Microfluidics

8.1 Introduction

Many high-performance separation techniques rely on flow of fluids through microchannels. Applications range from high-pressure liquid chromatography [Desmet et al., 2006], capillary zone electrophoresis [Jorgenson and Lukacs, 1983], and capillary electrokinetic chromatography [Terabe, 1989]. Technological progress in manufacturing microfluid components has lead to a spread of novel systems into diverse applications [Avram et al., 2006; Burns and Ramshaw, 2001; Nguyen and Wereley, 2006; Wang, 2000; Eijkel and van den Berg, 2005]. In chemical and biochemical analytics, as well as in medical diagnostics, these novel devices can be used to speed up the analysis while only relying on minute probe volumes. This is due to the huge surface to volume ratio achievable by micro channels. In the future, microfluidic applications will increase in significance for chemical production processes. Here, boundary conditions can be controlled much more accurately and set accordingly. This leads to better controllable and thus more efficient reaction kinetics with less by-products. Current research is very active in microfluidic lab-on-a-chip applications [Stone et al., 2004; Burns and Ramshaw, 2001], which are already hailed as a revolution in biological and medical sciences [Figeys and Pinto, 2000].

This increase of interest in microfluidic devices directly leads to the need for diagnostic tools for the visualization, analysis of flow structures, mixture formation and reaction behavior directly inside the micro channels [Sinton, 2004]. More complex microfabricated fluid systems raise new issues of optimal fluid control, minimization of dead volumes, and enhancing or retarding scalar mixing. Here, non destructive image-driven methods are preferable for various reasons.

Several different attempts have been made to image flows through microchannels. Basically, two approaches have emerged:

- *micro particle imaging velocimetry* (μPIV)
- *molecular tagging velocimetry* (MTV)

Taylor and Yeung [1993] where among the first to measure microchannel flow with particles. They seeded the flow with fluorescent latex microspheres. The motion was deduced from streaks obtained by illuminating the particles with continuous wave (cw) laser light for approximately 1 s. One major drawback Taylor and Yeung [1993] encountered with this technique of using dielectric particles as a tracer in electrokinetic liquid flows is the distinction between electroosmotic and electrophoretic forces acting on the particles. Furthermore, the local field gradients and fluid forces generated by polarizable or charged particles in a strong electric field also effect the motion of the tracer. Taylor and Yeung [1993] measured a small velocity deviation in the center of the capillary which they attributed to particle-induced viscous drag on the flow. Also, when using particle tracers, conditions in which there is a substantial velocity gradient across these particle have to be avoided. Otherwise, shear will lead to secondary motion due to the Magnus effect. This prerequisite often leads to extremely small tracers. Such submicrometer particles essentially precludes the use of elastic scattering and requires the use of fluorescent particles to achieve sufficient signal strength [Taylor and Yeung, 1993]. There are a number of applications, where particles are prohibitive. For example, the flow through systems with a dense internal geometry such as packed columns cannot be measured in this way, since these particles will be effectively filtered out of the fluid. Another problem of the technique presented by Taylor and Yeung [1993] is that the velocity was computed from the imaged streaks. This turned out to be limiting in terms of quantitative measurements as far as accuracy was concerned. Santiago et al. [1998] presented a μPIV technique that estimates motion from cross-correlation, similar to standard PIV techniques. This significantly increased accuracy and usability. Santiago et al. [1998] utilized an epifluorescent microscope, 100-300 nm diameter seed particles, and an intensified CCD camera to record high-resolution particle-image fields. A spatial resolution of $6.9 \times 6.9 \times 1.5$ μm was attainable. This technique was further improved by Olsen and Adrian [2000] who conducted diffusion measurements from μPIV. The diffusion is computed from a broadening of the correlation peak. A similar technique was used by Hohreiter et al. [2002] as a means of measuring temperature in microfluidic flows. Here the diffusion caused by temperature due to Brownian motion [Brown, 1828; Einstein, 1905] is estimated from the correlation peak.

In order to avoid disadvantages associated with using particles for visualizing microfluidic flows, different dyes have been used as markers. These were applied into the capillaries as either a constant stream or as a plug of dye [Taylor and Yeung, 1993; Kuhr et al., 1993; Tsuda et al., 1993]. Uses of dyes as tracer are widespread with applications ranging from imaging of flow through gel-filled packed columns [Fujimoto et al., 1996] to open microchannel systems. Such techniques have also been applied to study flows through micromachined channels on planar substrates and to evaluate different injection schemes for on-chip analysis and valveless pumping. Past implementations of this velocimetry approach include the use of photochromic molecules (LIPA [Falco and Chu, 1988; Chu et al., 1993]), excited-state oxygen fluorescence (RELIEF, [Miles et al., 1987], specially engineered water-soluble phosphorescent molecules [Koochesfahani et al., 1993], and caged fluorescein (PHANTOMM, [Lempert et al., 1995]). The scales on which measurements can be conducted range widely. Paul et al. [1998] have

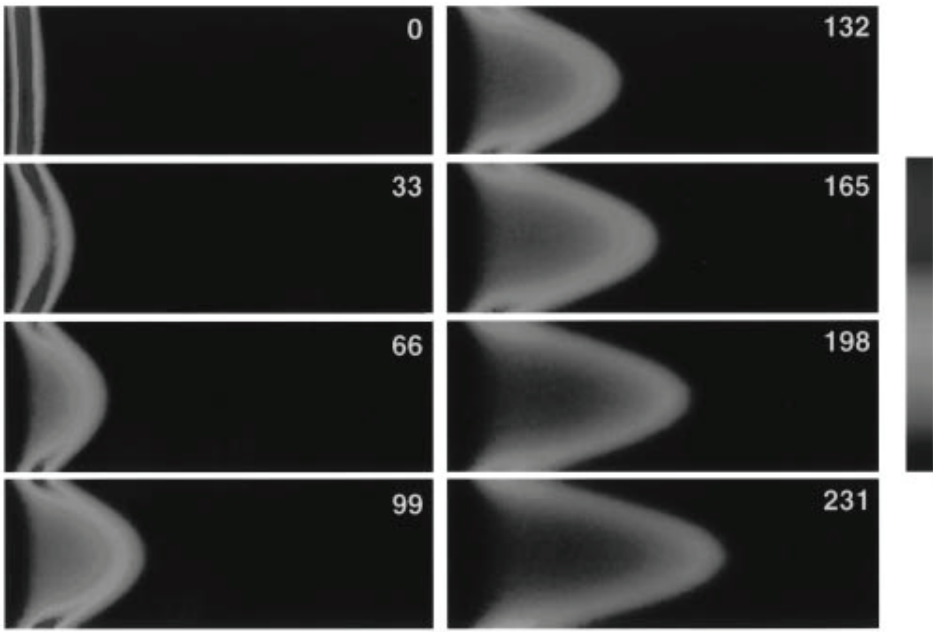

Figure 8.1: *Images of pressure-driven flow through an open 100 μm i.d. fused-silica capillary using a caged fluorescein dextran dye. The frames are numbered in ms as measured from the uncaging event. Taken from Paul et al. [1998].*

obtained quantitative velocity contours in pressure and electrokinetically driven flow through open capillaries of the order of 100 μm in diameter. Images of these measurements can be seen in Figure 8.1. On larger scales, Dussaud et al. [1998] utilized caged dyes to visualize the spreading of involatile and volatile surface films on water of a 16 cm diameter tank filled with a solution of caged fluorescein. Falco and Nocera [1993] and more recently Lempert and Harris [2000] compiled a review of efforts to measure flow velocities using molecular tagging. Laser line tagging is used in the works of Miles et al. [1987], Lempert et al. [1995] and Lempert and Harris [2000]. In these techniques a line is written to the fluid and the velocity is inferred from the displacement of the line centers. Due to the inherent aperture problem of such a pattern, only velocities normal to the pattern can be measured and no information can be found in the tangential direction. [Hill and Klewicki, 1996] analyzed implications of measuring with such a pattern. They then extended the line tagging technique to the use of a grid for marking the fluid [Hill and Klewicki, 1996]. Motion is estimated by locating the grid line centers using various techniques. The accuracy of this approach has been reported by Hill and Klewicki [1996] to be ≈ 0.35 pixel RMS. Gendrich and Koochesfahani [1996] and Gendrich et al. [1997] improved accuracy and implementation by estimation motion of the grid tagged fluid from spatial correlation. This algorithm is similar to that employed for PIV techniques.

One significant problem of the MTV techniques is that through the imaging process integration takes place along one dimension. This leads to a "smearing" of structures due to integration through depth. This problem could of course be solved by visualizing the struc-

tures with a laser sheet. This is often not feasible given the small dimensions of microfluidics. The effect can be seen in Figure 8.1, where dye is present in areas of the parabolic flow profile where it is not expected. This effect is commonly known as Taylor dispersion [Taylor, 1954]. Moreover, molecular diffusion leads to additional smearing of the structures. These effects lead to inaccuracies in the techniques used previously.

In this chapter, a novel technique of estimating microfluidic flow from MTV will be introduced. The effect of diffusion and Taylor dispersion are explicitly modeled in the underlying motion model. This makes it feasible to measure velocities very accurately in the presence of these processes. The technique was first described by Garbe et al. [2006] and more detailed in Garbe et al. [2008]. Measurements were presented by Roetmann et al. [2006] and in Roetmann et al. [2008].

This chapter is organized as follows: In Section 8.2 the effect of Taylor dispersion will be shown and the equation of motion resulting from the visualization process will be presented. The experimental setup will be detailed in Section 8.3. The technique of estimation motion with the underlying motion model will be explained in 8.4. Results of the technique will be presented both on simulated and ground truth data in Section 8.5. This chapter concludes with Section 8.6.

8.2 Taylor Dispersion

Taylor dispersion is an effect well known in microfluidics [Taylor, 1954]. A solute substance appears to be dispersed along the flow volume. This effect can be seen in Figure 8.1, where time steps of the spread of a marker in a flow through a capillary is shown. Due to the projection in visualizing the flow, the marker appears to diffuse into the region behind the leading front, deformed by the parabolic flow profile. This deformation leads to different effects due to molecular diffusion orthogonal to the dominant flow direction [Beard, 2001]. In a number of microfluidic flows, one tries to minimize the effect of Taylor dispersion. This is achieved by channel geometry and by driving the fluid electrokinetically by electrophoresis or electroosmosis. Despite these efforts, a pressure gradient and hence Taylor dispersion can never be avoided completely [Dutta and Leighton, 2001]. Due to Taylor dispersion, previous techniques for estimating microfluidic flows from MTV encountered a number of difficulties, resulting in suboptimal performance. To solve this problem, in this section an equation of motion is derived which explicitly models Taylor dispersion.

A viscous fluid driven by a pressure gradient in between two stationary plates is also known as Poiseuille flow in the case of purely laminar flows. In the present application of microfluidic flows, the Reynolds number Re is in the range of $10 < Re < 100$. This makes it safe to assume that the flow can be described by the laminar flow of a Newtonian fluid. The velocity profile of a Poiseuille flow is given as [Kundu, 1990]

$$v(y) = \frac{a}{2}y^2 - a \cdot b \cdot y \quad \text{with} \quad a = \frac{1}{\mu}\frac{dP}{dx},\ \frac{dP}{dx} \leq 0, \tag{8.1}$$

where $2b$ is the separation of the stationary plates, μ is the viscosity of the fluid and dP/dx is the pressure gradient along the direction of the flow. Taylor dispersion results from the fact, that an initial marker distribution is advected from this velocity profile. Subsequent imaging measurement techniques acquire a two-dimensional projection of this profile. This leads to an integration of the tracer with depth. The equation of motion for this type of configuration was derived in Section 2.7.2. The resulting motion constraint equation is given from Equation (2.76) to

$$\frac{dI}{dt} = d^\top \cdot p = \begin{bmatrix} \frac{1}{2t}I & \frac{\partial I}{\partial x} & \frac{\partial I}{\partial y} & \frac{\partial I}{\partial t} \end{bmatrix} \cdot \begin{bmatrix} 1 & u_1 & u_2 & 1 \end{bmatrix}^\top = 0, \tag{8.2}$$

where t is the time since uncaging the dyes.

Apart from Taylor dispersion, molecular diffusion is a dominant process in micfrofluidic flow visualization. This is due to the extremely small dimensions of the fluidic flows. The motion model for diffusion processes was derived in Section 2.5.4, resulting in Equation (2.30). Combining the model of Taylor dispersion and molecular diffusion leads to the following motion constraint equation

$$\frac{dI}{dt} = d^\top \cdot p = \begin{bmatrix} \frac{1}{2t}I & -\left(\frac{\partial^2 I}{\partial x^2} + \frac{\partial^2 I}{\partial y^2}\right) & \frac{\partial I}{\partial x} & \frac{\partial I}{\partial y} & \frac{\partial I}{\partial t} \end{bmatrix} \cdot \begin{bmatrix} 1 & D & u_1 & u_2 & 1 \end{bmatrix}^\top = 0. \tag{8.3}$$

Here D represents the diffusivity constant. It should be noted, that here only a two-dimensional, isotropic diffusion is assumed. This implies that diffusion with depth is taken to be negligible. It is obvious that this assumption is an oversimplification, since gradients with respect to z can be quite substantial in a parabolic flow profile. This is especially the case for long times t relative to the mean velocity of the fluid. Since $\partial^2 I/\partial z^2$ cannot be measured directly, explicit assumptions concerning the initial intensity distribution have to be made in order to derive a closed form expression. The resulting equations are difficult to manage, even with these limiting assumptions. As will be shown later, the technique presented here is most suitable for short times t since uncaging the dyes. Therefore, inaccuracies due to the assumption of two-dimensional diffusion are negligible.

8.3 Experimental Set-Up

The technique of measuring flow velocities of microfluidic flows presented in this work relies on caged dyes as markers of the flow. The tagging of the fluid is made possible through photo-chemical changes in the dye molecules [Roetmann et al., 2005, 2006]. To start off with, the ability of fluorescence is deactivated by an additional functional group. These dyes are therefore also known as *caged dyes* [Gee et al., 2001]. This functional group can be broken up by intensive UV light. The original, fluorescent dye is thus present following the exposure with UV light. This exposure can be achieved with a pulsed XeF Excimer Laser (COMPex 150, Lambda Physik AG) at a wavelength of $\lambda_{XeF} = 351\text{nm}$, which has to be spatially homogeneously widened. Through an image forming optical system arbitrary two dimensional patterns can be written to fluid using a structured mask. A range of different patterns used are shown in Figure 8.3. The pattern can be optimized depending on the flow velocity and

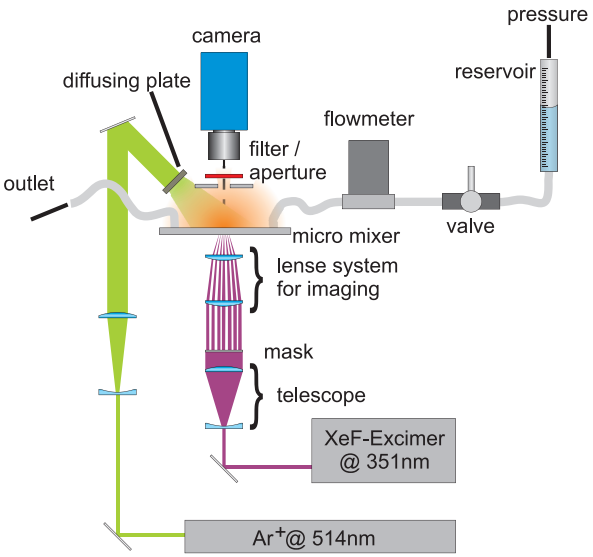

Figure 8.2: *A sketch of the experimantal set-up of measuring micro-fluidic flows with caged dyes.*

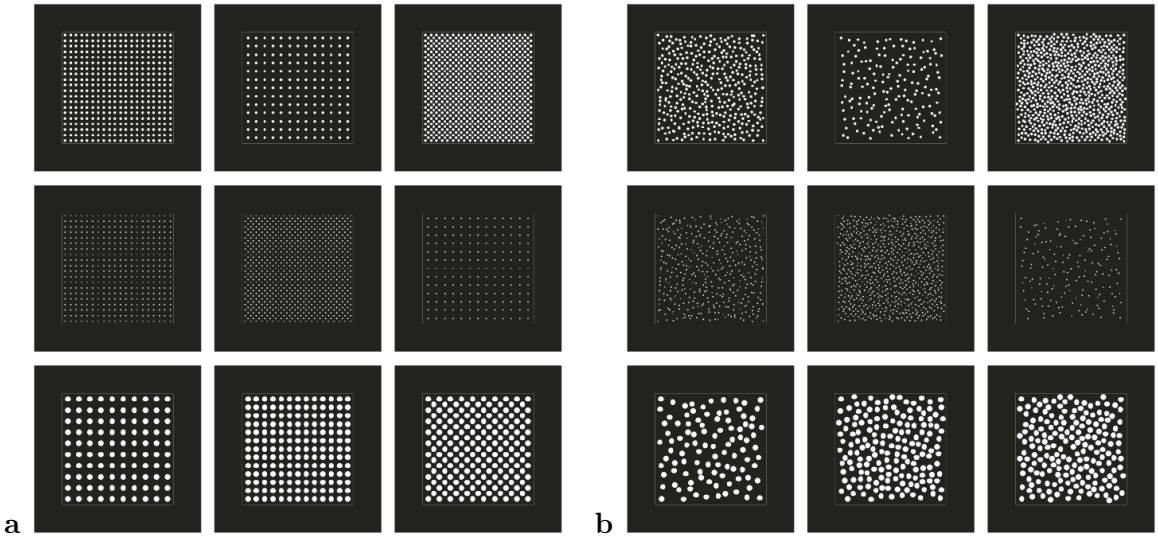

Figure 8.3: *Different mask used for writing intensity structures into the fluid.*

on the properties of the flow to be inspected. Generally, bigger structures with further spacing in between are used for fast fluid flows and long measurement times. Smaller structures with little spacing deliver higher spatial resolution but are only viable for smaller velocities or shorter measurement time, as will be detailed later. A pulse energy of 200mJ is used for a complete illumination of a 40x40mm2 mask with a well defined transmission pattern. The patterns of dyes in the fluid are visualized with a second laser which is spatially homogeneously widened. The fluorescence is excited with an Argon Ionic Laser (Ar^+) (Innova 310, Coherent) with a wavelength of $\lambda_{Ar^+} = 514$nm. The patterns in the fluid can be recorded temporally and spatially highly resolved with a standard CCD camera (Imager Compact QE, LaVision).

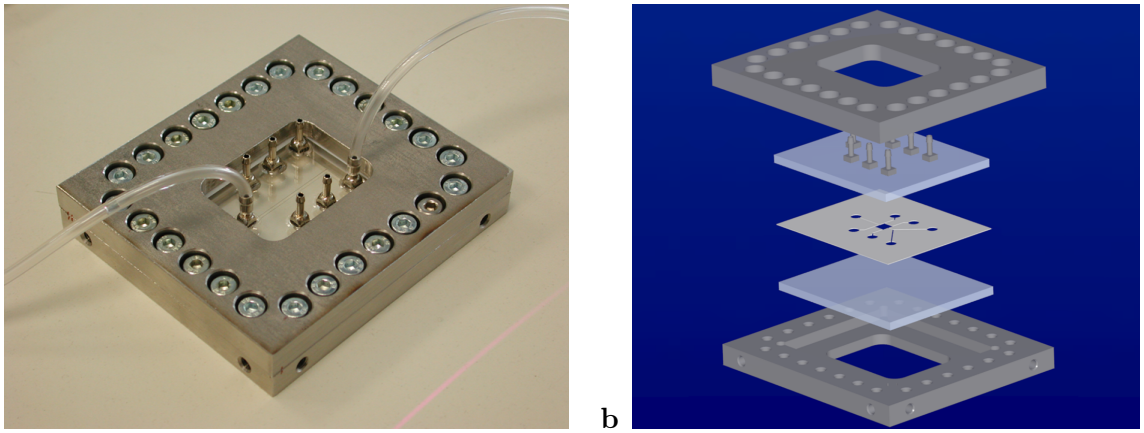

Figure 8.4: *The microfluidic mixing chamber.*

Fluorescence of the uncaged dyes is stimulated with continuous integral illumination from the Ar^+ Laser. Interfering excitation light is suppressed by an optical bandpass filter (OG570, Schott) and an aperture. A flow meter (SLG 1430, Sensirion) is recording the flow rates synchronously to the image acquisition as reference. The fluid being used was demineralized water with a low concentration (500mg/l) of the dissolved caged dye. This general set-up is sketched in Figure 8.2.

The microfluidic flows are measured in a specially prepared camber. The top and bottom boundary are constructed from quartz glass which is highly transparent in the visible and UV spectrum. Two glass plates are separated by $2d = 250\mu m$ with a metal plate. The width and depth of the chamber is 5×5 mm. Different flow geometries can be realized from channels in the metal plate. These channels are connected two an array of 7 plugs which can be used for driving the flow with individual pressures and volume throughputs [Roetmann et al., 2005]. A picture of the chamber together with an exploded drawing is presented in Figure 8.4.

The set-up and visualization process lead to the following procedure: at time $t_0 = 0$ the intensity structures are written into the fluid with the XeF Laser. The fluid inside the chamber is accessible non-invasively only through the glass plates on top and bottom of the Poiseuille flow. The beam of the laser writing the structured to the flow thus traverses through the whole depth of the fluid. A circular dot in the mask written to the fluid will thus appear as a cylinder in the flow structure. In later times, this 3D cylinder is sheared by the paraboloid velocity profile developed by the Poiseuille flow. These transformed 3D Structures are projected onto the CCD chip of the imaging device. Great care is taken to align the camera orthogonal to the glass plate. Through this projection, it appears as if the structure, written to the fluid, is smeared in the direction of the fluid flow over time. This process can be modeled from Taylor dispersion using Equation (8.3) taking isotropic diffusion also into account. Images of such recordings for two flow configurations are shown in Figure 8.5.

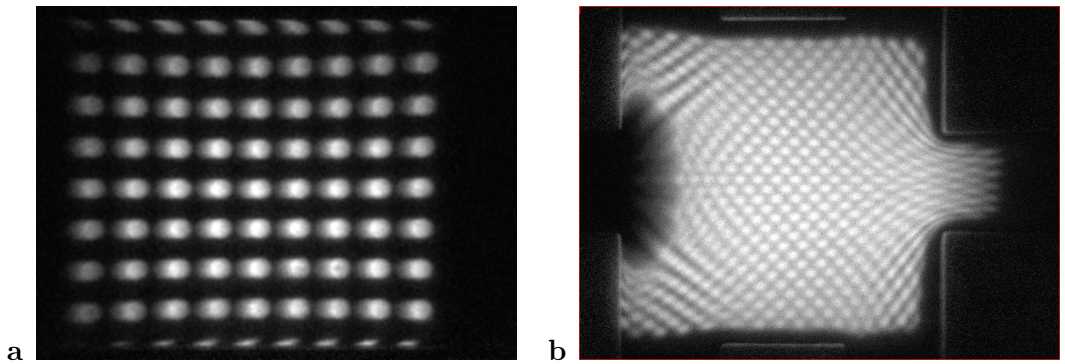

Figure 8.5: *A typical pattern written into a very simple microfluidic flow for calibration purposes in* ***a*** *and an inhomogeneous flow in* ***b****.*

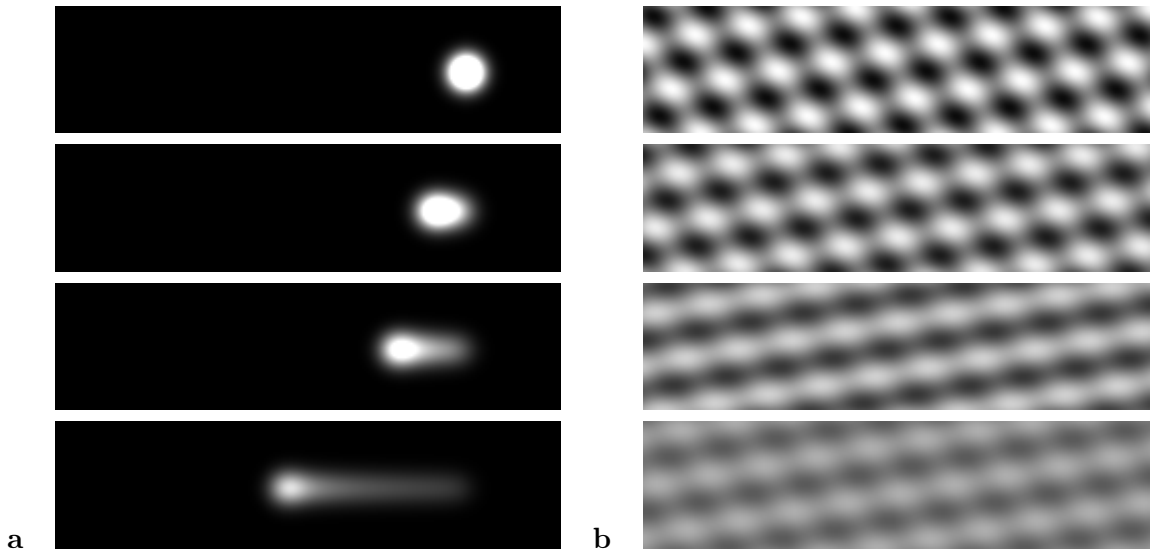

Figure 8.6: *Synthetic test sequences used for evaluating the proposed technique. In* ***a*** *a Gaussian pattern is written to the fluid and transformed according to Taylor dispersion. Shown in* ***b*** *is the same for a 2D sinusoidal pattern. Flow motion directed from right to left along x-axis. For each test sequence frame 1, 30, 60 and 150 are displayed. For display purposes frame 1 and 30 of* ***a*** *are scaled to overflow to be able to visualize all frames with the same gray value scaling.*

8.4 Motion Estimation

The motion constraint equation derived for microfluidic flow with Taylor dispersion and isotropic diffusion is given by Equation (8.3). This equation represents an ill-posed problem in the sense of Hadamard [1902]. In order to estimate the model parameters, additional constraints are necessary. These constraints can be constancy of parameters on a very local support in the sense of Lucas and Kanade [1981] or global smoothness as proposed by Horn and Schunk [1981]. The problem of estimating microfluidic motion can thus be estimated in a local framework as Garbe et al. [2003b] with robust extension presented by Garbe and Jähne [2001]. This local approach of motion estimation can be embedded in a global variational

approach as shown by Spies and Garbe [2002] and Spies et al. [2003]. A possible alternative is using a combined local global approach as proposed by Bruhn et al. [2005] which has been extended to brightness change models by Kondermann et al. [2007]. These approaches have been presented in Chapter 3.

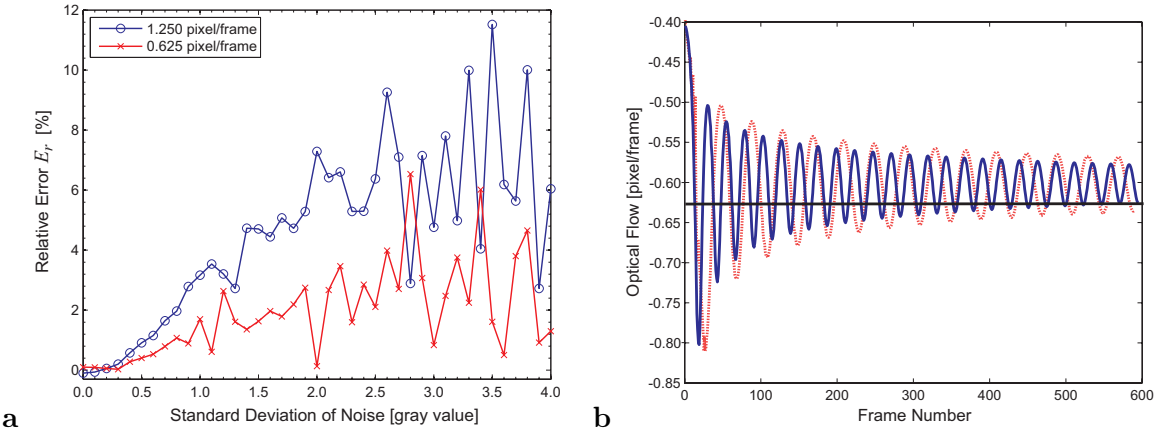

Figure 8.7: ***a*** *Relative error for the Gaussian test sequences with two different velocities ($u_1 = 0.625$ pixel/frame and $u_2 = 1.25$ pixel/frame) and varying noise levels.* ***b*** *Velocity of sine test sequences. It is readily observed that the velocity undulates due to interferences of the sine pattern. These fluctuations are shown for two test patterns of different frequencies. The true velocity is $u = 0.625$ pixel/frame.*

For the performance analysis presented here, dense flow fields are not of utmost importance. Therefore, only a total least squares (TLS) approach, also known as structure tensor approach [Bigün and Granlund, 1987; Bigün et al., 1991], was chosen here. It should be noted that accuracy could be improved by employing a more elaborate approach at the cost of additional computing complexity. The structure tensor was introduced in detail in Section 3.3 and will no be explained here. Because information can only be retrieved at locations where a dye is present, a mask was computed by thresholding the gray-value of the images. Instead of performing the integration of the structure tensor with a Gaussian smoothing filter, a normalized convolution was performed with this mask [Knutsson and Westin, 1993; Granlund and Knutsson, 1995]. This resulted in much better estimates as compared to standard smoothing. The reason is that wrong information (no motion) from areas without any dye diffuses into regions of dye concentration in the case of a normal convolution. This leads to a falsification and inaccurate estimates. The normalized convolution weights the smoothing with a certainty, which can be set to zero for areas without any dye. This leads to a more accurate estimation of motion.

8.5 Results

In order to test the presented algorithm, test measurements were performed. First, the basic applicability was tested on synthetic sequences. Here, a Gaussian uncaged dye distribution was modeled and transformed due to Taylor dispersion. Frame at different times of this test

pattern is displayed in Figure 8.6. This test pattern was corrupted with normally distributed noise of varying standard deviation. Also different flow velocities were simulated. The results of these measurements are presented in Figure 8.7**a**. The noise of current standard cameras are usually better than 0.9 gray-values. This means that the relative error to be expected is less than 2%. It should also be noted that the velocity computed is that of the center layer in between the two plates. This corresponds to the maximum velocity of the profile. In subsequent analyses, this maximum velocity $v_{\max}$ will be compared to ground truth.

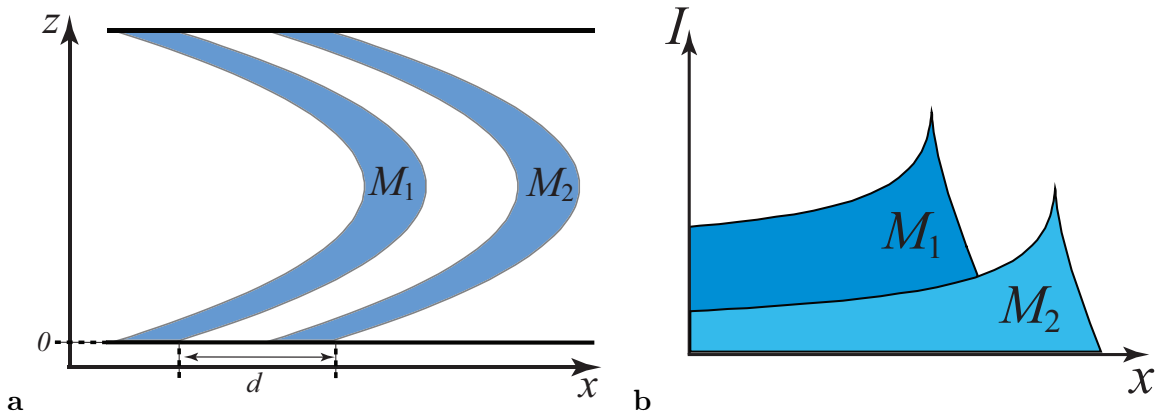

Figure 8.8: *Sketch of the effect of structure overlapping. In* **a** *the marked areas are transformed due to the parabolic flow profile. Two such structures separated by d overlap after time $t = d/v$. In* **b** *the corresponding projected intensities can be seen.*

In a second experiment on simulated data, the same measurements as with the Gaussian distribution were performed with two 2D sinusoidal patterns of different wavenumbers. The outcome of these measurements is presented in Figure 8.7**b**. It can be seen that the measured velocity oscillates around the true value with a slight bias to slow estimates. This is due to the fact that on "uncaged dye structures" overlap. For the sinusoidal pattern this happens almost immediately. The effect is sketched in Figure 8.8. It can be seen that after a time $t = d/v_{\max}$ the structures begin to overlap, where d is the initial distance between structures and $v_{\max}$ the maximum velocity in the center plane between the two plates. It can be seen from the projected intensities that the the intensity of the latter structure increases due to the added intensity of the former structure. This means that the intensity change is not correctly modeled by the presented approach. In order to correctly estimate motion under these circumstances, an extension to the motion model has to be found. This will be an area of future research. Currently, this technique is limited to cases where no such overlap is possible. This means that the measurement time $t = d/v_{\max}$ has to be short enough. This is achieved by choosing the correct spacing d depending on the maximum expected velocity $v_{\max}$.

Apart from measurements on simulated data, the technique was also tested on real world measurements with ground truth. For these measurements a simple geometry of the chamber was chosen. A purely laminar and parallel flow was adjusted to a number of different volume throughputs. One frame from such a sequence is shown in Figure 8.5**a**. These flow was measured accurately with a flow meter (SLG 1430, Sensirion). From the knowledge of the

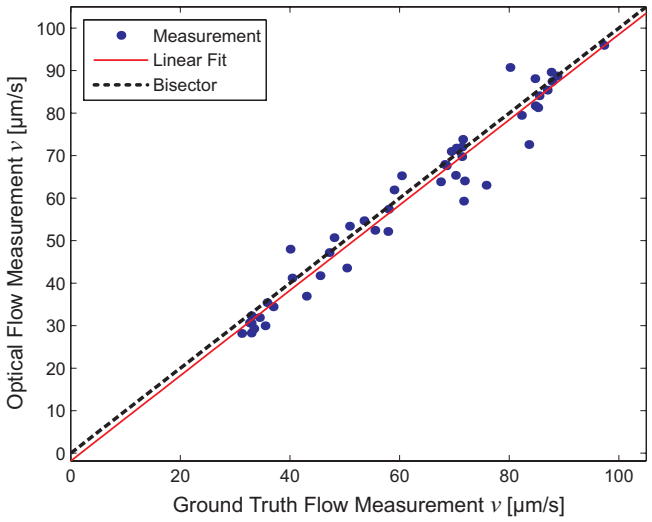

Figure 8.9: *Comparison of measured values compared to ground truth measurement. The measured values are plotted against the ground truth. A line with intersect ($y = a \cdot x + b$) was fitted to the data resulting in $a = 1.0029$ and $b = -1.8\mu m/s$.*

geometry of the chamber, the centerline velocity $v_{\max}$ was computed.

The results for the $n = 48$ conducted measurements is shown in Figure 8.9. Plotted are the results of optical flow measurements against the ground truth. For an ideal measurement, all data points are expected to lie on the bisect. This is almost perfectly true for the fitted linear curve. The slope of the fit is $a = 1.0029$ and the offset is $-1.8\mu m/s$. This slight bias of $2\mu m/s$ could well be due to uncertainties in the mixer geometry. The scatter in the data was found to be a little less than 5%. One significant problem in the present set-up were quite strong fluctuations in the read-out laser. The presented algorithm is based on spatio-temporal gradients of the fluorescence of the uncaged dyes. Fluctuations of these intensities due to the read-out laser will thus effect results of the computation. Due to the spatially inhomogeneous fluctuations, they could not be completely suppressed with an appropriate processing of the data. Hence, with a more stabilized set-up, results could be significantly improved.

The measurements performed on the simple, homogeneous pattern is very far removed from demands of applications. Therefore, measurements were also performed on inhomogeneous flows. An image from such a flow is presented in Figure 8.5**b**. The algorithm performed very well on these measurements. Results are presented in Figure 8.10. The qualitative picture corresponds very well to what is expected from this type of flow. A zoomed in view of the flow field estimated at one of the point is shown in Figure 8.10**a**. Quantitative comparisons cannot be made due to the lack of ground truth.

8.6 Conclusion

In this chapter, a novel technique was presented for measuring microfluidic flows with a molecular tagging velocimetry (MTV). In contrast to current techniques, this method explicitly

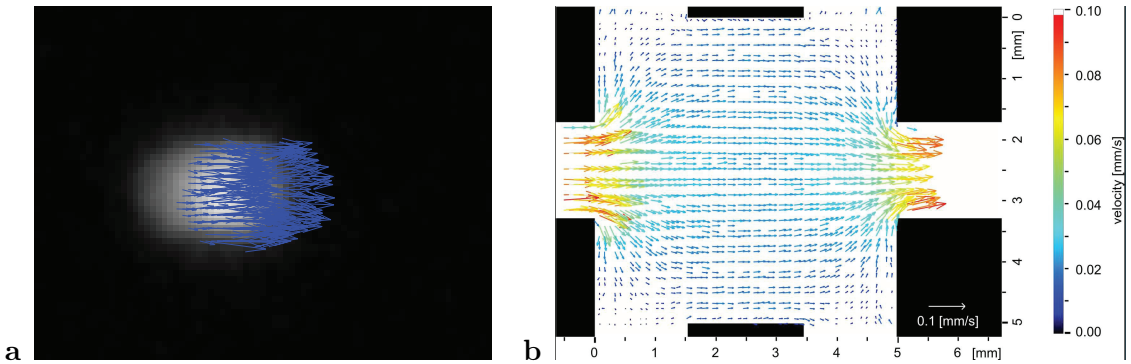

Figure 8.10: *Zoomed in view of the vector field around one of the dots written to the fluid is shown in* ***a****. The mean vector field of the mixing chamber can be seen in* ***b****.*

models Taylor dispersion [Taylor, 1954] and computes the motion parameters from an optical flow technique. Only though modeling this dispersion effect are accurate measurements feasible. Isotropic diffusion is estimated concurrently with the motion models. This might make it possible to measure temperature spatially resolved in microfluidic flow. This is subject of ongoing research.

The performance of the new technique was tested on synthetic test sequences that were corrupted by varying noise. Furthermore, ground truth measurements were conducted on a microfluidic channel with square geometry. This allowed to compare results of the motion estimation with actual flow through the mixer. In these measurements an excellent agreement in between measurement and ground truth was found. The scatter in the data was less than 5%. This scatter was in large parts due to intensity fluctuations in the read-out laser. The accuracy of the presented technique could be significantly improved by using a better stabilized read-out laser. First measurements on divergent flow geometries were also performed. The results were in excellent agreement with the expected flow field, underlining the applicability of the novel algorithm to more complex flow geometries.

Chapter 9

Botanical Transport Processes

9.1 Introduction

The passage of plants from water to land has necessitated the development of internal mechanisms to supply all the parts of the plant with water. Plants have developed complex vascular systems that move nutrients and water throughout the vascular tissues with xylem and phloem specialized in long distance transport. The xylem of vascular plants forms tunnels of dead cells through which water and minerals move upward from the roots, where they are taken in, to the rest of the plant. The phloem, which is made up of living cells, carries the products of photosynthesis (organic nutrients) from the leaves to the other parts [Lough and Lucas, 2006]. A microscopic picture of a cross section of the xylem and phloem in a plant leaf is shown in Figure 9.1. Terrestrial plants developed a complex control mechanism for water transport from the roots to the leaves [Gollan et al., 1992; Schurr et al., 1992]. Intercellular openings, stomatal pores, formed by two kidney-shaped cells, the guard cells, play a crucial role in controlling the gas fluxes from and into the leaf in order to optimize CO_2 uptake and to minimize water loss [Farquhar and Sharkey, 1982]. The transpiratory water loss creates a pressure difference that is a driving force for water transport in xylem according to the cohesion-tension theory as postulated over 100 years ago [Böhm, 1893]. For a number of physiological questions is the knowledge of transport velocities of basic interest [Sack and Holbrook, 2006]. Additionally, the rate of response of these transport processes to rapid changes of environmental conditions such as light, temperature and humidity is crucial to many aspects of plant metabolism, yet poorly understood because of the lack of appropriate measuring techniques.

A well known approach of measuring xylem sap flows in plant stems is based on the heat pulse velocity technique [Swanson, 1975]. This technique has been significantly improved in accuracy over the years [Avirav et al., 1990] but still retains one of it major drawbacks: it is an invasive technique that provides point measurements only. This drawback has been addressed with novel nuclear magnetic resonance imaging (NMRi) methods [Köckenberger et al., 1997; Scheenen et al., 2000; Peuke et al., 2001] at the expense of experimental ease and accessibility. Also, while providing a high spatial resolution, microscopic NMRi is not well suited for measuring extended areas such as a whole plant leaf. Hence a novel non-invasive

imaging technique was developed for measuring the water transport in plant leaves.

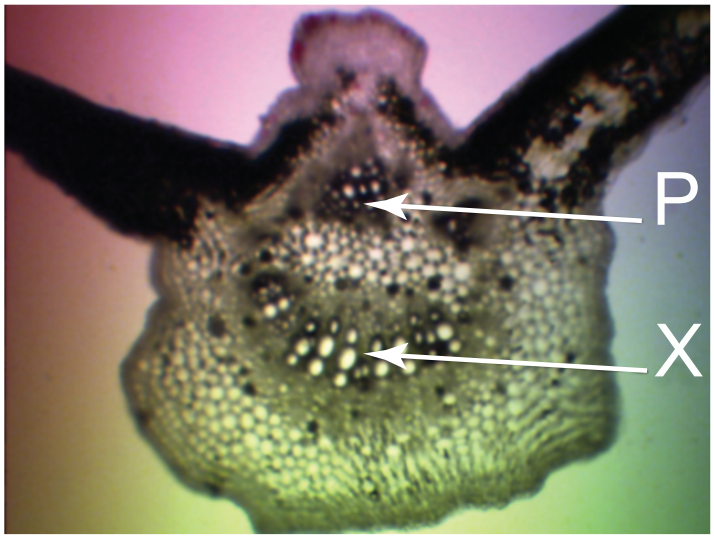

Figure 9.1: *A microscopic cross section of a* Ricinus communis *leaf. "P" indicates the phloem cells and "X" the xylem cells.*

Thermographic measurements have been applied to a number of scientific fields for an unobtrusive measurement of physical parameters to a high spatial and temporal resolution. However, this technique has been rarely applied in plant sciences, mainly to examine dynamics of stomatal behavior [West et al., 2005]. Also, previously, the water content of leaves and transpiration rates have been measured from thermographic techniques by Garbe et al. [2002d], Garbe et al. [2002c] and Garbe et al. [2003a]. While the transpiration rates can be computed from measuring the differential signal of leaf temperature to a non-transpiring reference body, measuring the water content from active thermography is very similar to the well known approach of lock-in thermography [Busse et al., 1992; Wu et al., 1996; Wu and Busse, 1996; Bendada et al., 2005; Meola et al., 2006]. Since only limited amount of modeling is involved in these techniques and motion is not computed from the results, these methods will not be presented in this theses. The interested reader is referred to the relevant publications. Topic of the thermographic technique presented in this thesis will be the estimation of flow velocities within the xylem of plant leaves. The main results will be presented in Garbe et al. [2007c]. The goal of the presented techniques is

1. to verify the termographic techniques in a defined artificial capillary system,
2. to test the techniques on detached *Ricinus communis* mid-vains with ground truth and,
3. to apply thermographic imaging techniques to measure flux velocities of intact attached leaves under various evaporative demand.

This chapter is organized as follows: In Section 9.2 the motion model of fluid flow in the xylem is motivated and derived. The experimental set-up employed during subsequent measurements is detailed in Section 9.3. The novel technique was verified in Section 9.4 where

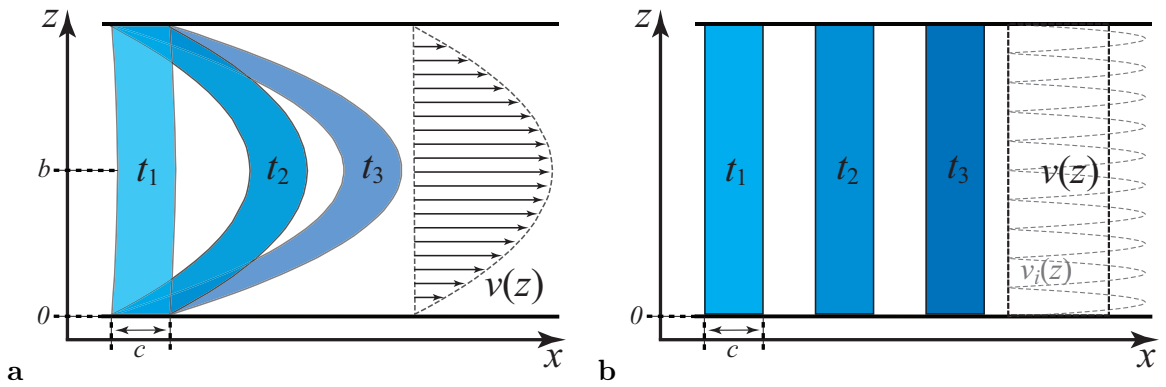

Figure 9.2: *In* ***a*** *a sketch of the Poiseuille flow in a hollow tube is presented. The velocity profile $v(z)$ leads to the heat distribution in the flow at the times t_1-t_3. In the xylem, the flow can be approximated by a number of small hollow tubes with a Poiseuille flow in between, as shown in* ***b****. The resulting velocity profile is a constant one.*

measurements were conducted on technical capillaries in Section 9.4.1 and on perfused *Ricinus communis* leaves in Section 9.4.2. The sensitivity of the technique was tested in Section 9.4.3 where the flow velocity was measured on the petiole of a leaf subject to different environmental forcing. Measurements were also conducted on corn leaves in Section 9.4.4. Here the flow velocity was shown qualitatively before and after cutting part of the leaf. In Section 9.4.5 the flow velocity in the xylem of *Ricinus communis* leaves was measured while varying parameters locally inside a climatic chamber, or locally inside a cuvette which enclosed only part of the leaf. Conclusions will be drawn in Section 9.5.

9.2 The Model of Fluid Flow in the Xylem

The visualization technique for measuring flow velocities in plant leaves are similar to the technique of molecular tagging velocimetry (MTV) presented in Chapter 8. In this thermographic application the flow is not marked with a caged dye that is uncaged at a certain time t_0, but heat is used for marking the fluid inside the xylem. As will be described in Section 9.3, the setup consist of a CO_2 laser that applies heat to the water which is then visualized with an infrared camera. The water inside the xylem is thus heated up and visualized by integrating the temperature across the depth of the vascular bundles. This will lead to an intensity change of the temperature due to the velocity profile inside the xylem as was shown in Section 2.7.

If one thinks of the vascular bundle of the xylem as a technical pipe, then the visualization technique of active thermography leads to Taylor dispersion as presented in Section 8.2. However, the vascular bundle is quite dissimilar to a hollow tube with a developed Poiseuille flow inside. However, it can be approximated by an array of equidistant small tubes of equal diameter. This approximation of the velocity profile $v(z)$ by a number of small tubes with a profile $v_i(z)$ is sketched in Figure 9.2. By looking at Figure 9.1 it becomes apparent that this

represents a very crude approximation. In a real leaf, the cells of the xylem have different sizes and are hence spaced differently. Moreover, the relative sizes and the spaces in between change along the length of the leaf. However, in the present context it is not practical to try to derive a more realistic model of velocity profiles in the xylem of plant leaves.

This type of velocity profile, made up of a high number of small parabolic velocity profiles, can be approximated by an n-th order profile $u(z) = A \cdot z^n$ as introduced in Section 2.7.3. The relevant equation of motion was given as Equation 2.80, which reads

$$\frac{dT}{dt} = d^\top \cdot p = \left[\begin{array}{cccc} \frac{1}{nt}T & \frac{\partial T}{\partial x} & \frac{\partial T}{\partial y} & \frac{\partial T}{\partial t} \end{array} \right] \cdot \left[\begin{array}{cccc} 1 & u_1 & u_2 & 1 \end{array} \right]^\top = 0, \tag{9.1}$$

where T is the temeperature as recorded with the infrared camera, n is the order of the velocity profile and t is the time since heating up water parcels with the CO_2 laser.

Typically, in a vascular bundle the number of such parabolic profiles is quite high so that it can be assumed that $n \to \infty$ at no loss of generality. The resulting equation of motion was given by Equation (2.81) to

$$\frac{dT}{dt} = u_1 \frac{\partial T}{\partial x} + u_2 \frac{\partial T}{\partial y} + \frac{\partial T}{\partial t} = -\frac{1}{n \cdot t} T, \quad \text{and} \quad n \overset{\lim}{\to} \infty \quad \frac{dT}{dt} = 0. \tag{9.2}$$

Effectively this means that the profile can be considered as constant and no intensity change is associated with it. This is expressed by the fact that the total derivative dT/dt, which is the rate of change in a coordinate frame affixed to the fluid parcels, is equal to zero. In the following, this type of constraint equation will be considered for the flow profile.

Currently, only the velocity profile within the xylem was considered. We assume this profile to be constant with depth. Due to the constancy of the velocity profile, no smearing of the heated water parcels will occur as in the case of Taylor dispersion presented in Section 8.2. However, since heat is uesd as a marker for the fluid, this heat will of course diffuse due to the conduction of heat. In order to estimate the xylem velocity accurately, this heat conduction has to be considered when deriving the equation of motion.

In a first approximation, the leaf can be considered to be made up of an isotopic material with an isotropic heat capacity c_{leaf} and an isotropic thermal conductivity k_{leaf}. Plant leaves consist roughly to 98% of water. Therefore, it can safely be assumed that both heat capacity and thermal conductivity are equal to that of water, thus $\rho_{H_2O} = 998$ kg/m^3, $c_{\text{leaf}} = c_{H_2O} = 4.193 \cdot 10^{-3}$ J/kg·K and $k_{\text{leaf}} = k_{H_2O} = 0.6622$ W/m·K at room temperature [1]. On both sides, the leaf is in contact with air. The thermal properties of air are $\rho_{\text{air}} = 1.205$ kg/m^3, $c_{p,\text{air}} = 1.005 \cdot 10^3$ J/kg·K and $k = k_{\text{air}} = 0.0257$ W/m·K. Due to convection in the air space, heat will be transported away from the plant leaves faster than would be expected from conduction alone. All this leads to a cooling of the plant leaf from the top and bottom interfaces. Heat applied to the leaf for marking water parcels will thus diffuse inside the water volume of the leaf. Due to the isotropic medium and the small depth of the leaf when compared to the surface ares, the diffusion process inside the leaf can be considered as a 2D

[1] This quantities were computed from functions provided by Daubert et al. [2000].

diffusion. Due to the additional heat flux at the air-leaf interfaces, cooling is faster than would be expected from the 2D diffusion inside the leaf, alone. Since one is not interested in the constant of diffusivity, but in the velocity of the xylem, this additional process needs not to be modeled correctly. It is sufficient to note that the 2D diffusion with observed with the IR camera which is faster that of pure diffusion in water.

Usually, plant leaves are not isotropic in their structure but very anisotropic. This anisotropic structure is expected to be found again in the conduction of heat. Therefore, the heat diffusion should be modeled by a process similar to anisotropic diffusion as detailed in Section 2.5.4. The relevant equation of motion is given by

$$\frac{dT}{dt} = v_x \frac{\partial T}{\partial x} + v_y \frac{\partial T}{\partial y} + \frac{\partial T}{\partial t} = \nabla \left(\boldsymbol{D} \nabla T \right), \tag{9.3}$$

with the temperatures T and the diffusiviy tensor $\boldsymbol{D}$. For purely isotropic diffusion, $\boldsymbol{D}$ becomes a scalar D and Equation (9.3) simplifies to

$$\frac{dT}{dt} = v_x \frac{\partial T}{\partial x} + v_y \frac{\partial T}{\partial y} + \frac{\partial T}{\partial t} = D \Delta T. \tag{9.4}$$

A diffusion process can be approximated by a linear temperature change for sufficiently small times. This is similar to the the extended brightness change constraint equation (eBCCE), which shows acceptable results for a linear model used for the estimation of motion subject to a diffusion process. Due to the second order derivatives of the Laplacian, Equation (9.3) needs a bigger support and is more susceptible to noise than the BCCE with linear temperature change, or

$$\frac{dT}{dt} = v_x \frac{\partial T}{\partial x} + v_y \frac{\partial T}{\partial y} + \frac{\partial T}{\partial t} = c, \tag{9.5}$$

where c is a parameter of local linear brightness change. Because the xylem and the heat marked water parcels therein is quite small in the imaged area, computing second order derivatives accurately on such a small area of support is problematic. Therefore, here it was chose to estimate motion with linear brightness change only, following Equation (9.5). For higher accuracy and when imaging a smaller area of the leaf, resulting in higher spatial resolution, the isotropic or anisotropic diffusion equations (9.4) or (9.3) should be chosen.

From the motion model, the thermographic data can be analyzed with the local structure tensor approach presented in Section 3.3 to estimate the model parameter.

9.3 Experimental Set-Up

As mentioned in the previous section, water inside the xylem is heated up and measured with an infrared camera as it moves through the vascular bundles. A well known approach of measuring xylem sap flows in plant stems is based on the heat pulse velocity technique [Swanson, 1975]. The technique presented here is thus similar to this technique. However, it is a technique for gaining temporally and spatially resolved technique as areas of the leaf are visualized with an infrared camera. The parameters of the motion model from Section 9.2 are then estimated locally from the observations.

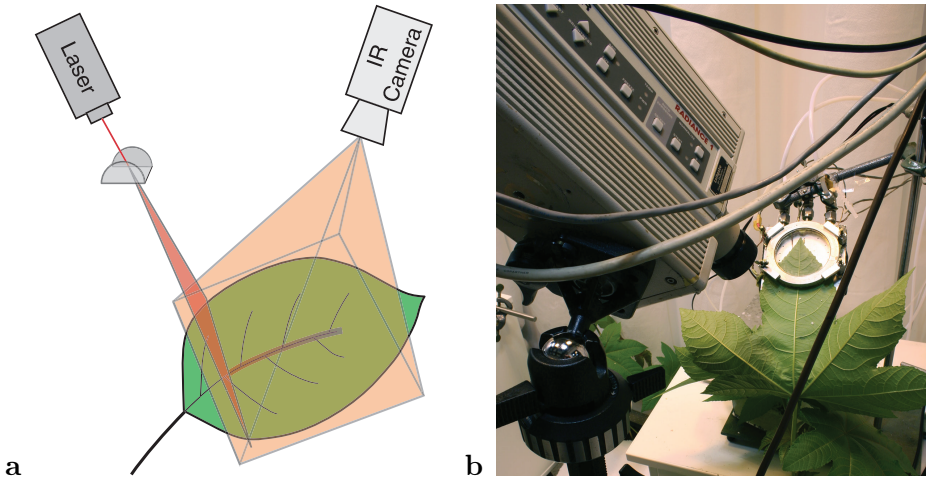

Figure 9.3: *The experimental set-up. A CO_2 laser is used to warm up water parcels in the plant leaves which are then visualized with an IR camera. In* ***b*** *a picture of the set-up is shown where part of the leaf is clamped by a cuvette.*

The technique relies on using heat as a marker for water parcels. Heat is applied to the regions of interest of the plant leaf with a 25W CO_2 laser (48-2, Synrad Inc., Mukilteo, USA). Different heat patterns are conceivable, but in order to minimize heat diffusion, line patterns were chosen. These line patterns were generated using a scanning mirror. The heated patterns are then visualized with an infrared camera. For the measurements presented in this thesis, an Amber™ Radiance 1 camera sensible in a spectral range of 3-5 µm was used. Due to the high temperature resolution of the IR imager (NEΔT is approximately 20 mK) the leaf only needs to be heated up by roughly 1K. Even from these slight heating of the leaf, an accurate estimation of the flow velocity is feasible. Stress on the plant and changes in physiological processes inside the plant leaf are thus limited by this non-invasive technique. Heat transport was measured on three different systems: capillaries, detached and attached mid-vain of *Ricinus communis* leaves. A sketch and picture of the experimental set-up can be seen in Figure 9.3.

The capillary system presents a very simple system that can easily be controlled. A range of Teflon tubes with different diameters of 0.17, 0.25 and 0.50 mm were used. A flow through these capillaries was preset with a pressure gradient induced from gravitation by placing a reservoir of water on top of the capillaries. The volume throughput was measured by collecting the water exiting the capillary and measuring its weight with a high precision scale. Multiple measurements ($n = 10$ each) were performed under different pressure gradients with different capillaries.

Detached central vein of a *Ricinus communis* leaf was perfused with water. The vein was cut on both ends and silicon tubes attached. These preparations were done under water to prevent air bubbles clogging up the xylem. A pressure driven water volume was then allowed to flow trough the *Ricinus communis* xylem. The pressure was generated as in the experiment

with the capillaries by elevating a water reservoir by a known distance from the perfused leaf. The pressure difference was recorded as was the volume of water flowing through the leaf measured by a highly accurate scale. Multiple flow measurements were performed under varying pressure gradients.

The experiments on attached *Ricinus communis* leaves were conducted in the climate chamber with controlled environmental conditions under constant temperature of 25°C and variable humidity with plants which were transported to a climate chamber a few days prior to the measurements. The tip of the main lobe of the leaf was clamped in the leaf chamber upside down. The heat transport was measured on the mid-vain on the adaxial leaf side outside the leaf cuvette. The clamped leaf showed an angle of approximately 45° with reference to the plant stem which allowed simultaneous heat pulsing, detection of the heat transfer and gas exchange measurement. The experiments started with photosynthetic photon flux density (PPFD) of 400-300 µmol Photons m^{-2} s^{-1} over the leaf surface and 30% relative humidity (r.h.) inside and outside the leaf cuvette. After steady state gas exchange was measured. The flow velocity was recorded on 4 different sites along the mid-vain. This procedure was repeated under 80% r.h. in light and in darkness. The resulting vapor pressure deficit (VPD) between the leaf and air ranged between 2.1 and 1.2 kPa. The difference between VPD inside and outside the leaf cuvette was < 0.1 kPa. The leaf temperature ranged between 25.4 and 27.5°C inside and outside the leaf cuvette depending on the transpiration rates.

Further experiments with attached *Ricinus communis* leaves were performed under constant conditions inside the climate chamber with 80% r.h. (VPD = 0.2-0.4) and a leaf temperature outside the leaf cuvette of 25.2 ± 0.7°C whereas the relative humidity and the resulting VPD inside the chamber was changed in 5 steps: 30%, 40%, 60%, 80% and 80% (no light), resulting in different VPD values inside the cuvette ranging between 2.8-0.6 kPa and leaf temperatures ranging between 25.3-27.4°C. The flow velocity was measured several times on 2 different points on the mid-vain. The measurement on intact attached leaves was combined with gas exchange measurements. Transpiration rates (E) and stomatal conductance of the leaf (gleaf) were measured on an apical part of the central lobe which was clamped in a cuvette. The measurement was performed in an open gas exchange system with a leaf cuvette as previously described [Jahnke, 2001; Pieruschka et al., 2005]. The mid-vain areas heated by the CO_2 laser were cut out after the experiment. Six cross-sections per every heated point were cut by hand and measured with a micrometer with microscale. Mean xylem diameter was determined by measuring the diameter of all vessels > 10µm (with largest vessel diameters of 70 µm) and adding the measured values to a cumulative mean xylem diameter (DmX).

9.3.1 Plant material

The plants of *Ricinus communis* were grown from seeds in 1.3 L pots with standardized soil (Einheitserde Typ ED 73, Balster-Feuerfest GmbH, Germany) in a greenhouse with highly

translucent glass panels transmissible (>96% transmission of sun light[2]), periodically irrigated with tap water and fertilized once a week (Hakaphos grün, COMPO GmbH & KG, Münster, Germany). When light intensity dropped below 110 µmol photons m^{-2} s^{-1}, artificial light was added (SON-T, 400W, Philips, Germany; HQI-Lamps, 400W Osram, München, Germany) providing photosynthetic photon flux density (PPFD) of 400-450 µmol m^{-2} s^{-1} at 30 cm above the pots. Measurements were conducted on mature leaves of 6-8 weeks old plants.

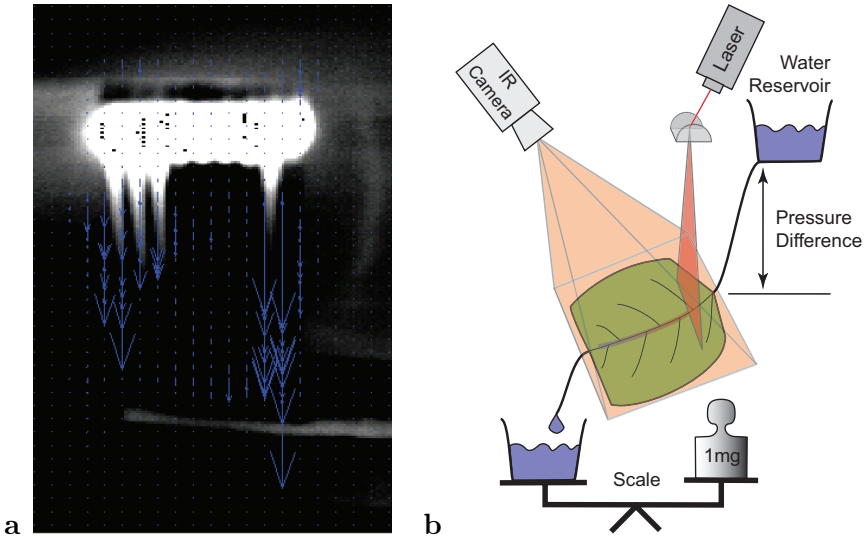

Figure 9.4: ***a*** *Example of flow measurement on an array of technical Teflon™ capillaries.* ***b*** *Schematic drawing of the thermographic set-up for the perfusion measurement.*

9.4 Verification of Technique

In order to verify the validity and accuracy of the novel technique, some test measurements were conducted. Here, the comparison of the measured velocities was compared to ground truth measurements derived by other means. In this work two different kinds of test measurements were conducted. The first one was to use technical Teflon™ capillaries. Due to a pressure gradient water flew through the capillaries. The volume throughput was measured with a scale and the flow velocity computed from knowledge of the diameter of the tubes. The thermographic technique was applied to this setting and flow velocities measured from the algorithm presented in this thesis. Results of this measurement are presented in Section 9.4.1. The main drawback of using technical capillaries for test measurements is that the xylem of plants has a completely different internal structure than a Teflon™ capillary. Therefore, meaningful comparisons can only be made through perfusion measurements. In this type of measurements presented in Section 9.4.2, a known volume of water flew through a vivisected vascular bundle. The flow velocity of xylem was also tested on the petiole of a leaf inside a cuvette. Here, no ground truth was available, but the applicability could be tested in controlled conditions. Results of this measurement are presented in Section 9.4.3.

[2]For details care for http://www.fz-juelich.de/icg/icg-iii/index.php?index=112 .

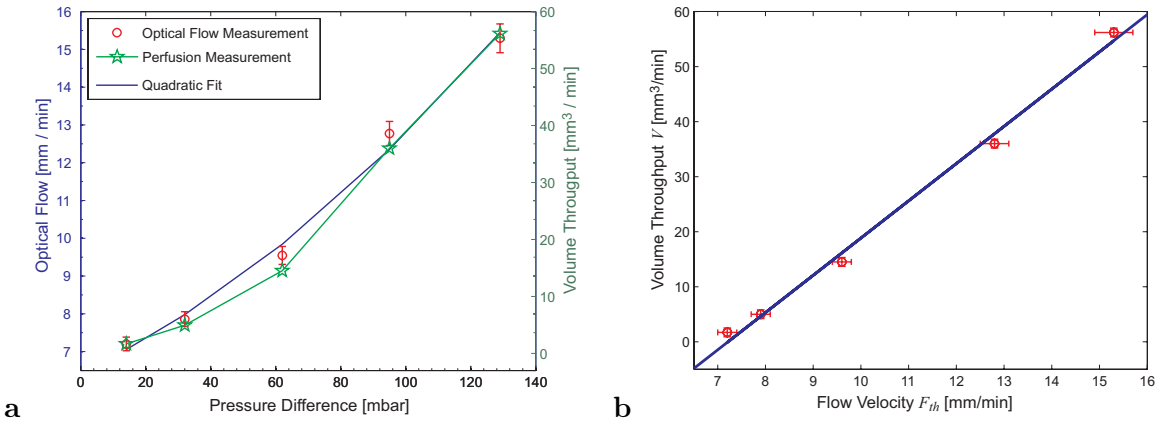

Figure 9.5: *Result of perfusion measurement. In* **a** *the volume throughput of the perfusion is shown on the right ordinate and the estimated optical flow on the left one. Error bars are computed from multiple measurements. In* **b** *the linear relationship in between flow velocity F_{th} and volume throughput V is shown.*

9.4.1 Test on Technical Capillaries

Technical capillaries present a very simple system that can easily be controlled. Through their wide application in a number of medical and chemical analytical processes, it is possible to acquire a range of tubes with different diameters. For the experiments three Teflon™ tubes with diameters of 0.17, 0.25 and 0.50 mm were used. A flow through these capillaries was preset with a pressure gradient. This gradient was induced from gravitation by placing a reservoir of water on top of the capillaries. The volume throughput was measured by collecting the water exiting the capillary and measuring its weight with a high precision scale. The set-up is the same as for the perfusion measurements in the next section. This is shown in Figure 9.4**b**. By heating up water parcels inside the capillaries with a CO_2 laser, the transport inside the capillaries was visualized with the IR camera. One frame of such a sequence is presented in Figure 9.4 **a**. Through a geometric calibration of the camera, the flow velocity through the capillary was mapped to the units pixel/frame of the camera and compared to the flow velocity estimated by our technique. Results are presented in Table 9.1.

As can be seen from analyzing Table 9.1, the measured flow velocity is in good agreement with the actual ground truth value at low flow rates. The measured values appear within the error bounds of the estimates. Errors were derived from multiple independent measurements.

Diameter [mm]	Flow Velocity [mm/s]	Flow Velocity [Pixel/Frame]	Optical Flow [Pixel / Frame]
0.17	2.20	0.173	0.199 ± 0.057
0.25	30.48	2.356	1.631 ± 0.434
0.50	91.16	7.380	2.274 ± 0.850

Table 9.1: *The results of comparing actual water flow through a Teflon™ capillary to the flow velocity estimated from the active thermographic measurement.*

Flow Measurement [mm / min]	Volume Throughput [mm^3 / min]	Pressure Difference [mbar]
15.3 ± 0.4	56.2	129
12.8 ± 0.3	36.0	95
9.6 ± 0.2	14.5	62
7.9 ± 0.2	5.0	32
7.2 ± 0.2	1.7	14

Table 9.2: *Results of perfusion measurements.*

However, at high flow rates the thermographic technique is no longer capable to resolve the fluid flow accurately. This is due to a much too high velocity of more than 7 pixel per frame. A local gradient based technique of optical flow computation is not able to estimate motion at these scales [Barron et al., 1994], particularly because the temporal sampling theorem might be violated. This deficiency can be made good by employing a multi-scale coarse to fine strategy in the optical flow computation. However, since flows expected in the xylem flow are nowhere near as high, it was chosen not to go this route. Therefore, the result presented in Table 9.1 for the capillary of 0.5mm should be taken with a grain of salt.

9.4.2 Perfusion Measurement

The accuracy of the novel technique was tested on real plant tissue. For these measurements, the central vein of a *Ricinus communis* leaf was perfused. The vein was cut on both ends and tubes attached. These preparations were done under water to prevent air bubbles clogging up the xylem. A pressure driven water volume was then allowed to flow trough the rizinus xylem. The pressure was generated by elevating a water reservoir by a known distance from the perfused leaf. The pressure difference was recorded as was the volume of water flowing through the leaf. The water volume was measured by a highly accurate scale. The set-up of this measurement is sketched in Figure 9.4**b**.

Results of these measurements are presented in Figure 9.5 and Table 9.2. A perfect agreement exists in between the optical flow measurements of the thermographic technique and the ground truth volume measurement of the perfused leaf. The ground truth data lies within the error bars for all data points. This can also be seen from Figure 9.5**b** which shows a linear relationship between volume throughput and flow measurement within the error bars of the measurement. The errors were computed from independent measurements. These results present a very good consistency to the measured values. From this relationship the mean diameter of the xylem can be computed. It was found to be $\varnothing = 1378$ µm, which is well within the values measured (ranging from 1000-1600µm).

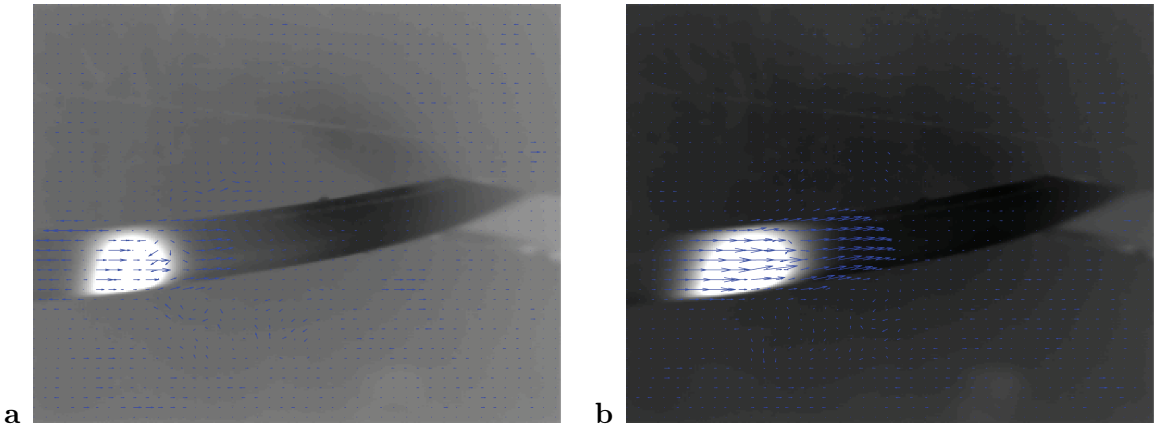

Figure 9.6: *Flow vectors from measurements at the petiole. In* **a** *the results are shown for normal air inside the cuvette, in* **b** *the same for the cuvette filled with synthetic air.*

9.4.3 Measurement at the Petiole

The measurements on technical capillaries in Section 9.4.1 and those on perfused leaves in Section 9.4.2 have shown an excellent agreement in between measurement and ground truth value. The applicability of the technique was to be tested on the petiole of a *Ricinus communis* leaf.

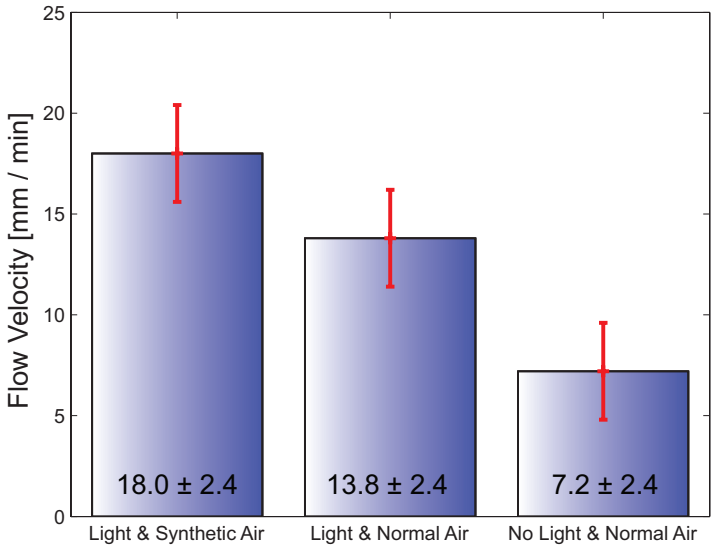

Figure 9.7: *Result of measurements of xylem flow inside the petiole of a leaf subject to different environmental forcing.*

In order to vary the flow velocity inside the xylem of the petiole, the leaf was clamped inside a cuvette. Inside the cuvette, important parameters influencing stomatal activity were changed. In a first measurement the air inside the cuvette was replaced by synthetic air. Synthetic air consists only of N_2 and O_2 in the relative quantities of 79% and 21%, respectively. Due to the absence of CO_2 in synthetic air, stomata are opened when the leaf is immersed in

this gas. Changing the airspace from synthetic air to 'normal air' (taken from pressurized air for constancy), less stomatal activity is induced as compared to synthetic air. Most stomata are closed in the last case in which in addition to normal air inside the cuvette, the light is turned off.

The flow velocity of the xylem inside the petiole is measured for those three cases outside the cuvette. Typical vector fields are shown in Figure 9.6. The actual measured values are displayed in Figure 9.7. The three cases of induced stomata activity can clearly be discriminated by the measurements. The sensitivity of the thermographic technique is thus good enough to detect xylem flow due to stomatal activity.

9.4.4 Measurements on Corn Leaves

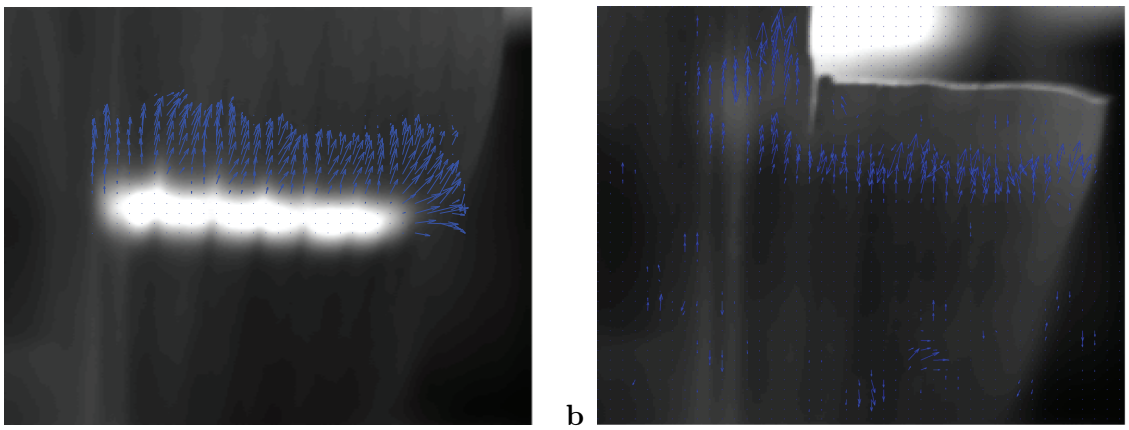

Figure 9.8: *Measurement of the xylem flow in a corn leaf is shown in* ***a****. The same leaf is cut and the resulting flow is presented in* ***b****.*

Measurements were conducted on leaves of *Zea mays*. The structure of the leaves is very simple. All the vascular bundles run in parallel along the length of the leaf. To leading order, the transport in the xylem should thus be directed only along the length of the leaf. The case is of course not this simple. It is known that if a corn leaf is cut, the area above the cut will not dry but is fed with water from leaf tissue next to it. Therefore, water can not only be transported along the length of the leaf but also across it. Generally however, water flow is directed almost entirely along the length of the leaf.

This was tested by performing a measurement on a corn leaf. The results are presented in Figure 9.8**a**. It can be seen quite nicely that all vectors are oriented along the length of the leaf as expected. Due to the spatial resolution, also an experiment was conducted where the leaf was cut on one point, and the resulting flow was measured. It was seen initially that the net flow inside the xylem was reduced but that the water flow next to the cut increased substantially. This indicates that following the cut more xylem sap has to be transported in adjacent vascular bundles to provide the leaf area above the cut with the sap. No quantitative measurements have been performed under controlled conditions. The qualitative agreement of measurement with intuition suggest to address this issue quantitatively in future research.

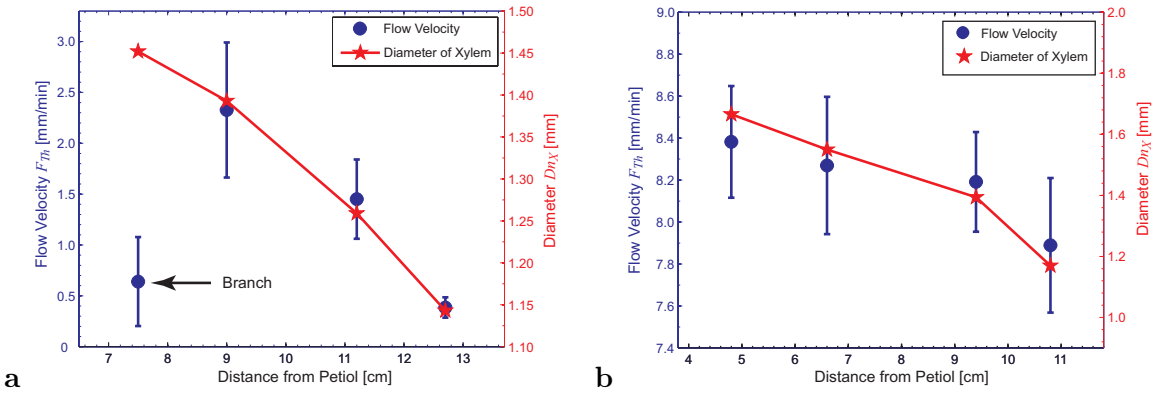

Figure 9.9: *Measurement conducted at* Ricinus communis *plant leaf. Measurements of two different plants are shown in* **a** *and* **b**. *The discrepancy of the first data point in* **a** *is due to the measurement location directly on a branch.*

9.4.5 Measurement at Varying Parameters

With a set of measurements at varying parameters, three questions were addressed:

1. How does the flow velocity in the xylem change with globally varying light and humidity?
2. How does it change with distance from the petiole?
3. Can a local change of these parameters be detected in the flow and what are the implications?

All these measurements were conducted in a climate chamber without any special measures taken for the thermographic setup. This makes the presented approach very usable for a wide range of conditions.

To address questions 1 and 2, measurements were conducted on a *Ricinus communis* leaf. Here the parameters humidity and light were changed, since these are the main factors influencing evaporation. At the same time, measurements were conducted at four points of different distance to the petiole. The external parameters were adjusted to the same values for these measurements with different plants on different days. It turns out that there is quite a high variability among different plants in the measured transport velocities in the xylem. Results for two plants are presented in Figure 9.9. It is evident that there is a decrease in flow velocity with distance to the petiole. The diameter of the xylem was measured microscopically at the same locations following the measurement. These diameters are also plotted in Figure 9.9. It appears that there is a strong correlation between fluid flow in the xylem and the diameter of this tissue. This correlation was shown in the plants tested, although the net fluid flow velocities were quite different. It should be noted that a big discrpancy in the first measured point at a distance of 7.5 cm from the petiole in Figure 9.9**a**. This is due to the fact that the measurement was conducted directly at a branch of two vascular bundles leading to a decrease in flow velocity.

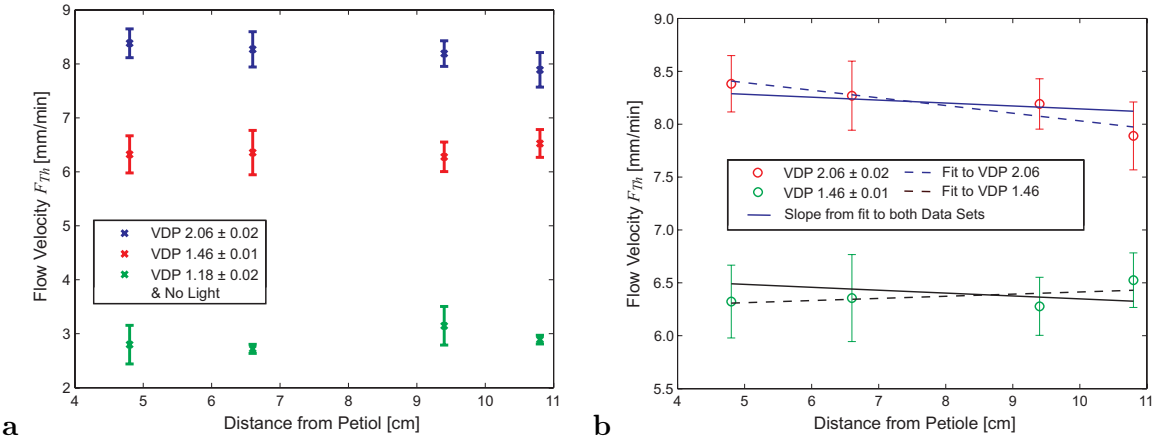

Figure 9.10: *Measurement at* Ricinus communis *leaf. The flow velocity is measured at three different locations for different relative humidities. In* **b** *a linear model is fit to the measurements at VDP 2.06 and VDP 1.46. The results are shown of fitting a linear model to both data sets individually or constraining the slope fixed for both of them.*

Measurements were conducted along the length of the central vain, while global parameters were systematically changed. The results of this measurement are shown in Figure 9.10. It can be seen that the variations due to a change in relative humidity (from 30% to 80%, which is equivalent to a VDP of 2.06 to 1.46, respectively) is significantly stronger than the velocity change with distance to petiole.

Question 3 was addressed by clamping a part of the leaf inside a small cuvette. The cuvette was placed at the tip of the central lobe of the *Ricinus communis* leaf. The relative humidity inside the climate chamber was set to 80% and the light was turned on. Inside the cuvette, the relative humidity was set to four different values. For minimal stomatal activity, in a fifth case the cuvette was set to the highest relative humidity and was darkened locally at the same time. For all cases, measurements were conducted at two points, separated by different distances from the petiole.

The results of these measurements are presented in Figure 9.11. It can be seen quite clearly that the flow velocity at two distances from the petiole is quite different in Figure 9.11**a** as would be expected from our previous measurements. The velocity increases linearly with the transpiration rate, except for the last point at the highest transpiration rate. This change in xylem flow is the same for the two measurement points, indicating that physiological changes in the plant's xylem transport might have taken place.

The same basic behavior can be seen in Figure 9.11**b**. Again, the difference in between velocities between the two points is visible, albeit not as pronounced as in **a**. This is due to the different scaling of the two plots with maximum flow velocities in **b** being much higher as in the case of **a**. However, a discrepancy seems to be present in the last data point of Point 0 which is significantly too low. This discrepancy might be due to a measurement error, where water parcels were heated directly in a junction. The same incidence was analyzed in Figure 9.9**a**. It should be noted that the estimated flow velocities were significantly lower than

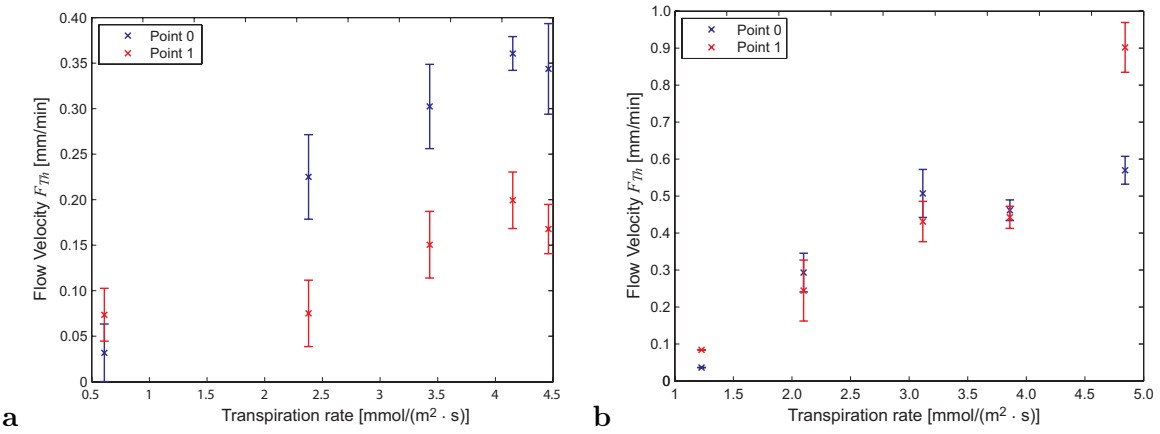

Figure 9.11: *Measurement of velocities inside the xylem on leaves of two different* Ricinus communis *plants. Point one and two indicate different distances to the petiole. While there is a strong difference in the velocity in between distances to the petiole in* ***a****, this difference is far less pronounced in* ***b****.*

recorded during previous measurements. This is due to the fact that evaporation took place inside the cuvette only. Only a small part of the leaf was covered during these measurements, as can be seen from Figure 9.3**b**.

9.5 Conclusion

A new technique has been presented that makes measurements of flow velocities inside the xylem of pant leaves feasible. Heat is used as a marker for water parcels. The heated water is then visualized with an infrared camera. The velocity profile inside the xylem is modeled with an n-dimensional profile with $n \to \infty$. This is equivalent to constant profile. It was shown that the intensities do not change due to the visualization process as has been observed in the case of Taylor dispersion in Chapter 8. It was shown how to model heat diffusion as a model for motion estimation.

Test measurements were performed on technical capillary tubes and on real plant tissue in perfusion measurements. The volume throughput was measured in both cases. The diameter in the technical capillaries was known precisely and hence the ground truth velocity computed. For the perfusion measurements the velocity was related to the pressure driving the water through the xylem. In both cases an excellent agreement between the measurements was observed. The error in the perfusion measurements was found to be ± 0.4 mm/min.

The sensitivity of the technique was tested through measurements on the petiole of a leaf clamped inside a cuvette. Inside the cuvette, environmental conditions were changes, ranging from high levels of CO_2 to no CO_2 as well as changing light intensities. From measuring the flow rates at the petiole, the stomatal activity could clearly be discriminated.

Measurements were also conducted on a leaf of *Zea mays*. Changes in flow velocity were quantitatively analyzed before and after cutting into the leaf. It could clearly be seen that the flow velocity decreased after the leaf had been cut. At the same time an increase in flow

velocity next to the cut was observed. This is probably due to the higher volume throughput needed in this part of the leaf to be able to supply leaf areas above the cut with fluid.

Measurements on *Ricinus communis* leaves were also conducted while varying the external parameters. It could clearly be seen that a strong correlation in between flow velocity and xylem diameter exists. The dependence on xylem diameter is not as strong as variations to vapor pressure deficit between air and leaf.

This technique of measuring fluid flow in the xylem of plant leafs is a powerful tool for performing a mapping of xylem flows in the plant leaves. This will be an objective of future research.

Chapter 10

Conclusion and Outlook

10.1 Summary

The main objective of this thesis has been the measurement of transport phenomena in fluid mechanic applications, encompassing complex systems in environmental physics, life-sciences and in microfluidics. The processes studied can only be apprehended by applying non-invasive imaging techniques. To this end, current state-of-the-art methods were extended, or completely new measuring techniques were developed. Closely related to these advances in imaging techniques have been developments in digital image processing. This has made it possible to measure a number of important quantities, especially in the field of air-sea interactions, for the first time both temporally and spatially highly resolved.

In terms of measuring fluid flows, two types of techniques have been employed: active and passive ones. For active techniques, fluid parcels are actively marked, either by heating them up with a CO_2 laser in botanical applications or at the water surface for research in air-sea interactions, or by uncaging a dye with an UV excimer laser in microfluids. The heat patterns are visualized with a thermographic camera, while a standard video camera suffices for visualizing the uncaged dyes in microfluidics. For this class of flow visualization techniques, arbitrary patterns can be written into the fluid. Flow parameter can then be estimated from the spatio-temporal change of these written density structures. While this measuring principle is known in microfluidics as molecular tagging velocimetry (MTV), previously it has never been used for this purpose in air-sea interactions and it also has never been applied to measure water flows in plants. Without the need for a laser, passive techniques visualize flows without accentuate any patterns artificially. These techniques have been used in air-sea interactions for the first time to measure surface flows as well as the net heat flux and other parameters of air-sea heat exchange.

In active techniques, the written patterns change their appearance due to transport processes such as diffusion or due to shearing effects from the underlying flow profile. New models were formulated as partial differential equations to explicitly take these effects into consideration. Only through this model formulation, fluid flows can be estimated accurately. Moreover, additional parameters can also be extracted from the imaged data. This makes it possible to

gain a deeper understanding of the processes involved and to derive quantities, which where not accessible previously. All the proposed models can be formulated in a similar fashion. Therefore, the same computational framework can be used to solve their parameters, making this approach very flexible. In this way, arbitrary combinations of the model are also feasible.

The parameters of the motion models were computed in a statistical parameter estimation framework. This has lead to an extension of a well known approach of motion estimation in image processing. Through this extension, maximum likelihood estimates of the parameters could be assessed based on the noise structure of the data terms entering the model. Computational speed of the estimator has been significantly increased by analyzing the underlying matrix diagonalization problem. Additionally, the estimator has been implemented on inexpensive graphics hardware to increase execution time further by a factor of five. These steps have lead to the estimation of parameters in real time. This is especially important since for temporally and spatially highly resolved measurements, large amounts of data can accumulate quickly. These data have to be analyzed in a reasonable period of time. Estimated parameter are also accessible during the experiment, significantly facilitating the measurement.

Techniques were developed to regularize parameters using information of the local spatio-temporal structure of objects. Estimates can be stabilized through this step without imposing too stringed constraints on the estimates and thus potentially falsifying the results. New confidence measures and situation measures were developed and compared to measures proposed previously in literature. The applicability and performance of situation and confidence measures have been increased due to these novel techniques. These measures are used to reject imprecise estimates of the model parameters and to detect areas where a full parameter set cannot be estimated. This knowledge can also be used in the aforementioned regularization of parameter fields.

A novel approach has also been developed that makes it possible to accurately extract edges of moving objects, denoise the data and estimate motion highly accurately at the same time. This is achieved by asking for a piecewise smooth motion field and formulating an energy functional in a variational phase field approach. This requires no prior knowledge on the shape or number of objects in the scene. This is particularly important in fluid dynamic applications, where knowledge of the shape of flow structures is not given. This algorithm can be used for computing motion in flow data that is corrupted by differently moving artifacts, such as reflections. Due to the piecewise smoothness, wrong information from these artifacts is not diffused into correct estimates of the surroundings.

These advances in measuring techniques, modeling of visualized processes and digital image sequence processing were applied to actually measure transport phenomena in three different applications: interfacial transfer across the water-sided atmosphere-ocean boundary layer, flow in microfluidic mixers and transport processes in plant leaves. Even though those fields are extremely diverse, the actual processes measured are remarkably similar. One similarity has been noted previously due to the measurement process. In all three applications, active visualization processes have been employed. Also, the fluid flow profile is of n-th order, with $n = 1$ for a linear shear induced profile at the viscous boundary layer at the air-water interface, $n = 2$ for a parabolic profile due to Poiseuille flow in pressure driven microfluidics, and $n \to \infty$

for the flow of xylem sap inside plant leaves.

A general formulation of the effects due to these velocity profiles and integration of tracers across them has lead to a model for n-th order velocity profiles. The three applications presented in this thesis are thus special cases of this model. This leads to the same framework and algorithms being applicable to all of the previously mentioned applications. There are of course combinations of additional models specific to the application, such as diffusion in microfluidic flows, which can be quite significant.

Most noteworthy advances where achieved in the field of air-sea interactions. A well known model of transport across the air-water interface, the surface renewal model, has been applied to data obtained from passive thermography. Parameters of this model, such as the residence time of water parcels at the interface, were measured and the probability density function (pdf) of this quantity obtained. As proposed previously, this pdf has been found to be a logarithmic normal distribution under all conditions observed. Using this model and the pdf, an analytic function for the temperature distribution at the water surface has been derived. This describes the experimental data very well, again under all analyzed conditions. From this analytical distribution, the temperature difference ΔT across the water sided thermal boundary layer can be estimated. Furthermore, using this surface renewal model, the net heat flux j_{heat} across the air-water interface could be measured temporally and spatially highly resolved, limited only by the resolution of the infrared camera. A related quantity, the transfer velocity of heat k_{heat}, could also be measured with the same high resolution. This is very important, as a scaling of transfer velocities between different tracers exists, based on their Schmidt numbers. Hence, from the transfer velocity of heat, the equivalent one for mass such as CO_2 or other greenhouse active gases can be deduced.

Measurements of all these quantities were tested in a laboratory settings with accurate ground truth over a wide range of environmental conditions. The measurements of all quantities agreed very well to the ground truth, often better than 6% for the fluxes and transfer velocities, and an accuracy of 3mK for ΔT (usually, ΔT ranges from $0.05-0.3$ K at conditions commonly found at the ocean during night time). Apart from laboratory experiments, field data, recorded during the GasExII cruise in the equatorial Pacific, has also been analyzed and compared to current parameterizations. Measurements were within the parameterization, although slightly larger than transfer velocities measured from eddy correlation techniques.

Apart from the surface renewal model, a new model has been developed which was termed eddy renewal model. This model differs from the surface renewal model in that it assumes temporal stationarity but no spatial homogeneity. This eddy renewal model tries to take into account the dominant streaky features observed in thermographic images at low to medium wind, similar in character to Langmuir turbulence. From this eddy renewal model, the same parameters estimated with the surface renewal model were computed. As it turned out, the measures of ΔT were almost identical to those obtained from the surface renewal model under all conditions observed. Estimates of the net heat flux j_{heat} are higher by about 6% for the eddy renewal model compared to the surface renewal model. This difference is just inside the uncertainty of measurements obtained from the techniques presented in this thesis. This good agreement between the models is quite startling as different assumptions were made in

deriving them.

Active thermography has been used for measuring surface flows at the air-water interface. While it has also been shown how these flows can be measured passively, active thermography has the added benefit that it does not rely on the presence of a natural heat flux. A CO_2 laser is used for heating up patches of water which are then visualized with an infrared camera. Due to a linear flow profile induced by the the wind at the surface, these temperature structures change their appearance over time. For accurately estimating the flow velocity, this process has to be modeled. In modeling the velocity profile as plane Couette flow, adverse effects were successfully avoided. Moreover, by also modeling the absorption of both the laser and the visualized radiation, the wind induced shear stress could be measured. This shear stress can also be considered as the flux of momentum from the atmosphere to the ocean. Thus, a convenient experimentally technique has been developed for estimating viscous shear stress directly at the sea surface. This is in principle not limited to laboratory measurements but can also be utilized in the field. The technique has been tested on simulated data as well as on test measurements in the laboratory. Since only shearing of the thermal structures is considered, only the viscous part of the momentum transport can be measured with this technique. The form drag due top the wave field cannot be determined. Therefore, laboratory measurements were conducted on a surfactant covered interface without any waves. These measurements were compared to ground truth obtained by other techniques. The difference in between measurements was close to 10%. Novel infrared cameras with a higher temporal resolution will help immensely to improve the accuracy of this technique.

With these techniques based on infrared thermography, it is for the first time possible to measure the transfer of energy and momentum at the sea surface highly resolved, both temporally and spatially. The measurements of both quantities are obtained in the same footprint and with the same sensor. The techniques are in principle applicable to the field as they are to the laboratory. This opens up new perspectives for process studies of air-sea exchange processes.

In microfluidics, the flow has been visualized by uncaging the fluorescence of special dyes and visualizing these written structures as they transform during time. This technique is known as molecular tagging velocimetry (MTV). Taylor dispersion due to integration across the parabolic flow profile has been modeled explicitly as has been molecular diffusion. The model parameter where estimated in the previously presented estimation framework. This represents the first approach where inaccuracies were avoided caused by disregarding of these processes. Measurements were conducted in a specially prepared microfluidic mixer of precisely known geometry, from which ground truth of the fluid flow could be extracted. Measurements with the presented technique were compared to the ground truth, resulting in excellent agreement with a scatter of less than 5%. Flow measurements were conducted on different written pattern, optimized for different aspects of the flow. Apart from the ground truth measurements, the micro mixer was adjusted to different flow geometries. This was done to test the applicability of the technique to more challenging conditions. Although ground truth could not be fixed, the measured flow agreed both quantitatively and qualitatively to expectations. Therefore, a novel technique was conceived that is well suited for performing accurate mea-

surements with MTV.

As an application from plant physiology, the fluid flow inside the xylem of plant leaves has been measured. Here, the flow has been visualized with active thermography in a process similar to that at the sea surface or MTV used in microfluidics. With a CO_2 laser, water parcels inside the xylem were heated up and their transport visualized with an infrared camera. The flow profile has been modeled to be $n \to \infty$ order. Flow measurements were tested on the perfused central vein of a *Ricinus communis* leaf. For this measurement ground truth was attained. An excellent agreement between ground truth and measurement was ascertained. The flow of xylem sap has subsequently been measured on plant leaves of *Ricinus communis* in vivo. These measurements were conducted on a free standing plant in a climatic chamber. Environmental conditions were varied to assess the influence on the sap flow measured. Also, by enclosing only a small area of the leaf in a cuvette, environmental parameters were also varied locally. Even these small changes in xylem flow due to local changes could readily be observed with the new technique. The change of flow velocity along the central vein of a *Ricinus communis* leaf has also been measured. A good agreement between xylem diameter and flow velocity has been found. Measurements were also conducted on a *Zea mays* leaf. Here, the effect of cutting part of the leaf was measured. It could clearly be seen that flow velocities in areas next to the cut rose. This could be caused by the fact that part of the leaf behind the cut has to be supplied with water, leading to an increase in flow rate next to the cut.

The developed techniques have been very successful in estimating parameters of transport processes for a number of different applications, opening up new perspectives in the relevant fields of research.

10.2 Outlook

Despite the significant advances achieved in the fields of scientific image sequence processing and fluid flow measurement, open questions remain and will be addressed in future research.

The development of motion models is driven by applications. Hence, applying the framework presented in this thesis to new fields will undoubtedly spawn new ideas in research and development. However, closely related to the motion models is the question of model selection which best describes the data. This question has to be answered in a statistical approach. First steps in this direction have been taken by Andres et al. [2006]. Often, a certain model is set by physical phenomena. In the sense of model selection, the question to answer is if all the model parameter can actually be estimated from the data available. In the case of very noisy data for example, a less complex model might be the only sensible choice as no additional information can be extracted from the data given.

In the field of parameter estimation, a image sequences of at least five frames is necessary to compute the temporal gradients accurate enough. For some applications where extremely fast time sampling is necessary, only two frames are available. Algorithmic advances might open up this type of application to the framework presented in this thesis. Prior knowledge might

be used in a statistical framework to accurately estimate the parameter of motion models with the noisy input data. With such an approach it might also be possible to gain advances in terms of spatial integration of the total least squares estimator. Depending on the complexity of the model and noise of input data, smoothing filters with mask sizes of 11×11 up to 22×22 might be necessary. By incorporating prior knowledge, these integration areas could be significantly reduced rendering a more localized estimate. Of course, special care in using this prior knowledge has to be taken into account. Approaches using this type of knowledge rely always on the expected estimates, rather than on the actual data.

In terms of real time parameter estimation, the rapid increase of processing power with each new generation of graphics processing units, the applicability of such hardware to complex algorithms will significantly increase. The implementation of the proposed regularization framework for parameter fields is almost within reach. Here the same performance improvements as presented for total least squares estimates should be feasible. First steps in this direction have already been taken. This will eventually lead to the implementation of much more complex algorithms on such hardware such as the the approach based on the phase field presented in this thesis.

Improvements for characterizing estimates are feasible. Most of the measures presented in this thesis take only the displacement vector field into consideration. An extension of these approaches to the more complex motion models is expected. To this end, it is important to extend the aperture problem as well as the occlusion problem to higher dimensions. This means that abrupt changes in image intensities can be thought of as a brightness occlusion or disocclusion. Such phenomena have to be detected automatically. The same holds true for the aperture problem, where a number of parameters could in principle be estimated accurately, but others not. These questions are related somewhat to the previously proposed research in model selection.

The phase field approach presented in this thesis could readily be extended to inpaint corrupted areas in the data. Such areas might be due to reflections or other processes that cannot be evaded successfully. These corrupted areas will be detected with the approaches of characterizing parameter estimates. Depending on the measure chosen, this detection process could also be formulated in the same energy functional. Information from inpainting could be chosen along trajectories from other frames of the image sequence, from prior knowledge, or in part from extracting some information from the corrupted areas.

In terms of applications, a number of future research activities are conceivable. For air-sea interaction, it is interesting to find out why the surface renewal and the eddy renewal model exhibit practically the same results. Here more data from a wider spread of conditions will be analyzed. Also the statistics of the eddy renewal model will be analyzed further. Questions about how eddy size distributions change with respect to environmental forcing might provide deeper insights into the mechanisms of transport at the air-sea interface. The estimates of ΔT will also be compared to measurements of temperature profiles through the thermal boundary layer. First measurements with advanced sensors have been conducted and provide valuable insights into the relation of thermographic measurements to standard techniques. The techniques of measuring friction velocities will be applied to the wavy interface. In this

fashion, the partitioning of the momentum flux to viscous shear drag and form drag due to the waves can be analyzed. These measurements should be conducted both in laboratory settings as well as in the field. Although previous measurements of the viscous shear stress have been measured with PIV in the laboratory, no such measurements have been carried out in the field yet. Also, measurements of heat and momentum transport from infrared thermnography could be conducted in conjunction with mass transfer measurements. Through these combined measurements, a physically based parameterization of transfer across the air-sea interface may finally be achievable. Such a parameterization will lead to less scatter in the data an a higher accuracy in estimates. Due to the use of such parameterizations in global climate modeling, a better parameterization will directly lead to better predictions of our future climate.

In microfluidics, the novel techniques will be applied to measure phenomena and parameter in micro mixers. Here, basic parameters such as the retention time of fluids inside the mixer are not well known or controlled by the boundary conditions. Dead water volumes eluded precise measurement. The improvements to MTV will make such measurements possible and may lead to significant advances in the understanding of transport processes in micromixers and an accurate controlling thereof. The MTV measurements can be also be combined with techniques of measuring concentration fields in such devices. For example, from Raman scattering the spreading of concentration fields can be measured and related to the flow velocity estimated from MTV. Per se the velocities of both the fluid velocity and that of concentrations need not to be identical. This would be the case for reactive flows. These measurements would thus provide extremely valuable insights into process control of microfluidic mixers. Here the flow geometry could be set in a way that different chemical species mix in optimal volume ratios.

The concept of MTV could also be applied to measurements at the air-sea interface. This technique would provide an additional tool for measuring velocity profiles at the air-water interface. For the applicability of this technique, a significant decline in prices of cages dyes would be required.

In plant physiology, hardly any data is available for the xylem flows and distribution thereof in plant leaves. A significant contribution is foreseeable by performing extensive measurements of mapping the xylem flow velocity throughout the leaf. Here measurements would have to be conducted spatially and temporally highly resolved. This would require measurements at different spatial scales with a refined heat pattern applied to the leaf. This might also require advances in parameter estimation, since the area of integration needs to be adapted to the structure of the vascular bundles. This mapping could be conducted on a wide range of species under different environmental conditions. Daily cycles of these measurements could also be performed, possibly on free plants in the field. This would shed new light on a number of extremely interesting questions for plant physiology. Here questions concerning the variability and control mechanisms are of great interest. How does the xylem flow react to a very localized stomatal patchiness and how do velocities vary across branchings of the xylem? Insights into these processes could also be valuable for engineering applications. Hardly any complex man-made system of fluid supply (water or gas) can rival the xylem system in plant leaves, both in terms of efficiency and reliability.

All these ideas give just a small impression of the possibility for future research by using

the techniques presented in this thesis. Advances in one field will certainly lead to advances in others, as has also happened for the techniques presented here. Only through interdisciplinary research will it be possible to tackle these problems and to achieve major advances in the relevant fields.

Bibliography

R. J. Adcock. A problem in least squares. *The Analyst*, 5:53–54, 1878.

L. Alvarez, J. Weickert, and J. Sánchez. A scale-space approach to nonlocal optical flow calculations. In *Scale-Space Theories in Computer Vision*, pages 235–246, 1999.

L. Alvarez, J. Weickert, and J. Sánchez. Reliable estimation of dense optical flow fields with large displacements. *International Journal of Computer Vision*, 39:41–56, 2000.

L. Ambrosio and V. M. Tortorelli. On the approximation of free discontinuity problems. *Boll.Un.Mat.Ital.B*, 6(7):105–123, 1992.

L. Ambrosio, N. Fusco, and D. Pallara. *Functions of bounded variation and free discontinuity problems*. Oxford University Press, 2000.

T. Amiaz and N. Kiryati. Dense discontinuous optical flow via contour-based segmentation. In *Proc. of ICIP 2005*, volume 3, pages 1264–1267, 2005.

T. Amiaz and N. Kiryati. Piecewise-smooth dense optical flow via level sets. *International Journal of Computer Vision*, 68(2):111–124, 2006. doi: 10.1007/s11263-005-6206-0.

P. Anandan. A computational framework and an algorithm for the measurement of visual motion. *International Journal of Computer Vision*, 2:283–319, 1989.

B. Andres, C. S. Garbe, and F. Hamprecht. Adaptive model selection in optical flow based motion estimation by confidence measure parameterization. Technical report, IWR, University of Heidelberg, 2006.

M. A. Atmane, W. Asher, and A. T. Jessup. On the use of the active infrared technique to infer heat and gas transfer velocities at the air-water interface. *Journal of Geophysical Research*, 109:C08S14, 2004. doi: 10.1029/2003JC001805.

Y. Avirav, H. Gutermann, and S. Ben-Yaakov. Implementation of digital signal processing techniques in the design of thermal pulse flowmeters. *IEEE Transactions on Instrumentation and Measurment*, 39(5):761–766, 1990.

M. Avram, A. Avram, and C. Iliescu. Biodynamical analysis microfluidic system. *Microelectronic Engineering*, 83(4-9):1688–1691, 2006.

S. Banerjee, D. Lakehal, and M. Fulgosi. Surface divergence models for scalar exchange between turbulent streams. *International Journal of Multiphase Flow*, 30(7-8):963–977, 2004. doi: 10.1016/j.ijmultiphaseflow.2004.05.004. J JUL-AUG.

M. L. Banner and W. Peirson. Tangential stress beneath wind-driven air-water interfaces. *Journal of Fluid Mechanics*, 364:115–145, 1998.

J. L. Barlow. More accurate bidiagonal reduction for computing the singular value decomposition. *SIAM Journal on Matrix Analysis and Applications*, 23(3):761–798, 2002. doi: 10.1137/S0895479898343541.

J. L. Barron and H. Spies. Quantitative regularized range flow. In *Vision Interface*, pages 203–210, Montreal, Canada, May 2000.

J. L. Barron and H. Spies. The fusion of image and range flow. In R. Klette, T. Huang, and G. Gimel'farb, editors, *Multi-Image Analysis*, Lecture Notes in Computer Sciences, pages 174–192. Springer, March 2001.

J. L. Barron, D. J. Fleet, and S. Beauchemin. Performance of optical flow techniques. *International Journal of Computer Vision*, 12(1):43–77, 1994.

E. Barth. The minors of the structure tensor. In *DAGM*, pages 221–228, Kiel, Germany, 2000.

D. A. Beard. Taylor dispersion of a solute in a microfluidic channel. *Journal of Applied Physics*, 89(8):4667–4669, 2001. doi: 10.1063/1.1357462.

S. S. Beauchemin and J. L. Barron. The computation of optical flow. *ACM Computing Surveys*, 27(3):433–467, 1995.

A. Bendada, F. Erchiqui, and M. Lamontagne. Pulsed thermography in the evaluation of an aircraft composite using 3d thermal quadrupoles and mathematical perturbations. *Inverse Problems*, 21(3):857–877, 2005.

J. Bigün. *Vision with Direction*. Springer Verlag, 2006.

J. Bigün and G. H. Granlund. Optimal orientation detection of linear symmetry. In *ICCV*, pages 433–438, London, UK, 1987.

J. Bigün, G. H. Granlund, and J. Wiklund. Multidimensional orientation estimation with application to texture analysis and optical flow. *IEEE Transactions on Pattern Analysis and Machine Intelligence*, 13(8):775–790, 1991.

A. Björck. Least squares methods. In P. G. Ciarlet and J. L. Lions, editors, *Finite Difference Methods (Part 1)*, volume 1 of *Handbook of Numerical Analysis*, pages 465–652. Elesvier Science Publishers, North-Holland, 1990.

M. J. Black and P. Anandan. The robust estimation of multiple motions: Parametric and piecewise-smooth flow fields. *Computer Vision and Image Understanding*, 63(1):75–104, January 1996.

B. Bourdin. Image segmentation with a Finite Element method. *ESIAM: Math.Modelling and Num.Analysis*, 33(2):229–244, 1999.

B. Bourdin and A. Chambolle. Implementation of an adaptive Finite-Element approximation of the Mumford-Shah functional. *Numerical Mathematics*, 85(4):609–646, 2000.

W. S. Broecker and T. H. Peng. Gas exchange rates between air and sea. *Tellus*, 24:21–35, 1974.

W. S. Broecker and T. H. Peng. *Tracers in the Sea*. Lamont-Doherty Geological Observatory, Columbia University, Palisades, New York, 1982.

I. N. Bronstein and K. A. Semendjajew. *Taschenbuch der Mathematik*. Verlag Harri Deutsch, Thun, 24 edition, 1989.

R. Brown. A brief account of microscopical observations made in the months of june, july and august, 1827, on the particles contained in the pollen of plants; and on the general existence of active molecules in organic and inorganic bodies. *Philosophical Magazine*, 4: 161–173, 1828.

T. Brox, A. Bruhn, N. Papenberg, and J. Weickert. High accuracy optical flow estimation based on a theory for warping. In T. Pajdla and J. Matas, editors, *Proc. of the 8th ECCV*, volume 3024, pages 25–36, 2004.

T. Brox, A. Bruhn, and J. Weickert. Variational motion segmentation with level sets. In *COMPUTER VISION - ECCV 2006*, volume 1 of *Lecture notes in computer science*, pages 471–483, 2006.

W. J. Brtko and R. L. Kabel. Pollutant transfer into water bodies. *Water, Air and Soil Pollution*, 6(1):71–95, 1976. doi: 10.1007/BF00158716.

A. Bruhn and J. Weickert. Confidence measures for variational optic flow methods. Technical report, Faculty of Mathematics and Computer Science, Saarland University, 2004.

A. Bruhn, J. Weickert, C. Feddern, T. Kohlberger, and C. Schnörr. Real-time optical flow computation with variational methods. In N. Petkov, M. A. Westenberg, and ., editors, *CAIP 2003*, volume 2756 of *Lecture Notes in Computer Science*, pages 222–229. Springer, 2003.

A. Bruhn, J. Weickert, and C. Schnörr. Lucas/kanade meets horn/schunck: combining local and global optic flow methods. *International Journal of Computer Vision*, 61(3):211–231, 2005.

W. Brutsaert. A theory for local evaporation (or heat transfer) from rough to smooth surfaces at ground level. *Water Resource Research*, 11:543–550, 1975a.

W. Brutsaert. The roughness length for water vapor, sensible heat, and other scalars. *Journal of Atmospherical Sciences*, 32(10):2028–2031, 1975b.

W. L. Burke. *Applied Differential Geometry*. Cambridge University Press, 1985.

J. R. Burns and C. Ramshaw. The intensification of rapid reactions in multiphase systems using slug flow in capillaries. *Lab on a Chip*, 1(1):10–15, 2001.

G. Busse, D. Wu, and W. Karpen. Thermal wave imaging with phase sensitive modulated thermography. *Journal of Applied Physics*, 71(8):3962–3965, 1992.

J. Böhm. Capillarität und saftsteigen. *Berichte der Deutschen Botanischen Gesellschaft*, 11: 203–212, 1893.

V. Caselles and B. Coll. Snakes in movement. *SIAM Journal on Numerical Analysis*, 33: 2445–2456, 1996.

C. C. Chu, C. T. Wang, and C. S. Hsieh. An experimental investigation of vortex motions near surfaces. *Physics of Fluids A*, 5(3):662–676, 1993. doi: 10.1063/1.858650.

C. H. Chu and E. J. Delp. Estimating displacement vectors from an image sequence. *Journal of the Optical Society of America A*, 6(6):871–878, 1989.

G. Coombe, M. J. Harris, and A. Lastra. Radiosity on graphics hardware. In *Proc. Graphics Interface 2004*, 2004.

D. Cremers and C. Schnörr. Motion competition: Variational integration of motion segmentation and shape regularization. In L. Van Gool, editor, *Pattern Recognition - Proc. of the DAGM*, volume 2449 of *Lecture Notes in Computer Science*, pages 472–480, 2002.

D. Cremers and S. Soatto. Motion competition: A variational framework for piecewise parametric motion segmentation. *International Journal of Computer Vision*, 62(3):249–265, 2004.

P. V. Danckwerts. Significance of a liquid-film coefficients in gas absorption. *Industrial and Engineering Chemistry*, 43:1460–1467, 1951.

T. E. Daubert, R. P. Danner, H. M. Sibul, C. C. Stebbins, J. L. Oscarson, R. L. Rowley, W. V. Wilding, M. E. Adams, T. L. Marshall, and N. A. Zundel. *DIPPR Data Compilation of Pure Compound Properties*. Design Institute for Physical Property Data, AIChe, New York, NY, 2000.

C. A. Davatzikos, R. N. Bryan, and J. L. Prince. Image registration based on boundary mapping. *IEEE Trans.on medical imaging*, 15(1):112–115, 1996.

E. L. Deacon. Gas transfer to and across an air-water interface. *Tellus*, 29:363–374, 1977.

J. W. Demmel and K. Veseliç. Jacobi's method is more accurate than QR. *SIAM Journal on Matrix Analysis and Applications*, 13(4):1204–1245, 1992.

G. Desmet, D. Cabooter, P. Gzil, H. Verelst, D. Mangelings, Y. V. Heyden, and D. Clicq. Future of high pressure liquid chromatography: Do we need porosity or do we need pressure? *Journal of Chromatography A*, 1130(Spec.Iss.1):158–166, 2006. doi: 10.1016/j.chroma.2006.05.082.

Z. Drmac. Implementation of Jacobi rotations for accurate singular value computation in floating point arithmetic. *SIAM Journal of Scientific Computing*, 18(4):1200–1222, 1997.

M. Droske, W. Ring, and M. Rumpf. Mumford-shah based registration. *Computing and Visualization in Science*, 2005. Submitted.

B. Duc. Motion estimation using invariance under group transformations. In *Proc. of the 12th IAPR International Conference on Pattern Recognition*, volume 1, pages 159–163, Los Alamitos, CA, 1994. IEEE Comput. Soc. Press.

B. Duc. *Feature Design: Applications to Motion Analysis and Identity Verification*. PhD thesis, École Polytechnique Fédérale de Lausanne, 1997.

A. D. Dussaud, S. M. Troian, and S. R. Harris. Fluorescence visualization of a convective instability which modulates the spreading of volatile surface films. *Physics of Fluids*, 10(7):1588–1596, 1998. doi: 10.1063/1.869678.

D. Dutta and J. Leighton, D. T. Dispersion reduction in pressure-driven flow through microetched channels. *Analytical Chemistry*, 73(3):504–513, 2001. doi: 10.1021/ac0008385.

C. Eckhart and G. Young. The approximation of one matrix by another of lower rank. *Psychometrica*, 1:211–218, 1936.

J. C. T. Eijkel and A. van den Berg. Nanofluidics: what is it and what can we expect from it? *Microfluidics and Nanofluidics*, 1(3):249–267, 2005.

A. Einstein. Über die von der molekularkinetischen Theorie der Wärme geforderte Bewegung von in ruhenden Flüssigkeiten suspendierten Teilchen. *Annalen der Physik*, 322(8):549–560, 1905. doi: 10.1002/andp.19053220806.

L. C. Evans and R. F. Gariepy. *Measure Theory and Fine Properties of Functions*. CRC PRess, 1992.

C. W. Fairall, E. F. Bradley, J. S. Godfrey, G. A. Wick, and J. B. Edson. Cool-skin and warm-layer effects on sea surface temperature. *Journal of Geophysical Research*, 101(C1):1295–1308, 1996a.

C. W. Fairall, E. F. Bradley, D. P. Rogers, J. B. Edson, and G. S. Young. Bulk parameterization of air-sea fluxes for tropical ocean-global atmosphere coupled-ocean atmosphere response experiment. *Journal of Geophysical Research*, 101(C2):3747–3764, 1996b.

C. W. Fairall, J. E. Hare, J. B. Edson, and W. R. McGillis. Parameterization and micrometeorological measurements of air-sea gas transfer. *Boundary-Layer Meteorology*, 96:63–105, 2000.

R. E. Falco and C. C. Chu. Measurement of two-dimensional fluid dynamic quantities using a photochromic grid tracing technique. In *International Conference on Photomechanics and Speckle Metrology*, volume 2, pages 706–710, San Diego, CA, 1988. SPIE.

R. E. Falco and D. G. Nocera. Quantitative multipoint measurements and visualization of dense liquid-solid flows using laser induced photochemical anemometry (lipa). In M. C. Rocco, editor, *Particulate Two-Phase Flow*, pages 59–126. Butterworth-Heinemann, 1993.

G. Farnebäck. Fast and accurate motion estimation using orientation tensors and parametric motion models. In *ICPR*, volume 1, pages 135–139, Barcelona, Spain, September 2000.

G. D. Farquhar and T. D. Sharkey. Stomatal conductance and photosynthesis. *Annual Review of Plant Physiology*, 33:317–345, 1982.

C. Fennema and W. Thompson. Velocity determination in scenes containing several moving objects. *Computer Graphics and Image Processing*, 9:301–315, 1979.

O. Feron and A. Mohammad-Djafari. A hidden markov model for image fusion and their joint segmentation in medical image computing. *ArXiv Physics e-prints*, 2004.

A. E. Fick. Über Diffusion. *Annalen der Physik*, 94(4):59–86, 1855.

D. Figeys and D. Pinto. Lab-on-a-chip: A revolution in biological and medical sciences. *Analytical Chemistry*, 72(9):330A–335A, 2000.

D. J. Fleet. *Measurement of Image Velocity*. Kluwer Academic Publishers, Dordrecht, The Netherlands, 1992.

G. E. Fortescue and J. R. A. Pearson. On gas absorption into a turbulent liquid. *Chemical Engineering Science*, pages 1163–1176, 1967.

J. B. Fourier. Théorie analytique de la chaleur. In *Œuvres de Fourier*. Gauthier-Villars et Fils, Paris, France, 1822.

N. M. Frew, E. J. Bock, W. R. McGillis, A. V. Karachintsev, T. Hara, T. Münsterer, and B. Jähne. Variation of air-water gas transfer with wind stress and surface viscoelasticity. In e. Jähne and E. C. Monahan, editors, *Air-water gas transfer, selected papers from the third international symposium on air-water gas transfer*, Hanau, 1995.

C. Fujimoto, Y. Fujise, and E. Matsuzawa. Fritless packed columns for capillary electrochromatography: Separation of uncharged compounds on hydrophobic hydrogels. *Analytical Chemistry*, 68(17):2753–2757, 1996. doi: 10.1021/ac9601775.

P. P. Gallo. Consistency of regression estimates when some variables are subject to error. *Communications in statistics / Theory and methods*, 11:973–983, 1982.

C. Garbe, K. Degreif, and B. Jähne. Estimating the viscous shear stress at the water surface from active thermography. In C. Garbe, R. A. Handler, and B. Jähne, editors, *Transport*

at the Air Sea Interface - Measurements, Models and Parametrizations, pages 223–239. Springer-Verlag, 2007a. doi: 10.1007/978-3-540-36906-6_16.

C. Garbe, R. A. Handler, and B. Jähne. *Transport at the Air-Sea Interface - Measurements, Models and Parameterizations*. Springer-Verlag, Heidelberg, 2007b. ISBN 978-3-540-36904-2. doi: 10.1007/978-3-540-36906-6.

C. Garbe, K. Roetmann, V. Beushausen, and B. Jähne. An optical flow MTV based technique for measuring microfluidic flow in the presence of diffusion and taylor dispersion. *Experiments in Fluids*, 44(3):439–450, 2008. doi: 10.1007/s00348-007-0435-7.

C. S. Garbe. *Measuring Heat Exchange Processes at the Air-Water Interface from Thermographic Image Sequence Analysis*. PhD thesis, University of Heidelberg, Heidelberg, Germany, December 2001.

C. S. Garbe and B. Jähne. Reliable estimates of the sea surface heat flux from image sequences. In B. Radig, editor, *Mustererkennung 2001, 23. DAGM Symposium, München*, number 2191 in LNCS Lecture notes on computer science, pages 194–201. Springer-Verlag, 2001.

C. S. Garbe and R. Strzodka. Real-time performance of range flow and optical flow with brightness change. *IEEE Transaction on Image Processing*, 2007. In Preparation.

C. S. Garbe, B. Jähne, and H. Haußecker. Measuring the sea surface heat flux and probability distribution of surface renewal events. *Gas Transfer at Water Surfaces, Geophysical Monograph*, 127:109–114, 2002a.

C. S. Garbe, U. Schimpf, and B. Jähne. Measuring important parameters for air-sea heat exchange. In X. P. Maldague and A. E. Rozlosnik, editors, *ThermoSense*, volume 4710, pages 171–182, Orlando, Florida, 2002b. The International Society for Optical Engineering, SPIE.

C. S. Garbe, U. Schimpf, U. Schurr, and B. Jähne. Thermographic measurements in environmental and bio sciences. In *Quantitative Infrared Thermography*, volume 6, pages 253–259, 2002c.

C. S. Garbe, U. Schurr, and B. Jähne. Thermographic measurements on plant leaves. In X. P. Maldague and A. E. Rozlosnik, editors, *ThermoSense*, volume 4710, pages 407–416. The International Society for Optical Engineering, SPIE, 2002d.

C. S. Garbe, H. Spies, and B. Jähne. Mixed ols-tls for the estimation of dynamic processes with a linear source term. In L. Van Gool, editor, *Pattern Recognition*, volume LNCS 2449 of *Lecture Notes in Computer Science*, pages 463–471, Zurich, CH, 2002e. Springer-Verlag.

C. S. Garbe, N. Smoljar, M. Komiyenko, and U. Schurr. Water relations in plant leaves. In B. Jähne, editor, *Image Sequence Analysis to Investigate Dynamic Processes*, LNCS, Lecture Notes in Computer Science, chapter 10, pages 180–220. Springer-Verlag, Heidelberg, 2003a. Accepted.

C. S. Garbe, H. Spies, and B. Jähne. Estimation of surface flow and net heat flux from infrared image sequences. *Journal of Mathematical Imaging and Vision*, 19(3):159–174, 2003b. doi: 10.1023/A:1026233919766.

C. S. Garbe, H. Spies, and B. Jähne. Estimation of complex motion from thermographic image sequences. In K. E. Cramer and X. P. Maldague, editors, *Thermosense XXV*, pages 303–317, 2003c.

C. S. Garbe, U. Schimpf, and B. Jähne. A surface renewal model to analyze infrared image sequences of the ocean surface for the study of air-sea heat and gas exchange. *Journal of Geophysical Research*, 109(C08S15):1–18, 2004. doi: 10.1029/2003JC001802.

C. S. Garbe, K. Roetmann, and B. Jähne. An optical flow based technique for the non-invasive measurement of microfluidic flows. In *12th International Symposium on Flow Visualization*, pages 1–10, Göttingen, Germany, 2006.

C. S. Garbe, R. Pieruschka, and U. Schurr. Thermographic measurements of xylem flow in plant leaves. *New Phytologist*, 2007c. In preparation.

C. F. Gauss. Theoria combinationis observationum erroribus minimis obnoxiae. *Comment.Soc.Reg.Sci.Gotten.Recent.*, 5:33–90, 1823.

K. R. Gee, E. S. Weinberg, and D. J. Kozlowski. Caged q-rhodamine dextran: a new photoactivated fluorescent tracer. *Bioorganic & Medicinal Chemistry Letters*, 11(16):2181–2183, 2001. doi: 10.1016/S0960-894X(01)00421-8.

G. L. Geernaert. Theory of air-sea momentum, heat and gas fluxes. In G. L. Geernaert, editor, *Air-Sea Exchange, Physics, Chemistry and Dynamics*, pages 25–48. Kluwer Academic Press, 1999.

D. Geiger, B. Ladendorf, and A. Yuille. Occlusions and binocular stereo. *International Journal of Computer Vision*, 14(3):211–226, 1995.

A. Gelb. *Applied Optimal Estimation*. M.I.T. Press, Cambridge, MA, 1974.

C. P. Gendrich and M. M. Koochesfahani. A spatial correlation technique for estimating velocity fields using molecular tagging velocimetry (mtv). *Experiments in Fluids*, 22(1): 67–77, 1996. doi: 10.1007/BF01893307.

C. P. Gendrich, M. M. Koochesfahani, and D. G. Nocera. Molecular tagging velocimetry and other novel applications of a new phosphorescent supramolecule. *Experiments in Fluids*, 23 (5):361–372, 1997. doi: 10.1007/s003480050123.

L. J. Gleser. Estimation in a multivariate "error in variables" regression model: Large sample results. *Annals of Statistics*, 9:24–44, 1981.

H. Goldstein. *Classical Mechanics*. Addison-Wesley Series in Physics. Addison-Wesley, Reading,MA, 2nd edition, 1980.

T. Gollan, U. Schurr, and E.-D. Schulze. Stomatal composition to drying soil in relation to changes in the xylem sap composition of Helianthus annuus I. The concentration of cations, anions, amino acids in, and pH of, the xylem sap. *Plant Cell Environ*, 15:551–559, 1992.

P. Golland and A. M. Bruckstein. Motion from color. *Computer Vision and Image Understanding*, 68(3):346–362, 1997.

G. H. Golub and C. F. van Loan. An analysis of the total least squares problem. *SIAM Journal on Numerical Analysis*, 17(6):883–893, December 1980.

G. H. Golub and C. F. van Loan. *Matrix Computations*. The Johns Hopkins University Press, Baltimore and London, 3 edition, 1996.

N. Goodnight, C. Woolley, G. Lewin, D. Luebke, and G. Humphreys. A multigrid solver for boundary-value problems using programmable graphics hardware. In *Eurographics/SIGGRAPH Workshop on Graphics Hardware*, 2003.

G. H. Granlund and H. Knutsson. *Signal Processing for Computer Vision*. Kluwer Academic, Dordrecht, The Netherlands, 1995.

C. W. Groetsch. *Inverse problems in the mathematical sciences*. Vieweg, Braunschweig, 1993.

P. Guillaurne, R. Pintelon, and J. Schoukens. Weighted total least squares estimator for multivariable systems with nearly maximum likelyhood properties. *IEEE Transactions on Instrumentation and Measurment*, 47(4):818–822, 1998.

S. N. Gupta and J. L. Prince. Stochastic models for div-curl optical flow methods. *IEEE Signal Processing Letters*, 3(2):32–34, 1996.

W. Hackbusch. *Theorie und Numerik elliptischer Differentialgleichungen*. Teubner, Stuttgart, Germany, 1986.

J. Hadamard. Sur les problèmes aux dérivées partielles et leur signification physique. *Princeton University Bulletin*, pages 49–52, 1902.

T. Hara, E. VanInwegen, J. Wendelbo, C. S. Garbe, U. Schimpf, B. Jähne, and N. M. Frew. Estimation of air-sea gas and heat fluxes from infrared imagery based on near surface turbulence models. In *Proc. International Workshop on Transport at the Air Sea Interface*, 2006.

J. E. Hare. Personal communication, 2001.

P. Hariott. A random eddy modification of the penetration theory. *Chemical Engineering Science*, 17:149–154, 1962.

R. Hartenstein. Data-stream-based computing: Models and architectural resources. In *International Conference on Microelectronics, Devices and Materials (MIDEM 2003)*, Ptuj, Slowenia, 2003.

K. M. Hasan, P. J. Basser, D. L. Parker, and A. L. Alexander. Analytical computation of the eigenvalues and eigenvectors in DT-MRI. *Journal of Magnetic Resonance*, 152:41–47, 2001. doi:10.1006/jmre.2001.2400.

H. Haußecker. *Messung und Simulation von kleinskaligen Austauschvorgängen an der Ozeanoberfläche mittels Thermographie*. PhD thesis, University of Heidelberg, 1996.

H. Haußecker and D. J. Fleet. Computing optical flow with physical models of brightness variation. *PAMI*, 23(6):661–673, June 2001.

H. Haußecker and H. Spies. Motion. In B. Jähne, H. Haußecker, and P. Geißler, editors, *Handbook of Computer Vision and Applications*, volume 2, chapter 13. Academic Press, 1999.

H. Haußecker, S. Reinelt, and B. Jähne. Heat as a proxy tracer for gas exchange measurements in the field: Principles and technical realization. In B. Jähne and E. C. Monahan, editors, *Air-Water Gas Transfer - Selected Papers from the Third International Symposium on Air-Water Gas Transfer*, pages 405–413, Heidelberg, 1995. AEON Verlag & Studio Hanau.

H. Haußecker, C. Garbe, H. Spies, and B. Jähne. A total least squares framework for low-level analysis of dynamic scenes and processes. In *DAGM*, pages 240–249, Bonn, Germany, 1999. Springer.

H. Haußecker, U. Schimpf, C. S. Garbe, and B. Jähne. Physics from IR image sequences: Quantitative analysis of transport models and parameters of air-sea gas transfer. In E. Saltzman, M. Donelan, W. Drennan, and R. Wanninkhof, editors, *Gas Transfer at Water Surfaces*, Geophysical Monograph. American Geophysical Union, 2001.

D. J. Heeger. Model for the extraction of image flow. *J.Opt.Soc.Am.A*, 4(8):1455–1471, 1987.

R. Higbie. The rate of absorption of a pure gas into a still liquid during short periods of exposure. *Trans.Am.Inst.Chem.Eng.*, 31:365–389, 1935.

E. C. Hildreth. Computations underlying the measurement of visual motion. *Artificial Intelligence*, 23:309–354, 1984.

R. B. Hill and J. C. Klewicki. Data reduction methods for flow tagging velocity measurements. *Experiments in Fluids*, 20(3):142–152, 1996. doi: 10.1007/BF00190270.

V. Hohreiter, S. T. Wereley, M. G. Olsen, and J. N. Chung. Cross-correlation analysis for temperature measurement. *Measurement Science and Technology*, 13(7):1072–1078, 2002. doi: 10.1088/0957-0233/13/7/314.

M. Hopf and T. Ertl. Accelerating 3d convolution using graphics hardware. In *Proc. IEEE Visualization 1999*, pages 471–474, 1999.

B. K. P. Horn and J. Harris. Rigid body motion from range image sequences. *CVGIP*, 53(1): 1–13, January 1991.

B. K. P. Horn and B. Schunk. Determining optical flow. *Artificial Intelligence*, 17:185–204, 1981.

A. S. Householder. Unitary triangularization of a nonsymmetric matrix. *Journal of the ACM Association for Computing Machinery*, 5(4):339–342, 1958. doi: 10.1145/320941.320947.

P. J. Huber. *Robust Statistics*. New York, Wiley, 1980.

P. J. Huber. *Robust Statistics*. John Wiley and Sons, New York, 1981.

J. Ilmberger. Impulsübertrag und Strömungsverhältnisse in einem runden Wind-Wasser Kanal. Master's thesis, University of Heidelberg, 1980.

S. Jahnke. Atmospheric co2 concentration does not directly affect leaf respiration in bean or poplar. *Plant Cell and Environment*, 24:1139–1151, 2001.

M. Jehle. *A novel method for spatiotemporal of flows within the water-side viscous boundary-layer*. PhD thesis, University of Heidelberg, 2007.

A. T. Jessup, C. J. Zappa, M. R. Loewen, and V. Hesany. Infrared remote sensing of breaking waves. *Nature*, 385(6611):52–55, 1997a.

A. T. Jessup, C. J. Zappa, and H. H. Yeh. Defining and quantifying microscale wave breaking with infrared imagery. *Journal of Geophysical Research*, 102(C10):23145–23153, 1997b.

J. W. Jorgenson and K. D. Lukacs. Capillary zone electrophoresis. *Science*, 222(4621):266–272, 1983. doi: 10.1126/science.6623076.

B. Jähne. *Parametrisierung des Gasaustausches mit Hilfe von Laborexperimenten*. PhD thesis, Institut für Umweltphysik, University of Heidelberg, 1980.

B. Jähne. *Spatio-Temporal Image Processing : Theory and Scientific Applications*. Lecture Notes in Computer Science. Springer-Verlag, 1993.

B. Jähne. *Digital Image Processing*. Springer, Berlin, Germany, 3 edition, 1995.

B. Jähne. *Digital Image Processing*. Springer, Berlin, Germany, 4th edition, 1997.

B. Jähne. Neighborhood operators. In B. Jähne, H. Haußecker, and P. Geißler, editors, *Handbook of Computer Vision and Applications*, volume 2, chapter 5, pages 93–124. Academic Press, 1999.

B. Jähne. *Digital Image Processing*. Springer, Berlin, Germany, 6 edition, 2005.

B. Jähne and C. S. Garbe. Towards objective performance analysis for estimation of complex motion: analytic motion modeling, filter optimization, and test sequences. In *Proc. of the International Conference on Image Processing (ICIP)*, volume 3, pages 73–76, 2003.

B. Jähne and H. Haußecker. Air-water gas exchange. *Annual Reviews Fluid Mechanics*, 30: 443–468, 1998.

B. Jähne, K. O. Münnich, R. Bösinger, A. Dutzi, W. Huber, and P. Libner. On the parameters influencing air-water gas exchange. *Journal of Geophysical Research*, 92(C2):1937–1949, 1987.

B. Jähne, P. Libner, R. Fischer, T. Billen, and E. J. Plate. Investigating the transfer process across the free aqueous boundary layer by the controlled flux method. *Tellus*, 41B(2): 177–195, 1989.

B. Jähne, H. Haußecker, H. Scharr, H. Spies, D. Schmundt, and U. Schurr. Study of dynamical processes with tensor-based spatiotemporal image processing techniques. In *ECCV*, pages 322–336. Springer, 1998.

B. Jähne, H. Scharr, and S. Körkel. Principles of filter design. In B. Jähne, H. Haußecker, and P. Geißler, editors, *Handbook of Computer Vision and Applications*, volume 2, pages 125–151. Academic Press, 1999.

B. Jähne, C. Popp, U. Schimpf, and C. S. Garbe. Analysis of the heat transfer process across the aqueous heat boundary layer by active thermography: mean transfer velocities and intermittence. In *Transport at the Air Sea Interface-Measurements, Models and Parameterizations*. Springer, 2007. Submitted for Review.

K. Kanatani. *Group-Theoretical Methods in Image Understanding*. Springer Series in Information Sciences. Springer-Verlag, Heidelberg, Germany, 1990.

T. Kapur, L. Yezzi, and L. Zöllei. A variational framework for joint segmentation and registration. In *Proc. of the CVPR*, pages 44–51, 2001.

M. Karczewicz, J. Nieweglowski, and P. Haavisto. Video coding using motion compensation with polynomial motion vector fields. *Signal Processing: Image Communication*, 10(1-3): 63–91, 1997.

S. L. Keeling and W. Ring. Medical image registration and interpolation by optical flow with maximal rigidity. *Journal of Mathematical Imaging and Vision*, 23(1):47–65, 2005. doi: 10.1007/s10851-005-4967-2.

H. Knutsson and G. Granlund. Texture analysis using two-dimensional quadrature filters. In H. Knutsson and G. Granlund, editors, *IEEE Workshop Comp. Arch. Patt. Anal. Im. Dat. Base Man*, Pasadena, CA, 1983.

H. Knutsson and C. F. Westin. Normalized and differential convolution: Methods for interpolation and filtering of incomplete and uncertain data. In *CVPR*, pages 515–516, New York City, June 1993.

K. R. Koch. *Parameter Estimation and Hypothesis Testing in Linear Models*. Springer-Verlag, Heidelberg, Germany, 1988.

A. N. Kolmogorov. A refinement of previous hypotheses concerning the local structure of turbulence in a viscous incompressible fluid at high reynolds number. *Journal of Fluid Mechanics*, 13:82–85, 1962.

D. Kondermann, C. Kondermann, C. S. Garbe, and B. Jähne. Global optical flow methods with brightness change invariance. *IEEE Transactions on Pattern Analysis and Machine Intelligence*, 2007. In preparation.

M. M. Koochesfahani, C. P. Gendrich, and D. G. Nocera. A new technique for studying the lagrangian evolution of mixing interfaces in water flows. *Bull Am Phy Soc*, 38:2287, 1993.

E. B. Kraus and J. A. Businger. *Atmosphere-ocean interaction*. Number 27 in Oxford monographs on geology and geophysics. Oxford University Press, New York, second edition, 1994.

W. G. Kuhr, L. Licklider, and L. Amankwa. Imaging of electrophoretic flow across a capillary junction. *Analytical Chemistry*, 65(3):277–282, 1993. doi: 10.1021/ac00051a015.

T. Kukulka and T. Hara. Momentum flux budget analysis of wind-driven air-water interfaces. *Journal of Geophysical Research*, 110:C12020, 2005. doi: 10.1029/2004JC002844.

P. K. Kundu. *Fluid Mechanics*. Academic Press, San Diego, CA, 1990.

W. Köckenberger, J. M. Pope, Y. Xia, K. R. Jeffrey, E. Komor, and P. T. Callaghan. A non-invasive measurement of phloem and xylem water flow in castor bean seedlings by nuclear resonance microimaging. *Planta*, 201(1):53–63, 1997.

J. C. Lamont and D. C. Scott. An eddy cell model of mass transfer into the surface of a turbulent liquid. *A.I.Ch.E.J*, 16(4):513–519, 1970. doi: 10.1002/aic.690160403.

L. D. Landau and E. M. Lifschitz. *Mechanik*. Lehrbuch der theoretischen Physik. Akademie Verlag, Berlin, 13th edition, 1990.

C. L. Lawson and D. J. Hanson. *Solving Least Squares Problems*. Prentice-Hall, Englewood Cliffs, New Jersey, 1974.

A. Lefohn, J. Kniss, C. Handen, and R. Whitaker. Interactive visualization and deformation of level set surfaces using graphics hardware. In *Proc. of IEEE Visualization 2003*, pages 73–82, 2003.

P. Lemmerling, I. Dologlou, and S. Van Huffel. On the formal equivalence between static and dynamic least squares and total least squares models. Technical Report TR 1998-95, Department of Electrical Engineering, ESAT-SISTA, Katholieke Universiteit Leuven, Heverlee, Belgium, 1998.

W. R. Lempert and S. R. Harris. Flow tagging velocimetry using caged dye photo-activated fluorophores. *Measurement Science and Technology*, 11(9):1251–1258, 2000. doi: 10.1088/0957-0233/11/9/302.

W. R. Lempert, P. Ronney, K. Magee, K. R. Gee, and R. P. Haugland. Flow tagging velocimetry in incompressible flow using photo-activated nonintrusive tracking of molecular motion (phantomm). *Experiments in Fluids*, 18(4), 1995. doi: 10.1007/BF00195095.

M. H. Lin and C. Tomasi. Surfaces with occlusions from layered stereo. *IEEE Transactions on Pattern Analysis and Machine Intelligence*, 26(8):1073–1078, 2004.

P. S. Liss and L. Merlivat. Air-sea gas exchange rates: Introduction and synthesis. In P. Buat-Menard, editor, *The role of air-sea exchange in geochemical cycling*, pages 113–129. Reidel, Boston,MA, 1986.

P. S. Liss and P. G. Slater. Flux of gases across the air-sea interface. *Nature*, 247:181–184, 1974. doi: 10.1038/247181a0.

W. T. Liu and J. A. Businger. Temperature profile in the molecular sublayer near the interface of a fluid in turbulent motion. *Geophysical Research Letters*, 2:403, 1975.

W. T. Liu, K. B. Katsaros, and J. A. Businger. Bulk parameterization of air-sea exchanges of heat and water vapor including the molecular constraints at the interface. *Journal of Atmospherical Sciences*, 36(9):1722–1735, 1979.

T. J. Lough and W. J. Lucas. Integrative plant biology: Role of phloem long-distance macromolecular trafficking. *Annual Review of Plant Biology*, 57:203–232, 2006. doi: 10.1146/annurev.arplant.56.032604.144145.

B. Lucas and T. Kanade. An iterative image registration technique with an application to stereo vision. In *DARPA Image Understanding Workshop*, pages 121–130, 1981.

B. D. Lucas. *Generalized image matching by the method of differences*. PhD thesis, Carnegie-Mellon University, Pittsburgh, PA, 1984.

M. R. Luettgen, W. C. Karl, and A. S. Willsky. Efficient multiscale regularization with application to the computation of optical flow. *IEEE Transactions on Image Processing*, 3 (1):41–64, 1994.

K. V. Mardia, J. T. Kent, and J. M. Bibby. *Multivariate Analysis*. Probability and Mathematical Statistics. Academic Press, San Diego, 1979.

B. McCane, K. Novins, D. Crannitch, and B. Galvin. On benchmarking optical flow. *Computer Vision and Image Understanding*, 84(1):126–143, 2001.

W. R. McGillis, J. B. Edson, J. E. Hare, and C. W. Fairall. Direct covariance air-sea CO_2 fluxes. *Journal of Geophysical Research*, 106(C8):16729–16745, 2001a.

W. R. McGillis, J. B. Edson, J. D. Ware, J. W. H. Dacey, J. E. Hare, C. W. Fairall, and R. Wanninkhof. Carbon dioxide flux techniques performed during gasex-98. *Marine Chemistry*, 75(4):267–280, 2001b.

W. R. McGillis, J. B. Edson, C. J. Zappa, J. D. Ware, S. P. McKenna, E. A. Terray, J. E. Hare, C. W. Fairall, W. Drennan, M. Donelan, M. D. DeGrandpre, R. Wanninkhof, and R. A. Feely. Air-sea CO_2 exchange in the equatorial Pacific. *Journal of Geophysical Research-Oceans*, 109(C8):C08S02, 2004.

S. P. McKenna and W. R. McGillis. The role of free-surface turbulence and surfactants in air-water gas transfer. *International Journal of Heat and Mass Transfer*, 47(3):539–553, 2004. doi: 10.1016/j.ijheatmasstransfer.2003.06.001.

W. McLeish and G. E. Putland. Measurements of wind-driven flow profiles in the top millimeter of water. *Journal of Physical Oceanography*, 5(3):516–518, 1975. doi: 10.1175/1520-0485(1975)005<0516:MOWDFP>2.0.CO;2.

W. Menke. *Geophysical Data Analysis: Discrete Inverse Theory*. International Geophysics Series. Academic Press, San Diego, 1989.

C. Meola, G. M. Carlomagno, A. Squillace, and A. Vitiello. Non-destructive evaluation of aerospace materials with lock-in thermography. *Engineering Failure Analysis*, 13(3):380–388, 2006.

A. Merz. Die Oberflächentemperatur der Gewässer, Methoden und Ergebnisse. In *Veröffentlichungen des Instituts für Meereskunde*, volume 5 of *Neue Folge, A*, page 42pp. Universität Berlin, 1920.

R. Mester and M. Mühlich. Improving motion and orientation estimation using an equilibrated total least squares approach. In *ICIP*, Greece, October 2001.

R. Miles, C. Cohen, J. Connors, P. Howard, and S. Huang. Velocity measurements by vibrational tagging and fluorescent probing of oxygen. *Optics Letters*, 12:861–863, 1987.

L. Mirsky. Symmetric gauge functions and unitarily invariant norms. *The Quarterly Journal of Mathematics*, 11:50–59, 1960.

C. Mota, I. Stuke, and E. Barth. Analytic solutions for multiple motions. In *Proc. of International Conference on Image Processing*, volume 2, pages 917–920, 2001.

D. Mumford and J. Shah. Optimal approximation by piecewise smooth functions and associated variational problems. *Communications on Pure and Applied Mathematics*, 42:577–685, 1989.

E. Mémin and P. Pérez. A multigrid approach for hierarchical motion estimation. In *ICCV*, pages 933–938, 1998.

M. Mühlich and T. Aach. A theory of multiple orientation estimation. In A. Leonardis, H. Bischof, and A. Pinz, editors, *Computer Vision – ECCV 2006*, volume 3952 of *Lecture Notes in Computer Science*, pages 69–82. Springer, 2006.

M. Mühlich and R. Mester. Subspace methods and equilibration in computer vision. Technical Report XP-TR-C-21, Institute for Applied Physics, Goethe-Universitaet, Frankfurt, Germany, November 1999.

K. O. Münnich and D. Flothmann. Gas exchange in relation to other air-sea interaction phenomena. In *SCOR Workshop on Air-Sea Interaction Phenomena*, Miami, FL, USA, 1975.

T. Münsterer and B. Jähne. Lif measurements of concentration profiles in the aqueous mass boundary layer. *Experiments in Fluids*, 25(3):190–196, 1998. doi: 10.1007/s003480050223.

H. H. Nagel. Displacement vectors derived from second-order intensity variations in image sequences. *Computer Graphics and Image Processing*, 21:85–117, 1983.

H. H. Nagel. On the estimation of optical flow: Relations between different approaches and some new results. *Artificial Intelligence*, 33(3):299–324, 1987.

H. H. Nagel and W. Enkelmann. An investigation of smoothness constraints for the estimation of dispalcement vector fields from image sequences. *PAMI*, 8(5):565–593, September 1986.

S. Negahdaripour and C. H. Yu. A generalized brightness chane model for computing optical flow. In *International Conference in Computer Vision*, pages 2–7, Berlin, 1993.

P. Nesi. Variational approach to optical flow estimation managing discontinuities. *Image and Vision Computing*, 11(7):419–439, 1993. doi: 10.1016/0262-8856(93)90046-J.

N.-T. Nguyen and S. T. Wereley. *Fundamentals And Applications of Microfluidics, Second Edition*. Artech House Publishers, 2006.

R. Nielsen. *Gasaustausch - Entwicklung und Ergebnis eines schnellen Massenbilanzverfahrens zur Messung der Austauschparameter*. PhD thesis, Institut für Umweltphysik, University of Heidelberg, Heidelberg, Germany, 2004.

C. Nieuwenhuis, D. Kondermann, B. Jähne, and C. S. Garbe. On confidence measures and their optimality for optical flows. *International Journal of Computer Vision*, 2007. In preparation.

T. Nir, R. Kimmel, and A. M. Bruckstein. Variational approach for joint optic-flow computation and video restoration. Technical report, Department of Computer Science - Israel Institute of Technology, Haifa, Israel, 2005.

A. Nomura, H. Miike, and K. Koga. Determining motion fields under non-uniform illumination. *Pattern Recognition Letters*, 16:285–296, 1995.

NVIDIA. Cg programming language. http://developer.nvidia.com/view.asp?PAGE=cg_main, 2002.

J.-M. Odobez and P. Bouthemy. Robust multiresolution estimation of parametric motion models. *Journal of Visual Communication and Image Representation*, 6(4):348–365, 1995.

J.-M. Odobez and P. Bouthemy. Direct incremental model-based image motion segmentation for video analysis. *Signal Processing*, 66:143–155, 1998.

N. Ohta. Optical flow detection by color images. In *Proc. of the IEEE International Conference on Image Processing*, pages 801–805, 1989.

K. Okuda, S. Kawai, and Y. Toba. Measurement of skin friction distribution along the surface of wind waves. *Journal of Oceanography*, 33(4):190–198, 1977. doi: 10.1007/BF02109691.

M. G. Olsen and R. J. Adrian. Out-of-focus effects on particle image visibility and correlation in microscopic particle image velocimetry. *Experiments in Fluids*, 29(7):166–174, 2000. doi: 10.1007/s003480070018.

P. J. Olver. *Applications of Lie Groups to Differential Equations*. Springer-Verlag, 1986.

M. Otte and H. H. Nagel. Optical flow estimation: Advances and comparisons. In J. O. Eklundh, editor, *Proc. Third European Conference on Computer Vision*, pages 51–60, 1994.

M. Otte and H.-H. Nagel. Estimation of optical flow based on higher-order spatiotemporal derivatives in interlaced and non-interlaced image sequences. *Artifical Intelligence*, 78(1): 5–43, 1995.

N. Papenberg, A. Bruhn, T. Brox, S. Didas, and J. Weickert. Highly accurate optic flow computation with theoretically justified warping. *International Journal of Computer Vision*, 67(2):141–158, 2006. doi: 10.1007/s11263-005-3960-y.

N. Paragios and R. Deriche. Geodesic active contours and level sets for the detection and tracking of moving objects. *IEEE Trans.Pattern Analysis and Machine Intelligence*, 22(3): 266–280, 2000.

P. H. Paul, M. G. Garguilo, and D. J. Rakestraw. Imaging of pressure- and electrokinetically driven flows through open capillaries. *Analytical Chemistry*, 70(13):2459–2467, 1998. doi: 10.1021/ac9709662.

P. Perona and J. Malik. Scale space and edge detection using anisotropic diffusion. *PAMI*, 12:629–639, July 1990.

A. D. Peuke, M. Rokitta, U. Zimmermann, L. Schreiber, and A. Haase. Simultaneous measurement of water flow velocity and solute transport in xylem and phloem of adult plants of ricinus communis over a daily time course by nuclear magnetic resonance spectrometry. *Plant, Cell and Environment*, 24:491–503, 2001.

R. Pieruschka, U. Schurr, and S. Jahnke. Lateral gas diffusion inside leaves. *Journal of Experimental Botany*, 56:857–864, 2005.

Prema. *User Manual Prema 3040 High Precision Thermometer*. Mainz, Germany, 2000.

W. Press, S. Teukolsky, W. Vetterling, and B. Flannery. *Numerical Recipes in C*. Cambridge University Press, Cambridge, MA, 2 edition, 1992.

T. Preusser, M. Droske, C. Garbe, A. Telea, and M. Rumpf. A phase filed method for joint denoising, edge detection, and motion estimation in image sequence processing. *SIAM Journal of Applied Mathematics*, 68(3):599–618, 2007. doi: 10.1137/060677409.

K. N. Rao, R. Narasimah, and M. B. Narayanan. The 'bursting' phenomenon in a turbulent boundary layer. *Journal of Fluid Mechanics*, 48:339–352, 1971.

Y. Rathi, N. Vaswani, A. Tannenbaum, and A. Yezzi. Particle filtering for geometric active contours with application to tracking moving and deforming objects. In *Proc. of the IEEE Conference on Computer Vision and Pattern Recognition*, volume 2, pages 2–9. Georgia Institute of Technology, School of Electrical and Computer Engineering, Atlanta, GA 30332, United States, 2005.

K. Roetmann, C. S. Garbe, and V. Beushausen. 2d-molecular Tagging Velocimetry zur Analyse Mikrofluidischer Strömungen. In *Tagungsband Lasermethoden in der Strömungsmesstechnik (GALA)*, pages 26/1–26/10, 2005.

K. Roetmann, C. S. Garbe, W. Schmunk, and V. Beushausen. Micro-flow analysis by molecular tagging velocimetry and planar raman-scattering. In *Proc. of 12th International Symposium on Flow Visualization*, Göttingen, Germany, 2006.

K. Roetmann, W. Schmunk, C. Garbe, and V. Beushausen. Micro-Flow Analysis by Molecular Tagging Velocimetry and Planar Raman-Scattering. *Experiments in Fluids*, 44:419–430, 2008. doi: 10.1007/s00348-007-0420-1.

L. I. Rudin, S. Osher, and E. Fatemi. Nonlinear total variation based noise removal algorithms. *Physica D*, 60(1-4):259–268, 1992. doi: 10.1016/0167-2789(92)90242-F.

L. Sack and N. M. Holbrook. Leaf hydraulics. *Annual Review of Plant Biology*, 57:361–381, 2006. doi: 10.1146/annurev.arplant.56.032604.144141.

J. G. Santiago, S. T. Wereley, C. D. Meinhart, D. J. Beebe, and R. J. Adrian. A particle image velocimetry system for microfluidics. *Experiments in Fluids*, 25(4):316–319, 1998. doi: 10.1007/s003480050235.

H. Scharr. *Optimale Operatoren in der Digitalen Bildverarbeitung*. PhD thesis, University of Heidelberg, Heidelberg, Germany, 2000.

H. Scharr. Optimal filters for extended optical flow. In *Complex Motion*, LNCS. Springer Verlag, 2006.

T. W. J. Scheenen, D. van Dusschoten, P. A. de Jager, and H. Van As. Quantification of water transport in plants with nmr imaging. *Journal of Experimental Botany*, 51(351):1751–1759, 2000.

U. Schimpf. *Untersuchung des Gasaustausches und der Mikroturbulenz an der Meeresoberfläche mittels Thermographie*. PhD thesis, University of Heidelberg, Heidelberg, Germany, 2000.

U. Schimpf, C. S. Garbe, and B. Jähne. Investigation of transport processes across the sea surface microlayer by infrared imagery. *Journal of Geophysical Research*, 109(C08S13), 2004. doi: 10.1029/2003JC001803.

P. Schlüssel, W. J. Emery, H. Grassl, and T. Mammen. On the bulk-skin temperature difference and its impact on satellite remote sensing of sea surface temperature. *Journal of Geophysical Research*, 95(C8):13341–13356, 1990.

C. Schnörr. Determining optical flow for irregular domains by minimizing quadratic functionals of a certain class. *International Journal of Computer Vision*, 6(1):25–38, 1991.

C. Schnörr. On functionals with greyvalue-controlled smoothness terms for determining optical flow. *PAMI*, 15(10):1074–1079, October 1993.

C. Schnörr. Segmentation of visual motion by minimizing convex non-quadratic functionals. In *Proc. of the 12th ICPR*, 1994.

C. Schnörr. Variational methods for adaptive image smoothing and segmentation. In B. Jähne, H. Haußecker, and P. Geißler, editors, *Handbook of Computer Vision and Applications*, volume 2, pages 451–484. Academic Press, 1999.

C. Schnörr and J. Weickert. Variational image motion computation: Theoretical framework, problems and perspectives. In *DAGM 2000*, pages 476–487, Kiel. Germany, 2000.

B. Schunk. The image flow constraint equation. *Computer Vision, Graphics and Image Processing*, 35:20–46, 1986.

U. Schurr, T. Gollan, and E.-D. Schulze. Stomatal response to drying soil in relation to changes in the xylem sap composition of Helianthus annuus. II stomatal sensitivity to abscisic acid imported from the xylem sap. *Plant Cell Environ*, 15:561–567, 1992.

R. Schwarte, H. Heinol, B. Buxbaum, T. Ringbeck, Z. Xu, and K. Hartmann. Principles of three-dimensional imaging techniques. In B. Jähne, H. Haußecker, and P. Geißler, editors, *Handbook of Computer Vision and Applications*, volume 1, pages 463–484. Academic Press, 1999.

C. E. Shannon. Communication in the presence of noise. *Proc.Institute of Radio Engineers*, 37(1):10–21, 1949.

C. Silva and J. S. Santos. Motion from occlusions. *Robotics and Autonomous Systems*, 35 (3-4):153–162, 2001.

D. Sinton. Microscale flow visualization. *Microfluidics and Nanofluidics*, 1(1):2–21, 2004.

P. Smith, T. Drummond, and R. Cipolla. Layered motion segmentation and depth ordering by tracking edges. *IEEE Transactions on Pattern Analysis and Machine Intelligence*, 26 (4):479–494, 2004.

A. V. Soloviev and P. Schlüssel. Parameterization of the cool skin of the ocean and the air-ocean gas transfer on the basis of modeling surface renewal. *Journal of Physical Oceanography*, 24(6):1339–1346, 1994.

A. V. Soloviev and P. Schlüssel. Evolution of cool skin and direct air-sea gas transfer coefficient during daytime. *Boundary-Layer Meteorology*, 77:45–68, 1996.

H. Spies. *Analysing Dynamic Processes in Range Data Sequences.* PhD thesis, University of Heidelberg, Heidelberg, Germany, July 2001.

H. Spies and C. S. Garbe. Dense parameter fields from total least squares. In L. Van Gool, editor, *Pattern Recognition*, volume LNCS 2449 of *Lecture Notes in Computer Science*, pages 379–386, Zurich, CH, 2002. Springer-Verlag.

H. Spies, T. Dierig, and C. S. Garbe. Local models for dynamic processes in image sequences. In R. P. Würtz and M. Lappe, editors, *Dynamic Perception*, pages 59–64, Berlin, 2002a. Aka GmbH.

H. Spies, B. Jähne, and J. L. Barron. Range flow estimation. *Computer Vision and Image Understanding*, 85:209–231, 2002b. doi:10.1006/cviu.2002.0970.

H. Spies, C. S. Garbe, H. Scharr, H. Haußecker, and B. Jähne. Flexible regularization schemes. In *Image Sequence Analysis to Investigate Dynamic Processes*, chapter 8. Springer-Verlag, 2003. Accepted.

M. Spivak. *A Comprehensive Introduction to Differential Geometry.* 0914098705, 3 edition, 1999.

C. Stiller and J. Konrad. Estimating motion in image sequences. *IEEE Signal Processing Magazine*, 16(4):70–91, 1999.

H. A. Stone, A. D. Stroock, and A. Ajdari. Engineering flows in small devices: Microfluidics toward a lab-on-a-chip. *Annual Review of Fluid Mechanics*, 36:381–411, 2004.

R. Strzodka and C. S. Garbe. Real-time motion estimation and visualization on graphics cards. In *Proceedings IEEE Visualization 2004*, pages 545–552, 2004.

D. Suter. Mixed finite elements and whitney forms for visual reconstruction. In B. C. Vemuri, editor, *Proceedings of SPIE - Geometric Methods in Computer Vision II*, volume 2031, pages 51–62, 1993. DOI:10.1117/12.146645.

D. Suter. Motion estimation and vector splines. In *Proc. IEEE Computer Vision and Pattern Recognition*, pages 939–942, 1994.

R. H. Swanson. A thermal flowmeter for estimating the rate of xylem sap ascent in trees. *Flow, its Measurement and Control in Science and Industry*, 1:647–652, 1975.

H. Tao, H. S. Sawhney, and R. Kumar. Object tracking with bayesian estimation of dynamic layer representations. *IEEE Transactions on Pattern Analysis and Machine Intelligence*, 24 (1):75–89, 2002.

G. Taylor. The spectrum of turbulence. In *Proc. Royal Society*, volume 102, pages 817–822, 1938.

G. Taylor. Conditions under which dispersion of a solute in a stream of solvent can be used to measure molecular diffusion. *Proc.Royal Soc.London Ser.A*, 225:473–477, 1954.

J. A. Taylor and E. S. Yeung. Imaging of hydrodynamic and electrokinetic flow profiles in capillaries. *Analytical Chemistry*, 65(20):2928–2932, 1993.

A. Telea, T. Preusser, C. S. Garbe, M. Droske, and M. Rumpf. A variational approach to joint denoising, edge detection and motion estimation. In *Pattern Recognition*, volume 4174 of *Lecture Notes in Computer Science*, pages 525–535. Springer, 2006. 10.1007/11861898.

S. Terabe. Electrokinetic chromatography: An interface between electrophoresis and chromatography. *TrAC - Trends in Analytical Chemistry*, 8(4):129–134, 1989. doi: 10.1016/0165-9936(89)85022-8.

D. Terzopoulos. Regularization of inverse visual problems involving discontinuities. *PAMI*, 8 (4):413–424, 1986.

D. Travis. *Effective Color Displays*. Academic Press, 1991.

O. Tretiak and L. Pastor. Velocity estimation from image sequences with second order differential operators. In *Proc. 7th International Conference on Pattern Recognition*, pages 20–22, 1984.

R. Tsai and T. Huang. Estimating three-dimensional motion parameters of a rigid planar patch. *IEEE Transactions on Acoustics, Speech and Signal Processing*, 29:1147–1152, 1981.

T. Tsuda, M. Ikedo, G. Jones, R. Dadoo, and R. N. Zare. Observation of flow profiles in electroosmosis in a rectangular capillary. *Journal of Chromatography A*, 632(1-2):201–207, 1993. doi: 10.1016/0021-9673(93)80045-A.

D. E. Turney, W. C. Smith, and S. Banerjee. A measure of near-surface fluid motions that predicts air-water gas transfer in a wide range of conditions. *Geophysical Research Letters*, 32(4):L04607, 2005. doi: 10.1029/2004GL021671.

S. Ullman. *The interpretation of visual motion*. The MIT Press Series in Artificial Intelligence. MIT Press, Cambridge, MA, 1979.

G. Unal, G. Slabaugch, A. Yezzi, and J. Tyan. Joint segmentation and non-rigid registration without shape priors. 2004.

S. Uras, F. Girosi, A. Verri, and V. Torre. A computational approach to motion perception. *Biological Cybernetics*, 60:79–87, 1988.

B. M. Uz, M. A. Donelan, T. Hara, and E. J. Bock. Laboratory studies of wind stress over surfacewaves. *Boundary-Layer Meteorology*, 102(2):301–331, 2002. doi: 10.1023/A:1013119313063.

H. A. van der Vorst and G. H. Golub. 150 years old and still alive: eigenproblems. In I. S. Duff and G. A. Watson, editors, *The State of the Art in Numerical Analysis*, pages 93–119. Clarendon Press, Oxford, UK, 1997.

S. Van Huffel. Total Least Squares netlib routines, http://www.netlib.org/vanhuffel/. 1989.

S. Van Huffel. On the significance of nongeneric total least squares problems. *SIAM Journal on Matrix Analysis and Applications*, 13(1):20–35, 1992.

S. Van Huffel and J. Vandewalle. Analysis and solutuion of the nongeneric total least squares problem. *SIAM Journal on Matrix Analysis and Applications*, 9:360–372, 1988.

S. Van Huffel and J. Vandewalle. Analysis and properties of the generalized total least squares problem $\boldsymbol{AX} \approx \boldsymbol{B}$ when some or all columns in A are subject to error. *SIAM Journal on Matrix Analysis and Applications*, 10(3):294–315, 1989.

S. Van Huffel and J. Vandewalle. *The Total Least Squares Problem: Computational Aspects and Analysis*. Society for Industrial and Applied Mathematics, Philadelphia, 1991.

B. C. Vemuri, J. Ye, Y. Chen, and C. M. Leonard. Image registration via level-set motion: Applications to atlas-based segmentation. *Medical Image Analysis*, 7:1–20, 2003.

F. Veron and W. K. Melville. Experiments on the stability and transition of wind-driven water surfaces. *Journal of Fluid Mechanics*, 446:25–65, 2001.

A. Verri and T. Poggio. Motion field and optical flow: Qualitative properties. *IEEE Transactions on Pattern Analysis and Machine Intelligence*, 11(5):490–498, 1989.

L. A. Vese and T. F. Chan. A multiphase level set framework for image segmentation using the mumford and shah model. *International Journal of Computer Vision*, 50:271–293, 2002.

J. Wang. From dna biosensors to gene chips. *Nucleic Acids Res.*, 28(16):3011–3016, 2000.

J. Y. A. Wang and E. H. Adelson. Representating moving images with layers. *IEEE Transaction on Image Processing*, 3(5):625–638, 1994.

R. Wanninkhof. Relationship between gas exchange and wind speed over the ocean. *Journal of Geophysical Research*, 97(C5):7373–7382, 1992.

R. Wanninkhof and W. R. McGillis. A cubic relationship between gas transfer and wind speed. *Geophysical Research Letters*, 26(13):1889–1892, 1999. doi: 10.1029/1999GL900363.

R. Wanninkhof, W. Asher, R. Wepperning, C. Hua, P. Schlosser, C. Langdon, and R. Sambrotto. Gas transfer experiment on georges bank using two volatile deliberate tracers. *Journal of Geophysical Research*, 98(C11):20237–20248, 1993.

B. Ward and S. Redfern. A neural network model for predicting the bulk-skin temperature difference at the sea surface. *International Journal of Remote Sensing*, 20(18):3533–3548, 1999.

A. J. Watson, R. C. Upstill-Goddard, and P. S. Liss. Air-sea exchange in rough and stormy seas measured by a dual tracer technique. *Nature*, 349(6305):145–147, 1991.

A. M. Waxman and K. Wohn. Contour evolution, neighborhood deformation, and global image flow: planar surfaces in motion. *International Journal of Robotics Research*, 4(3): 95–108, 1985.

A. M. Waxman, J. Wu, and F. Bergholm. Convected activation profiles and receptive fields for real time measurement of short range visual motion. In *Proc. Conf. Comput. Vis. Patt. Recog*, pages 771–723, Ann Arbor, 1988.

M. Wei. The analysis for the total least squares problem with more than one solution. *SIAM Journal on Matrix Analysis and Applications*, 13(3):746–763, 1992.

J. Weickert and C. Schnörr. A theoretical framework for convex regularizers in pde-based computation of image motion. *International Journal of Computer Vision*, 45(3):245–264, 2001.

J. D. West, D. Peak, J. Q. Peterson, and K. A. Mott. Dynamics of stomatal patches for a single surface of Xanthium strumarium L. leaves observed with fluorescence and thermal images. *Plant Cell Environ*, 28:633–641, 2005.

G. A. Wick, W. J. Emery, L. H. Kantha, and P. Schlüssel. The behavior of the bulk-skin sea surface temperature difference under varying wind speed and heat flux. *Journal of Physical Oceanography*, 26:1969–1988, 1996.

M. Wilkes. The memory gap. In *Solving the Memory Wall Problem Workshop*, http://www.ece.neu.edu/conf/wall2k/wilkes1.pdf, 2000.

A. H. Woodcock and H. Stommel. Temperatures observed near the surface of a fresh-water pond at night. *Journal of Meteorology*, 4:102–103, 1947.

D. Wu and G. Busse. Remote inspection of wood with lock-in-thermography. *Tappi Journal*, 79(8):119–123, 1996.

D. Wu, A. Salerno, J. Rantala, and G. Busse. Characterization of layered materials using lock-in thermography. *Progress in Natural Science*, 6:S76–S79, 1996.

J. Wu. On the cool skin of the ocean. *Boundary-Layer Meteorology*, 31:203–207, 1985.

J. J. Xiao and M. Shah. Motion layer extraction in the presence of occlusion using graph cuts. *IEEE Transactions on Pattern Analysis and Machine Intelligence*, 27(10):1644–1659, 2005.

M. Yamamoto, P. Boulanger, J. Beraldin, and M. Rioux. Direct estimation of range flow on deformable shape from a video rate range camera. *PAMI*, 15(1):82–89, January 1993.

J. Yuan, P. Ruhnau, E. Mémin, and C. Schnörr. Discrete orthogonal decomposition and variational fluid flow estimation. In *Proc. 5th Int. Conference on Scale Space and PDE Methods in Computer Vision*, volume 3459 of *LNCS*, pages 267–278. Springer, 2005.

X. Zhang and W.-J. Cai. On some biases of estimating the global distribution of air-sea co2 flux by bulk parameterizations. *Geophysical Research Letters*, 2006. Accepted.

X. Zhang and S. Harrison. A laboratory observation of the surface temperature and velocity distributions on a wavy and windy air–water interface. *Physics of Fluids*, 16(1):L5–L8, 2004. doi: 10.1063/1.1631813.

Acknowledgements

This work would not have been possible without a number of people that supported me to carry out this work.

First of all I would like to express my gratitude to Prof. Dr. Bernd Jähne for encouraging me to follow this line of research. It was he who introduced me to the fascinating fields of digital image processing and air-sea gas exchange. He supported me generously and gave me a lot of freedom to carry out my own research. It has always been a pleasure to work with and learn from him.

I would also like to thank Prof. Dr. Fred Hamprecht for stimulating discussions and an amicable atmosphere both when working together on our joint project, or when conducting diploma examinations together.

Also, my thanks go to everybody in the research group at the Interdisciplinary Center for Scientific computing and the Institute of Environmental Physics, particularly to Björn Andres, Dr. Günther Balschbach, Dr. Kai Degreif, Achim Falkenroth, Alexandra Herzog, Markus Jehle, Michael Kelm, Marc Kirchner, Daniel Kondermann, Claudia Niuewenhuis, Pavel Pavlov, Roland Rocholz, Dr. Uwe Schimpf and Martin Schmidt. Due to discussions and help whenever it was needed all of them have supported me tremendously throughout my scientific work.

Moreover, I am grateful to Karin Kubessa-Nasri and Barbara Werner who helped me efficiently with more than just administrative tasks.

Interdisciplinary research is only possible through close collaborations with experts in the relevant fields. I am very grateful to have had the opportunity to work together with such people through various projects. I would like to thank all of them! Although they are too numerous to list them all here, I would especially like to thank Dr. Volker Beushausen, Dr. Marc Droske, Dr. Nelson Frew, Prof. Dr. Tetsu Hara, Dr. Roland Pieruschka, Dr. Tobias Preußer, Karsten Roetmann, Prof. Dr. Martin Rumpf, Dr. Jochen Scholz, Prof. Dr. Ulrich Schurr, Dr. Robert Strzodka, and of course all the people I have left out.

Also, I would like to thank the German Science Foundation and NOAA for making this work possible through their funding.

I wish to thank my parents for their continuous support during all these years, my sister and grandparents for their well meant advice.

Last but not least my special gratitude goes to my girlfriend Annegret Brandt, who has always taken a huge share in the success of my scientific work. Through proof reading this

thesis she has learned more about my work than she ever wanted to know!